ELECTRON SPECTROSCOPY OF METAL OXIDES

A Thesis submitted for the Degree of Doctor of Philosophy to the Board of the Faculty of Physical Sciences (Chemistry sub-faculty) in the University of Oxford.

W.R. Flavell, St. John's College

Hilary 1986

ELECTRON SPECTROSCOPY OF METAL OXIDES

W.R. Flavell,

St. John's College.

Submitted for the Degree of Doctor of Philosophy

Hilary, 1986.

ABSTRACT

The validity of the classical dielectric theory of HREELS is investigated. Group theory is employed to obtain a tabulation of SO phonon modes expected to appear strongly in the spectra of given faces of many common crystal structures. The effects of crystalline anisotropy and surface defects are considered in detail. The theoretical investigation is used in conjunction with experiment to obtain a more detailed understanding of the HREELS of rutile (110), (100) and (001) surfaces than has been obtained previously.

XPS, UPS and HREELS are used to investigate the surface composition and electronic structure of Sn-doped In_2O_3 ceramics (containing 1-6 at.% Sn) and thin films. XPS of the well-equilibrated ceramics reveals substantial tin enrichment in the surface atomic layer, with a heat of segregation of $\sim -20 kJmol^{-1}$, and provides evidence for a sub-surface region partly depleted in tin. UPS and HREELS results are consistent with a free-carrier concentration close to the surface considerably below the bulk nominal value.

XPS of the thin films reveals considerably less surface tin segregation, suggesting that thermal equilibrium is not attained during film production. Vacuum annealing dramatically increases the free carrier concentration, as shown by the shift in the surface plasmon frequency in HREELS. There is a substantial discrepancy between the bulk plasmon frequency predicted from HREELS, and that measured directly from optical transmission. The shift and attenuation of the HREELS plasmon is compared with a model where the surface layer is completely depleted of free carriers.

Surface depletion layers have been created on rutile (001), and Sb-doped SnO_2 ceramics containing 0.1 and 1 at.% Sb, by adsorption of Cl_2 and NO_2. The surface coverage of adsorbate is monitored by XPS. Shifts in work function and valence band edge are measured by UPS. HREELS of Cl_2-dosed Sb-doped SnO_2 show changes consistent with a depletion layer model.

ACKNOWLEDGEMENTS

I would like to thank my supervisor, Dr.P.A. Cox, for his invaluable guidance and assistance, and his continuing enthusiasm throughout the last two and a half years. Thanks are also due to Dr.R.G. Egdell of Imperial College, London, for many stimulating discussions and helpful collaboration, particularly in relation to the HREELS studies of rutile.

I would also like to thank all those in the 10 Parks Rd. group who have contributed directly or indirectly to my work: Simon Rowe, Mary Hynes, Rob Sulley and Kevin Joyce. Special thanks are due to Adrian Williams and Phil Tavener, for their patience and help, sometimes in very trying circumstances! The technical and clerical staff of the Inorganic Chemistry Laboratory have provided essential support.

Professor V.E. Henrich of Yale University collaborated in the study of the HREELS of rutile, and together with Professor J. Cunningham of the University College, Cork, kindly provided the rutile crystals, which were prepared by Mr.G. Read of the Clarendon Laboratory. Mr.F. Wondre of the same laboratory helped with Laue Back Reflection, and Mrs.A. Stoker of the Chemical Crystallography Department operated the JEOL JEM 2000FX electron microscope.

I would like to thank my parents for their continuing support and encouragement during my time in Oxford, and finally, my long-suffering husband, Mike, for enduring the production of this thesis.

CONTENTS

Introduction: the Purpose of the Work Undertaken

The work included in this thesis forms part of an extended programme of research being undertaken in this laboratory, dedicated to the investigation of the surface properties of metal oxides, and the adsorption of gases on metal oxide substrates. The techniques employed and the apparatus used are described in Chapters 1 and 2. This programme is important because of the many technological applications of pure or doped metal oxides, for example as gas sensors, transparent electrodes, or heterogeneous catalysts, where surface-adsorbate interactions are of vital importance. The work presented here represents a continuation of previous studies by the author on single-crystal tin dioxide and antimony-doped tin dioxide ceramics.

Chapter 3 describes work aimed at increasing the accuracy with which we are able to predict high resolution electron energy loss spectra of metal oxide substrates. It is particularly important to have a very detailed knowledge of the substrate spectrum before adsorbate studies are carried out. Experimental spectra for the (100), (110) and (001) surfaces of rutile are presented, and compared with theoretical models.

Chapter 4 describes studies aimed at gaining a more detailed understanding of the electronic structure and surface composition of tin-doped indium oxide (ITO) ceramics and thin films. ITO thin films are used as heat-reflecting mirrors, as they reflect almost completely in the infra-red, whilst having high transmittance in the visible region. Despite the technological importance of ITO materials, their surface, and, to some extent, their bulk properties are poorly characterised - for example, there is still considerable controversy

about the way in which the tin dopant is incorporated into the In_2O_3 lattice.

Chapter 5 is concerned with the deliberate creation of surface depletion layers on the n-type substrates TiO_2 and Sb-doped SnO_2 by adsorption of Cl_2 and NO_2. The study of such depletion layers is of relevance to gas-sensor technology, where doped tin dioxide ceramics are already widely employed.

Chapter One

Electron Spectroscopy

1.1 Introduction

Until relatively recently, investigation of the electronic structure of solids has relied heavily on the measurement of transport properties and other bulk transfer characteristics. These properties tend to depend on rather subtle features of the band structure, and may be difficult to relate to chemical models. At best, they provide an indirect means of determining electronic structure and of monitoring the changes which occur with composition. In contrast, electron spectroscopic techniques provide a direct source of information on the electronic energy levels of solids; for example, photoelectron spectra are, to a first approximation, a representation of the joint density of states function (JDOS) of the initial and final states of the system, modulated by the photoionisation matrix elements.

All the spectroscopic techniques described in this work involve the use of either photons or electrons to probe the sample, and the detection of the resulting electrons. As such electrons must travel a distance of roughly one metre between the sample and the detector, high vacuum conditions must be used. The low energies of the electron beams employed, and of the detected electrons, mean that the techniques used show extreme surface sensitivity, all techniques sampling only 10 -100Å into the specimen. Thus electron spectroscopy, whilst yielding information about bulk electronic levels, provides a powerful means of obtaining information specifically about the composition and electronic structure of the surface. Because of the surface sensitivity of the techniques used, samples examined must be kept free of all contaminants for prolonged periods, necessitating the use of ultra-high vacuum (UHV) conditions. A monolayer of contaminants (mainly water and hydrocarbon fragments from the pump oil) will form on a sample in 1 second at pressures of 10^{-6} torr. Thus base pressures of around 10^{-10}torr are

required in order to maintain sample cleanliness for the necessary periods.

The following sections describe the spectroscopic techniques used in this work: X-ray and ultra-violet photoelectron spectroscopy, high resolution electron energy loss spectroscopy and low energy electron diffraction.

1.2 Photoelectron Spectroscopy (PES)

Ultra-Violet and X-ray Photoelectron Spectroscopy both make use of the photoelectric effect to investigate the electronic structure of materials. The two techniques were developed at the same period by different groups of workers; Turner and co-workers[1,2] used UV radiation produced in a helium discharge to study the ionisation of molecules, while Siegbahn and co-workers[3] studied the emission from solids caused by narrow line-width X-rays produced by magnesium and aluminium targets. Recently it has become possible to bridge the gap between the two techniques using monochromated synchrotron radiation, which in some cases is tuneable from photoemission thresholds to the hard X-ray region[4].

A photon $h\upsilon$ incident upon a solid may interact to eject an electron k with kinetic energy E_k. This energy is given by the Einstein equation[5], modified in the case of solids to include the workfunction, φ of the material:

$$E_k = h\upsilon - I_k - \varphi \qquad (1)$$

where I_k is the binding energy of the electron. If the incident radiation is of sufficiently high energy to cause the emission of electrons with a range of different binding energies, these will have a corresponding range of kinetic energies. The resulting distribution

therefore yields information about the band structure of the solid (rather than about discrete energy levels as in the case of atoms and molecules).

1.2.1 The Three-Step Model

A theoretical description of photoemission from solids must take into account both the band structure of the solid, and the fact that photoelectrons are created in the bulk of the sample, and must propagate to the surface in order to be detected. The three-step model of Berglund and Spicer[6] assumes that the three main physical ingredients, electron excitation, propagation, and ejection, can be decoupled and treated sequentially, each by a simple model. This model has been succeeded by "one-step" theories[7,8,9] which treat the three stages simultaneously, but the three-step model is quite adequate in many cases, and has the advantage that it is physically transparent. The three steps are discussed below:

i) Excitation of an electron of energy E_i in the bulk of the solid to the excited level $E_j = E_i + h\upsilon$. Assuming to a first approximation, that steps ii) and iii) make no contribution to the appearance of the spectrum, then electrons excited to states with energies greater than the work function, φ, will contribute to the photoemission. The spectrum will then depend on the transition probability between levels i and j. The probability of transition is generally proportional to both the density of occupied states at E_i and the density of empty states at E_j; the energy distribution curve obtained (at least in the angle-integrated technique - section 1.2.2) is representative of the joint density of states (JDOS) function of the initial and final states. In XPS, as opposed to UPS, because of the higher energy photons used, the

resulting photoelectron will be excited to the structureless high energy part of the DOS, which can, for most purposes, be treated as a continuum. The resulting spectrum is then dependent only on the occupied DOS of the ground state.

The dependence of a photoelectron spectrum on some density of states function will be modulated by the photoionisation cross-sections, σ. These are proportional to the squares of matrix elements representing the probability of transition between the initial and final states. The intensities of PE bands will thus be weighted according to the cross-sections of the orbitals which contribute to them. The matrix elements depend on the exciting photon energy in a complex way which is related to the form of the radial distribution function of the initial state wavefunctions. However, these variations are now well documented, and tables of both semi-empirical and theoretical cross-sections have been constructed for a variety of incident photon energies[10,11]. In general, the matrix elements tend to become smaller as the exciting photon energy increases and the initial and final states become more widely separated. The energy dependence of the cross-sections can be advantageously used to extract the partial densities of valence states, i.e. to split the DOS into components of a given atomic parentage[12].

ii) Propagation of the excited electron to the surface of the solid. The excited electrons travelling through the material to the surface have a high probability of undergoing inelastic collisions, resulting in a loss of kinetic energy. This gives rise to an inelastic or secondary electron background which modifies the spectrum, producing a secondary structure to the low kinetic energy side of the primary photoemission features. Due to this strong

interaction of electrons with solids, only a small proportion of the primary photoelectrons (those created relatively close to the surface) actually emerge from the sample to reach the detector. Experimentally it is found that the attenuation of the primary photoelectron flux is given by equation (2)[13]:

$$I(x) = I_o(x)\exp(-x/\lambda) \qquad (2)$$

where I(x) is the emerging flux of photoelectrons, and $I_o(x)$ is the flux of electrons of energy E originating at a depth x below the surface. λ is the electron escape depth or mean-free-path length. Leckey and co-workers[14,15] have shown that λ in a wide range of materials (including metals, inorganic insulators and semiconductors) is dependent on electron energy as $AE^{3/4}$, in the range $200<E<2000$eV, where A is sample dependent. "Universal curves" which represent a broad range of mean-free-path data for particular types of substrate have been compiled; a typical example for heavy metals is shown in figure 1[16].

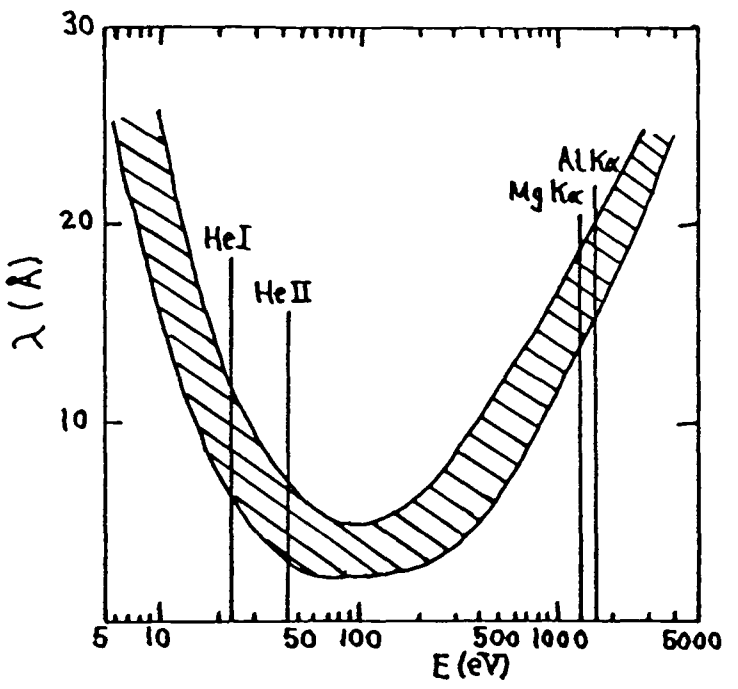

Figure 1:[16] The universal curve of electron attenuation length in various heavy metals, drawn as a band encompassing most of the existing experimental data.

Whilst it can be seen that λ is larger in XPS than in UPS ($\sim$20Å c.f. $\sim$ 10Å in UPS), it is apparent that both techniques are extremely surface sensitive. The effectively sampled depth extends to only around 3λ[17], defining the surface sensitivity of both techniques to be between roughly 30 and 60Å.

Four processes contribute to the photoelectron-solid interaction; electron-phonon interactions, electron-electron interactions (where the emitted electron causes the ejection of a second spectator electron), interband transitions (where the emitted electron causes the excitation of another electron from a valence band to a conduction band), and plasmon excitations (collective oscillations of the valence or conduction electrons of a solid). The latter are responsible in the main for the very broad minimum at approximately 100eV in the universal curve of figure 1. At kinetic energies above the plasmon energy (typically 10-15eV in metals), electrons travelling through metals are subject to energy loss via plasmon creation, and the electron mean-free-path length decreases markedly. Surface sensitivity in semiconductors is similar to that in metals, although as yet not so well characterised. In molecular solids, the surface sensitivity appears to be much lower, as the plasmon loss mechanism is absent[18]. Electron-phonon interactions are usually only important for electrons of low KE (<5eV), as phonon energies are small (<0.2eV). Interband transitions generally have energies in the range 1 - 10eV for metals or semi-conductors, and may create artefacts to the low energy side of the primary peak in XPS spectra (see section 1.2.6). However, the major part of the inelastic background in a photoelectron spectrum is due to electron-electron interaction. The resulting electrons are known as the "true

secondary electrons", and are located in the very low energy range. As only a small amount of energy is transferred in each collision, a single primary electron can create several secondary electrons, and the background tends to rise steeply at low energies.

iii) Ejection of the electron from the surface of the solid into the vacuum. The photoelectron must overcome a potential energy barrier at the surface in order to escape from the solid into the vacuum. This shifts the spectrum to lower kinetic energy. The effect is particularly pronounced in instances of sample charging (section 1.2.4 iii)), which is observed when insulating, and in some cases, semi-conducting solids are subjected to ionising radiation. The resulting photoemission causes the sample to become positively charged, even though it may be earthed.

Escape from the surface involves a matching at the vacuum interface between the excited state and a vacuum free electron state. This matching determines the angular effects in photoemission which are discussed in the next section.

1.2.2 Conservation of Momentum

In a crystalline solid, transitions from E_i to E_j are normally direct. This is illustrated in figure 2[19], which shows a direct transition at some point along an arbitrary direction in k-space. If the resulting excited electron propagates to the surface without scattering, the escape across the surface is determined by the conservation of wave vector parallel to the surface,

$$\underline{K}_{\parallel} = \underline{k}_{\parallel} + \underline{G}_{\parallel} \qquad (3)$$

Here $\underline{K}_{\parallel}$ is the parallel component of the external photoelectron

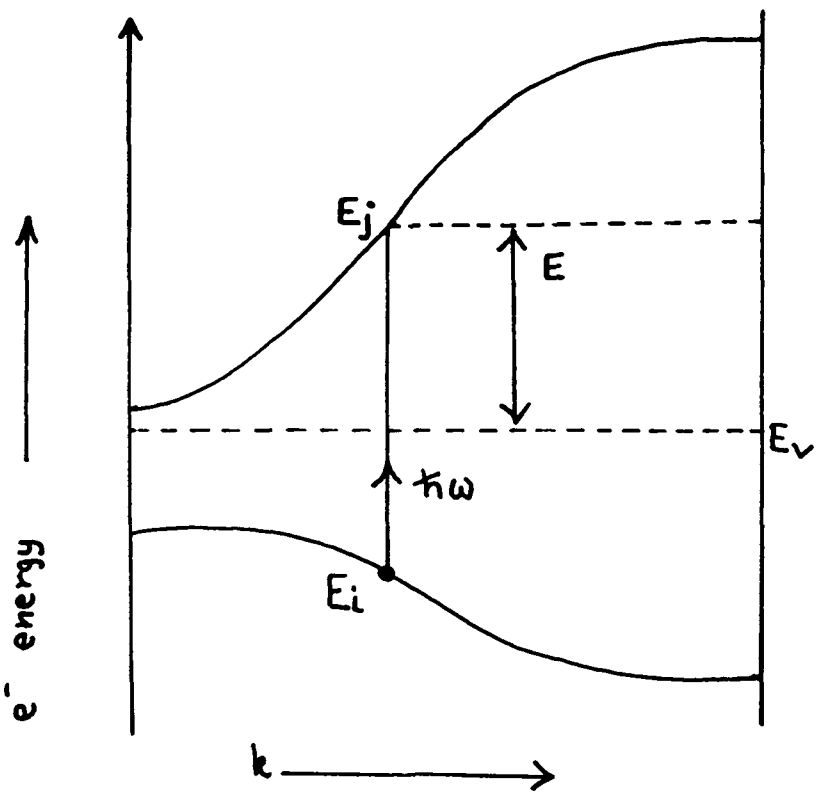

Figure 2:[19] Energetics of a direct transition at a point along some arbitrary direction in k-space. E_v is the vacuum level and E represents the kinetic energy of the photoemitted electron.

wave vector, $\underline{k}_{\parallel}$ is the parallel component of the reduced vector $\underline{k}$ of the electron state within the solid, and $\underline{G}_{\parallel}$ is the parallel component of any reciprocal lattice vector $\underline{G}$. Various $\underline{G}$ vectors are included, because the final state wavefunction is a Bloch wave containing components of the form $\exp(i\underline{k}.\underline{r})$ and $\exp[i(\underline{k}+\underline{G}).\underline{r}]$. For each component there exists the possibility of matching onto a running wave outside the crystal. Thus the photoelectron can emerge from the crystal in a number of different directions. The kinetic energy of the emerging photoelectron is

$$E = \hbar^2(\underline{K}_{\perp}^2 + \underline{K}_{\parallel}^2)/2m = E_j(\underline{k}) - E_v \qquad (4)$$

where E_v is the vacuum level, and $\underline{K}_{\perp}$ is the component of the photoelectron wave vector perpendicular to the surface. Substituting for $\underline{K}_{\parallel}$ from (3):

$$\hbar^2\underline{K}_{\perp}^2/2m = [E_j(\underline{k})-E_v] - \hbar^2(\underline{k}_{\parallel} + \underline{G}_{\parallel})^2/2m \qquad (5)$$

From (3) and (5), it is seen that if $E_j(\underline{k})$ and E_v are known, then $\underline{K}_{\perp}$ and $\underline{K}_{\parallel}$ are fixed. Thus, the direction of photoelectrons generated by bulk optical transitions are completely determined, given a good band

structure calculation. It would be very useful if this argument could be reversed, i.e. if knowing the measured energies and directions of the emitted electrons, the E vs $\underline{k}$ dispersion relations for the electronic states within the solid could be deduced. However, although $k_{\parallel}$ is determined by equation (3), $\underline{k}_{\perp}$, the component of $\underline{k}$ perpendicular to the surface does not appear explicitly in any of the equations given above, and therefore remains indeterminate. The presence of the surface, and the short mean-free-path of the photoelectrons in the solid destroy the translational symmetry in the direction perpendicular to the surface that is necessary to define $k_{\perp}$ as a good quantum number. Thus the three dimensional band structure of a solid cannot be determined directly from experiment. However, a number of models have been devised that make an assignment of $k_{\perp}$ to each transition possible (for example, the direct transition model[20]). There are also a number of special situations in which the ambiguity in the definition of k is removed. One of these is normal emission, where $\underline{K}_{\parallel}=0$. The bulk electronic states can then be sampled as a function of $k_{\perp}$ along a specific line in k-space.

In general, for a three-dimensional solid, the most profitable way of proceeding is to take angle-resolved measurements of the photoemission, to calculate band structure predictions and then to achieve a match between the two. Thus angle-resolved photoelectron spectroscopy (ARPES) is increasingly being used as a powerful technique for mapping band structure. The samples used must be single crystals. In polycrystalline samples or with disordered materials, which lack any long range order, k is no longer well defined, and the resulting spectra are effectively "angle integrated". The uncertainty $\Delta k_{\parallel}$ attached to $k_{\parallel}$ depends on the acceptance angle of the electron analyser and the square root of the electron energy. Only at low electron energies is the resolution in $k_{\parallel}$ good enough to locate a transition to within a small fraction of the typical dimension of a Brillouin zone[19]. Thus angle-

resolved measurements are possible only in the UV region: X-ray photoelectron spectra may be regarded as angle integrated, being representative of a total density of states function. The spectrometer used in our laboratory has a fixed angle between the source of radiation and the analyser, so angle dispersive spectra cannot be obtained. In addition, the direct transition probability is likely to be low for the polar materials studied (due to interaction with phonons etc.). This, combined with the relatively large acceptance angle of the spectrometer, means that the resulting ultra-violet photoelectron spectra may be regarded as sampling the whole Brillouin zone, even when single crystal samples are used.

1.2.3 Fine Structure

The principal sources of fine structure in PES are described below:

a) Satellites in the Exciting Radiation

Both the UV and X-ray sources used in this work were unmonochromated, so that the effects due to such satellites must be considered.

i) UPS

In a helium discharge, the two major lines are He Iα (21.22eV) and He IIα (40.81eV). The He Iα line is the strongest emission line, corresponding to the $^1P \longrightarrow ^1S$ transition ($1s2p \longrightarrow 1s^2$) in neutral helium. Other He I lines are also present (labelled β, γ etc), corresponding to the $1snp \longrightarrow 1s^2$ (n=3,4...) series of transitions. Because of internal de-activation of helium atoms in the higher excited configurations[21], these lines are weak. The

effect of these satellites is to create faint "echoes" of the spectrum to higher kinetic energy, which can obscure the often weak conduction band of the sample. It is therefore essential that these satellites are stripped from the spectra (by computer programme, Appendix I) before the conduction to valence band intensity ratio can be obtained.

The He IIα line is the most intense of the He II lines, and is due to the 2p$\longrightarrow$1s transition in the He^+ ion. However,the flux of He IIβ photons ($h\upsilon$=48.37eV) may account for roughly 10% of the total HeII output. This problem can be overcome by monochromation, but the resulting flux is very much reduced.

The relative intensities of the He lines tend to depend on the precise operating conditions, typical values being shown in table 1[22,23].

Table 1[22,23]

line	energy/(eV)	relative intensity
He I α	21.22	100
He I β	23.09	1.7
He I γ	23.75	0.17
He II α	40.81	1.25
He II β	48.87	0.13

The intensity ratios of He Iα,$\beta$and γ radiation are easily determined by taking a spectrum of a sample having a strong Fermi edge, such as the platinum sample holder or a ruthenium single crystal. These ratios can then be entered in the satellite stripping programme as variable parameters. The relative proportions of He I and He II radiation produced depend on the pressure of helium used; if the pressure is lowered, the proportion

of He II radiation increases (Chapter 2, section 2.2 ii)).

ii) XPS

Satellite structure is very much more prominent in XPS than in UPS. The two commonly used sources are Mg Kα and Al Kα. The strongest lines in both cases are Kα_1 and Kα_2. These correspond to the transitions $^2P_{1/2,3/2} \longrightarrow {}^1S$ in singly ionised Al or Mg, and form a close doublet. However, a number of other lines are also present in the unmonochromated radiation. The strongest of these are the K$\alpha_{3,4}$ lines which arise from the equivalent transitions in doubly ionised Al or Mg. These lines appear as a "shadow" to the high kinetic energy side of the principal peaks, and can often create difficulties in measuring intensities. K$\alpha_{5,6...}$ lines, corresponding to multiple ionisations are also present with very low intensity, and there is a very small contribution from Kβ radiation. The satellites may be removed by use of a monochromator, but this reduces the X-ray flux. Alternatively, the spectra may be stripped of satellite peaks using computer programmes.

The intensities of the main XPS lines and their satellites are given in table 2^{24}.

Table 2^{24}

	Mg		Al	
line	E_{rel}/eV	I_{rel}	E_{rel}/eV	I_{rel}
K$\alpha_{1,2}$	0	1	0	1
Kα_3	8.4	0.085	9.6	0.072
Kα_4	10.1	0.046	11.6	0.036

b) Spin-Orbit Coupling

This causes fine structure for electrons with orbital angular momentum $l \neq 0$. Ionisation of an electron from a closed shell leaves an electron with resultant total angular momentum $j = l \pm 1/2$. An example is seen in the XPS of the tin doped indium oxide ceramic samples shown in figure 4b). Both tin and indium 3d peaks are split into $^2D_{5/2,3/2}$ doublets. The intensity ratio should be given by their degeneracies:

$$[2j_2+1]/[2j_1+1] = I(^2D_{5/2})/I(^2D_{3/2}) = 6/4 \qquad (6)$$

Ionisation from a partially filled shell may result in a large number of peaks, as there will be several possible J values in the ground and excited states.

c) Exchange Splitting

This effect is seen in photoionisation from an unfilled shell, or from a closed shell in the presence of an unfilled shell, and is due to exchange interaction between the different spin states which arise on ionisation. In the case of orbitally degenerate shells where $l \gg 1$, analysis of this splitting may be complex.

d) Shake-up and Shake-off Features

This is often apparent in XPS, resulting in peaks on the low KE side of the parent peak. In shake-up, a second spectator electron is excited to a higher energy level, whilst in shake-off, the second electron is ejected completely. In shake-off events, the excess energy is thus distributed between two electrons, and they do not contribute discrete structure to the spectrum. Both processes have been treated by the sudden approximation[25], which leads to the

so-called monopole selection rule, which implies that shake-up can only take place between initial and final states having the same symmetry[26]. However, this result must be treated with caution[27].

1.2.4 Line Broadening Effects

Spectral linewidth in PES is determined by a number of factors:

i) The intrinsic linewidth of the exciting radiation. For UPS this is of the order of a few meV or less. However, in XPS, due to the high energy of the exciting radiation, the natural linewidth (FWHM) is around 1eV, and is thus a major factor in determining the resolution obtained. The higher resolution offered by UPS makes it the preferred technique for the study of the valence bands of solids, as different bands may be distinguished, even when they are quite close in energy. Although valence bands may be observed in XPS, it is often difficult to separate them. XPS is thus generally used for observing core levels, which are inaccessible to UV radiation. UPS and XPS therefore provide complementary information about electronic structure.

ii) The lifetime of the core hole. The lifetime broadening of a signal in XPS is given by the Uncertainty Principle:

$$\tau . \Delta E \geqslant (1/2)\hbar \qquad (7)$$

where τ is the lifetime of the core hole, and ΔE is the uncertainty in its energy. The hole may be destroyed by either X-ray fluorescence or Auger emission. The KE of an Auger electron is independent of the exciting radiation, as it is determined solely by internal transitions within the ionised core. Thus, Auger signals may be differentiated from XPS signals simply by changing the energy of the exciting radiation. For light atoms, radiationless Auger decay is usually more probable than X-ray

fluorescence, while the reverse is true for heavier elements.

iii) Sample charging. This may create problems when the samples used are insulating or semi-conducting (as are the majority of the samples studied in this laboratory). As discussed earlier (section 1.2.1 iii)), the effect of sample charging in UPS is usually to shift the entire spectrum, often by several electron volts, to higher binding energy. In XPS, the effects of sample charging may be inhomogeneous, causing shifting, splitting and broadening of the peaks.

iv) Instrumental broadening. This is dependent on the resolving power $R=E/\Delta E$ of the analyser system. ΔE is the resolution obtainable for electrons of energy E. For a fixed R, ΔE is better at lower electron energies: electron energies are thus measured by retarding the electrons on entry into the analyser. The resolving power increases with the length of the focussed electron trajectory.

1.2.5 Features of Ultra-Violet Photoelectron Spectra

A typical valence band photoelectron spectrum (figure 3) consists of a primary signal overlying a secondary electron background. There are sharp edges at both high and low kinetic energies.

The edge observed at high kinetic energy is known as the Fermi edge, E_f, and corresponds to the ejection of electrons from the highest occupied states of the system. At temperatures above absolute zero, the cut-off is not completely sharp, being broadened by a Fermi-Dirac function representing the population distribution of thermally excited electrons. The spectrometer is calibrated so that the Fermi energy for all samples corresponds to the energy of the incident radiation (21.22eV for He Iα). This is made possible by the electrical contact to earth through the spectrometer.

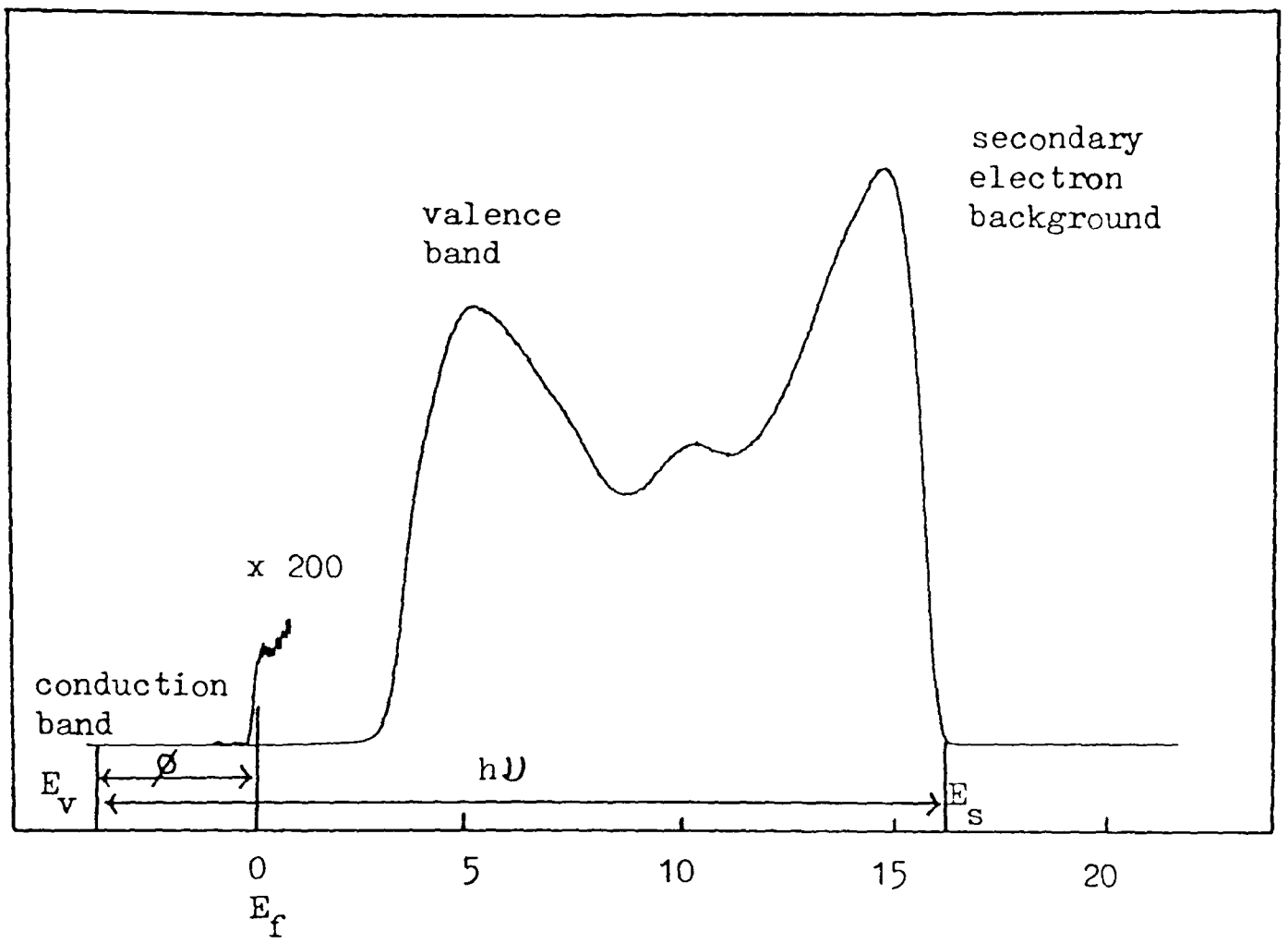

Figure 3: Features of a typical UPS spectrum. The sample is polycrystalline indium oxide containing nominally 6 at.% tin. Satellites due to He Iβ and γ radiation have been removed.

φ work function
$h\upsilon$ energy of incident radiation
E_s SEED edge
E_f Fermi edge
E_v vacuum level

The edge at lower kinetic energy is known as the Secondary Electron Distribution Edge (SEED edge). The low KE onset of secondary electron emission defines the true zero of the photoelectron KE scale for the sample in question, as the slowest electrons leave the surface with zero kinetic energy. The position of the vacuum level, E_v can thus be established - it must lie 21.22eV (the photon energy, $h\upsilon$) higher in kinetic energy. The work function, φ, (the separation of the vacuum and Fermi levels of the sample), is then the energy separation between E_v and the observed high KE photoemission threshold. In principle, this enables the determination of the workfunction, φ [28].

From figure 3, it follows that

$$\varphi + E_f = E_s + h\upsilon \qquad (8)$$

As the spectrometer is calibrated such that $E_f = h\upsilon$, then $E_s = \varphi$. Measurement of the position of the SEED edge will therefore also give an estimate of the workfunction, although in practice a small negative bias (several volts) is applied to the sample to allow the transmission of electrons leaving the sample with zero kinetic energy. This is then subtracted from the value of E_s obtained.

1.2.6 Features of X-ray Photoelectron Spectra

A typical widescan X-ray photoelectron spectrum is shown in figure 4a). Again, this consists of a series of primary peaks overlying a secondary electron background which rises steeply to low kinetic energy. Auger peaks are indicated. Figure 4b) shows an expanded scan of a part of this spectrum, showing 3d peaks due to tin and indium, and the 1s peak of oxygen. The 3d peaks are clearly split due to spin-orbit coupling. Also evident are satellites due to $K\alpha_{3,4}$ radiation, and some structure due to shake-up following the indium 3d peaks. The underlying secondary electron background tends to rise in a stepwise fashion, following each major primary peak - this is most evident in the case of the indium 3d peaks. It can be seen that there is a definite gap between these peaks and the onset of the increased background following them. This type of feature is obviously associated with some minimum photoelectron energy loss mechanism, and thus with the band gap of the material. This may need to be taken into account in subtracting secondary electron background from the spectrum.

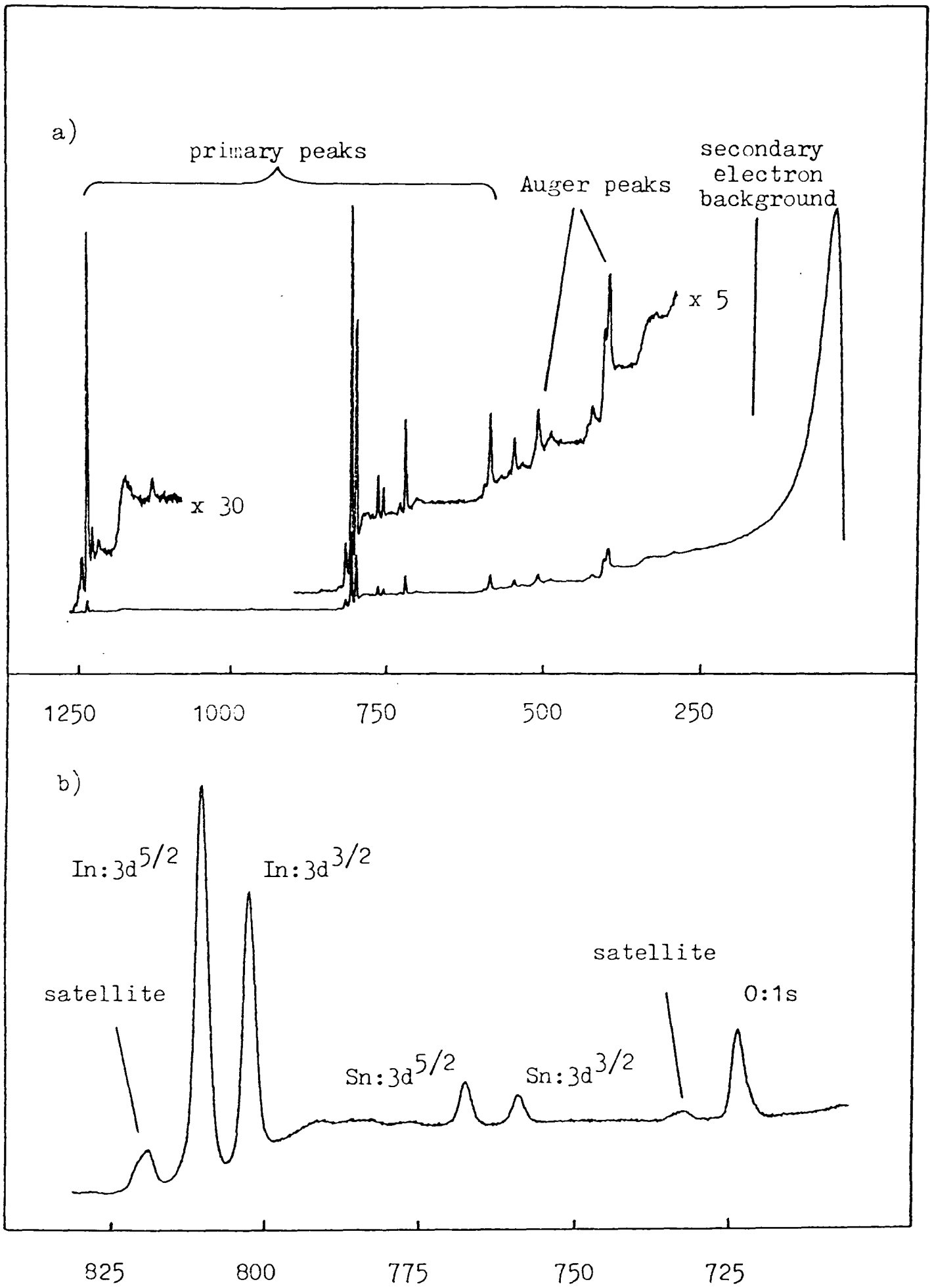

Figure 4: Typical wide scan (4a)) and narrow scan (4b)) X-ray photoelectron spectra. The sample is polycrystalline indium oxide containing nominally 4 at.% tin.

1.3 Electron Energy Loss Spectroscopy

Electron energy loss spectroscopy (EELS) is one of the most powerful techniques of electron spectroscopy, and is well suited to the study of vibrational and electronic excitations. It is a relatively modern technique which has been developed extensively over the last fifteen years. It has been used in the study of gas phase samples[29] (where electronically "forbidden" transitions can be observed), and in the study of thin films[30,31,32] by transmission of high energy electron beams (5 - 50keV). In the last decade a further application has been developed using the reflection of highly monochromated low energy beams (0 - 50eV) in UHV conditions to study surfaces. Vibrational and electronic excitations are observed as energy losses in the electron beam reflected by the sample.

In the present work, high resolution electron energy loss spectroscopy (HREELS) is used. The resolution offered by HREELS (around 15meV in our system), though substantially less than is customarily encountered in optical spectroscopies, is adequate for study of both the vibrational excitations of clean surfaces and those of molecules adsorbed on the surface. Moreover, as the incident electron beam is readily tuneable, the scope of the technique is easily widened to include higher energy electronic excitations, such as plasmon excitations, and single electron interband and intraband transitions. The penetration depth of the technique depends on the energy of the beam used and to some extent on whether the sample is metallic or not. However, it is typically of the order of 50Å, so the technique is capable of high surface sensitivity. The method is non-destructive at the low energies and incident currents used. This is particularly important when studying metal oxide samples which are often very

susceptible to beam damage under other techniques, such as XPS.

The semiclassical theory described by Mahan[33] leads to an equation describing the surface loss spectrum; this theory is discussed in detail in Chapter 3. For the present purposes, it is sufficient to note that this theory yields

$$P_{surf}(\omega) \propto Im(\epsilon(\omega)+1)^{-1} \tag{9}$$

where $P_{surf}(\omega)$ represents the surface loss probability and $\epsilon(\omega)$ is the complex dielectric function of the material. Only surface losses are detected in EELS used in the reflectance mode with low KE incident electrons, and these occur when

$$Re(\epsilon(\omega)) = -1 \tag{10}$$

In contrast, for bulk losses (which may be observed in the transmission mode), we have:

$$P_{bulk}(\omega) \propto Im(\epsilon(\omega))^{-1} \tag{11}$$

which attains a maximum when

$$Re(\epsilon(\omega)) = 0 \tag{12}$$

Four specific types of excitation commonly result in surface loss peaks; phonon excitations, plasmon excitations, single electron interband and intraband transitions, and excitations of adsorbed molecules. These are discussed below.

1.3.1 Phonon Excitations

These are the extended vibrational excitations of crystalline solids, which propagate through the medium as elastic waves. In a three-dimensional lattice with a basis, for each value of $\underline{k}$, the wave vector, there are 3N normal modes, where N is the number of ions in the basis. Three of the 3N modes are the so-called "acoustic" modes, in which all ions within a primitive cell move essentially in phase as a

unit under the influence of a net force from surrounding cells. These modes are thus analogous to the 3 translational degrees of freedom of an N-atomic molecule, and vanish linearly with k in the long wavelength limit. At this limit, λ is infinite, corresponding to a bulk translation. As $k \longrightarrow 0$, the wave velocity c ($=\omega/k$) is a constant, corresponding to the speed of sound in the solid. The three acoustic modes are made up of two transverse acoustic (TA) modes (with the direction of propagation perpendicular to the atomic displacements), and one longitudinal (LA) mode (with the direction of propagation parallel to the atomic displacements).

The remaining 3(N-1) modes are "optical" - here the ions within each primitive cell are executing essentially a molecular vibratory mode, which is broadened out into a band of frequencies by intercellular interactions. These modes are equivalent to the 3(N-1) vibrational and rotational degrees of freedom of an N-atomic molecule. As such, their frequencies are largely determined by bond force constants and angle strains within the unit cell - quantities independent of k. The longer-range k-dependent interactions between cells, while still serving to propagate the waves, have little effect on the frequency. The resulting dispersion curves (frequency vs momentum) are therefore much flatter than for the acoustic modes. A typical dispersion curve for the case N=2 is shown in figure 5[34].

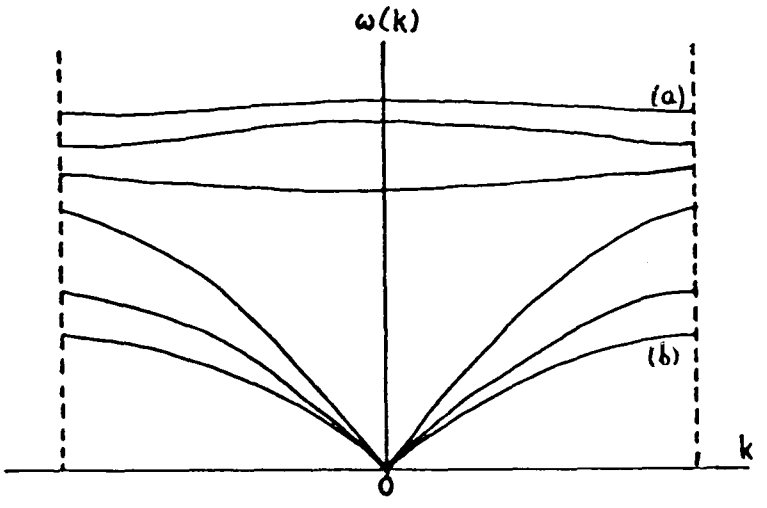

Figure 5:[34] Typical dispersion curves for (a) optical and (b) acoustic phonons along a general direction in k-space for a lattice with a two-ion basis.

Only the first Brillouin zone ($-\pi/a \leqslant \underline{k} \leqslant +\pi/a$, corresponding to $\infty \rangg \lambda \rangg a$, where a is the lattice parameter) is shown, since solutions for $\lambda < a$ are simply multiples of solutions at longer wavelength, and so the dispersion curves repeat in subsequent zones. The optical modes may be split into transverse and longitudinal modes in the same way as the acoustic modes. In general, the energy of a longitudinal mode is greater than that of a transverse mode due to electrostatic effects. Optical modes are so-called because in ionic crystals they give rise to oscillating dipoles which interact with electromagnetic radiation. The electric field of the electron beam in the EELS experiment varies only longitudinally, so in high energy transmission EELS only the longitudinal modes are normally observed (although the transverse optical modes may appear weakly[35]). In contrast, experiments using photons couple only to the TO modes, as the incident beam is then a transverse electromagnetic wave.

In the reflection EELS experiment, where only the surface of the specimen is sampled, phonon modes are observed having frequencies lying between the bulk LO and TO phonon frequencies. These are the so-called surface optical (SO) phonons or Fuchs Kliewer modes[36], and do not correspond to either transverse or longitudinal modes. They may be regarded as arising from the changes in electrostatic effects which occur when the bulk periodicity is terminated in one dimension due to the presence of the surface. The SO phonons are long wavelength optical vibrations which propagate along the surface of the crystal in two dimensions, their spatial variation being represented by $\exp(i\underline{k}_{\parallel} \cdot \underline{\rho}_{\parallel})$ where $\underline{\rho}_{\parallel}$ represents the xy plane. It can be shown that a wave having such spatial variation must necessarily decay as $\exp(-k_{\parallel} z)$ both above and below the surface, where z is the perpendicular distance from the substrate[37]. Thus, SO phonons extend roughly a distance $k_{\parallel}^{-1}$ into the

bulk; this usually corresponds to several hundred angstroms, as $\underline{k}_{\parallel}$ is small.

The SO phonons retain their surface character only in the long wavelength limit (small $\underline{k}_{\parallel}$) near the Brillouin zone centre. Further from the zone centre, they disperse into the frequency bands of bulk modes having wave vectors $\underline{k}$ with projection onto the surface plane equal to $\underline{k}_{\parallel}$. The energy associated with the SO modes then propagates into the bulk in the form of bulk phonons[37]. For the same reason, it is clear that the frequency of a SO phonon must lie outside the frequency bands of bulk phonons having the same surface plane projected wave vector $\underline{k}_{\parallel}$ if it is to retain its surface character.

As the SO phonons decay only slowly with distance from the surface, they generate long range electric fields above the crystal surface on approach of an electron. The resulting scattering is then mainly in the specular direction, and may in principle be accounted for by theories based on the dielectric response of the surface to the potential of the incident electron. The observation of surface phonons in this "dipole-scattering" regime forms the basis of Chapter 3 of this thesis, and is discussed in detail there.

In the HREELS experiment, SO phonon losses appear as peaks immediately to the right of the elastic peak, having energy losses typically less than 0.2eV[34]. High resolution (of the order of 15meV or less) is therefore required to observe the fine structure of the spectra.

1.3.2 Plasmon Excitations

A plasmon is a collective oscillation of the conduction electrons of a solid. Thus in materials containing a high concentration of free

or quasi-free donor electrons, it is possible to excite a plasmon by passing electrons through a thin film of the material, or by reflecting electrons from the sample as in EELS. The Coulomb field of the electron couples with the electrostatic field fluctuations of the plasma oscillations. A plasmon may be viewed as a longitudinal optical phonon in which the electron gas plays the part of the negative ions.

If we approximate the dielectric function $\epsilon(\omega)$ to the Drude dielectric function for a free-electron gas, then

$$\epsilon(\omega) = \epsilon_{\infty} - ne^2/m^* \epsilon_o \omega^2 \qquad (13)$$

Here n is the concentation of oscillators, each with dynamic charge e and effective mass m^*, ϵ_o is the permittivity of free space, and ϵ_{∞} is the background (high frequency) dielectric constant.

By substituting this expression into equations (10) and (12), we obtain

$$\omega_{surf}/\omega_{bulk} = [\epsilon_{\infty}/(\epsilon_{\infty}+1)]^{1/2} \qquad (14)$$

Thus, in general, surface losses will appear at slightly lower energies than the corresponding bulk losses. This phenomenon is discussed in greater detail in Chapter 4 section 4.6.3. Surface plasmons are usually seen as relatively broad peaks in HREELS, at higher energy than the phonon peaks (typically 0.3 - 1eV).

1.3.3 Single Electron Excitations

Single electrons may also be excited by the incident electron beam giving rise to inter- and intraband transitions and consequent loss features in the spectrum. Interband transitions, such as those between the conduction and valence bands of semi-conductors can make a substantial contribution to the loss spectrum in the appropriate energy

loss range. These transitions are often broad and featureless, reflecting the band structure of the solid. However, direct transitions of localised electrons may sometimes be observed. One such example of this is in the HREEL spectrum of NiO[38], where the ligand field transitions of the localised Ni:3d levels have been observed below the absorption edge. Here peaks corresponding to the transitions $^3A_{2g} \longrightarrow {}^3T_{2g}, {}^1E_g, {}^3T_{1g}(F)$ and $^3T_{1g}(P)$ in Ni^{2+} are clearly seen, with energies corresponding well with those obtained from UV absorption experiments.

1.3.4 Excitations of Adsorbed Molecules

Excitations of molecules adsorbed on the surface, whether vibrational or electronic, may give rise to EELS features. Vibrational losses in particular, may reveal valuable information. The number and positions of the peaks may indicate whether the adsorbate is associatively or dissociatively adsorbed onto the surface. In some cases its configuration relative to the surface and the strength of its bonding to the surface may be inferred.

1.4 Low Energy Electron Diffraction

As has been discussed (section 1.3.1), the dominant scattering mechanism in EELS is dipole scattering, producing pronounced forward scattering. At large deflection angles, however, impact scattering, in which the electron beam is scattered by the localised atomic potential of the ions and atoms at the surface becomes important. A special case of impact scattering occurs when the beam is coherently and elastically scattered. Constructive interference of the scattered beams occurs when the momentum change involved satisfies the Bragg condition, and a low

energy electron diffraction (LEED) pattern results. The background intensity on which the pattern is superimposed is due to incoherent, inelastic scattering, and is known as the thermal diffuse background.

In common with EELS, LEED is sensitive only to layers of the sample close to the surface, in contrast to X-ray diffraction which samples the bulk. Accordingly, the interpretation of LEED data is based on two-dimensional nets, rather than three-dimensional lattices. Because of the two-dimensional periodicity of a perfect surface, scattering occurs with wave vector conservation in a plane parallel to the surface. For elastic scattering, the scattering amplitude is non-zero only when

$$\underline{k}_{\parallel}^{S} = \underline{k}_{\parallel}^{I} + G_{\parallel} \tag{15}$$

where $\underline{k}_{\parallel}^{I}$, $\underline{k}_{\parallel}^{S}$ are the parallel components of the incident and scattered electron wave vectors, and $G_{\parallel}$ is a surface reciprocal lattice vector describing diffraction. Thus, from a perfectly periodic structure, we have only Bragg scattering, satisfying the 2-dimensional Bragg condition:

$$n\lambda = d\sin\theta \tag{16}$$

The wavelength of the electrons is given by the de Broglie relationship,

$$\lambda(\text{Å}) = 12.26/[E(eV)]^{1/2} \tag{17}$$

where E is the beam energy, typically in the range 50 - 100eV. λ is thus typically in the range 1.2 - 1.7Å, and must remain less than the interatomic spacing for diffraction to be observed.

Although there are fewer distinct 2-dimensional Bravais nets than 3-dimensional Bravais lattices, in practice the interpretation of LEED patterns may be more difficult than the interpretation of XRD patterns, as it may often be difficult to distinguish between two lattices. The presence of a glide plane may lead to systematic absences. However,

LEED may yield important qualitative information, for example about overlayer reconstructions or the presence of an adsorbate layer commensurate with the lattice. Some information about the degree of periodicity of the surface may be revealed, for example irregular stepping of the surface results in streaking of the diffraction spots in the direction of the disorder. Faceted surfaces may usually be distinguished by altering the beam energy. On increasing the beam energy, the LEED spots should converge towards the (0,0) specular beam (as $\theta \propto \lambda \propto 1/E^{1/2}$). However, on a faceted surface, there are different (0,0) beams corresponding to different facets, and this is apparent from the way in which the pattern changes with beam energy. The electron beam used in LEED is thermally broadened ($\sim$500meV FWHM), and has some angular divergence. Because of this, the electrons have a limited coherence length at the surface, typically $\sim$50Å. Thus disorder which occurs on larger scales than this will not be detected.

Uncertainties in the sample position relative to the screen, and in the beam energy using our system mean that the technique is only used to extract the type of qualitative information described above. Analysis of the diffracted beam intensities (which show pronounced beam energy dependence[39]) is not possible.

Chapter Two

The Spectrometer

2.1 General Description

All the electron spectra presented in this thesis were obtained using an ESCALAB 5 spectrometer (VG Scientific, East Grinstead, U.K.), shown in figure 1[40]. The spectrometer has been discussed in detail elsewhere[41,42,43], and only a brief description will be attempted here.

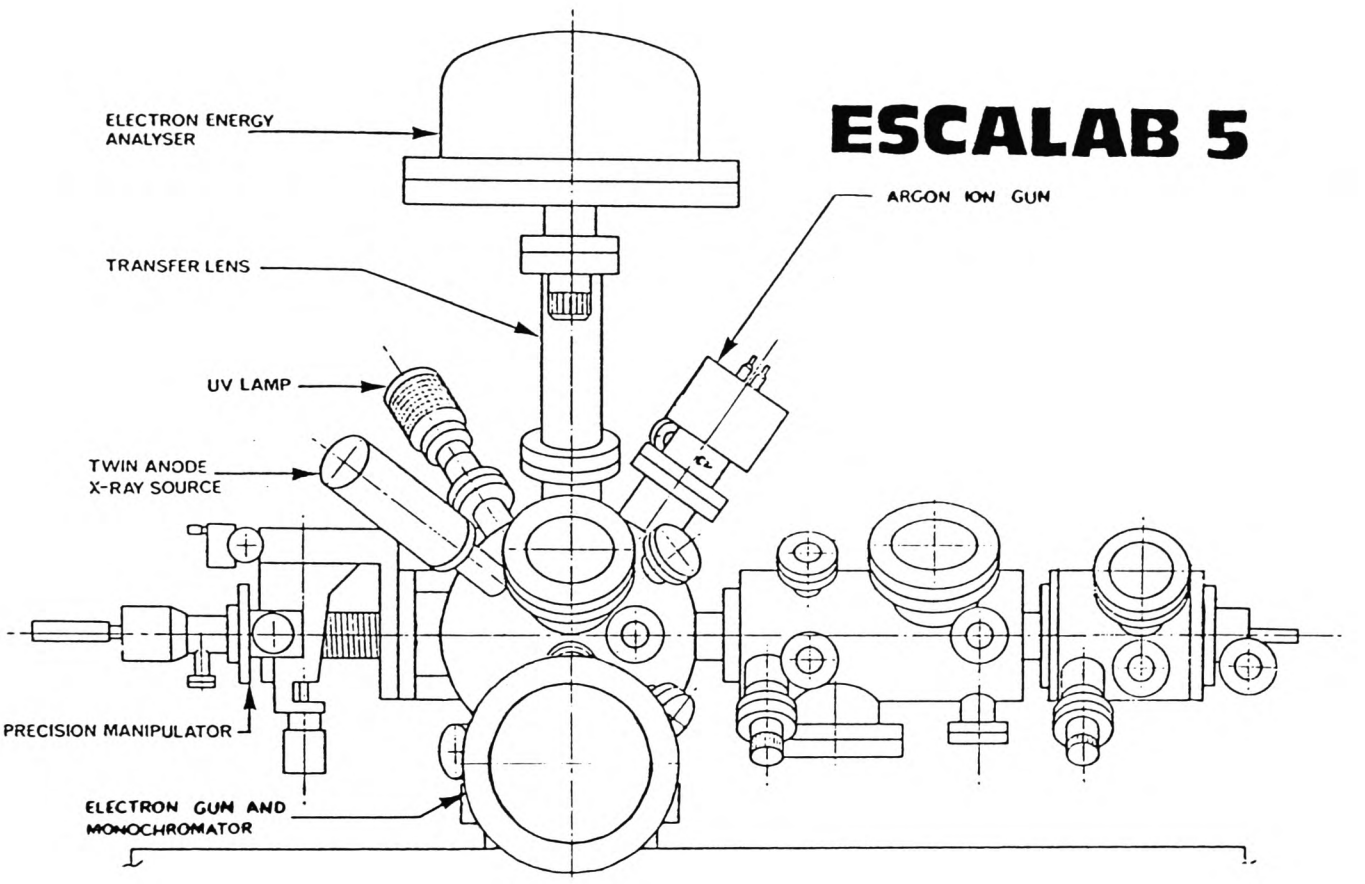

Figure 1: The spectrometer.

The spectrometer consists of three chambers. The largest of these is the main chamber in which experiments are carried out. This is constructed of mu-metal in order to shield the electrons from stray magnetic fields. Facilities mounted on the main chamber include an X-ray source, a UV source, an electron monochromator unit, an electron gun and screen for low energy electron diffraction, and an electron energy analyser. Samples may be resistively heated to 600^{o}C or cooled to liquid nitrogen temperatures whilst inside the chamber. There are also facilities for sputter etching the sample with argon ions at energies of

up to 10keV. Adjoining the main chamber is the stainless steel preparation chamber. This chamber is used for sample cleaning and other treatments prior to introduction into the main chamber. It incorporates facilities for both resistive heating (up to 600°C), radio-frequency heating (up to 1500°C), and heating by electron bombardment (up to 50mA, 2250V). The pumping of the chamber is such that it allows sample cleaning to be carried out either in a controlled atmosphere of the required gas, or in vacuo. The chamber is provided with a rotary drive operated track with a sample carrier for transfer of samples through the spectrometer. The third chamber, connected to the preparation chamber, is the stainless steel fast entry lock. This is independently pumped, allowing for rapid introduction of samples into the spectrometer, without loss of UHV conditions. The arrangement of the three chambers is shown in figure 2[40]. Most of the spectrometer can be baked at temperatures of up to 250°C, in order to desorb impurities, notably water, which accumulate on the inside walls.

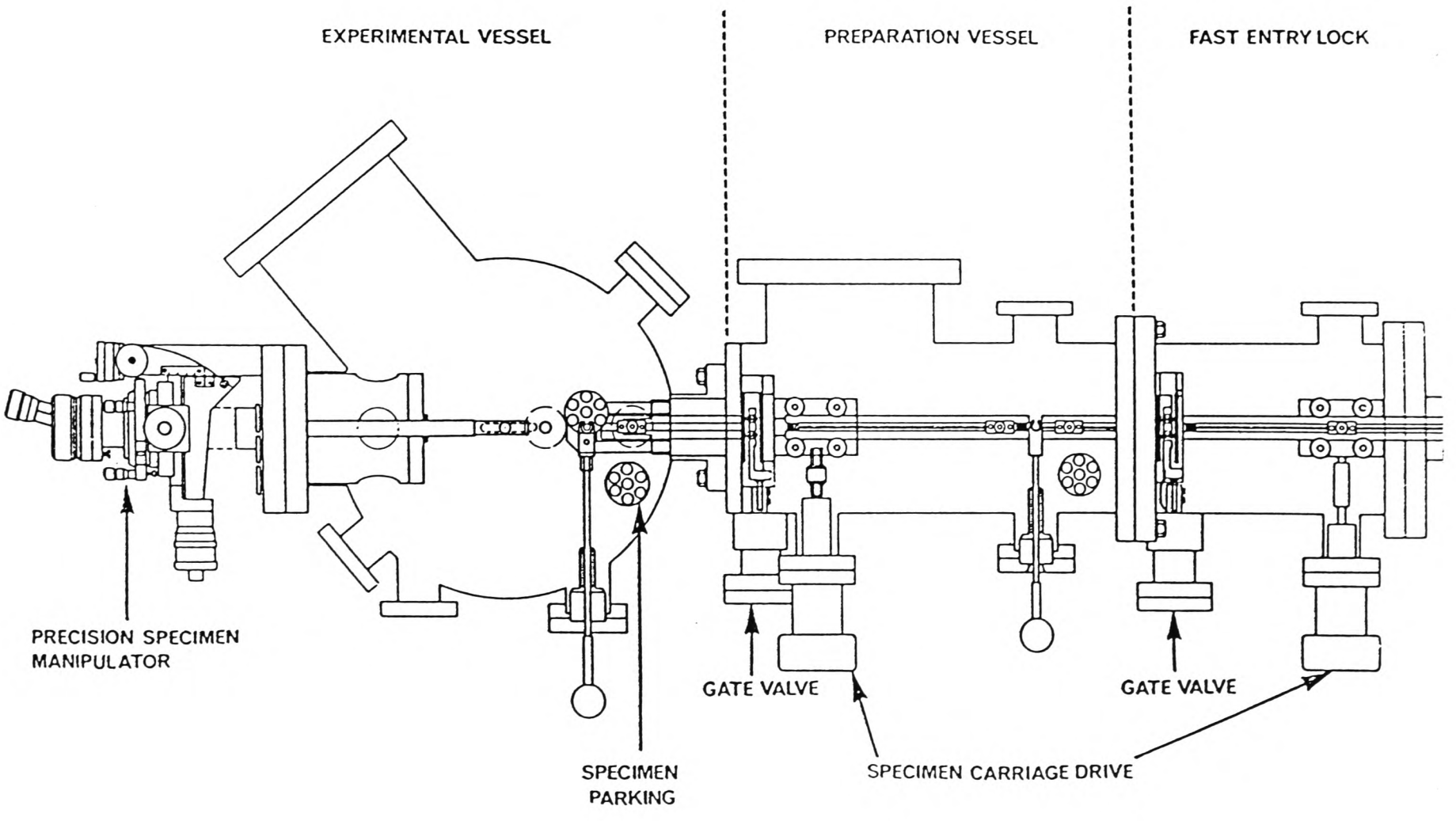

Figure 2:[40] The sample transfer system, showing the arrangement of chambers.

Three types of pumping are employed to maintain UHV conditions. The main and preparation chambers are each pumped by an Edwards E04 diffusion pump using polyphenyl ether pumping fluid and incorporating a liquid nitrogen cold trap. The main function of the cold traps is to act as high speed pumps for the removal of water vapour, which forms a major constituent of the residual atmosphere. The diffusion pumps are backed by Edwards E2M5 direct drive rotary pumps. These also rough the spectrometer from atmospheric pressure to around 10^{-2}mbar after bakeout. The diffusion pumping is supplemented by titanium sublimation pumps in both the main and preparation chambers. These operate by subliming a thin film of titanium onto the inside surfaces of the spectrometer, onto which residual gas molecules may adsorb. The titanium film is particularly effective in the removal of oxygen and water. The pumping system, in combination with metal-to-metal seals throughout the spectrometer, and frequent bakeout means that typical base pressures of 10^{-10}mbar in the main chamber, and 5.10^{-8}mbar in the preparation chamber can be obtained. Gases or vapours (e.g. for use in adsorbate studies or sample treatment) may be introduced into either the main or preparation chamber via a gas handling line. When not in use, this may be pumped under either rough or UHV conditions.

Pressure measurement over the entire range 10^{-12}mbar - atmospheric is achieved at various points in the system using three different gauges: ion gauges (10^{-12} - 10^{-2}mbar), Pirani gauges (10^{-2} - 1mbar) and barometric gauges (10 - 10^{3}mbar).

2.2 Radiation Sources

i) X-ray Gun: A twin anode, soft X-ray source giving unmonochromated Mg Kα ($h\upsilon$=1253.6eV) or Al Kα($h\upsilon$=1486.6eV) radiation. The primary component of the radiation is the $K\alpha_{1,2}$ lines. A small

contribution from the $K\alpha_{3,4}$,α' and β lines can be subtracted from the resulting spectra using a computer programme (section 2.5). The gun consists basically of a water-cooled copper central anode, with a wedge-shaped tip, coated on one side with magnesium, and on the other with aluminium. This is surrounded by the cathode filaments. X-rays are stimulated by applying a 10kV positive bias to the anode, keeping the cathode near earth potential. A thin aluminium window filters out secondary electrons and some of the Bremsstrahlung radiation emitted from the targets during stimulation of the X-rays. The gun is mounted on a linear drive, enabling it to be removed from the sample region when not in use.

ii) UV Source: This is a DC gas discharge lamp with a helium supply. The discharge is confined within a narrow quartz capillary. An EHT power supply delivers a 3kV potential between tantalum electrodes to start the discharge. As most window materials absorb in the UV region, the lamp is windowless and is therefore double-differentially pumped. The source gives predominantly (>99%) He Iα radiation ($h\upsilon$=21.22eV) at operating pressures of around 5.10^{-7}mbar. However, if the pressure is reduced to 2.10^{-8}mbar, up to 10% He IIα radiation ($h\upsilon$=40.81eV) can be obtained. The source is unmonochromated to maximise photon flux; satellite structure present in the resulting spectra may be removed using a stripping programme (Appendix I).

iii) Electron Gun: This produces a thermally broadened electron beam of energy up to 1000eV. This is suitable for LEED. The gun assembly is mounted in the centre of a curved viewing screen. The required beam energy may be selected by biasing a series of accelerating

elements. The quality of the LEED image reflected by the sample is improved by a series of grids in front of the screen which remove electrons having lower energy than the primary beam, so suppressing the inelastic background intensity. The LEED images may be photographed by mounting a camera on the front viewing port of the spectrometer.

iv) Monochromated Electron Source: This is a VG EMU50 electron monochromator, which produces a beam with FWHM in the range 8 - 20meV. The beam energy is tuneable in the range 0 - 100eV. These characteristics are suitable for HREELS. The electron monochromator unit is shown in figure 3.

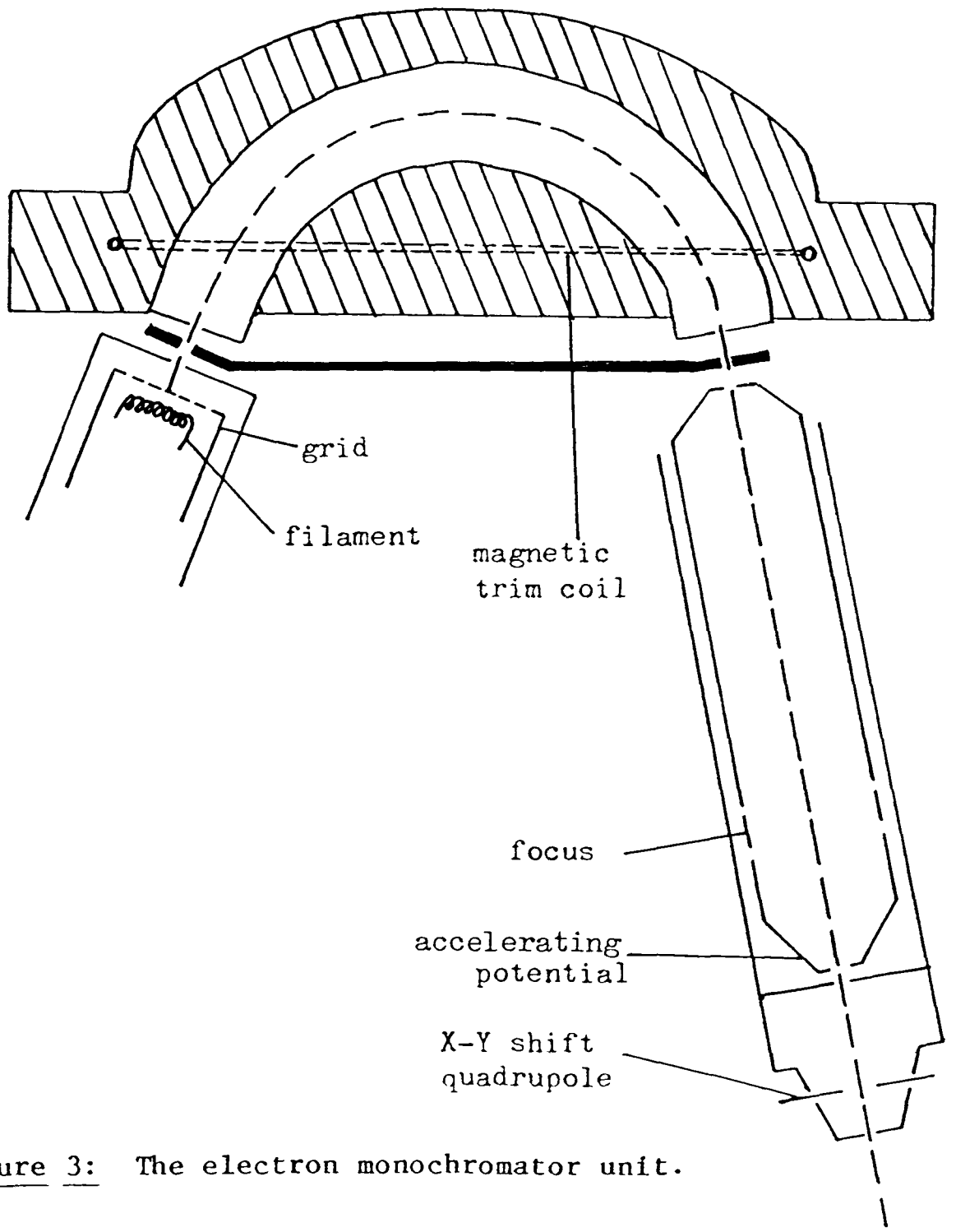

Figure 3: The electron monochromator unit.

The electrons are produced by thermionic emission from a tungsten hairpin filament. The emission from the filament is controlled by a negatively biased grid. The degree to which the electron beam is monochromated is selected by the value of the pass energy, HV, applied to a small 150^{o} spherical sector analyser. If a voltage V is applied between the inner and outer hemispheres of the analyser, then the energy of the electrons able to pass round the analyser is HV=E, where H is a constant of the analyser. The resolution of the analyser is given approximately by

$$\Delta E/E = \Delta r/2r \qquad (1)$$

(ignoring entrance angle effects). ΔE is the resolution, r is the mean radius of the hemispheres, and Δr is the analyser aperture diameter. For a pass energy of 1.0eV, this gives a resolution of around 6meV. To correct for any magnetic fields within the analyser, a magnetic trim coil is placed around it. On leaving the exit aperture of the analyser, the electrons pass through the transfer lens, then through an X-Y shift quadrupole which guides the beam to the centre of the sample. Between the final lens and the sample, the electrons are accelerated to the beam energy.

2.3 The Electron Energy Analyser

This is shown in figure 4. Electrons emitted or scattered from the surface of the sample pass through a mu-metal shielded double Einzel electrostatic lens, with an acceptance cone of 13.2^{o}. The electrons are retarded to an energy of HV (the pass energy), by a scanning retarding potential -R, immediately before passing into a 150^{o} spherical sector analyser, via a changeable entry slit. The sample is normally held at earth potential, so that -R volts is the electrical centre point of the

analyser. The kinetic energy, K, with respect to the Fermi level, of the electron leaving the sample is given by

$$K = R + HV + W \qquad (2)$$

where W is the work function of the spectrometer.

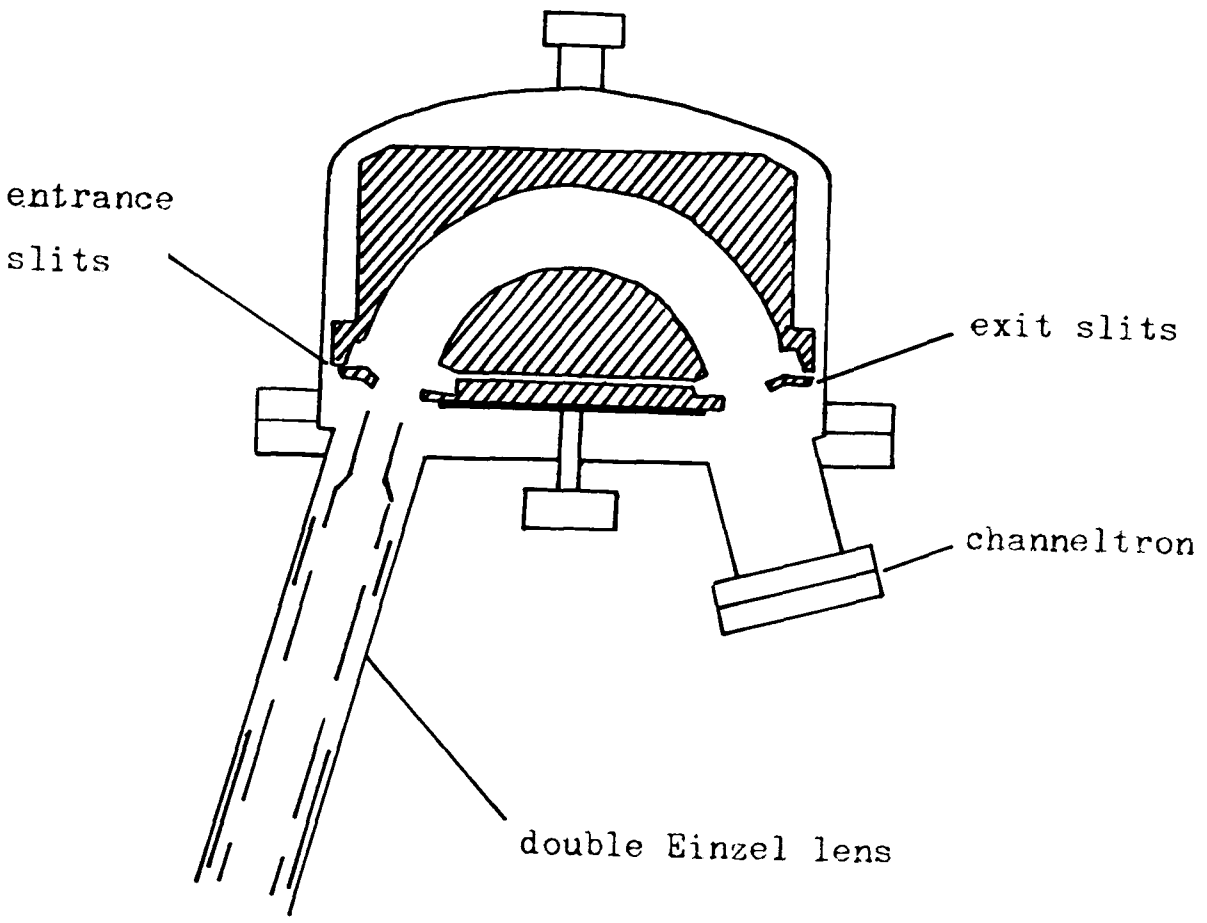

Figure 4: The electron energy analyser.

The analyser may operate in two modes:

i) Constant Analyser Energy (CAE)

This is the most commonly used mode, and is the mode in which all spectra in this thesis were recorded. In this mode, the pass energy HV remains constant, whilst the retard grid voltage is scanned linearly with respect to (K-W). The lens voltage is also swept to maintain focussing. The CAE mode has the advantage that the resolution is set by the value of the pass energy chosen, and is constant for all kinetic energies. In CAE mode the sensitivity of detection increases as the kinetic energy decreases. One effect of

this is to increase the secondary electron background seen in XPS spectra at low kinetic energies.

ii) Constant Retard Ratio (CRR)

In this mode the "retard ratio", k is kept constant:

$$k = (K-W)/HV \qquad (3)$$

The retard grid voltage, lens voltage and pass energy are all swept during scanning. As the pass energy decreases on scanning from high KE to low KE, the resolution is smaller the lower the KE. The sensitivity decreases as the KE decreases. The effect of the CRR mode is thus to artificially "flatten" the secondary electron background, and it is thus the mode of choice for recording Auger electron spectra, where the peaks of interest may occur at low KE on a large background.

2.4 Electron Counting

The current reaching the analyser exit is typically in the region 10^{-16} - 10^{-14}A, which is well below the detection limits of conventional current measuring techniques. A pulse counting method is necessary. A channel electron multiplier (channeltron) is used as a high gain amplifier. The channeltron consists of a small spiral glass tube, coated on the inside with a material of high resistance. A high potential (3-3.75kV maximum in our system) is applied between the ends of the spiral. Electrons enter the low potential end of the tube, and strike the walls, generating secondary electrons. These secondary electrons may also strike the walls, and so an avalanche effect is created. A typical overall gain on passage of an electron through the channeltron is 10^8: the duration of such a pulse of charge is about 10ns.

The pulses of electrons from the channeltron first enter a preamplifier mounted close to the channeltron and then pass through a discriminator which rejects pulses with amplitude below a selected threshold level. The remaining pulses, of 5V amplitude and 500ns duration are fed to a ratemeter to produce an analogue DC level proportional to the count rate which may be directly fed to an XY chart recorder. Alternatively, pulses from the discriminator may be accumulated and counted in a multi-channel analyser (MCA).

2.5 Data Handling

The spectra are accumulated on an ORTEC 6240B 1024 channel multi-channel analyser[44]. An internal clock generates square pulses which effect sequential stepping through the channels of the MCA with a dwell time of 0.1 seconds per channel. The channel advance pulses are also fed to a digital-to-analogue converter, which generates a linear DC ramp used to control the potentials on the lens elements and the retard grid at the entrance to the analyser, so changing the energy of the electrons being collected. The information from successive scans of the spectrum is added, and accumulated in the MCA memory bank. As

$$S/N \propto n^{1/2} \qquad (4)$$

where n is the number of scans, S/N is the signal-to-noise ratio, and the dwell time is constant, the noise in the spectrum is thus reduced. Digital spectra are then transferred onto floppy discs via a Research Machines 380Z micro-computer for subsequent analysis and plotting. Refinement of the experimental data may thus be carried out using a series of computer programmes. X-ray photoelectron spectra may be stripped of both satellites due to $K\alpha_{3,4}$, α' and β radiation, and secondary electron background, and the area of peaks in the spectrum may be determined by integration, using a programme devised by

Dr.A.A. Williams. UV photoelectron spectra may be stripped of satellites due to He Iβ and γ radiation using a programme adapted by the author from an existing routine (Appendix I). The basic spectrum reading and plotting routines were written by Dr.P.A. Cox.

Chapter Three

Surface Optical Phonons Observed by HREELS:

Theoretical Models and Experimental Results for TiO_2

3.1 Introduction

The aim of the work included in this chapter was twofold. Firstly, it was intended to increase the accuracy of the predicted HREEL spectra which we were previously able to obtain using simple dielectric theory. Thus the effects of crystalline anisotropy and surface defects were considered in detail. It was also intended to produce a useful tabulation of the vibrational modes expected to appear strongly in the HREEL spectrum of any given face of any commonly occurring crystal structure. Group theoretical calculation was employed to obtain this.

The second aim was to use the modified theories obtained to gain a more detailed understanding of the experimental HREELS of TiO_2 than had been obtained previously. In particular, it was envisaged that a detailed experimental study would throw light on matters of controversy in the existing literature, such as the magnitude of the effects due to crystalline anisotropy, the effects of surface defects, and the detailed assignment of the spectra.

The ultimate aim of the work carried out in this laboratory is to study adsorbates on metal oxide surfaces. This is particularly important because of the many technological applications of pure or doped metal oxides, for example as gas sensors, transparent electrodes, or heterogeneous catalysts, where surace-adsorbate interactions are of vital importance. However, in the case of non-metallic oxides (where the dielectric response of the bulk is not screened by conduction electrons), the solid exhibits very strong intrinsic losses in the vibrational region. The overtones of these losses tend to obscure the losses due to the adsorbate. In some cases it is found that a recently developed method based on Fourier transformation of the experimental spectrum which deconvolutes the overtone structure is successful in producing a surface loss function free from overtone and combination

structure[45]. This enables all adsorbate losses occurring above the phonon fundamentals to be clearly observed. However, in many cases, such Fourier deconvolution is not successful. This is usually due to a poor signal-to-noise ratio in the experimental data, or to the presence of surface defects, which change the intensities of the SO phonons from those seen on a defect-free surface. Thus it remains of crucial importance in studies on oxides to have a very detailed understanding of the HREEL spectrum of the substrate before beginning a study of adsorbates. It is particularly important to be able to make very accurate predictions of the substrate spectrum.

Our interest in rutile stems from its great technological importance, particularly as a catalyst for the photoelectrolysis of water[46,47,48]. Ultra-violet irradiation of n-type TiO_2 as the single crystal electrode of an aqueous electrochemical cell evolves O_2 at the TiO_2 electrode and H_2 at the Pt electrode. The photovoltage generated in the cell is not sufficient itself for the electrolysis, which requires an applied voltage. However, values as low as 0.25eV do allow the photoassisted electrolysis to proceed[46]. TiO_2 acts as a photoassistance catalyst according to the following scheme:

excitation of TiO_2 by light:

$$TiO_2 + 2h\upsilon \longrightarrow 2e^- + 2h^+ \qquad (1)$$

at the TiO_2 electrode:

$$2h^+ + H_2O \longrightarrow 1/2O_2 + 2H^+ \qquad (2)$$

at the Pt electrode:

$$2e^- + 2H^+ \longrightarrow H_2 \qquad (3)$$

overall:

$$H_2O + 2h\upsilon \longrightarrow 1/2O_2 + H_2 \qquad (4)$$

Coatings of TiO_2 have also been used as the selective absorber layer covering the reflector base of dark mirrors[48]. The TiO_2 layer absorbs UV solar radiation, becoming transparent at longer wavelengths, so that the reflector layer is able to act to suppress emittance in the thermal infra-red.

Doped TiO_2 is used widely as a heterogeneous catalyst. In particular, catalysts containing typically 3% V_2O_5 and 2-10% WO_3 are used with ammonia to reduce NO present in waste gases[49,50]. TiO_2 doped with Ga or V is used to oxidise CO to CO_2[51], and V-doped TiO_2 containing promoters such as Al, W, P and the rare earths is used to oxidise xylene to phthalic anhydride[52].

It is clear that the surface properties of TiO_2 are a crucial factor in determining its practical importance, whether as a gas sensor, heterogeneous catalyst, semiconductor electrode, or in the photodecomposition of water.

In the following sections, a short account of the theory of vibrational EELS is given. Simple dielectric theory is introduced, and the symmetry considerations necessary to predict a loss function using this theory are discussed in detail. A table of the vibrational modes expected to be excited in the spectra of different surfaces of some common crystal structures is compiled. Simple dielectric theory is used to predict the HREEL spectra of TiO_2 (110), (100) and (001) surfaces, and the results are compared with experiment. The simple dielectric theory is then modified to take into account the tensor properties of the dielectric function. The magnitude of this effect under various conditions are considered, and compared with results obtained both in this laboratory, and by Dr.R.G. Egdell and co-workers[53]. Finally, the dielectric theory is modified by the introduction of a term representing electronic excitations. The theoretical predictions are compared with results obtained by Dr.R.G. Egdell on defected surfaces[53].

3.2 Theory of Electron Energy Loss Spectroscopy

An electron incident on a crystal with energy E_I may excite a quantised vibrational mode with energy $\hbar\omega$ before being backscattered into the vacuum. It thus emerges with energy $E_S=E_I-\hbar\omega$, so an analysis of the energy spectrum of the backscattered electrons provides direct information on the vibrational frequencies of the substrate, or on those of atoms or molecules adsorbed on the surface. The method is surface sensitive, as with the incident KE E_I chosen suitably, the electron penetrates only a few atomic layers into the crystal.

There are three limiting mechanisms by which an electron may be inelastically scattered from the surface. These are dipole scattering, inelastic scattering via an intermediate negative ion resonance, and impact scattering. The only mechanism of importance to the present work is dipole scattering.

In the dipole scattering regime, the loss spectra can in principle be accounted for by theories based on the dielectric response of the surface to the potential of the incident electron. The basic properties of the surface optical phonon modes of the lattice which are excited may be described by the essentially classical theory of Mahan[33], although some of the finer details require a quantum mechanical treatment. These SO phonons were first predicted theoretically by Fuchs and Kliewer in 1965[36]. Because the theoretical model involves Coulombic interactions over long distances, the solid is treated as uniform. In order to make the problem mathematically tractable, it is assumed that the dielectric response function $\epsilon(\omega)$ depends only upon frequency, rather than upon both frequency and momentum or wave vector $\epsilon(\omega,k)$. The absence of appreciable momentum transfer parallel to the surface in the dipole scattering regime justifies the use of the long wavelength limit $\epsilon(\omega,0)$ of the wavevector dependent dielectric function $\epsilon(\omega,k)$. The loss

probability $P(\omega)$ of an electron losing energy $\hbar\omega$ is calculated from the electrostatic work done on the electron by the solid. A brief outline of the classical theory is given in Appendix II. The resulting loss probability is given by

$$P(\omega) = [e^2/v\hbar\omega]\,\mathrm{Im}(\epsilon(\omega)-1)/(\epsilon(\omega)+1) \qquad (5)$$

where v is the velocity component normal to the surface. This loss function is integrated over all angles of scattering, but peaks strongly in the specular direction (with a characteristic angular distribution narrower than the acceptance of our analyser system). An example is shown in figure 1[54]. This pronounced forward scattering is a consequence of wave vector conservation. Considering components parallel to the surface we have

$$\underline{K}_{I_{\parallel}} = \underline{K}_{S_{\parallel}} + \underline{K}_{\parallel} \qquad (6)$$

where $\underline{K}_{I_{\parallel}}$, $\underline{K}_{S_{\parallel}}$ are the initial and scattered wave vectors of the electron, and $\underline{K}_{\parallel}$ is the wave vector of the excited mode. This is usually small compared with $\underline{K}_{S_{\parallel}}$ and $\underline{K}_{I_{\parallel}}$, resulting in scattering around the specular direction.

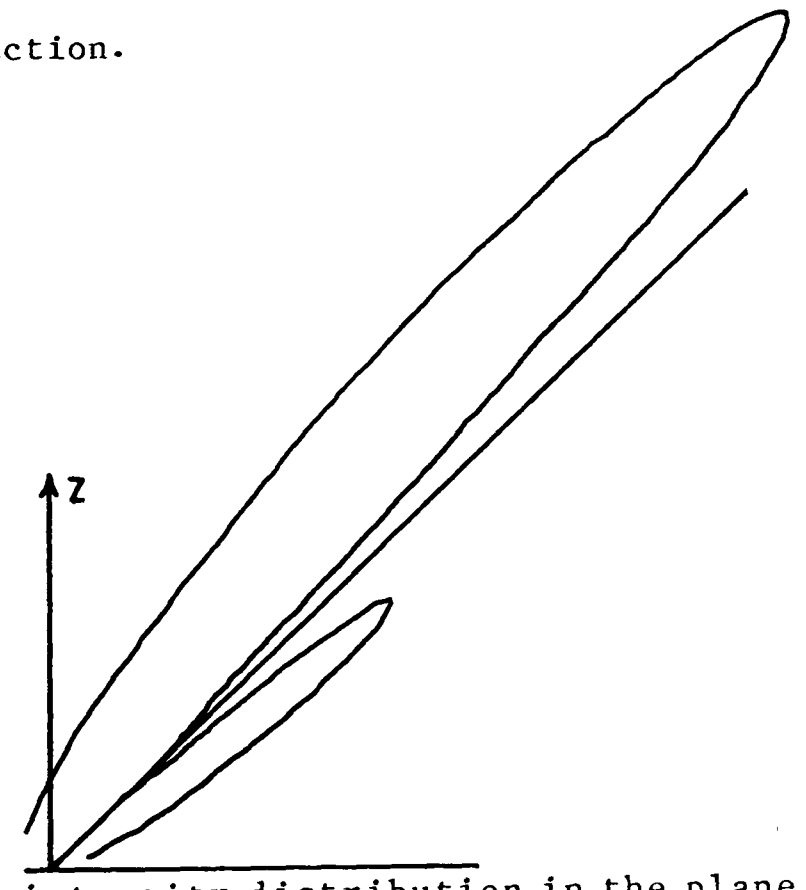

Figure 1:[54] The intensity distribution in the plane of incidence for inelastically scattered electrons.
Molecular excitation energy $\hbar\omega$ = 0.25eV
Electron energy E = 1.4eV
Angle of incidence = 47.7^{o}

An important result of dipole scattering is the "normal dipole selection rule", i.e. only vibrational modes with a component of dipole moment normal to the surface can be active in EELS. This can be understood by considering figure 2[55].

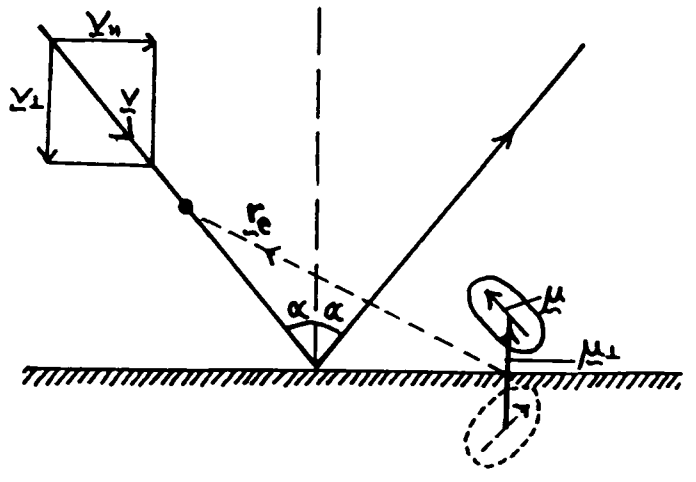

Figure 2:[55] The origin of the normal dipole selection rule. r_e is the elecron-dipole distance, μ is the instantaneous dipole of a molecule adsorbed at the surface, and $\mu_\perp$ is the total resultant normal dipole.

If r_e is much greater than the distance of the dipole from the surface, only the dipole $\mu_\perp$ is seen by the electron. This is because the dipole produces an image dipole in the substrate. Components of the image dipole parallel to the surface tend to cancel the parallel components of the adsorbate SO phonon dipole, μ. It can be shown that vibrations which induce dipole moments parallel to the surface scatter electrons less by a factor of $|\varepsilon|^{-2}$ than those with perpendicular dipole moments[56]. This selection rule applies both to the vibrational modes of the substrate and to those of any adsorbate present.

The first experimental observation of SO phonons was made by Ibach on the $(1\bar{1}00)$ surface of ZnO[57,58]. A loss was observed at 68.8meV, between the bulk longitudinal optical and transverse optical frequencies. The energy of the loss was in excellent agreement with the calculations of Fuchs and Kliewer[36].

The loss probability of equation (5) is a maximum when

$$\mathrm{Re}[\varepsilon(\omega)] = -1 \qquad (6)$$

This is illustrated in figure 3.

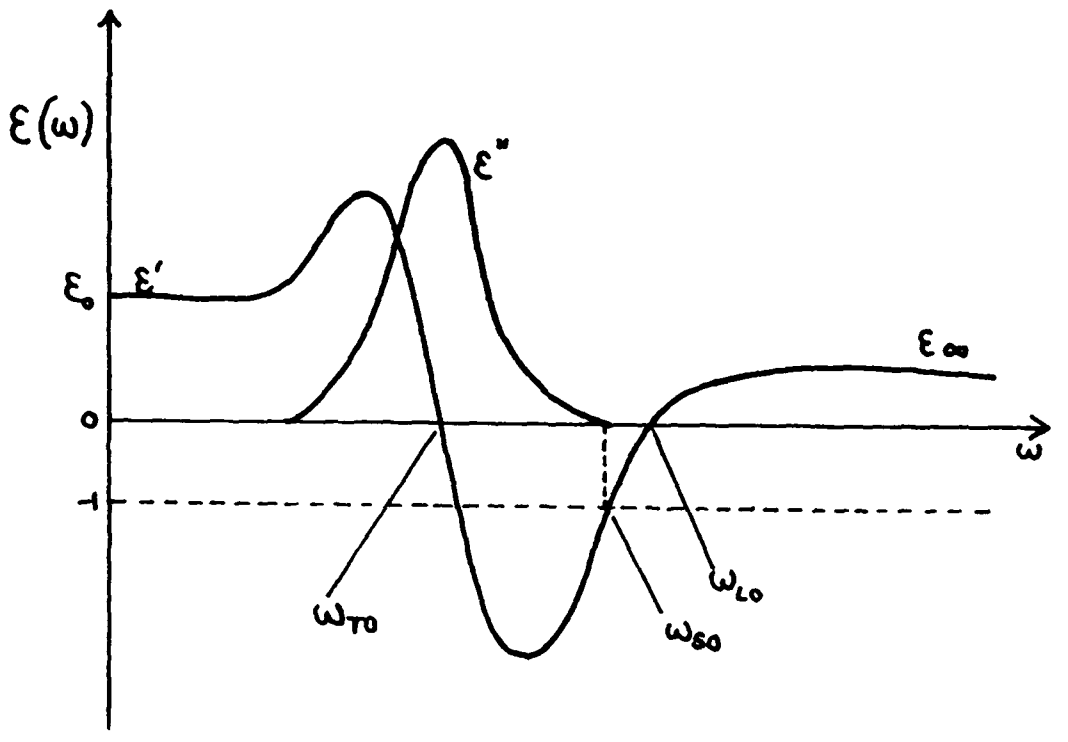

Figure 3: The real ($\epsilon'(\omega)$) and imaginary ($\epsilon''(\omega)$) parts of the dielectric function for a solid having a single optical phonon mode. the TO, LO and SO phonon frequencies are shown. ϵ_o, ϵ_∞ are the static and high frequency dielectric constants, respectively.

It can be seen that there are two points at which $\epsilon'=-1$. Only the second gives rise to a SO phonon, as ϵ'' is a maximum at the first point. (When $\epsilon'=-1$, the loss probability depends on $1/\epsilon''$). It can be seen that

$$\omega_{TO}<\omega_{SO}<\omega_{LO} \tag{7}$$

as observed by Ibach[57,58]. The theory developed by Fuchs and Kliewer[36] predicts that ω_{SO} should be related to ω_{TO} by the equation

$$\omega_{SO} = [(\epsilon_o+1)/(\epsilon_\infty+1)]^{1/2}\omega_{TO} \tag{8}$$

A number of other features of the theory were verified explicitly by Ibach. The loss function (equation (5)) predicts that the loss intensity should be proportional to $E^{-1/2}$, where E is the beam energy, as $P(\omega)$ is proportional to 1/v. This was observed. However, this is only true at higher beam energies[37]. At very low energies where the beam energy becomes comparable to that of the excitation, scattering becomes increasingly off-specular, and other scattering mechanisms predominate.

Ibach also observed that for one-phonon events, the ratio of the energy gain scattering to energy loss is given by

$$I_{gain}/I_{loss} = n_1/n_0 = \exp(-\hbar\omega_{SO}/k_BT) \qquad (9)$$

where n_0, n_1 are the populations of the ground and first excited states. It was also observed that the loss intensity varies as $(\cos\alpha)^{-1}$ over a wide range of incident angles. This is expected as $P(\omega)$ depends on $1/v$, where v is the perpendicular component of the electron velocity, i.e. $\underline{v}\cos\alpha$.

Other scattering mechanisms are inelastic scattering via an intermediate negative ion resonance, and impact scattering. Negative ion resonances are observed in elastic collisions between electrons and molecules in the gas phase[59]. On a surface, one may expect the lifetime of such resonances, where the electron enters an antibonding level, to be short when a chemisorbed molecule is coupled to the substrate electron states. To date, negative ion resonances for molecules adsorbed on surfaces have only been observed in a few experiments[60,61].

At large deflection angles, impact scattering, in which the electron beam is scattered inelastically by the localised atomic potential of the ions and atoms at the surface becomes important. It is necessary to turn to a fully microscopic description to describe the scattering cross-section theoretically. This large deflection angle regime, outside the "dipolar lobe", is often referred to as the impact scattering regime. Using time-reversal symmetry, and assuming no appreciable momentum transfer parallel to the surface, the normal dipole selection rule may be formulated for this regime.

As a result of the short-range portion of the electron-molecular interaction, the angular distribution of the electrons scattered inelastically from a molecular vibration is relatively broad. Typical high resolution spectrometers (including ours) accept a very small solid

angle only. Thus, typical count rates of inelastically scattered electrons from impact scattering are small, and can be ignored for the purposes of this work.

3.3 Calculation of Theoretical HREEL Spectra using Dielectric Theory

The form of the dielectric function $\varepsilon(\omega)$ appropriate to the calculation of the loss function may be derived from infra-red reflectivity data. The reflectivity, R, of radiation at normal incidence is related to the refractive index n, and extinction coefficient k, by the equation:

$$R(\omega) = [(n(\omega)-1)^2+k(\omega)^2]/[(n(\omega)+1)^2+k(\omega)^2] \qquad (10)$$

The real (ε_1) and complex (ε_2) parts of the dielectric function are themselves related to n and k through equations (11) and (12):

$$\varepsilon_1(\omega) = n^2 - k^2 \qquad (11)$$

$$\varepsilon_2(\omega) = 2nk \qquad (12)$$

The complex oscillator analysis of infra-red reflectivity gives:

$$\varepsilon(\omega) = \varepsilon_\infty + \Sigma_{j=1}^{n} 4\pi\rho_j/[\omega_j^2-\omega^2+i\omega\gamma_j] \qquad (13)$$

where ε_∞ is the high frequency dielectric constant, and ρ_j, ω_j and γ_j are respectively the dipole strength, frequency and damping constant for the jth oscillator. The number of oscillators, n, which must be included in the calculation is deduced from group theoretical considerations. This is most easily illustrated by reference to specific examples.

3.3.1 Illustration of the Symmetry Considerations

a) Rutile

The rutile structure (figure 4) contains two formula units per cell and belongs to the space group D_{4h}^{14} ($P4_2/nmn$). This is closely related to the point group D_{4h}, but some of the operations of the group involve a non-primitive translation τ_a. When the origin of rotations is located in the centre of the unit cell, the non-primitive translation τ_a is

$$\tau_a = (1/2)\underline{a}_1 + (1/2)\underline{a}_2 + (1/2)\underline{a}_3 \qquad (14)$$

where $\underline{a}_1$, $\underline{a}_2$ and $\underline{a}_3$ are the basis vectors of the Bravais lattice,

$$\underline{a}_1 = t\hat{x} \qquad (15)$$

$$\underline{a}_2 = t\hat{y} \qquad (16)$$

$$\underline{a}_3 = t\hat{z} \qquad (17)$$

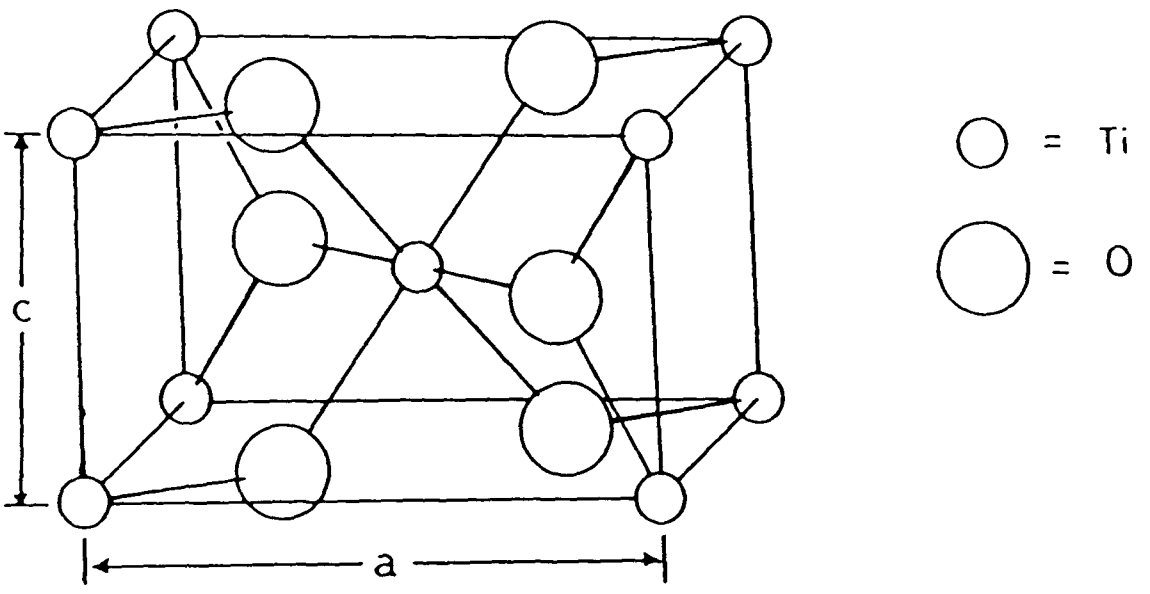

Figure 4: The unit cell of the rutile structure of TiO_2.

The 16 point symmetry operations for the D_{4h}^{14} space group are shown in table 1[62]. At the zone centre, vibrations may be classified

according to the irreducible representations of the point group D_{4h}. From the character table given by Gay et al[62] (table 2), the 15 normal modes may be shown to span irreducible representations as follows:

$$\Gamma_{vib} = A_{1g} + A_{2g} + A_{2u} + B_{1g} + B_{2g} + 2B_{1u} + E_g + 3E_u \qquad (18)$$

Here the acoustic normal modes, which transform as the translations x,y,z of the group and thus have the symmetries $E_u + A_{2u}$, have been omitted.

Table 1[62] The 16 Point Symmetry Operations for D_{4h}^{14}

Point Operations	Non-primitive Translation	Description
E	0	identity
C_4^+	τ	$\pi/2$ rotation about z axis
C_4^-	τ	$-\pi/2$ " " " "
C_2	0	π " " " "
C_{v1}	τ	" " " x axis
C_{v2}	τ	" " " y axis
C_{d1}	0	" " " x + y
C_{d2}	0	" " " x - y
I	0	inversion
S_4^+	τ	inversion x C_4^+
S_4^-	τ	inversion x C_4^-
σ_h	0	reflection in xy plane
σ_{v1}	τ	" " yz plane
σ_{v2}	τ	" " xz plane
σ_{d1}	0	" " (x - y)z plane
σ_{d2}	0	" " (x + y)z plane

Table 2[62] Character Table for D_{4h}^{14}.

D_{4h}^{14}	E	C_4^+	C_4^-	C_2	σ_{v2}	σ_{d1}	σ_{d2}	σ_{v1}	σ_h	S_4^-	S_4^+	I	C_{v1}	C_{d2}	C_{d1}	C_{v2}
A_{1g}, A_{2u}	1	1	1	1	1	1	1	1	1	1	1	1	1	1	1	1
A_{1u}, A_{2g}	1	1	1	1	-1	-1	-1	-1	1	1	1	1	-1	-1	-1	-1
B_{1g}, B_{2u}	1	-1	-1	1	1	-1	-1	1	1	-1	-1	1	1	-1	-1	1
B_{2g}, B_{1u}	1	-1	-1	1	-1	1	1	-1	1	-1	-1	1	-1	1	1	-1
E_g, E_u	2	0	0	-2	0	0	0	0	2	0	0	-2	0	0	0	0
Γ_{disp}	18	0	0	-2	0	-4	12	0	6	0	0	-6	0	-12	4	0

For a vibrational mode to be detected in IR or in HREELS, the molecule must possess an oscillating dipole moment, i.e.

$$\mu_i = \mu_i(0) + \partial\mu_i/\partial Q_a + \ldots\ldots \qquad (19)$$

where Q_a = normal displacement,

$$\partial\mu_i/\partial Q_a \neq 0 \qquad (20)$$

Since the translation operations are of symmetry A_{2u} and E_u, only modes having these symmetries will be allowed. Moreover, the A_{2u} mode corresponds to the z translation operation and thus involves displacements parallel to the [001] c-axis, in contrast to the E_u modes which correspond to x and y translations, and involve displacements perpendicular to the c-axis (figure 5[63]). In HREELS, energy loss may occur only to those modes with a dipole change normal to the surface. Thus we predict that the E_u modes will be observed in HREEL spectra of all surfaces where the c-axis lies within the plane (i.e. all surfaces corresponding to indices (h,k,0), for example (110), figure 6). These modes may be seen in the reflection spectrum from TiO_2 with the electric vector polarised normal to the

c-axis ($E_{\perp}c$). In contrast, the A_{2u} mode will be observed in the HREEL spectrum in the case where the c-axis lies along the surface normal (i.e. the (001) surface). This mode is observed in the reflection spectrum from TiO_2 with $E_{\parallel}c$.

For all other surfaces, some combination of the two cases above will be observed. The nature of this combination is considered in more detail below.

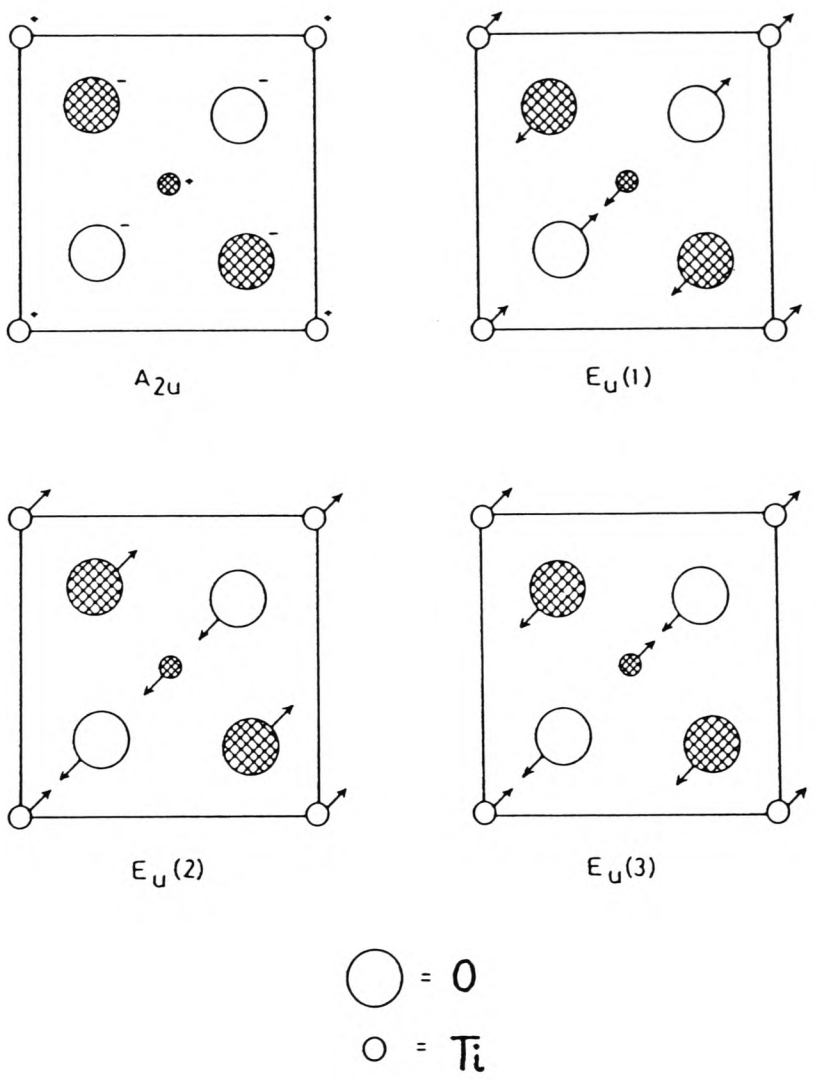

Figure 5: Atomic displacements in the infrared active modes of the rutile structure. Hatched circles are atoms 1/2c above the basal (001) plane. + and - indicate atomic displacements along the [001] axis. The E_u modes are shown in order of increasing frequency.

a)

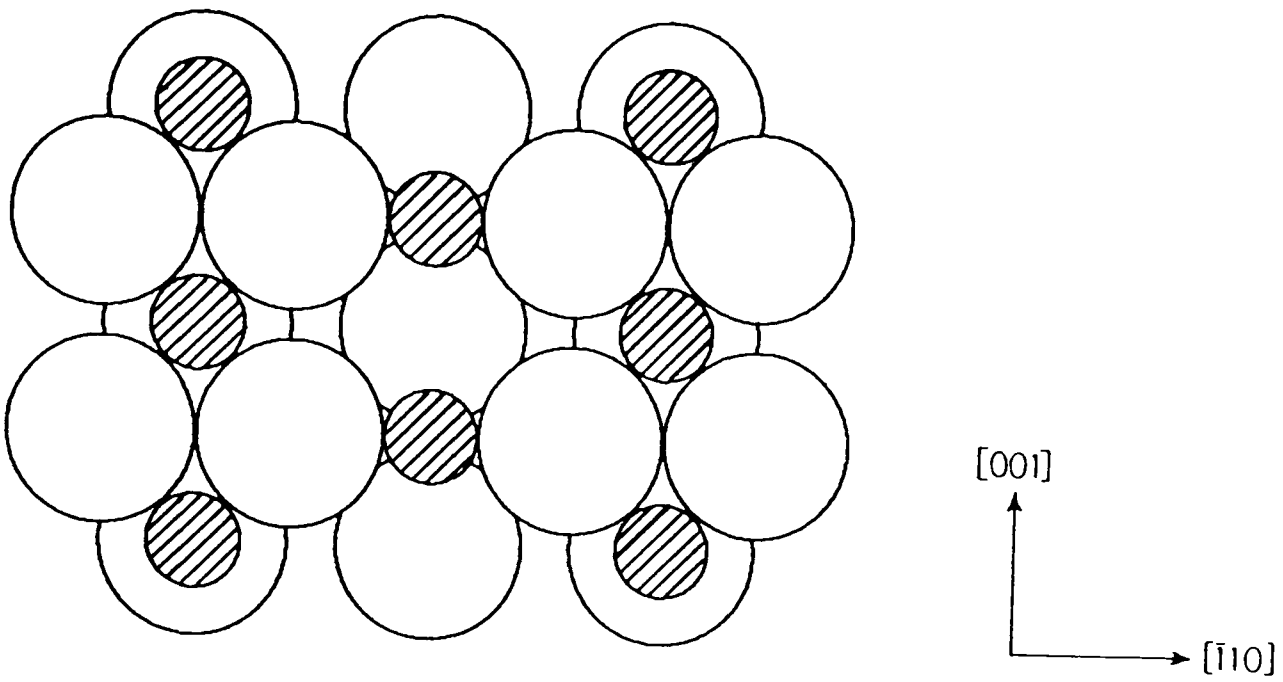

b)

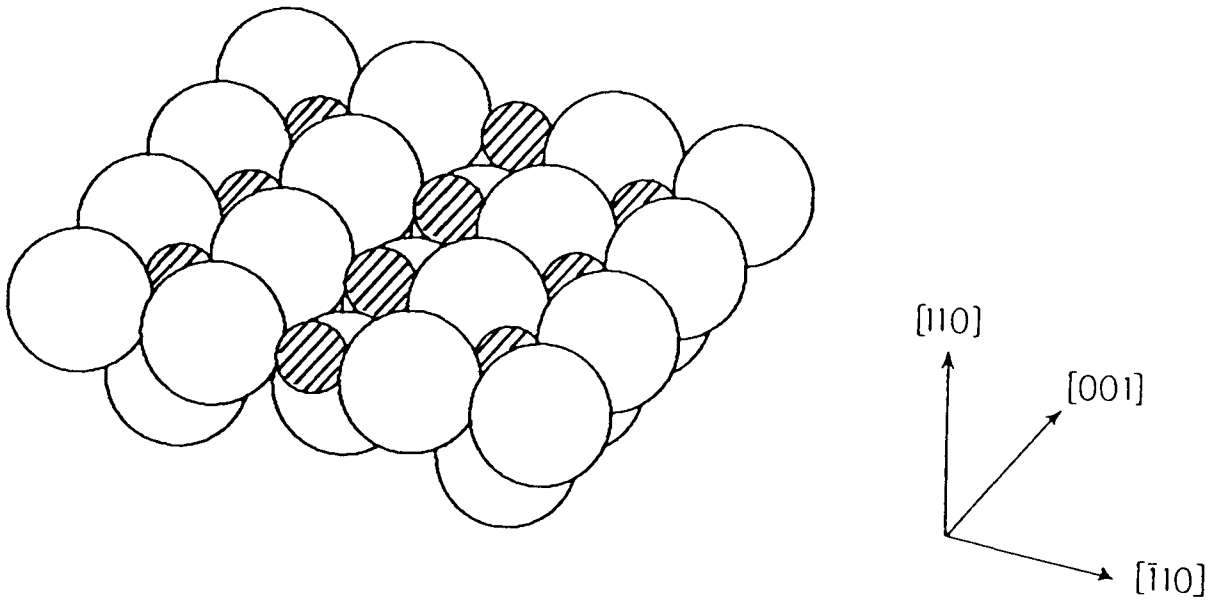

Figure 6: Two views of the (110) surface of the rutile structure of TiO_2.

a) plan view down the [110] axis
b) side view

Small hatched spheres represent titanium ions, whilst large open spheres represent oxygen ions.

It follows that the infra-red reflection spectrum of TiO_2 with $E_\perp c$ contains all the information necessary to calculate the HREEL spectra of the (100) and (110) surfaces. Conversely, the reflection spectrum with $E_\parallel c$ may be used to calculate the spectrum of the (001) surface. Parameter values due to Spitzer et al[64] are given in table 3, and are used to calculate the loss function $P(\omega)$, through equation (5).

Table 3[64] Parameter values from the classical oscillator analysis of the infra-red reflection spectrum of TiO_2 at 309K.

Mode	frequency $\hbar\omega$ (cm^{-1})	linewidth $\gamma/\hbar\omega$	absorption strength $4\pi\rho$
	$E_\perp c$		
$t_1(E_u)$	183	0.19	81.5
$t_2(E_u)$	388	0.058	1.08
$t_3(E_u)$	500	0.044	2.0
$l_1(E_u)$	373	-	-
$l_2(E_u)$	458	-	-
$l_3(E_u)$	806	-	-
	$E_\parallel c$		
$t(A_{2u})$	189	0.17[a]	165
$l(A_{2u})$	811	-	-

high frequency dielectric constants: $\epsilon_{\infty\perp}=6$, $\epsilon_{\infty\parallel}=8.4$

[a] An arbitrary linewidth is inserted here. This should have no effect on the resulting spectrum as it is considerably less than the instrumental broadening commonly employed ($\sim 120 cm^{-1}$).

The loss function itself predicts only single phonon losses. However, in the case of many non-metallic compounds, the total loss probability is so large that electrons may sequentially excite two or more phonons in separate loss events. The intensities of multiple

excitations in HREELS follow a Poisson distribution: in calculating the multiphonon loss spectrum, the single phonon loss function is self-convoluted, leading to the theoretical loss spectra of figures 7a) and b).

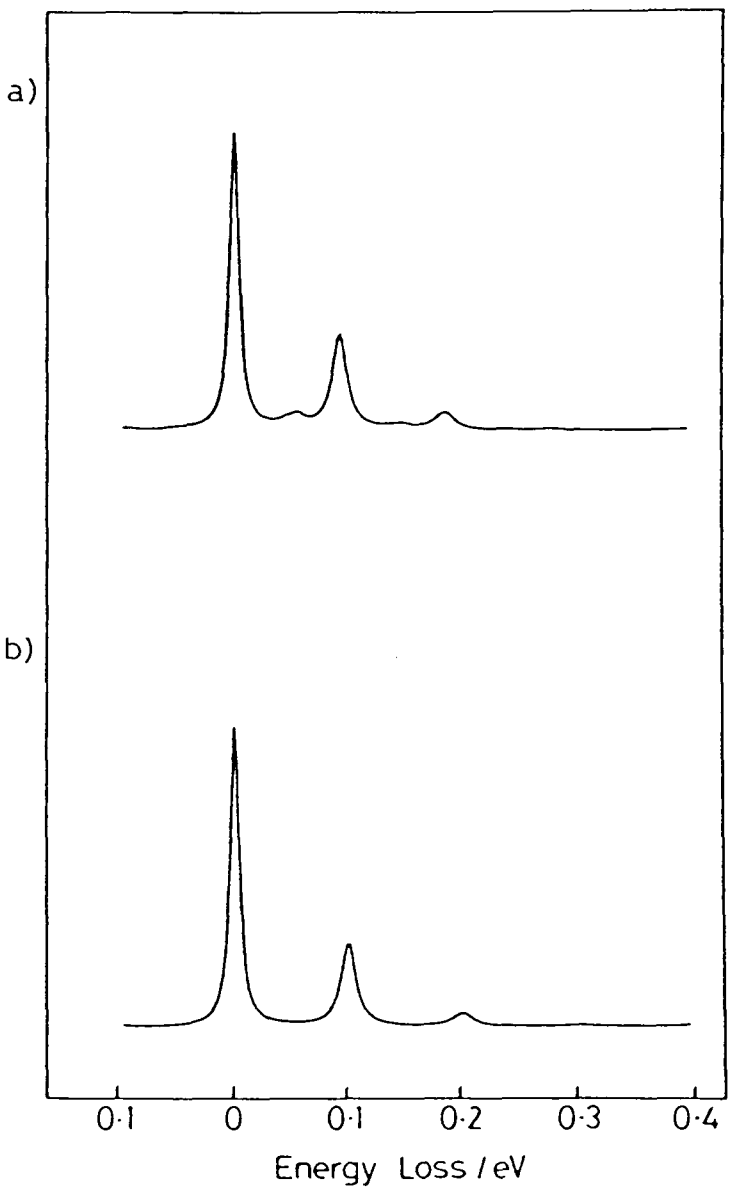

Figure 7: Theoretical HREEL spectra of rutile (100),(110) (a) and (001) (b), using the parameter values of reference 64, electron beam energy of 14eV, and elastic peak width of $80cm^{-1}$ (corresponding to the conditions of Kesmodel et al[65]).

These theoretical results are compared with experimental results obtained in our laboratory and elsewhere in sections 3.4 and 3.5. An assignment of the features appearing in the spectra is also given in table 7.

b) Corundum

The unit cell of corundum (figure 8) is a rhombohedron containing two molecules. The space group is D_{3d}^6 ($R\bar{3}c$), the symmetry reducing to D_{3d} at the zone centre.

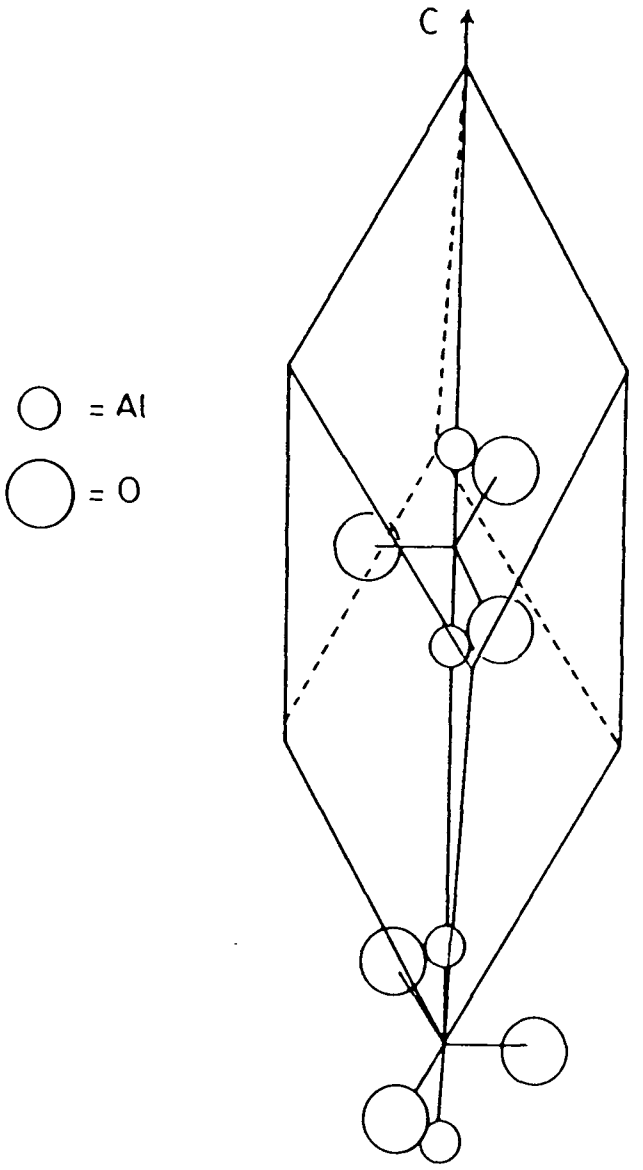

Figure 8: Unit cell of the corundum structure.

From the character table given by Bhagavantam and Venkatarayudu[66], the 30 normal modes may be shown to span irreducible representations as follows:

$$\Gamma = 2A_{1g} + 2A_{1u} + 3A_{2g} + 2A_{2u} + 5E_g + 4E_u \qquad (21)$$

for the optical modes, and $A_{2u} + E_u$ for the acoustic modes. Applying the same argument as in the case of rutile, we see that the only modes allowed in infra-red spectroscopy or in HREELS are the two A_{2u}

and four E_u modes. As the z translation operation has A_{2u} symmetry, and the x and y translations have E_u symmetry, similar results to those found in the rutile case follow. Thus the E_u modes will be observed in HREEL spectra of all surfaces where the c-axis lies within the plane, which in the case of a hexagonal system corresponds to all (x,y,z,0) surfaces. These modes may be seen in the reflection spectrum from Al_2O_3 with $E_\perp c$. The A_{2u} modes will be observed in the HREEL spectrum in the case where the c-axis lies along the surface normal, i.e. the (0001) surface. These modes are observed in infra-red reflectance with $E_\parallel c$. Parameter values due to Gervais et al[67,68] and Piriou[69] are given in table 4, and are used to calculate the theoretical spectra of figures 9a) and b). An assignment of the features appearing in these spectra is given in table 5.

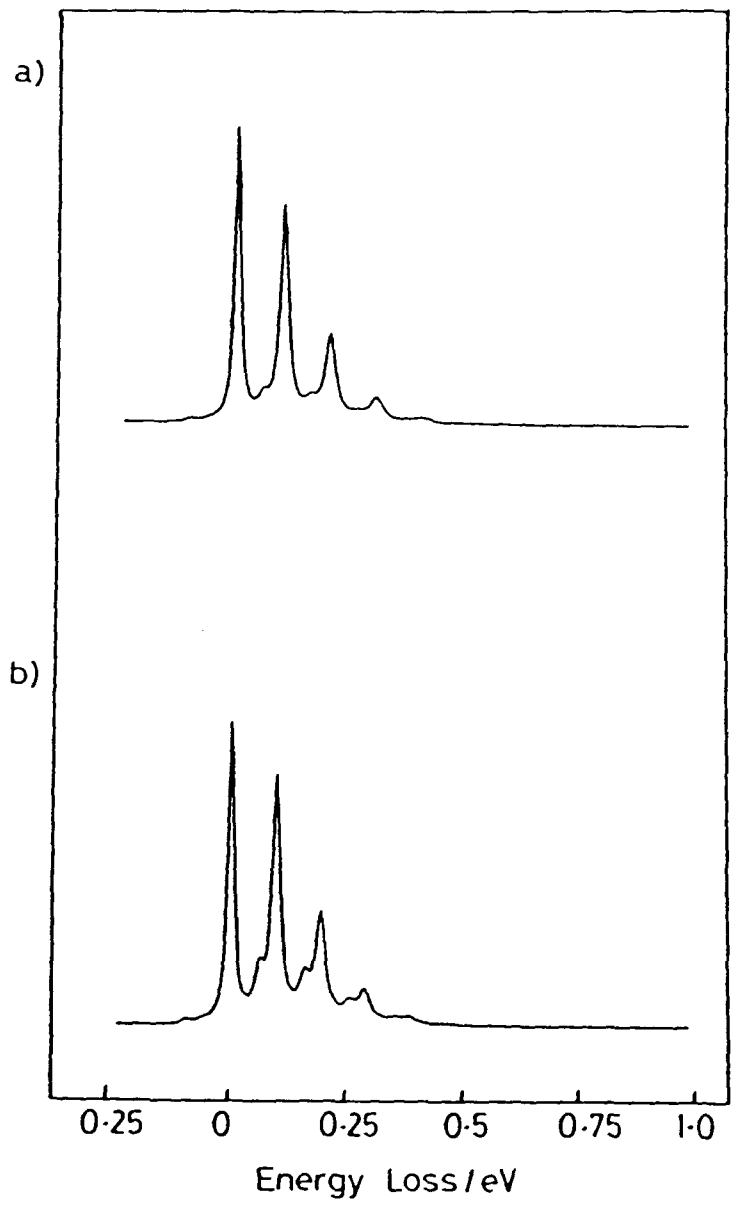

Figure 9: Theoretical HREEL spectra of corundum (x,y,z,0) (a), and (0001) (b) using the parameter values of references 67-69, an electron beam energy of 5eV and elastic peak width of 120cm^{-1} (corresponding to the conditions normally employed in our spectrometer).

Table 4 Parameter values from dispersion analysis of the infra-red reflectance spectrum of Al_2O_3.

mode	frequency $\hbar\omega$ (cm^{-1})	linewidth $\gamma/\hbar\omega$	absorption strength $4\pi\rho$
	$E_\perp c$		
$t_1(E_u)$	384.6[a]	0.0135[b]	0.37[b]
$t_2(E_u)$	439.3[a]	0.0086[b]	2.74[b]
$t_3(E_u)$	569.5[a]	0.0123[b]	2.98[b]
$t_4(E_u)$	634.0[a]	0.0132[b]	0.24[b]
$l_1(E_u)$	387.7[a]	-	-
$l_2(E_u)$	482[a]	-	-
$l_3(E_u)$	908[a]	-	-
$l_4(E_u)$	630.5[a]	-	-
	$E_\parallel c$		
$t_1(A_{2u})$	399.5[c]	0.0212[c]	649[c]
$t_2(A_{2u})$	584[c]	0.0128[c]	1.41[c]
$l_1(A_{2u})$	514[c]	-	-
$l_2(A_{2u})$	886.5[c]	-	-

high frequency dielectric constants: $\epsilon_{\infty\perp}=3.08$[a], $\epsilon_{\infty\parallel}=3$[c]

[a] from reference 67, T=295K

[b] from reference 68, T=293K

[c] from reference 69, T=300K

Table 5 Assignment of the peaks in the predicted HREELS of Al_2O_3 (x,y,z,0) (a) and (0001) (b)

a) the (x,y,z,0) surface

assignment	predicted frequency/cm^{-1}
v_1	468
v_2	831
v_1+v_2	1307
$2v_2$	1661
v_1+2v_2	2145
$3v_2$	2500
$3v_2+v_1$	2944
$4v_2$	3327
$5v_2$	4154

b) the (0001) surface

assignment	predicted frequency/cm^{-1}
v_1	500
v_2	790
v_1+v_2	1290
$2v_2$	1581
v_1+2v_2	2089
$3v_2$	2363
v_1+3v_2	2879
$4v_2$	3154
$5v_2$	3952

In the spectrum of the (x,y,z,0) surface, peaks due to all four E_u modes are not resolved, and only two main resonances for single phonon excitation are observed. These resonances correspond most directly to the t_2 and t_3 resonances observed in infra-red reflectance. Note that HREEL spectra are dominated by high frequency modes, and so the "t_2" mode appears with very much lower intensity than the "t_3" mode, even though they have very similar absorption strengths (table 4). In all cases, our predicted SO frequency falls between the TO and LO frequencies given by IR reflectance, as expected. The single phonon loss frequencies of figure 9 correspond to the loss condition of equation (6). For the bulk LO phonon frequencies we have

$$\mathrm{Re}(\epsilon(\omega)) = 0 \qquad (22)$$

The shift between bulk and surface frequencies is dependent upon the gradient of $\epsilon_1(\omega)$ close to the $\epsilon=0$ axis.

Energy gain peaks (analogous to anti-Stokes peaks in Raman spectroscopy) are also observed. The loss features of figures 9a) and b) are much stronger than those of figures 7a) and b). This is due to two factors. The intensity of scattering is dependent on the inverse square root of the beam energy (14eV for figure 7, 5eV for figure 9). The high frequency dielectric constants for both Al_2O_3 surfaces are smaller than those for TiO_2, which also favours stronger

loss peaks in the Al_2O_3 case. The theoretical results will be compared with existing experimental results in section 3.6.

3.3.2 Tabulation of Results

Similar group theoretical calculations can be carried out for other commonly occurring crystal structures. In this way a useful tabulation of the HREEL-active modes expected to appear in the spectra of different faces of many crystal structures can be arrived at. However, the calculation ignores effects due to crystalline anisotropy which can result in "mixing" of modes expected to appear in different orientations, with the result that some combination of the infra-red active vibrations appears. This question will be considered in depth later in the chapter, where it will be shown that under normal experimental conditions, such effects are often small, or even completely negligible, particularly in relation to the variations which can be created by differences in surface defect concentration. Thus the tabulation shown (table 6) remains useful as a rough guide to which modes are expected to appear in the HREEL spectrum of a given crystal face.

As is expected, in cubic systems where a=b=c, triply degenerate modes are predicted, and all faces should yield the same HREEL spectrum. In the remaining cases, where $a=b\neq c$, the degeneracy is split, and A and E modes are seen for planes perpendicular and parallel to the c-axis respectively. All observed modes are odd with respect to inversion, following from the properties of the dipole moment operator.

Table 6 Expected HREEL-active modes for various crystal structures.

unit cell symmetry	space group	structure	HREEL-active modes	
			all (h,k,l)	
cubic	O_h^5	NaCl	T_{1u}	
	O_h^1	CsCl	T_{1u}	
	T_d^2	ZnS (zinc blende)	T_2	
	O_h^5	CaF_2	$2T_{1u}$	
	T_h^6	FeS_2	$5T_u$	
			(h,k,0) (a)	(0,0,1) (b)
tetragonal	D_{4h}^{14}	TiO_2	$3E_u$	A_{2u}
			(x,y,z,0) (a)	(0,0,0,1) (b)
hexagonal	C_{6v}^4	ZnS (wurtzite)	E_1	A_1
	D_{6h}^4	NiAs	E_{1u}	A_{2u}
rhombohedral	D_{3d}^6	Al_2O_3	$4E_u$	$2A_{2u}$

(a) corresponding to modes seen in infra-red reflectance with $E_{\perp}c$
(b) corresponding to modes seen in infra-red reflectance with $E_{\parallel}c$

3.3.3 Intermediate Cases

It is interesting to consider how the HREEL spectra will appear in cases where the surface normal is neither perpendicular to nor parallel to the c-axis. If the tensor properties of the dielectric function in anisotropic materials are ignored, then in trigonal and tetragonal systems with a=b≠c, the parameter which determines the appearance of the spectrum is the angle between the surface normal and the c-axis. If the tensor properties of the dipole moment associated with a vibrational mode are considered, it is easily shown that, in the general case, the high frequency dielectric constant, ε_∞ is given by

$$\varepsilon_\infty = \cos^2\theta\,\varepsilon_{\infty\parallel} + \sin^2\theta\,\varepsilon_{\infty\perp} \qquad (23)$$

where $\varepsilon_{\infty\parallel}$ is the high frequency dielectric constant observed in infra-red reflectance with $E_\parallel c$, and $\varepsilon_{\infty\perp}$ is the corresponding dielectric constant with $E_\perp c$. Similarly, the absorption strengths, $4\pi\rho$, for modes observed in infra-red reflectance with $E_\parallel c$ are multiplied by $\cos^2\theta$, and those for modes observed with $E_\perp c$ are multiplied by $\sin^2\theta$, in calculating the loss function. Thus to a first approximation, all HREEL active modes are expected to appear in the spectrum, with diminished intensity.

3.4 Comparison of Theoretical Predictions with Existing Experimental Data for Rutile

The predicted spectrum of the (100) or (110) face (figure 7) is in reasonable agreement with the experimental spectra of Kesmodel et al[65] and Rocker et al[70] (figures 10 and 11), as regards positions and widths of the various loss features. Table 7 shows an assignment of the peaks appearing in these spectra. Again, the SO phonon frequencies lie between the bulk LO and TO frequencies of table 3. The HREEL spectra

are dominated by high frequency modes, so that the lowest frequency E_u mode is observed as a slight shoulder or is not resolved at all in the experimental spectra.

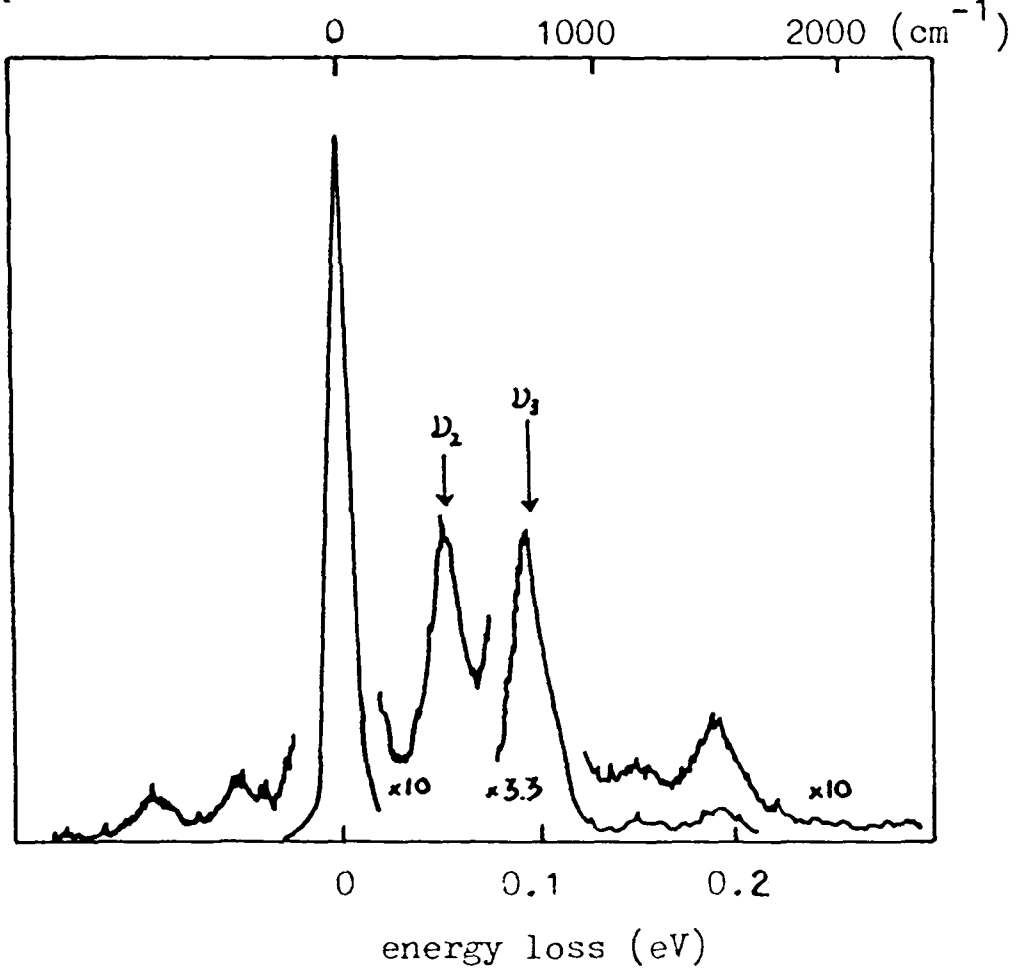

Figure 10[65] Experimental spectrum of rutile (100) recorded in the specular direction using an electron beam energy of 14eV. FWHM is 80cm^{-1} (10meV).

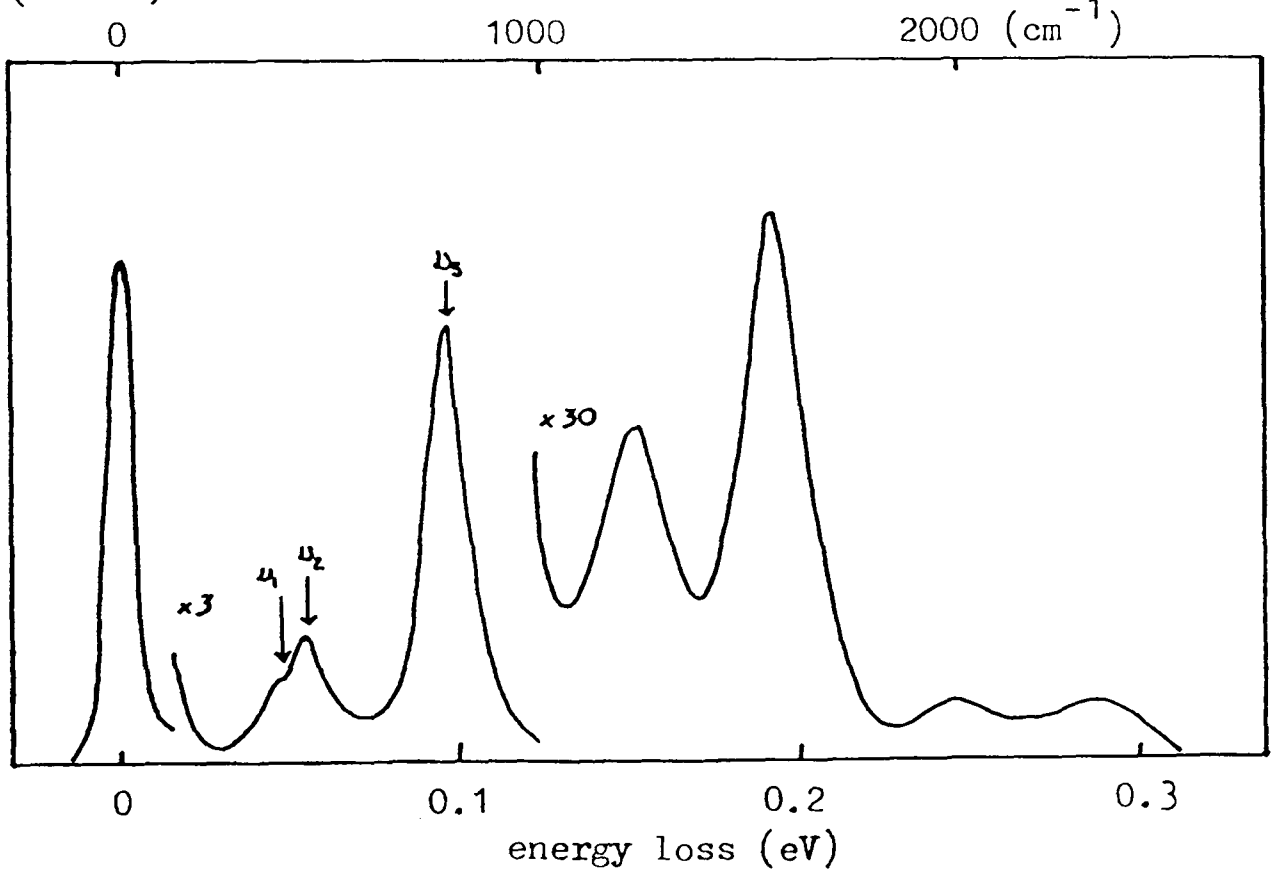

Figure 11[70] Experimental spectrum of rutile (110) recorded in the specular direction using an electron beam energy of 6.4eV. FWHM is 50cm^{-1} (6.5meV)

Table 7 Assignment of the peaks in the HREELS of TiO_2 (100),(110).

assignment	experimental frequency(cm^{-1})		predicted frequency	
	(a)	(b)	cm^{-1}	eV
v_1	not observed	371	371	0.046
v_2	436	435	436	0.054
v_3	766	766	762	0.094
v_1+v_3	not resolved	1137	1133	0.140
v_2+v_3	1202	1202	1198	0.149
$2v_3$	1532	1532	1524	0.189
v_2+2v_3	1968	1968	1960	0.243
$3v_3$	2298	2299	2291	0.284

(a) from reference 65
(b) from reference 70

The main difference between the predicted and experimental spectra lies in the relative intensities of the v_2 and v_3 single phonon excitations. The predicted intensity ratio $v_2:v_3$ is approximately 1:12, in contrast with the approximate ratio observed by Kesmodel of 1:4, and a similar ratio observed by Rocker. However, the calculated results are in very much better agreement with experiment than the surface phonon calculation for TiO_2 (100) carried out by Mahan[71] (and cited by Kesmodel et al) which predicts a $v_2:v_3$ intensity ratio of approximately 1:33.

One factor which may contribute to the difference between experiment and theory is the fact that the intensities (and to some extent, the frequencies) of surface optical phonons are influenced by surface defects. This effect will be discussed in detail later: meanwhile, it is sufficient to note that the sample preparation conditions employed by Kesmodel involved several minutes of 500eV argon-ion bombardment at a temperature of 650K, a treatment likely to produce surface oxygen defects. The sample treatment used by Rocker involved similar argon ion bombardment and subsequent heat treatment at 870K for 300 seconds in a pressure of 10^{-6}mbar of oxygen. Although this

treatment was designed to restore the surface stoichiometry it seems unlikely that it would be completely effective. It has been shown by UPS in this laboratory that exposure of TiO_2 single crystals to 100mbar of oxygen for several hours at 750K after argon-ion bombardment ($80\mu Acm^{-2}$, 5kV for 2 minutes) does not result in a completely defect free surface[72]. After 2kV argon-ion bombardment at $10-20\mu Acm^{-2}$ for 10 minutes, resistive heating at 1000K for periods of up to 70 hours has been found necessary to produce a clean, defect free surface[53]. (It would also be difficult to record a HREEL spectrum of a totally defect free rutile crystal due to charging problems.)

In an attempt to clarify the position, HREEL spectra were recorded of nominally (100), (001) and (110) faces of rutile. These experiments are described below.

3.5 Experimental

Rods of single crystal TiO_2 were provided by Professor V.E. Henrich of Yale University. These were cut from a boule at three different orientations, giving samples with (100), (110) or (001) faces at the ends of the rods. These end faces measured 4mmx4mm, and the rods were typically 10-15mm long. The rods were supplied in both stoichiometric (clear) form, and lightly reduced (metallic grey) form. However, it was found that the two forms were readily interconvertible, the transition from reduced to unreduced form being made by calcining overnight in air at 1300K in a muffle oven. The reverse process was achieved by electron bombardment at 1.5kV and 21mA for periods of up to several minutes in vacuo (in the preparation chamber of the spectrometer). Typical examples of the rods are shown in figure 12.

The orientation of the end faces of the rods was checked by Laue back reflection. Laue photographs taken with a flat photographic film

perpendicular to the X-ray beam give direct information about the Friedel symmetry of that direction. This symmetry includes both the axial symmetry of the direction, and any mirror symmetry containing the axis. The only finite symmetries that can be diplayed in two dimensions are the 10 crystallographic point groups in a plane. Table 8[73] shows the projection symmetries of Laue photographs taken with the X-ray beam in specified directions for tetragonal systems.

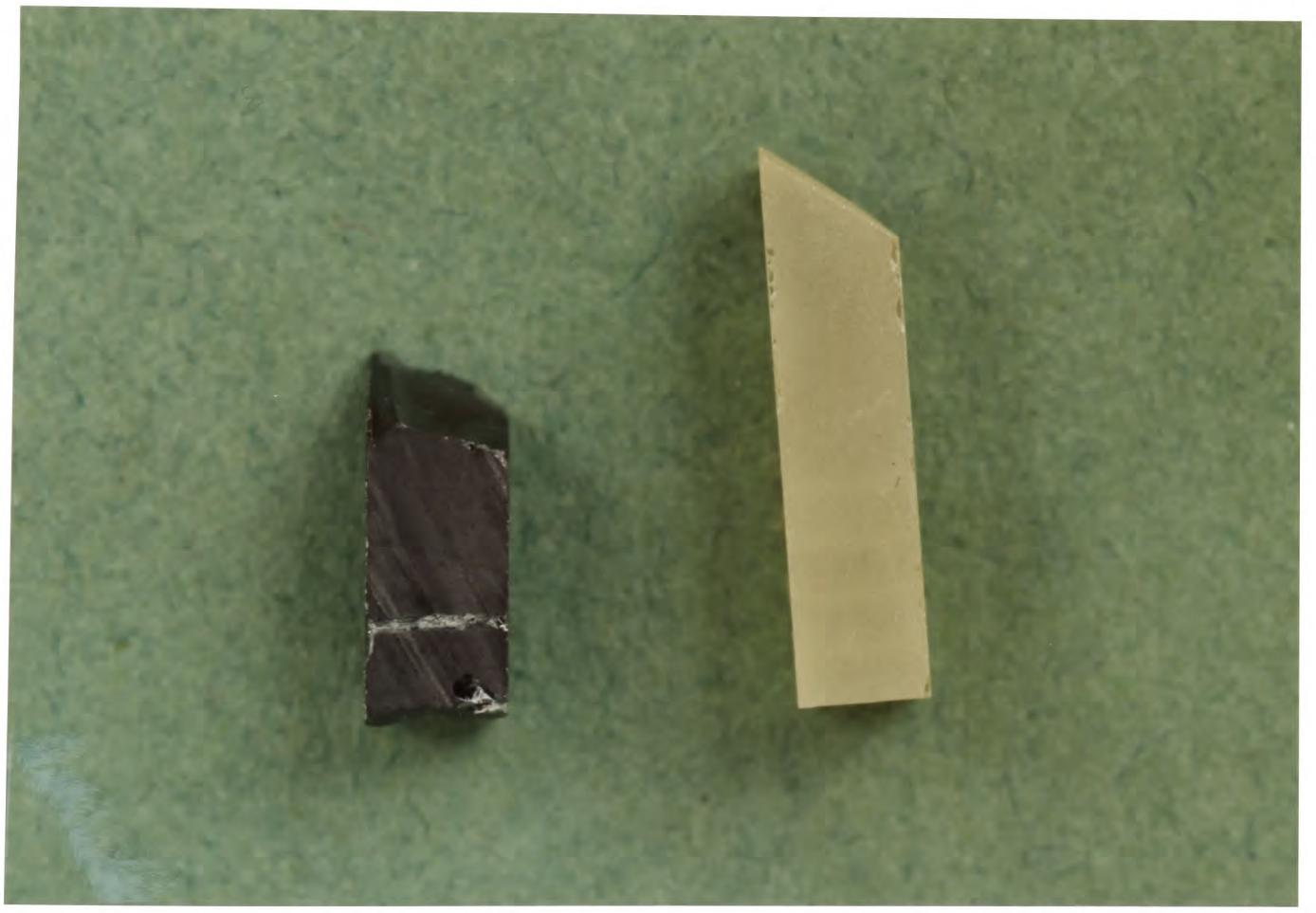

Figure 12: Stoichiometric (right) and reduced (left) examples of the single crystal rutile rods used.

Table 8[73]

		Direction of X-ray beam						
System	Friedel Class	[100]	[001]	[110]	[uv0]	[u0w]	[uuw]	[uvw]
Tetragonal	4/m	m	4	m	m	1	1	1
	4/m 2/m 2/m	2mm	4mm	2mm	m	m	1	1

TiO_2 belongs to the Friedel class 4/m 2/m 2/m. Photographs of the (001) face exhibit a four-fold axis, whilst those of the (100) and (110) faces show two mirror planes and display 2mm (C_{2v}) symmetry. The photographs of the (100) and (110) directions can be distinguished as the photographs display angles between the lines of diffraction spots which are characteristic of the faces being studied.

In order to aid cleavage of the crystals, several closely spaced grooves were made along one length of the rods, parallel with the end faces, by Mr.G. Read of the Clarendon Laboratory. This enabled several crystal slices of a specified orientation to be obtained from each rod. Rutile is a rather hard material, and cleavage of the crystal rods proved difficult. It was eventually achieved using a brass cleaving block and a carbon steel chisel, placed in the specially cut grooves. In this way, clean, freshly prepared surfaces of specified orientation were obtained, and a minimal amount of sample preparation inside the spectrometer was required.

The crystal slices were mounted on platinum sample stubs and held in place with platinum wires. Sample cleaning was undertaken in the spectrometer preparation chamber. Before moving the samples into the chamber, the titanium sublimation pumps were fired for a short period. This has the effect of preferentially removing oxygen-containing contaminants from the atmosphere, which would otherwise readily react with the rutile surface under study. The samples were cleaned by electron bombardment under mild conditions - 1.5kV and 21mA for 5 seconds. Following this treatment, the XPS were free of loss features due to carbon or other contaminants, and the EELS were free of loss features characteristic of adsorbed species such as H_2O, CO or hydrocarbons. LEED patterns with well resolved spots were obtainable from most slices, indicating that the surfaces were well ordered.

Photographs of the (110) face exhibited the characteristic 1x1 LEED pattern expected for the unreconstructed surface[74].

It was found that, due to charging problems, spectra of completely unreduced samples could not be obtained, so all the samples used were lightly reduced.

The HREEL spectra peaked quite strongly in the specular direction. Figure 13 shows typical spectra obtained for (110) and (100) surfaces, recorded in the specular mode with a 5eV electron beam incident at 45^{o} to the sample surface. Also shown in the diagram is the spectrum predicted by the simple dielectric theory for the experimental conditions employed. It can be seen that the predicted spectrum is in very good agreement with the experimental results as regards positions and widths of the loss features. The main difference between experiment and theory again lies in the v_2:v_3 intensity ratio, which, in the experimental spectra is in the region of 1:5 or 1:6. Small, but experimentally unreproducible fluctuations in this ratio were observed from sample to sample. This supports the view that this parameter is quite strongly dependent on the degree of reduction of the sample.

Further spectra obtained from an (001) cleave are shown in figure 14. It will be seen that these spectra are very similar to those obtained for the (100) and (110) surfaces. The (001) surface of rutile is unstable and reconstructs or facets when annealed[74]. In contrast, the (100) and (110) faces are stable, the latter being a growth face in vapour-transport-grown crystals. The nature of the reconstruction is complex and as yet unclear[74], but it seems likely that the electron bombardment necessary to free the crystal from hydrocarbon impurities promoted the reconstruction, and that the resulting HREEL spectrum is from facets of stable (h,k,0) surfaces, which would be predicted to give the spectrum which is observed. LEED obtained from the electron bombarded (001) surface showed spots which did not converge to the (0,0)

beam on increasing the beam energy, indicating faceting. Spectra taken without sample cleaning were dominated by the strong C-H stretch, and were poorly resolved.

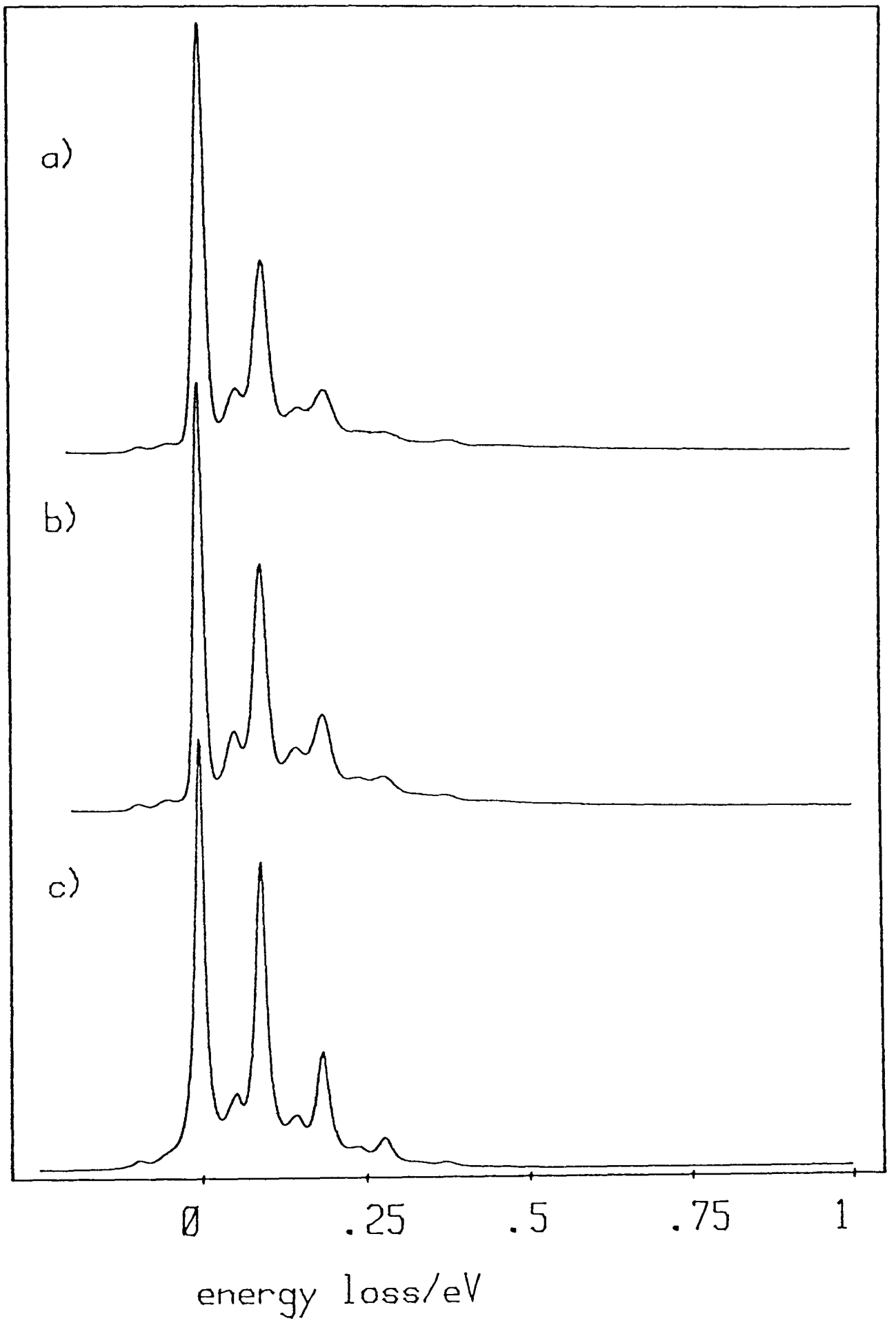

Figure 13: HREEL spectra recorded in the specular mode using a 5eV beam for rutile (110) (a) and (100) (b) surfaces. FWHM 15meV. (c) shows the dielectric theory prediction for the (h,k,0) surface under these experimental conditions.

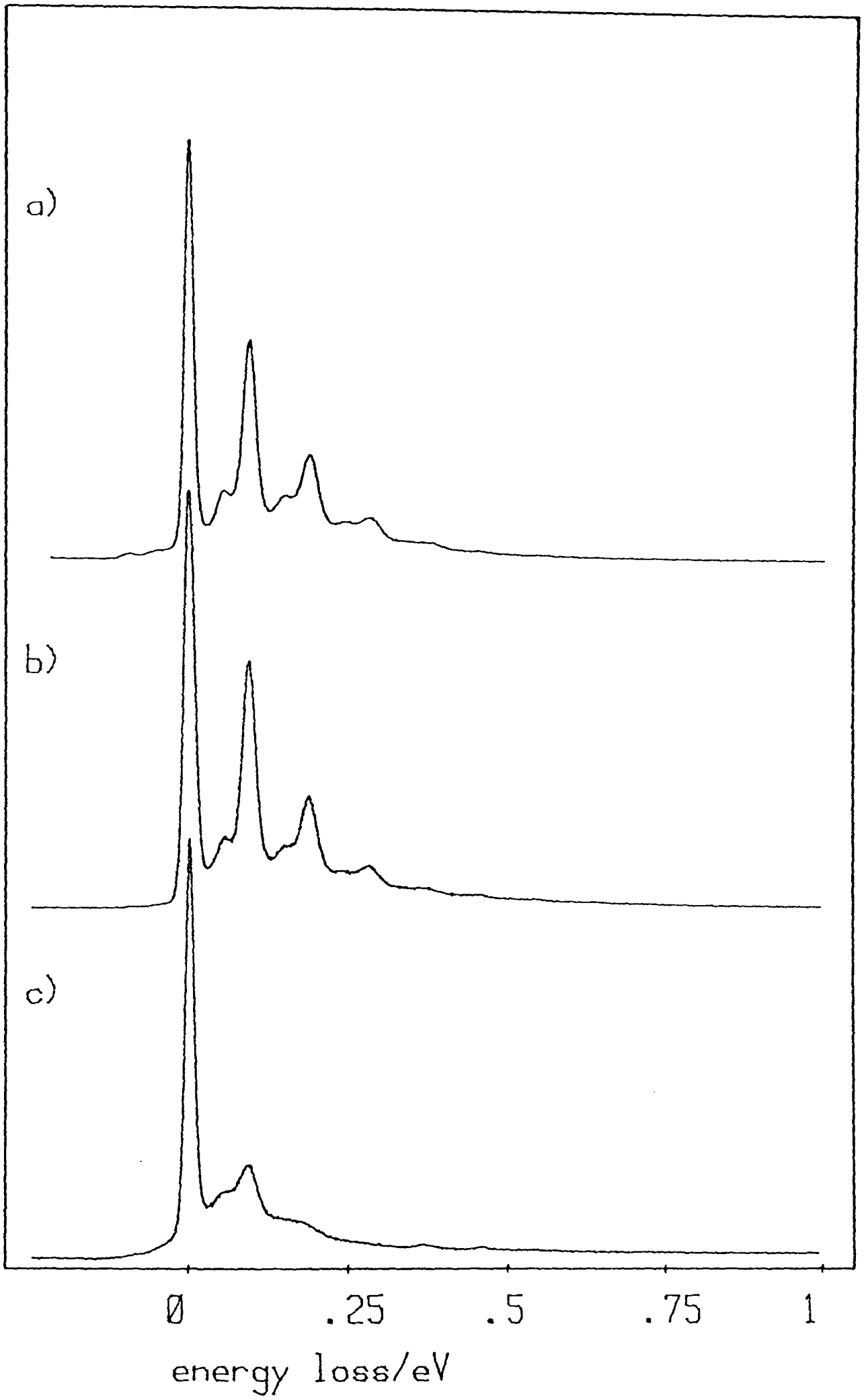

Figure 14: HREEL spectra of the rutile (001) surface recorded in the specular mode using an electron beam energy of 5eV. FWHM 15-20meV.
(a) room temperature
(b) 150K
(c) after argon-ion bombardment (500-1000V at 1-2$\mu A cm^{-2}$ for 20 minutes)

Figure 14b) shows a spectrum of the (001) surface at roughly 150K. As expected, the electron energy gain peaks to the left of the elastic peak are almost completely absent at this temperature. Figure 14c) shows the effect of argon-ion bombardment on the (001) surface. Here the surface was bombarded with 500-1000V Ar^+ ions in 4.10^{-5}mbar argon for 20 minutes at 1-2$\mu A cm^{-2}$. The strong phonon loss peaks are "damped" by the creation of a large concentration of surface defects, and there are small shifts in their frequencies. The damage to the surface could not be reversed by exposing the crystal to 50mbar O_2 for a few seconds in the preparation chamber of the spectrometer. The effects of argon-ion bombardment on the HREEL spectra of rutile are considered more fully in section 3.7.

3.6 Crystalline Anisotropy

So far, it appears that the loss spectra of TiO_2 are well described by a relatively simple theory based on the dielectric response of the crystal surface to the potential of the incident electron via long-range dipole coupling. The dielectric function $\epsilon(\omega)$ has been treated as a scalar quantity. This is obviously not correct in the case of anisotropic materials, where ϵ is a tensor. The simple dielectric theory thus makes no allowance for coupling of modes observed in orthogonal directions. Theory appropriate to anisotropic materials has only been developed very recently[75,76], and no comparison of the results of this theory with those obtained experimentally has been published, except for the most simple case[75,76]. In the following section, the theory is compared with experiment, and its usefulness assessed. Details of the calculation of the loss function are given in Appendix III.

After checking the theoretical results as far as equation AIII(12), two computer programmes were written by the author to predict HREEL spectra using the modified theory. The relevant sections of these programmes are given, with explanation in Appendices IV and V. As can be seen, two simple limiting cases were considered, with the c-axis pointing along the surface normal (programme FTSOPHW2) and lying in the surface plane (FTSOPHW3). These two situations corresponded to the cases considered previously using the simple dielectric theory. The simplest possible case is that treated by FTSOPHW2. This corresponds to the (001) or (0001) surfaces of anisotropic crystals. In this case the ξ function in equation AIII(9) simply reduces to the geometrical mean $(\varepsilon_{\perp}(\omega)\varepsilon_{\parallel}(\omega))^{1/2}$ of the two dielectric components. The effects of anisotropy can then be reproduced simply by replacing $\varepsilon(\omega)$ in the classical loss function by $(\varepsilon_{\perp}(\omega)\varepsilon_{\parallel}(\omega))^{1/2}$. An example of this case for which experimental results have been obtained is the (0001) surface of Al_2O_3[76]. Figure 15 shows the experimental spectrum, together with the prediction from FTSOPHW2, and the prediction obtained using the simple dielectric theory. Parameter values from infra-red reflectivity[67,68,69] are again used to calculate the theoretical spectra. The experimental spectrum has been fitted by Liehr et al to their theory, which takes into account the tensor properties of ε[76]. It can be seen that there are small but significant changes in intensities and frequencies of the phonon modes between figures 15b) and c). Note that, where effects due to anisotropy are significant, it is impossible to unambiguously label the phonon modes observed due to the "mixing" which occurs between $\varepsilon_{\perp}(\omega)$ and $\varepsilon_{\parallel}(\omega)$. The experimental resolution obtained by Liehr et al was 4meV, and is amongst the best currently attainable. Optimum resolution on our VG ESCALAB spectrometer is roughly 15meV, so such small effects would be unlikely to be experimentally observable using our HREELS facility.

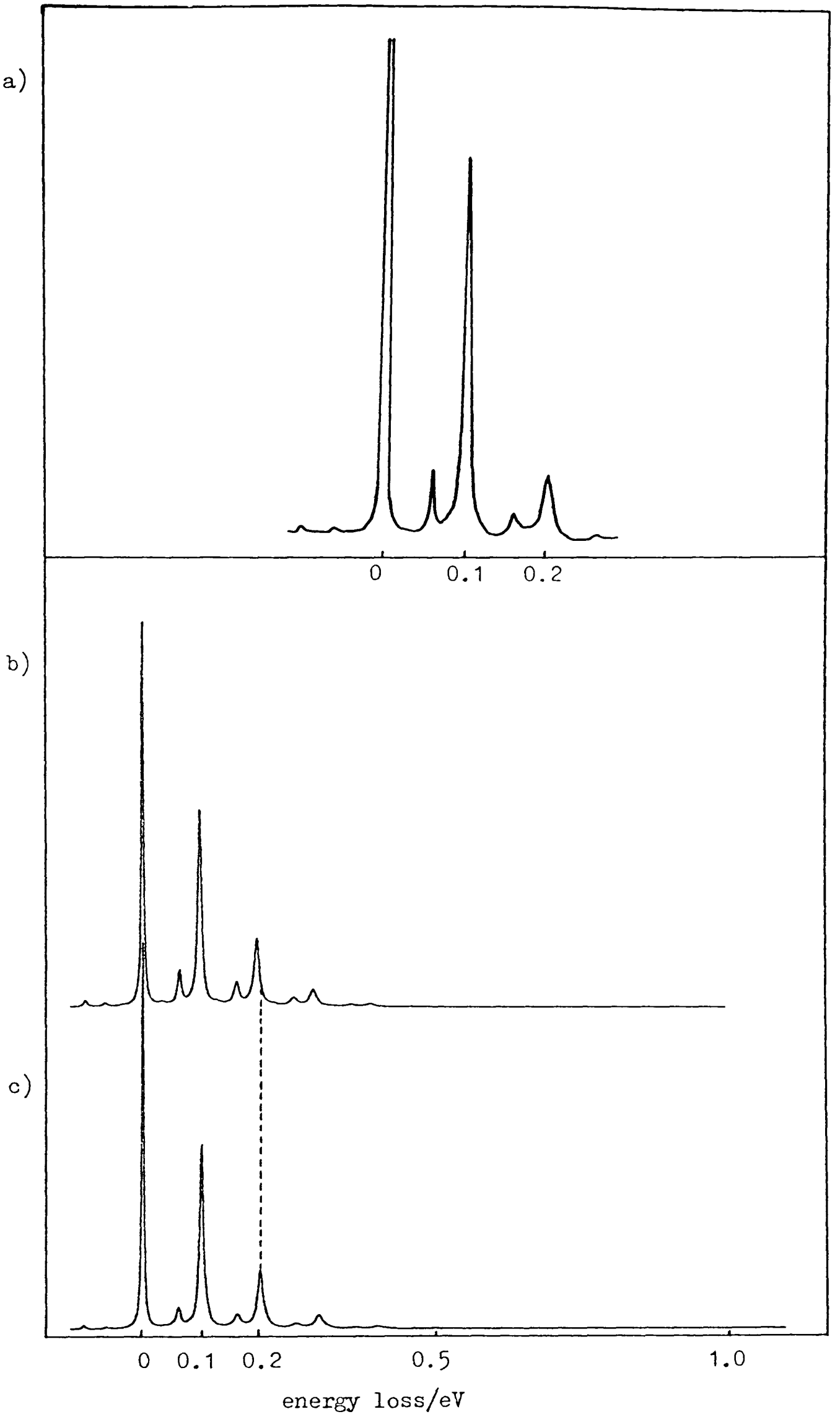

Figure 15: The experimental HREEL spectrum for corundum (0001) (a) from reference 76, recorded in the specular direction with a 6.1eV beam. Also shown are the predicted spectra under these experimental conditions using the simple dielectric theory (b) and including the tensor properties of ε (c).

The other case considered (and treated in the programme FTSOPHW3) is more complex. If the c-axis lies in the surface plane,

$$\varepsilon_{\perp} = \varepsilon_{zz} \tag{24}$$

and so equation AIII(9) becomes

$$\xi = [\varepsilon_{\perp}\varepsilon_{\parallel} \cos^2\varphi + \varepsilon_{\perp}^2 \sin^2\varphi]^{1/2} \tag{25}$$

The integration of the loss function AIII(11) is then done numerically using Simpson's rule (Appendix V).

It will be noted that one result of consideration of the tensor properties of the dielectric function is that the HREEL spectrum of a particular surface is expected to depend on the orientation of the c-axis within the surface plane relative to the plane of incidence of the electron beam. During the course of the experiments on TiO_2 single crystal surfaces detailed earlier, extensive work was carried out to try to observe such variations. All the crystal slices examined were observed at orientations such that the c-axis was parallel to, perpendicular to and at 45^{o} to the plane of the incident beam of electrons. Any variations with orientation which could be detected were small and were experimentally unreproducible. This result was initially rather surprising, but was confirmed by predictions made using the programme FTSOPHW3 for the prevailing experimental conditions. These predicted spectra showed that no experimentally significant orientational variation of the spectra was to be expected.

One reason for this became readily apparent on a closer examination of the loss function AIII(11). If the half acceptance angle of the spectrometer, Ψ_a is large, then

$$\lim_{\Psi_a \longrightarrow \infty} I(\varphi,\omega) \longrightarrow \eta/(1+\eta^2) + \pi/2 - \tan^{-1}\eta \tag{26}$$

In this case it can be shown that the loss function $P(\omega,\varphi)$ becomes independent of φ_v, the azimuthal angle made by the plane of incidence of

the electron beam with the x-axis (figure AIII.1). Examination of the loss function leads to the conclusion that it may become independent of φ_v at spectrometer half-acceptance angles which are greater than a few degrees. The acceptance angle of our spectrometer is 6.5^o, and so no orientational effects are expected to be observed. Another factor which hampers the observation of small changes in HREEL spectra is the relatively poor resolution of our instrument. It was concluded that, in principle, such effects might be observable using an instrument offering "state-of-the-art" ($\sim$3meV) resolution, and a half acceptance angle of less than a few degrees. Results from such a spectrometer are discussed later in the chapter (section 3.7).

In the special case considered, where the c-axis lies in the plane, k_x and k_y become the components of the total momentum transfer, k, parallel and perpendicular to the c-axis respectively (figure AIII.1) Thus, using equation (25), we can envisage two limiting loss functions determined by $\varepsilon_\perp(\omega)$ and $(\varepsilon_\perp(\omega)\varepsilon_{||}(\omega))^{1/2}$ which could in principle be observed in off-specular scattering in the plane of incidence (so that there is appreciable momentum transfer parallel to the surface). These two limiting cases would correspond to the electron beam directed respectively in the $[\bar{1}10]$ azimuth (to ensure dominant momentum transfer perpendicular to the c-axis) and in the [001] azimuth (to ensure dominant momentum transfer parallel to the c-axis). A schematic illustration is shown in figure 16. Figure 17 shows the loss functions AIII(11) for the two limiting cases. Also shown for comparison purposes is a hypothetical loss function determined by $\varepsilon_{||}(\omega)$ alone. The "perpendicular" loss function contains contributions only from the E_u modes. The highest energy peak at 94.5meV (corresponding to the ν_3 mode of table 7) falls just below the LO phonon frequency of 99.9meV. Due to the "mixing" of the modes in the "parallel" loss function determined by $(\varepsilon_\perp(\omega)\varepsilon_{||}(\omega))^{1/2}$, it is no longer possible to make rigorous symmetry

assignments of the losses. However, it can be seen that the two lower energy peaks correlate strongly with the lower energy E_u losses of $\varepsilon_\perp(\omega)$. The energies are shifted upwards by experimentally negligible increments of 0.3meV and 1.2meV. The high energy loss has mixed A_{2u} and E_u character, and peaks at the intermediate energy of 91.5meV. The peak has a high energy shoulder reflecting the mixing. The introduction of the A_{2u} mode also leads to additional screening of the low energy E_u modes which are relatively weaker than in the "perpendicular" spectrum. However, the differences between "parallel" and "perpendicular" spectra become almost insignificant after convolution with instrumental broadening and allowance for the range of momentum transfer allowed by our analyser system, to produce the predicted spectra.

a)

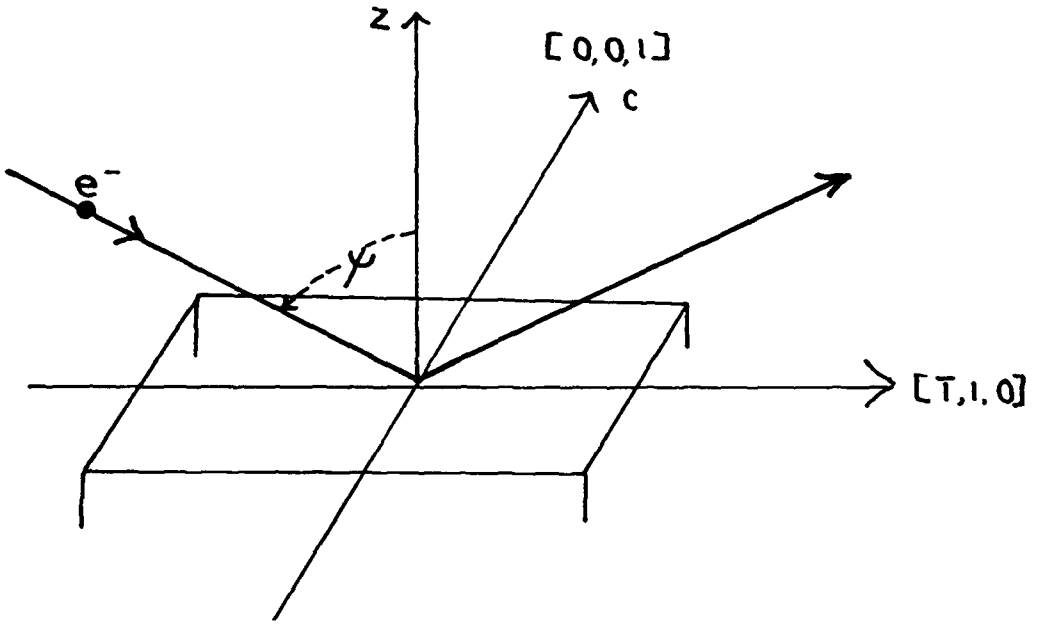

b)

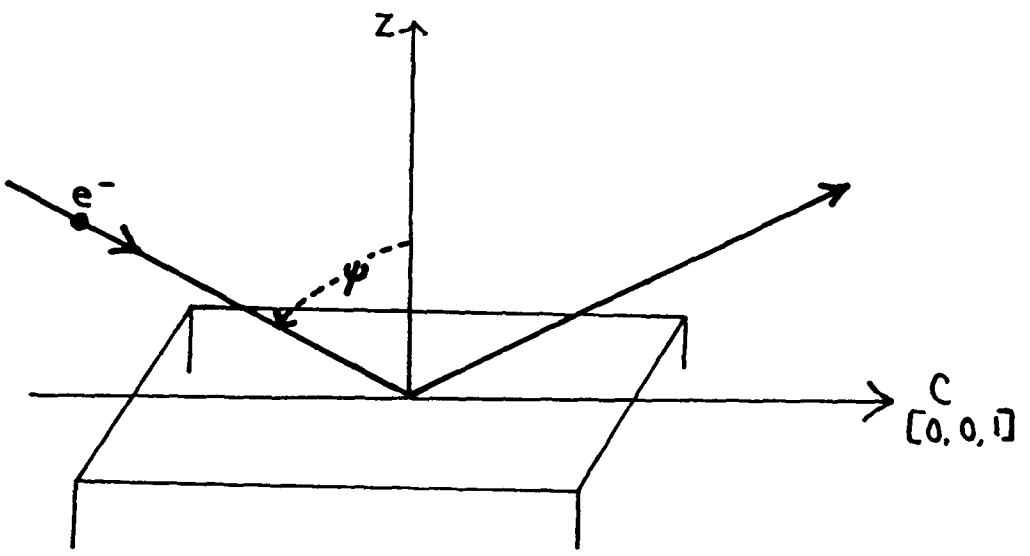

Figure 16: Scattering geometries corresponding to the limiting loss functions a) $\varepsilon_\perp(\omega)$, b) $\sqrt{\varepsilon_\perp(\omega)\varepsilon_\parallel(\omega)}$.

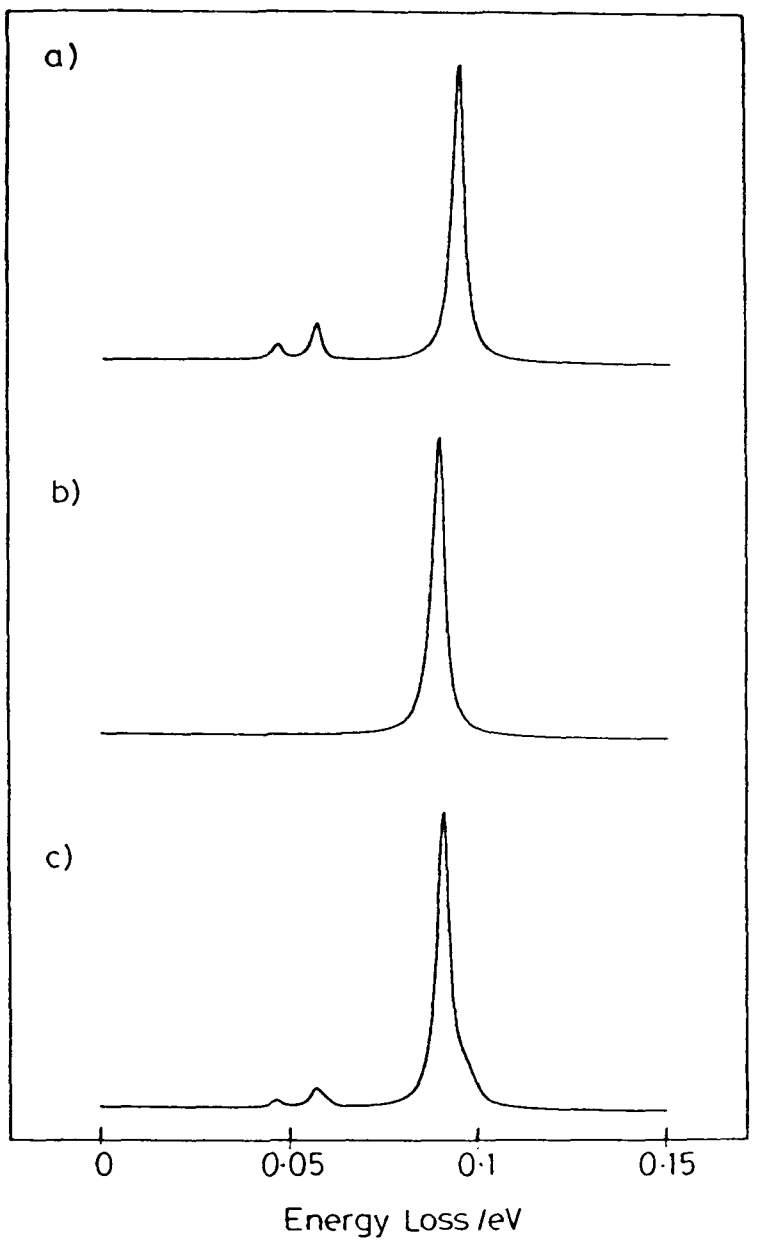

Figure 17: Loss functions for rutile (h,k,0) calculated a) from the perpendicular dielectric function $\varepsilon_{\perp}(\omega)$, b) from $\varepsilon_{\parallel}(\omega)$ and c) from the square root dielectric function $\sqrt{\varepsilon_{\perp}(\omega)\varepsilon_{\parallel}(\omega)}$.

In the experiments described earlier using TiO_2 single crystal surfaces, all spectra were recorded in specular and slightly off-specular (10^{o} from specular) directions. Only slightly off-specular directions can be explored, as in this region, the selection rules for dipole scattering still hold, and the intensities of the phonon losses

are still quite large. In specular scattering experiments, the non-vanishing angular acceptance of the analyser system allows both k_x and k_y transfer. It was found experimentally that the resolution attainable from our spectrometer was not sufficiently good to distinguish between the two limiting spectra.

Thus, it appears that the effects of crystalline anisotropy in many cases are likely to be so small as to be completely negligible from an experimental point of view. This reinforces the opinion that the simple dielectric theory, which has been used with considerable success to predict HREEL spectra by our group, remains a good approximation.

In particular, the effects of anisotropy on the HREELS of TiO_2 (110) and (100) are rather small, the main effect being to introduce mixed E_u/A_{2u} character into the highest energy loss peak. Loss peaks occur at energies close to those of LO phonons, although their energies are ultimately determined by the transverse resonance frequencies. Thus, the earlier assignments of references 65 and 70 are incorrect in that they imply that the lowest energy loss has predominant E_u(TO) character, whereas the two higher losses have E_u and A_{2u}(LO) character respectively.

3.7 The Influence of Surface Defects on the HREELS of TiO_2 (110)

As the theoretical predictions showed that the effects of crystalline anisotropy were very small, it became necessary to obtain results from a spectrometer having both very good resolution and very small half-acceptance angle. Such a spectrometer became available at Imperial College London. Any experimental HREEL or ELS spectra shown in the following sections were obtained by Dr.R.G. Egdell and Miss S. Eriksen using a Leybold-Heraues ELS 22 spectrometer. This is mounted in

an ion pumped chamber (base pressure 10^{-10}mbar) and is equipped additionally with front view LEED optics, a Leybold-Heraues EA10/100 100cm hemispherical analyser and a 5kV electron gun for N(E) Auger spectroscopy and low-resolution electron energy loss spectroscopy (ELS).

In these studies, the crystal (a polished (110) face, 1cmx1cm) was mounted in a tantalum tray, and could be heated either by electron bombardment or by resistive heating. It was found that clean, defect-free surfaces could be produced by 2kV argon-ion bombardment at 10-20$\mu A cm^{-2}$ for 10 minutes, followed by resistive heating at 1000K for periods of up to 70 hours. These surfaces exhibited well-defined (1x1) LEED patterns, gave Auger spectra free of signals due to carbon or other contaminants, and produced ELS showing no losses in the bandgap region. The influence of surface defects was explored using 2kV argon-ion bombardment to produce the defects. The resulting HREEL spectra and corresponding ELS spectra for the annealed crystal and three different damaged surfaces are shown in figures 18 and 19. The ELS spectra show that damage of the surface is associated with the growth of an electronic loss in the bandgap region close to the elastic peak.

It is well established that argon-ion bombardment of rutile causes preferential sputtering of oxygen and introduction of occupied Ti:3d states as a result of oxygen deficiency[70,77,78,79]. Electron bombardment leads to oxygen desorption through Knotek-Feibelman and related mechanisms[80]. The Ti:3d states give rise to a new electronic loss feature in the bandgap region, although the energy and origin of the feature are matters of some controversy. Henrich[77] and Somorjai[78] observed defect induced losses on argon-ion bombarded TiO_2 (110) and (100) at energies of 1.9eV and 1.6eV respectively. Both measured spectra in the dN/dE mode. Gopel[70,79] found defect induced losses at 0.8eV using a monochromated 20eV exciting beam and a HREELS analyser with an angular acceptance of 1.4^{o}. The loss appears at roughly 1.3eV

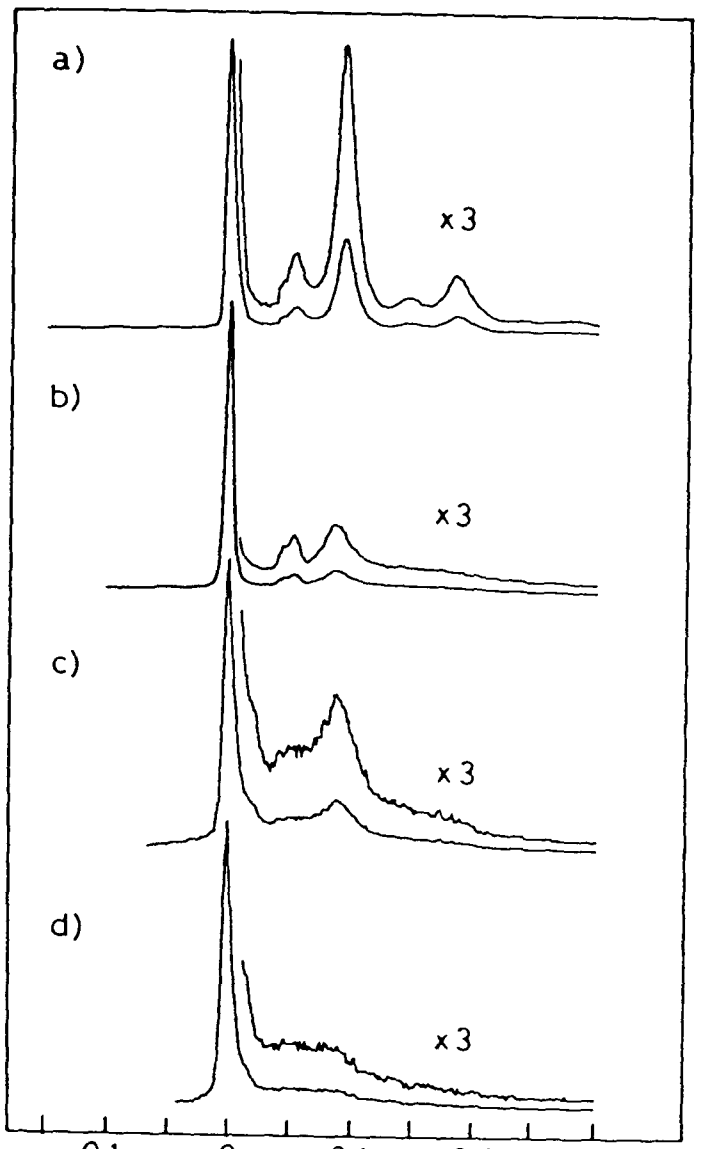

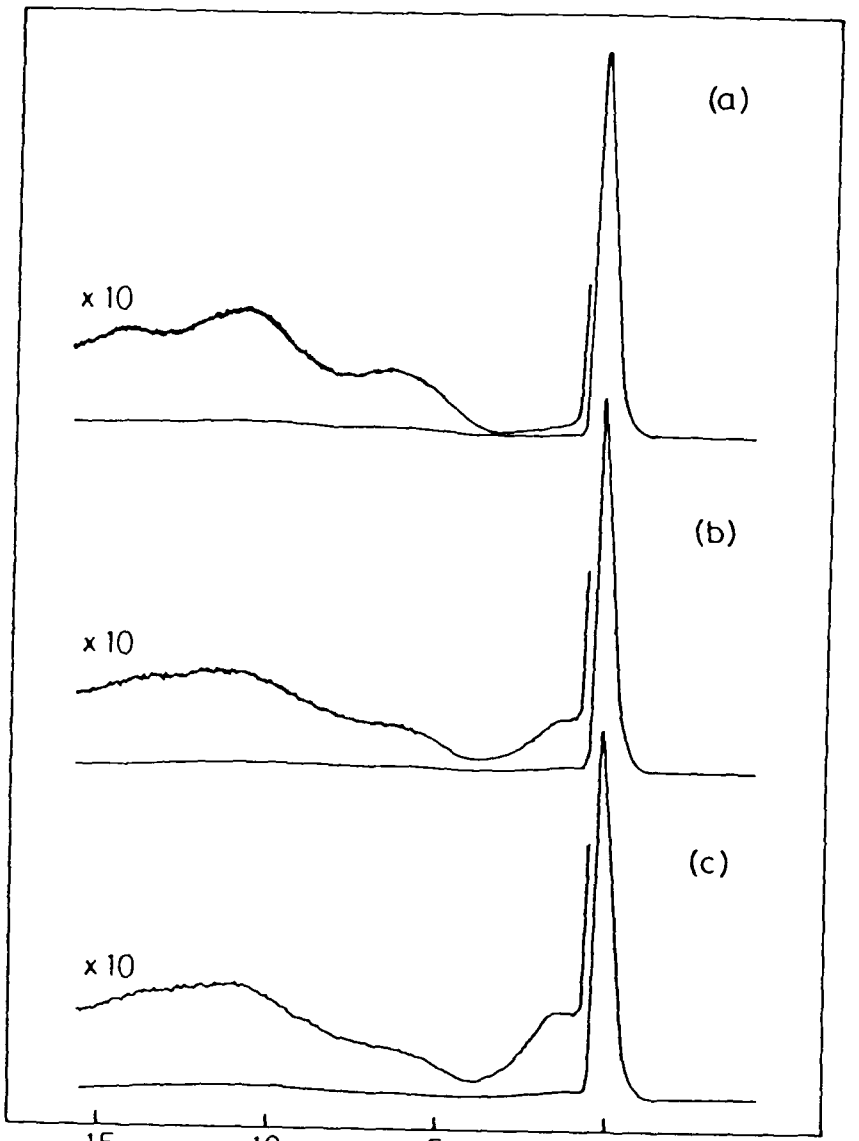

Figure 18: (left hand panel) HREEL spectra of rutile (110) excited by a 7.35eV electron beam, incident along the [001] azimuth, recorded in the specular direction with a 30° incidence angle.(a) Ordered annealed surface. Note single phonon losses at 44meV (shoulder), 52meV and 94meV, together with combination and overtone peaks at higher energy. (b) Electron bombarded surface; 20mA/2kV for two hours onto Ta backing plate. Note losses at 46meV, 53meV and 86meV. (c) Argon-ion bombarded surface, using 0.0015C 2kV ions incident on crystal surface. Losses at 50meV (ill-defined) and 88meV. (d) Argon-ion bombarded surface. 0.0060C 2kV ions onto crystal surface. Ill-defined loss peak at 80meV.

Figure 19: (right hand panel) ELS spectra excited with an unmonochromated 500eV electron beam incident at 45° to the crystal surface with analysis of specular electrons. (a) Ordered annealed surface as in (a) above. (b) Argon-ion bombarded surface as in (c) above. (c) Argon-ion bombarded surface as in (d) above. Note growth of loss peak at 1.3eV with increasing bombardment.

in the spectra shown in figure 19. The bulk defect absorption energy in TiO_2 shifts to higher energy with increasing degree of reduction[81], but it seems likely that the use of differing electron excitation energies and differing modes of energy analysis of the scattered electrons is of importance.

Some results of a previous study by the author of the effects of defects on the UPS of polycrystalline TiO_2 are shown in figure 20[82]. This shows the UPS of a ceramic pellet of TiO_2 before and after a mild argon-ion etch at 1kV and $2\mu Acm^{-2}$ for five minutes. The dominant features are due to the filled oxygen 2p valence band with an onset at around 3.5eV below Ef, and the strong secondary electron background at higher binding energies. The features of interest are those to the low binding energy side of the valence band edge. In the unetched spectrum, there is a single feature forming a shoulder to the valence band. In the etched spectrum, two features are present; a shoulder to the low binding energy side of the valence band edge, and an additional peak with an onset at E_f. This peak is in the position expected for the conduction band, and is thus assigned as the bulk TiO_2 conduction band.

This "double-peaked" structure has been previously observed in studies of both TiO_2 and $SrTiO_3$[78,83,84,85], although its origin is little commented on. It is seen very clearly in the UPS spectrum due to Ferrer and Somorjai[83] of reduced $SrTiO_3$ (111) after argon-ion etching and annealing, and in the UPS of argon-ion bombarded TiO_2 (110) due to Henrich, Dresselhaus and Zeiger[85]. It is noticeably weak in the UPS of vacuum-fractured $SrTiO_3$ (100) due to the previous authors[86], and is attributed to the presence of residual surface defects. When surface defects are produced by argon-ion bombardment, a much stronger band of surface states appears in the band gap[86].

Henrich *et al*[86] find that exposure to oxygen depopulates the band gap surface states on both vacuum fractured and ion bombarded $SrTiO_3$

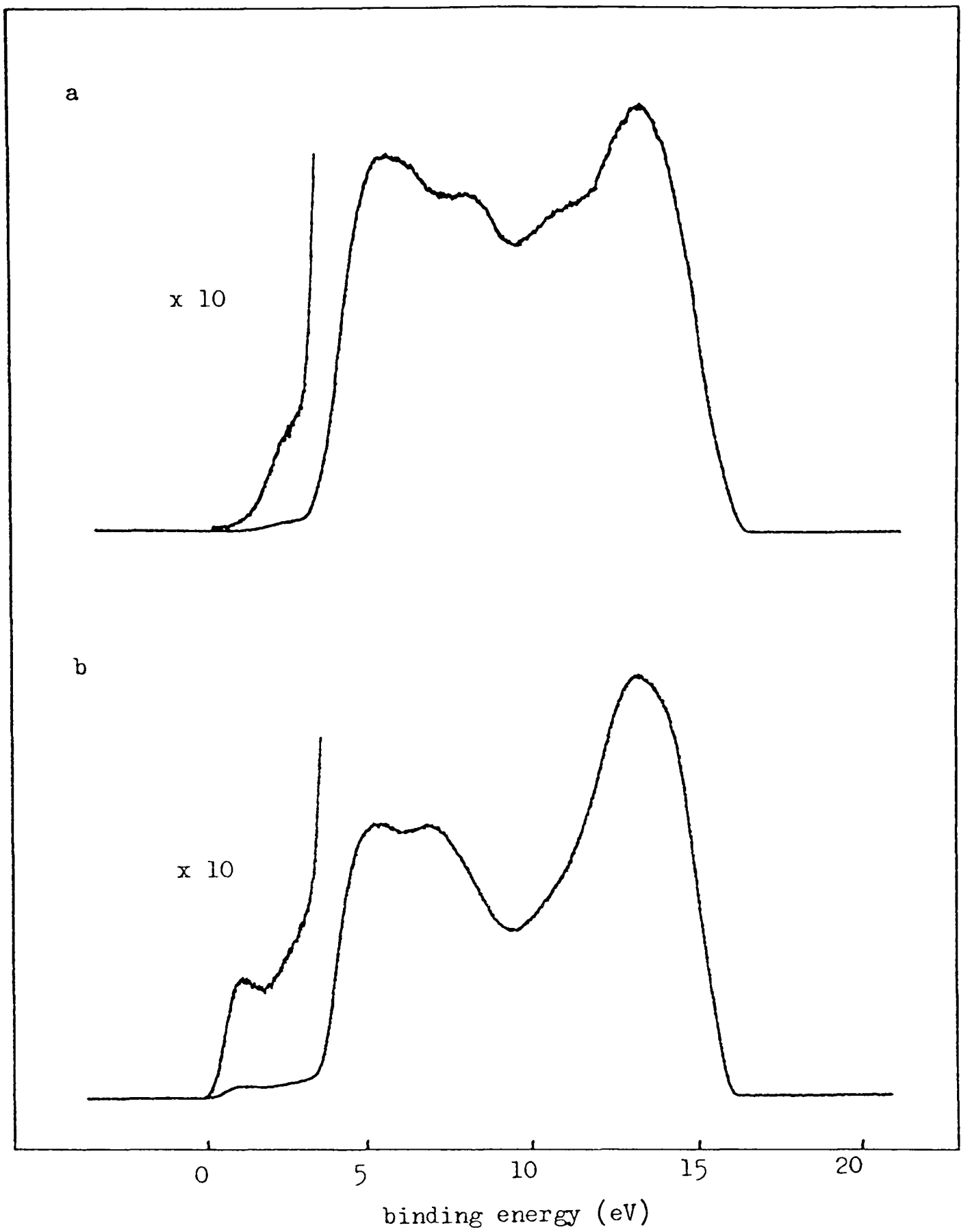

Figure 20: UPS of polycrystalline TiO_2
(a) prior to argon-ion etching
(b) following etching for 5 minutes with 1kV argon ions at $2\mu Acm^{-2}$

surfaces. They suggest that the surface states arise from the creation of Ti^{3+}-O vacancy complexes, and are of predominantly d-electron character. These are also postulated for TiO_2 by the same authors[77]. It is suggested that when TiO_2 is bombarded for long periods with argon

ions, the equilibrium surface structure that results is essentially Ti_2O_3, i.e. removal of one oxygen atom for every two TiO_2 units. For shorter bombardment times, a pairing of Ti^{3+} ions similar to that in Ti_2O_3 is suggested.

Ti atoms at the surface of stoichiometric TiO_2 will be 5-coordinate. On removal of an oxygen atom a four-coordinate Ti^{3+}-□ structure is created. It may be envisaged that, due to decreased Madelung destabilisation of electrons on Ti sites upon the removal of oxygen atoms, the energy of the surface state will be lowered, and will split away from the conduction band, becoming visible in the band gap. The Ti^{3+} 3d orbitals are small and compact. If pairing of the Ti^{3+} ions occurs, Ti^{3+}-□-Ti^{3+}, it seems likely that, due to strong Coulombic repulsion, only one electron can be localised on a cation adjacent to the defect site. The remaining electron is forced to enter the Ti:3d conduction band. If both electrons were localised on titanium cations, the energy of the surface state would be raised above that of the conduction band. Thus it seems likely that in figure 20b), the peak at roughly 1eV binding energy is due to electrons in the Ti:3d conduction band, whilst the shoulder at around 2.5eV is due to electrons localised by oxygen vacancies. The losses due to surface defects observed in ELS of argon-ion bombarded TiO_2 thus seem likely to be due to polaronic excitations, possibly involving bipolaronic Ti^{3+}-Ti^{3+} pairs.

3.8 Theoretical Modelling of the HREEL Spectra for Defected Rutile Surfaces

It was found that the influence of the defects on the vibrational HREEL spectra could be understood simply in terms of modification of the dielectric function of the damaged surface of the crystal. A Lorentzian oscillator term with parameter values ρ_e, ω_e and γ_e was added to the

summation in equation (13) to represent the defect excitations: the defects are thus assumed to extend into the bulk of the solid. In the vibrational region where $\omega_e >> \omega$, the effect of the added electronic term is basically to increase the background dielectric constant by ρ_e. Having established that the effects of crystalline anisotropy were small, the "perpendicular" loss function (equation (5)), and hence the predicted HREEL spectra for the defected surfaces were calculated using our original computer programme, FTSOPHW. Optimum values of ρ_e, ω_e and γ_e for fitting the experimental data were found by Dr.R.G. Egdell and Miss S. Eriksen, making use of model calculations of the loss function in which the background dielectric constant was treated as a variable parameter. The results are shown in figures 21 and 22.

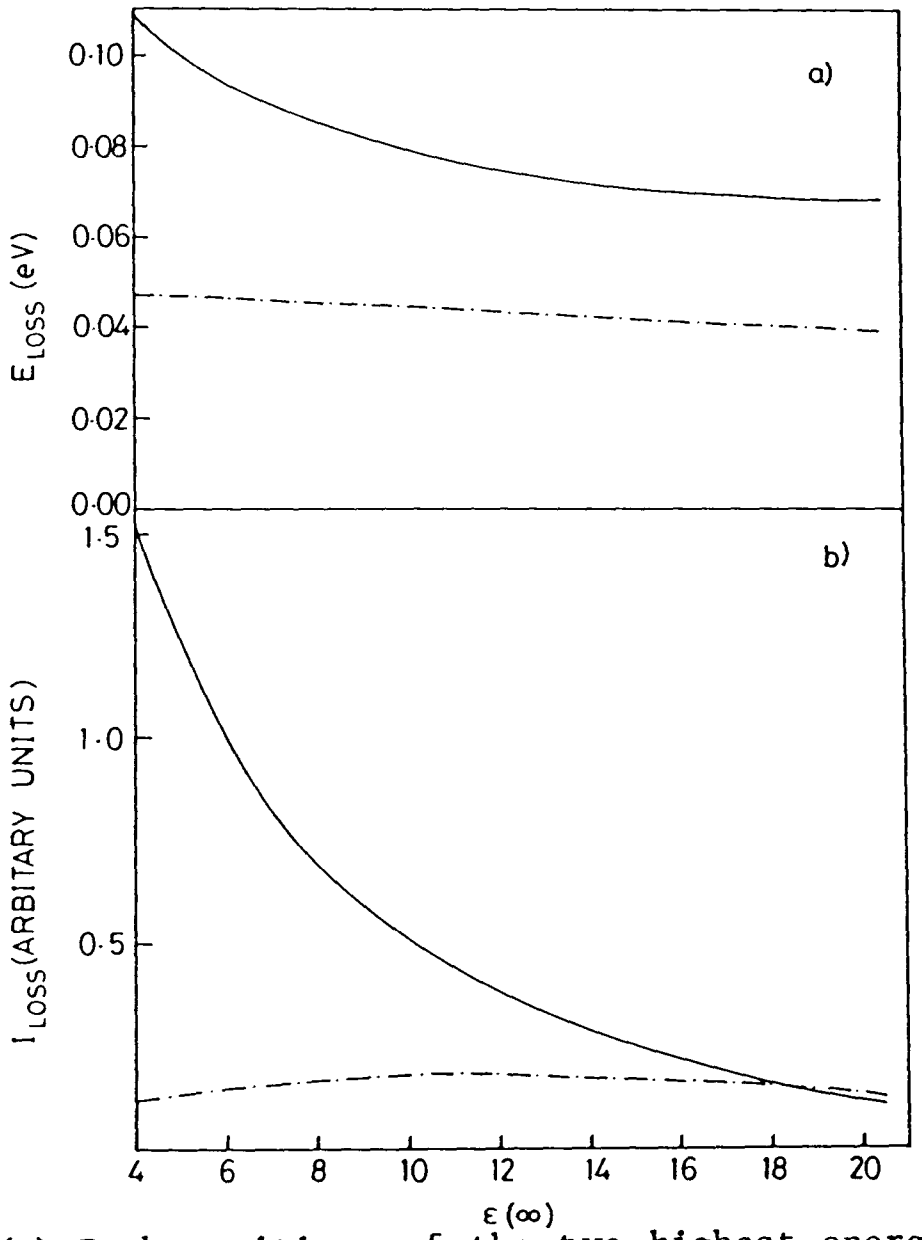

Figure 21: (a) Peak positions of the two highest energy loss features in the loss function for rutile (110) calculated from the parameter values of table 3 with variable background dielectric function. Only E_u terms are included in the dielectric function. (b) Maximum peak intensities of losses as in (a). The intensities have been normalised to the intensity of the higher energy loss at $\varepsilon_\infty(\omega)=6.0$.

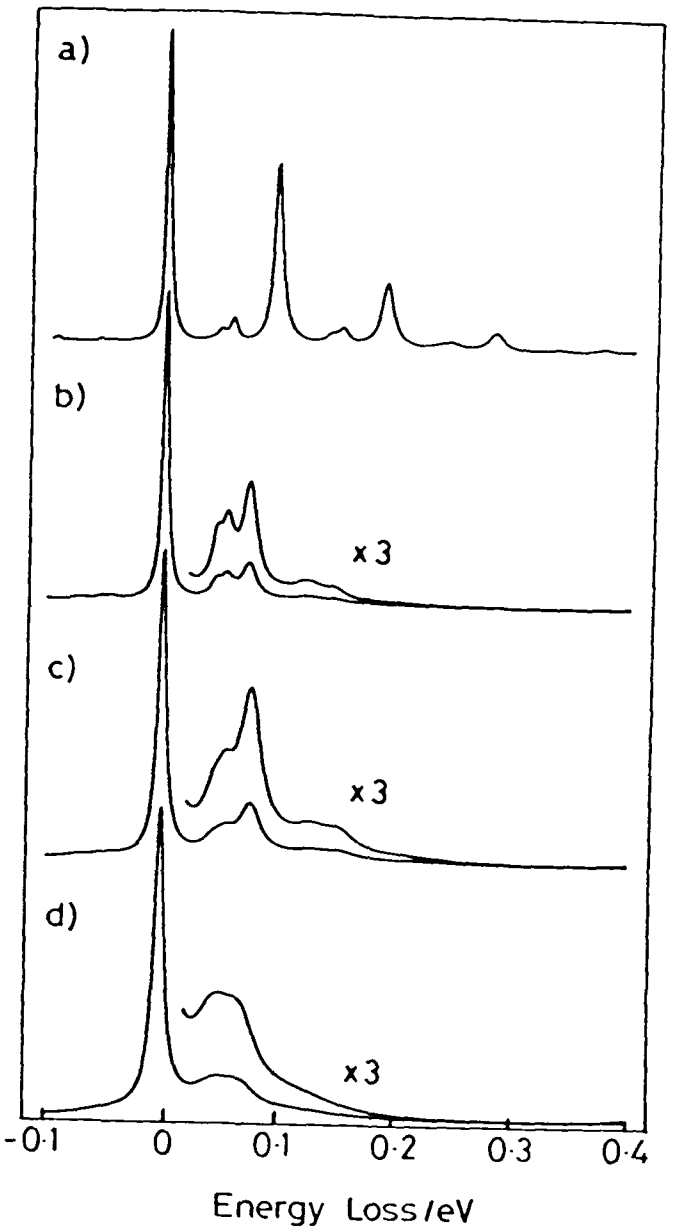

Figure 22: Simulated HREEL spectra of rutile (110), corresponding to the experimental spectra of figure 18 (a)-(d). Thus (a) represents the defect free surface, whilst (b)-(d) represent successively more damaged surfaces.

From figures 21 and 22, we see that the energy and intensity of the highest energy E_u loss peak decreases as the background dielectric constant increases due to screening of the vibrational mode by the electronic excitation. The lower energy E_u modes are much less sensitive to variation in E_u, as the dominant screening of these modes always comes from the higher energy E_u mode. Thus the relative

intensity of these modes increases with increasing dielectric constant. Electron or argon-ion bombardment leads to a pronounced attenuation of the highest energy phonon loss, together with a dramatic shift in its energy. The lower energy E_u modes do not experience such a large shift. Taking into account the simplicity of this model, the agreement of our predictions with the experimental spectra of figure 18 is very good. The experimental spectra for the argon-ion bombarded surfaces are generally less well resolved than those of the annealed and electron bombarded surfaces due to degradation in resolution and broadening of the phonon loss peaks. The main problem with the model used was that it proved difficult to reproduce the change in intensity of the highest energy phonon loss, without producing an unduly large downward shift in its energy. This problem may be eliminated in future studies by allowing the defect concentration to vary as a function of depth below the surface.

3.9 Conclusion

Work has been undertaken to investigate the validity of the simple dielectric theory in conjunction with group theoretical calculation to predict the HREEL spectra of various faces of commonly occurring crystal structures. Particular emphasis has been laid on the spectra of TiO_2. The present study has led to a more detailed understanding of the HREELS of defect-free TiO_2 than has been achieved previously. The effects of crystalline anisotropy on HREEL spectra in general, and upon the spectra of TiO_2 in particular have been investigated in detail. These have been demonstrated to be small, and, for example in the case of Al_2O_3, requiring a spectrometer of very high resolution before they can be observed experimentally. In the case of the (110) and (100) faces of

TiO_2, the effects due to anisotropy are, for experimental purposes, completely negligible. This is partly due to the intrinsically small nature of the effect, and partly to the near coincidence of the frequencies of the highest energy E_u mode and the A_{2u} mode with which it mixes. The spectrum of the (001) face of TiO_2 would be expected to show more significant effects due to anisotropy, with the lower energy E_u modes becoming visible. However, it has been demonstrated that a clean, defect-free (001) surface per se cannot be obtained, as it undergoes rearrangement and faceting during the heating processes required to clean the surface.

Differences between the predictions of the simple dielectric theory and experiment are found to be more likely to be due to the effect of surface defects than any effects due to anisotropy. The former are found to exert a marked influence in the spectra of argon-ion bombarded samples. Even a relatively small concentration of defects is seen to result in a marked damping of the phonon modes, and a slight shift in their frequencies.

It is also established that the conditions used by previous workers[70] to obtain a "defect-free" surface were unlikely to result in the production of such a surface. Thus it appears likely that the differences (in particular in the relative intensities of the phonon modes) between the dielectric theory predictions and the previously existing experimental data are due to a small concentration of surface defects in the TiO_2 samples used. In collaboration with Dr.R.G. Egdell, it is also found that the effect of the defects may be modelled by a simple extension of the dielectric theory in which a Lorentzian oscillator term for the electronic excitation is added to the expression for the dielectric function $\varepsilon(\omega)$. In view of the simplicity of this model, the agreement with results obtained by Dr.R.G. Egdell and co-workers is very good.

It appears that under normal conditions where the surface is not heavily defected, the dielectric theory will provide at the very least a useful first approximation to the predicted spectrum. Group theoretical calculations provide a guide to the numbers and types of the vibrations appearing strongly in the spectra, which we feel will be of use to other authors.

Chapter Four

Tin-Doped Indium Oxide Ceramics and Thin Films:

Surface Composition and Electronic Structure

4.1 Introduction

Thin films of tin-doped indium oxide (ITO) deposited on glass substrates have been shown to reflect almost completely in the infra-red, whilst having high transmittance in the visible region[88]. This leads to important technological applications as heat reflecting mirrors, for example in sodium discharge lamps, solar collectors or even double glazing. The films are conducting, those showing optimum properties usually displaying a carrier concentration of around $10^{21}cm^{-3}$ (89). Despite their potential importance, the surface properties of such films have been little studied. Research to date has been largely concerned with devising methods of preparation which produce films displaying optimum properties. As a result, several methods are employed, each having several experimental variables which can be optimised. The properties of the films tend to be heavily dependent on these parameters, and also on the method of production of the film. The nature of the underlying substrate can also affect the film properties. Typical tin doping levels range between 4 and 20 at.%, despite the fact that the equilibrium solubility limit of tin in indium oxide is 6 ± 2 at.%[90].

The aim of the present work was to use the complementary techniques of XPS, UPS, and HREELS to explore the surface properties of ITO materials. It was intended to begin the work with a study of well-characterised ITO ceramics, having tin doping levels below the solubility limit of 6 at.%. It was hoped that this would yield information useful in interpreting the results from a further study of ITO films, having a tin doping level of around 9 at.%.

The work included in this chapter was seen as a useful continuation of previous work by the author[82,91] on a formally related system,

antimony-doped tin (IV) oxide. To a first approximation, it might be expected that these n-type systems would show similar electronic properties. It was hoped that a comparison of the differences in behaviour between the two systems would increase our understanding of both systems. In previous studies[82,91,92,93], polycrystalline tin dioxide pellets containing 0.1-3 at.% antimony were examined using HREELS, UPS and XPS. XPS revealed substantial antimony enrichment in the surface atomic layer, the heat of segregation decreasing slightly with increasing antimony doping level. Both UPS and HREELS results were consistent with a concentration of electrons in the Sn:5s conduction band close to the bulk nominal value. The results suggested the existence of a lone-pair-like surface state split off from the conduction band.

4.2 ITO Films: Preparation, Properties and Applications

Numerous methods have been used to obtain ITO films which are very conductive and highly transparent in the visible and near infra-red. The four main methods are listed below.

i) Spray pyro-hydrolysis[94].

An aerosol stream containing an alcoholic solution of $SnCl_4$ and $InCl_3$ is sprayed through a preheating furnace (temperature T_1) onto a heated substrate (temperature T_2). N_2 is used as the carrier gas. The hydrolysis is based on the reversible and endothermic reactions:

$$SnCl_4 + 2H_2O \rightleftharpoons SnO_2 + 4HCl \quad (1)$$

$$2InCl_3 + 3H_2O \rightleftharpoons In_2O_3 + 6HCl \quad (2)$$

T_1, T_2 and the solution composition are optimised to give the highest possible transparency and conductivity. T_1 and T_2 typically lie between 400°C and 600°C.

ii) Sputtering from mixed oxide targets[88].

A typical experimental arrangement is shown in figure 1[88].

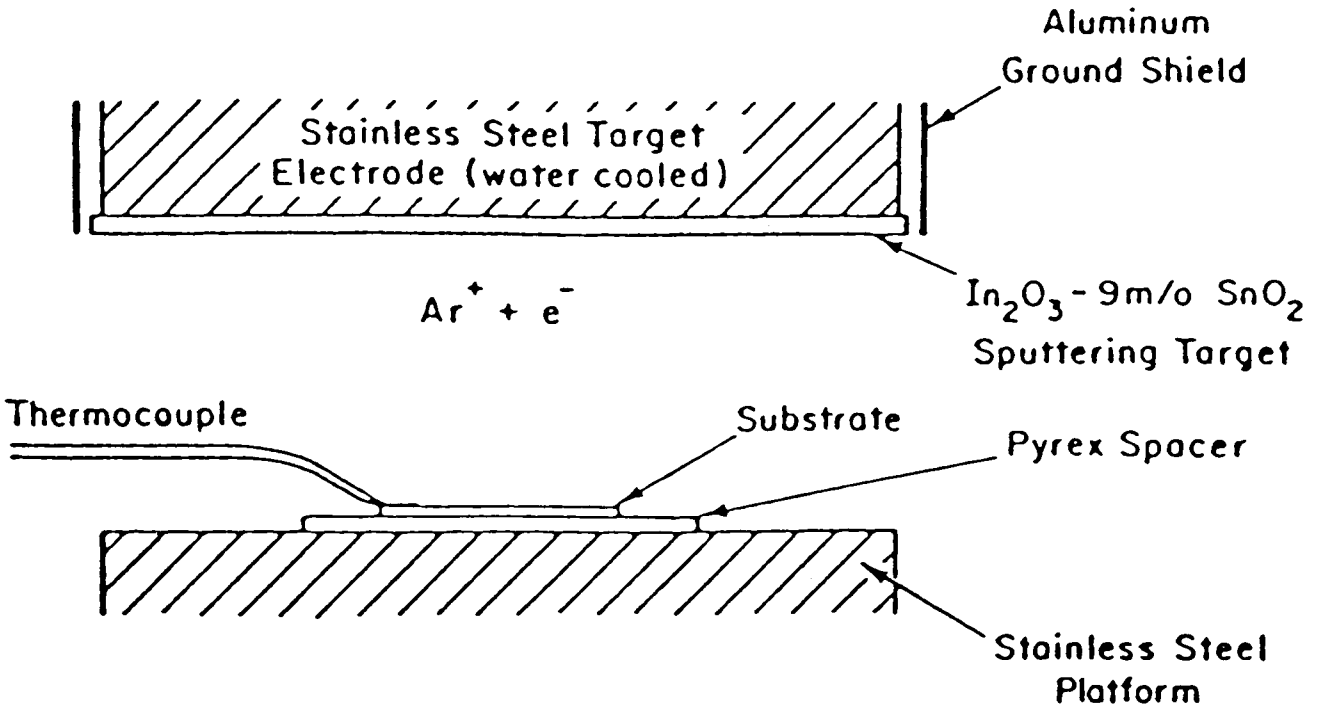

Figure 1:[88] Schematic diagram of target and substrate configuration in rf sputtering apparatus.

This apparatus consists of a commercial rf diode unit with a diffusion pump. Argon at typically 10^{-2}mbar is used in the discharge. The target used is a hot pressed In_2O_3 ceramic containing 9 at.% Sn. The maximum substrate temperature reached during deposition is roughly 600°C, 500W power being commonly employed. The deposition rate is around 250Åmin^{-1}, which is quite slow, but good quality films are produced. The film quality is sensitive to changes in sputtering power, apparently due to the resulting changes in substrate temperature.

iii) Reactive sputtering from alloy targets[95,96]

This is similar in principle to method ii), but employs an indium-tin alloy target. Sputtering takes place in O_2, so that a mixed

oxide film is formed.

iv) Chemical vapour deposition[97]

The CVD process is based on the decomposition of a volatile organometallic compound of each metal. Good quality ITO fims have been deposited by this method, but to adapt the process for commercial production, a cheap volatile indium compound needs to be found.

Of the processes listed above, the first two are the most frequently used. None of the methods employs substrate temperatures of more than around 600°C during film deposition, and it seems likely that the films are produced under non-equilibrium conditions.

For applications as a heat reflecting transparent filter, low light absorption in the visible range of the spectrum and high reflectivity in the near infra-red are the most important requirements. From the Drude theory, it can be shown that, in terms of carrier concentration N and mobility μ, the first requirement demands a low value of N/μ, whereas the second demands a low value of $1/(N\mu)$ [98]. Both of these conditions imply that high carrier mobilities are desirable. Using the preparative methods described above, minimum resistivities of $\rho \lesssim 2.10^{-4}\Omega$cm have been reported at doping concentrations between 4 and 20 at.% Sn[99-102]. Films prepared under optimised conditions have mobility values of 30-50cm^2/Vs [88,103,104], whereas films prepared at low substrate temperatures tend to have mobility values of $\sim$10-20cm^2/Vs [105,106]. Figure 2[88] shows the transmission and reflectivity as a function of wavelength for a typical film deposited by sputtering from a mixed oxide target. Transmission in the visible region is usually >80%, whilst reflectivity increases abruptly at 1.5μm and is >90% at 10μm.

Figure 3[89] shows a typical dependence of the carrier concentration N on x, the concentration of tin in at.%. It can be seen that the

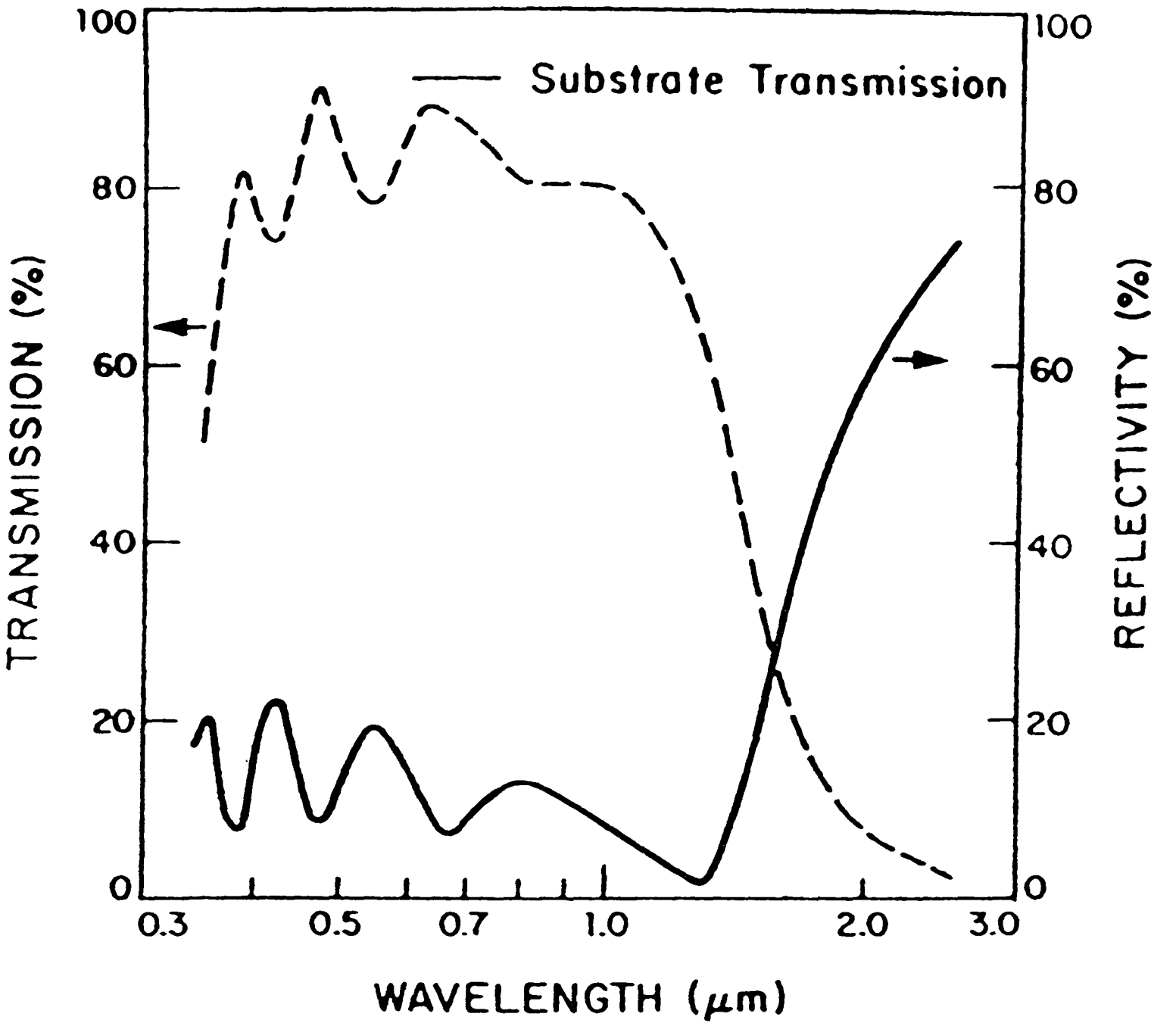

Figure 2:[88] Transmission and reflectivity as a function of wavelength for an ITO film deposited by sputtering from a mixed oxide target. The sputtering target contained 9 at.% Sn. The transmission of the glass substrate is indicated.

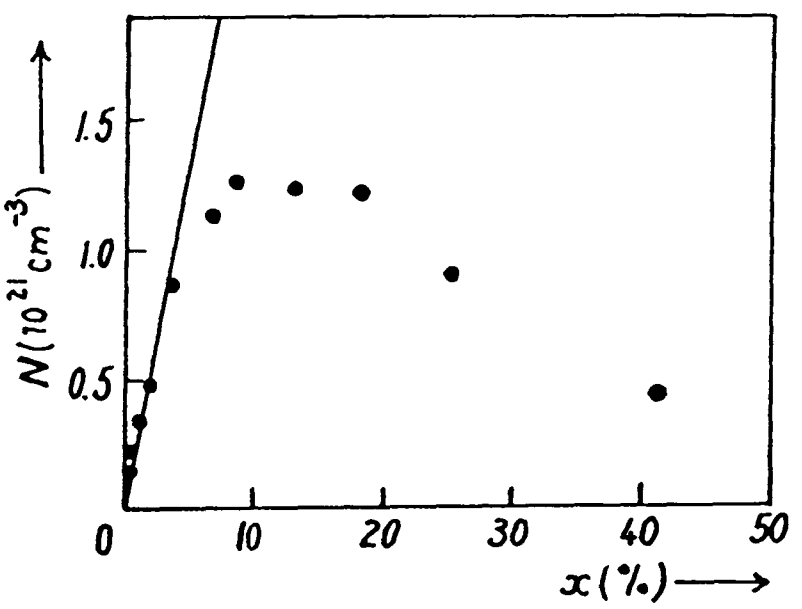

Figure 3:[89] Dependence of the free-electron density N on the Sn concentration x for ITO films prepared by the spray pyro-hydrolysis method.

maximum value of N is $\sim 1.3 \times 10^{21} cm^{-3}$. The curve is linear up to x~5 at.%, implying that up to this concentration, each tin atom introduced is contributing one electron to the conduction band of the material. This would seem to be consistent with the solubility limit of 6±2 at.% Sn determined by Frank et al[90]. Films displaying the best qualities have a plasmon wavelength of around 1μm (~1.25eV).

The properties displayed by the films are used in heat reflecting filters, for example in the thermal insulation of sodium discharge lamps[107]. In a low pressure sodium discharge lamp, the discharge tube has to be kept at a temperature of nearly 260°C in order to provide the optimum sodium pressure. The power which heats the tube is taken from the gas discharge tube. Convection and conduction losses of the tube are eliminated by evacuating the envelope of the lamp. To reduce the remaining losses, which are mainly due to thermal radiation of the discharge tube, the interior surface of the outer tube is coated with a tin doped indium oxide film, as shown in figure 4[107]. The transmission and reflection curves show that the major fraction of the infra-red radiation is reflected back onto the discharge tube. This increases the luminous efficiency of the lamp by 100%.

Another application is in solar collectors[107]. A solar collector consists basically of a black absorber plate through which the heat exchange fluid circulates. At least one glass cover is added to reduce the air convection losses of the absorber plate. To reduce the heat re-radiation losses, the collector plate should have a low infra-red emittance (as in a "dark" mirror where for example TiO_2 may be used as the absorber), or the adjacent glass cover should have a high infra-red reflectance (a heat mirror). An ITO film, sometimes with an additional SiO_2 anti-reflection coating may be used if a heat reflecting filter is used.

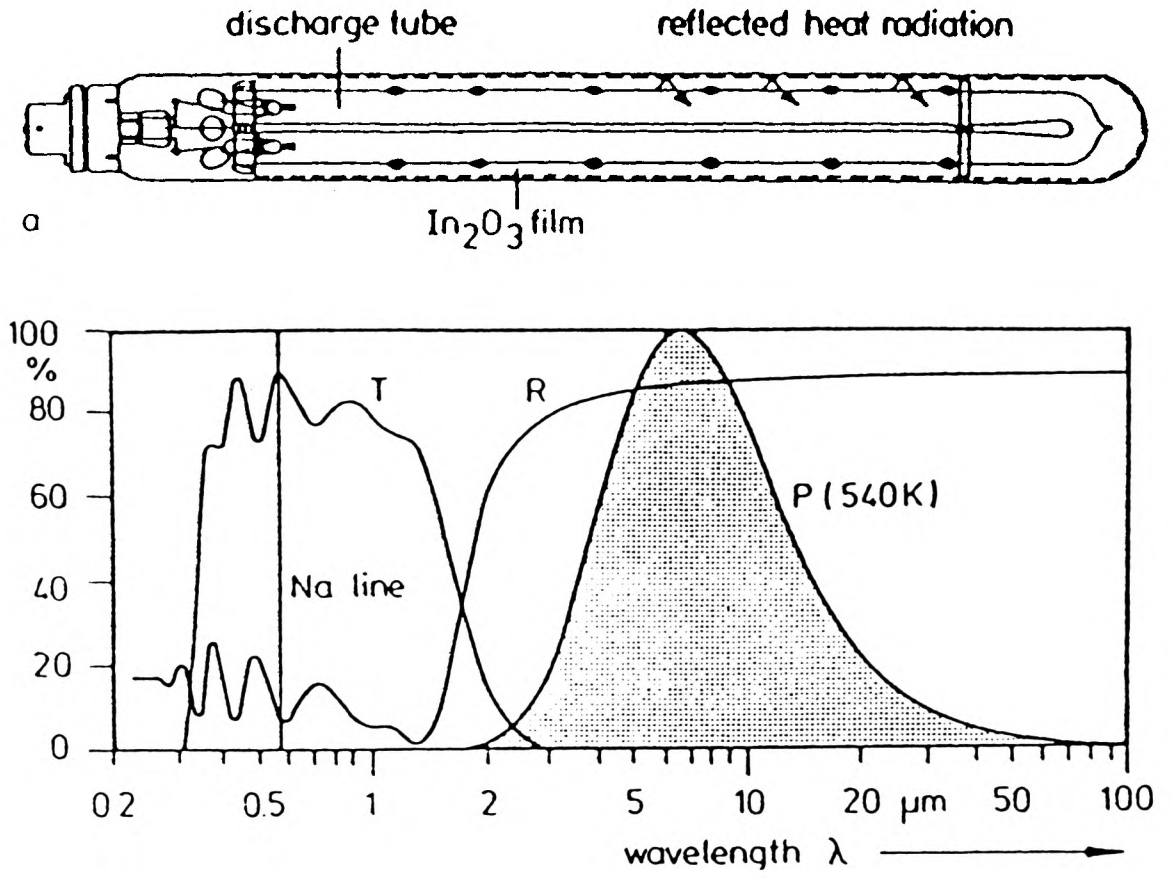

Figure 4:[107] Sodium lamp with an ITO heat reflecting filter on the inner side of the envelope. Spectral transmittance T and reflectance R of the filter, compared to 540K black-body radiation P (of the discharge tube) and sodium emission.

In double glazed windows, about two thirds of the heat transport takes place via thermal radiation between the glass surfaces. This can be reduced by coating the inner surfaces with an infra-red reflecting filter. Currently, thin evaporated gold films are often used for this purpose. However, the transparency, stability and relatively low cost of ITO films mean that it may prove to be a viable alternative. Radiation losses can be cut down by a factor of 6, while the transmission of light is almost unimpaired[108].

Despite their increasing technological use, the properties of ITO materials appear to have been little studied. In particular, the nature of the species contributing to the carrier concentration is a matter of

some considerable controversy. In_2O_3 itself is a semiconductor with a direct band gap of about 3.6eV[109], and an indirect band gap of about 2.6eV[110]. As prepared, indium oxide is generally somewhat reduced, containing oxygen vacancies. The electrical conductivity is accordingly n-type. The undoped substoichiometric In_2O_3, containing x doubly charged oxygen vacancies $V_o^{\cdot\cdot}$ may be written formally as $In_2O_{3-x}(V_o^{\cdot\cdot})_x e'_{2x}$ where $x<0.01$[111,112]. In_2O_3 has the cubic bixbyite structure, in which the O^{2-} ions occupy three quarters of the tetrahedral interstices of a face centred cubic In^{3+} array, in an ordered fashion (figure 5[113]).

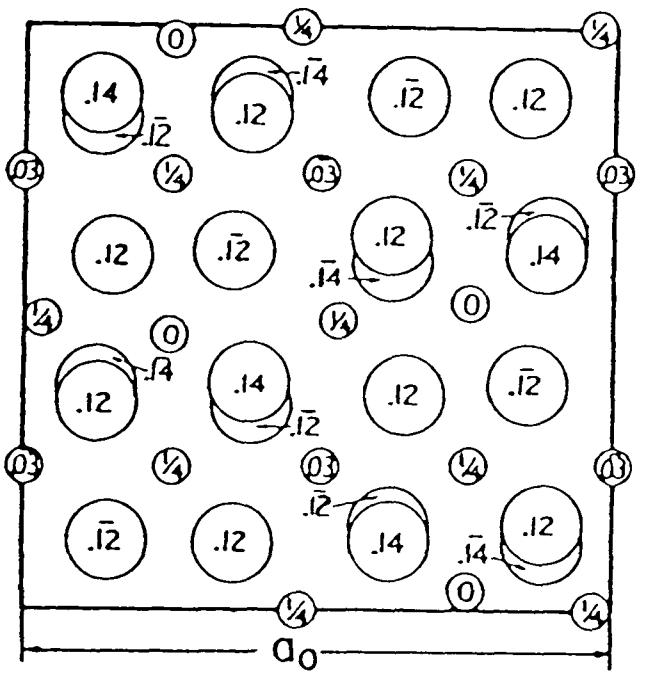

Figure 5:[113] A projection on a cube face of half the contents of the unit cell of the bixbyite structure. The larger circles are the oxygen atoms.

The properties of tin doped indium oxide described in the literature often differ considerably from each other. In particular, the ambient oxygen pressure during film preparation seems to be of importance, and in most cases the oxidation state of the samples is not defined with sufficient accuracy. The tin dopant is thought to be substitutionally incorporated on indium sites. In sputtered ITO films,

prepared at low oxygen pressure, an incorporation as Sn^{2+} has sometimes been postulated[88,114,115]. This conclusion has been based mainly on X-ray diffraction results, and on the interpretation of results from XPS. The latter must be regarded as dubious, as it has been observed in our laboratory that changes in the energy of XPS peaks in metal oxide spectra cannot be reliably correlated with changes in the metal valency. Both SnO[114] and Sn_3O_4-like[115] phases have been suggested; Fan and Goodenough[116] propose that in films prepared under non-equilibrium conditions, Sn-rich regions could nucleate an Sn_3O_4-like phase. The structure of Sn_3O_4 is not well determined, but it is envisaged to be a mixed valence compound, $Sn_2^{2+}Sn^{4+}O_4$. This is suggested to be the cause of film darkening and high electrical resistivity observed in such films. It is suggested that, at high deposition rates and low deposition temperatures, the atomic mobilities, relative to the rate of film growth, are high enough for any second phase to be ejected to the surface[116]. Such a surface enrichment in tin has been observed by XPS[116,117], and depth profiling Auger electron spectroscopy[88,117,118], although the enhancement observed using the latter technique was attributed by one author to differential sputtering effects[88].

In films prepared under oxygen-rich conditions and at higher substrate temperatures (around 500°C), only Sn^{4+} has been detected by Mossbauer spectroscopy both in the as-grown state, and after annealing under reducing conditions (e.g. in the presence of a 1:1 $CO:CO_2$ mixture)[89,119]. The donor activity of the Sn dopant is thus attributed to substitutional Sn^{4+} on In^{3+} sites. A detailed study of such films has been carried out by Köstlin *et al*[89,90,107,120]. It was discovered that if films were prepared under oxygen-rich conditions, an uncontrollable amount of oxygen was introduced into the films during preparation. The incorporated oxygen reduced the conductivity of the films in two ways, firstly by acting as a trap for the free electrons

primarily contributed by the donor, and secondly acting as a scattering centre for the remaining free electrons. To eliminate the incorporated oxygen, it was found to be necessary to anneal the films at around 450°C, either in vacuo, or with forming gas (80% N_2:20% H_2) or with a 1:1 CO:CO_2 mixture. The strong trapping effect of oxygen in doped In_2O_3 is due to the bixbyite structure of the In_2O_3 lattice, which allows the incorporation of oxygen on preferential, quasi-oxygen vacancy interstitial sites. In the "reduced" films, it was found that, up to a doping concentration of around 6 at.% Sn, each tin atom was electrically active, having donated a conduction electron, $In_{2-\delta}Sn_\delta^{\cdot}O_3e'_\delta$ (neglecting the negligible oxygen vacancy concentration). The neutralisation of the δ ionised tin donors by interstitial oxygen anions can be represented formally as $In_{2-\delta}Sn_\delta^{\cdot}(O_i'')_{\delta/2}O_3$. Frank and Köstlin[119] have made a detailed study of the electrical properties of these films, as a function of both tin dopant concentration, and the oxygen partial pressure in the annealing atmosphere. From an analysis of the carrier concentration and measurements of the lattice constants and film thicknesses, a detailed defect model is developed. It is envisaged that at low oxygen partial pressures the predominant defects are substitutionally incorporated Sn^{4+} ($Sn^{\cdot}$) and oxygen vacancies, $V_O^{\cdot\cdot}$. At higher partial pressures, three types of cluster are suggested, which involve interstitial oxygen anions, trapping the electrons contributed by the tin dopant. These are:

i) $(Sn_2^{\cdot}O_i'')$ (I) This consists of an O^{2-} ion on an interstitial quasi-anion site, loosely bound to two Sn^{4+} ions which are not on nearest neighbour In^{3+} positions.

ii) $(Sn_2O_4)^x$ (C) This is a strongly bound complex composed of two nearest neighbour Sn^{4+} ions, surrounded by three nearest neighbour O^{2-} ions on regular anion sites, and one additional O^{2-} ion on an empty nearest neighbour anion site of the In_2O_3 lattice.

iii) $((Sn_2^{\cdot}O_i'')(Sn_2O_4)^x)$ (A) This is an associate of I and C.

All three defect clusters are neutral.

It is envisaged that in the as-deposited films, these clusters are finely dispersed. On heat treatment for prolonged periods at temperatures above 600°C, it is suggested that these defects nucleate by a slow diffusion process to form an SnO_2-phase[121]. This would explain the fact that, even though a solubility limit for tin in ITO ceramics of 6±2 at.% has been established[90], no separate tin dioxide phase has been observed in as-prepared ITO thin films for tin doping levels of up to 60 at.%[89,114]. Frank et al[90] have shown that ITO films containing 20 at.% Sn prepared by spray techniques at 550°C on fused silica substrates showed no SnO_2 reflections in XRD. However, after heat treatment for 2 weeks at 950°C, SnO_2 reflections appeared[90].

4.3 Experimental: ITO Ceramics

4.3.1 Preparation

Powder samples of tin-doped indium oxide were prepared by the coprecipitation technique of Frank et al[120]. ITO powders over the complete composition range In_2O_3-SnO_2 have been prepared using this technique[90]. The expected advantage of coprecipitation is a quicker attainment of thermodynamic equilibrium during annealing, due to more effective mixing of tin and indium than would normally result from blending the solid oxides.

The specifications of the materials used were as follows:

indium foil	Johnson Matthey	Puratronic	
tin wire	" "	"	
hydrochloric acid	Analar	specific gravity	1.16
ammonia solution	"	" "	0.88
nitric acid	"	" "	1.42

The required quantities of tin and indium in the form of small chips were accurately weighed. The metals were then dissolved in separate aqua regia solutions. Both metals were added over a period of 8 hours without heating. In the case of the tin solution, this was necessary to prevent the loss of $SnCl_4$ vapour[92]. The solutions were mixed, and ammonia was added until the solution was alkaline. The solution was boiled for several hours, and the white precipitate was dried by heating overnight at 120°C. After being ground to constant particle size, the precipitate was calcined at a temperature at, or in excess of 1000°C for a period of approximately 14 days (see below), in a recrystallised alumina crucible.

Samples containing nominally 1,4 and 6 at.% Sn were prepared using this method. After calcining in air at 1000°C for an initial period, the samples were pressed (at 10 tons) into pellets (13mm in diameter and approximately 2mm thick) between optically smooth tungsten carbide discs, and were sintered in air for further periods at 1000°C, 1200°C or 1360°C to yield mechanically robust ceramic discs. Details of annealing treatments and temperatures, for all the pellets are given in table 1. It can be seen that the minimum firing period was 11 days, whilst pellets ultimately heated at the highest temperature of 1360°C were subject to up to 5 weeks firing at temperatures $\geq$ 1000°C. We therefore feel confident that thermal equilibrium has been attained at all the temperatures used.

Table 1 Annealing conditions used in the preparation of ITO ceramics

	Firing Conditions
a) "1000°C samples"	powdered material fired 1000°C, 7-14 days, pelletised, then fired 1000°C, 4-7 days
b) "1200°C samples"	as a), then pellets fired 1200°C, 4-7 days
c) "1360°C samples"	as b), then pellets fired 1360°C, 4 days

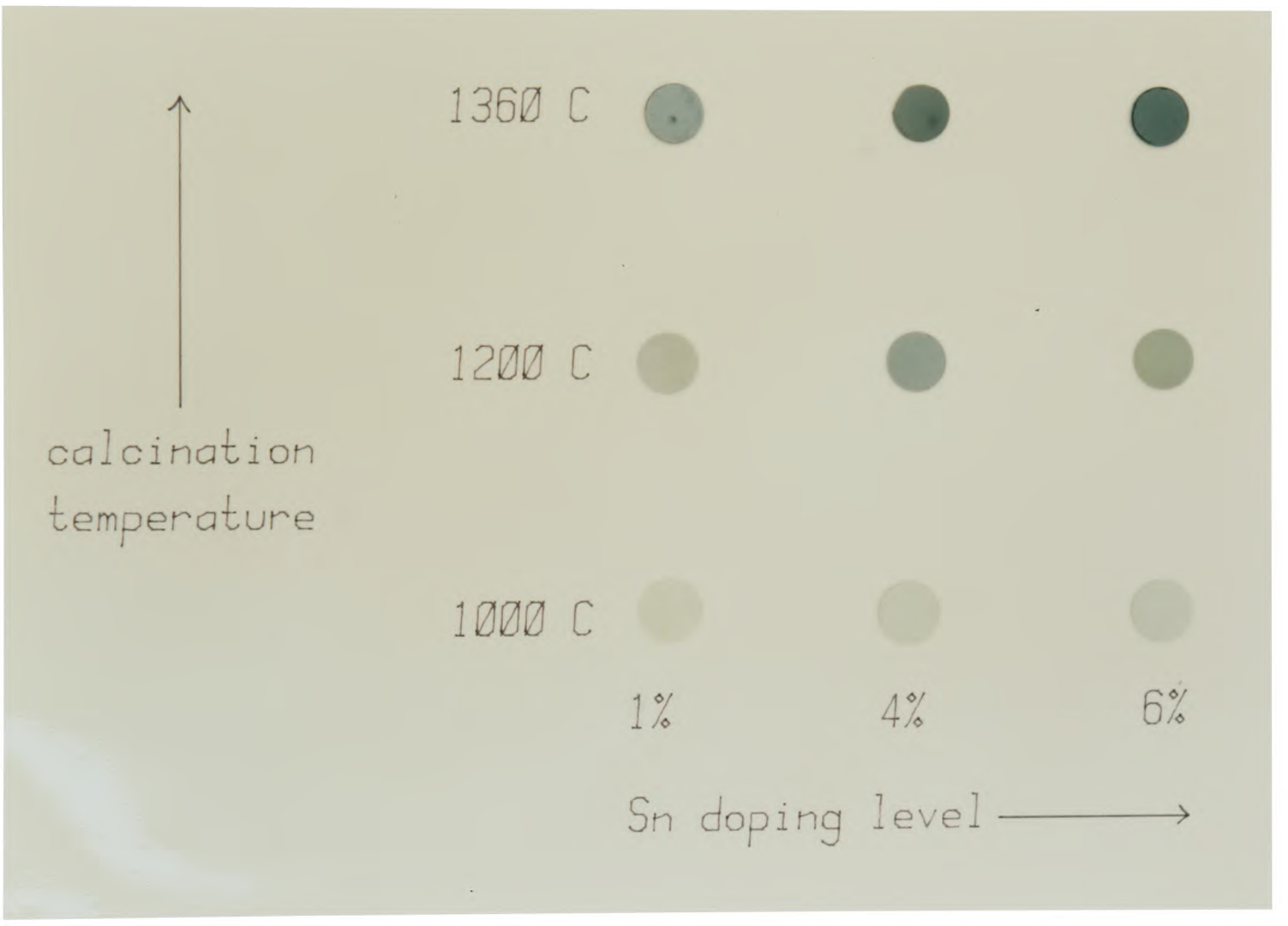

Figure 6 Examples of the ITO ceramic samples.

Examples of the pellets are shown in figure 6. It can be seen that pellets annealed at 1000°C are pale blue or green in colour; the colour progressively deepens to a deep blue/grey as the annealing temperature is raised. The colour also tends to deepen as the tin doping level increases.

4.3.2 Characterisation

Techniques used in the initial characterisation of the ceramics were X-ray powder diffraction, electron microscopy (scanning electron microscopy (SEM) and transmission electron microscopy (TEM)), and solid state laser-induced Raman spectroscopy. The results are described below.

i) X-ray Powder Diffraction

Continuous diffraction profiles were obtained from all of the different samples using a Philips moving arm diffractometer. This consists of an X-ray generator (producing Cu $K\alpha_{1,2}$ radiation), coupled to a moving arm counter and goniometer which measures the angles at which diffraction occurs. The equipment is controlled by a Philips PW1710 diffractometer control unit, and interfaced to a microprocessor which produces a digital readout of the diffraction data, in addition to a trace simultaneously produced on a stripchart recorder.

The samples were finely ground and were introduced into the diffractometer after mounting in thin aluminium plates. Reflections were recorded between 2θ values of 10^{o} and 80^{o}. Doublet structure was observed at high values of 2θ due to resolution of the $K\alpha_{1,2}$ doublet.

All profiles showed narrow peaks associated with a well-crystallised cubic (Ia3) In_2O_3 phase[122] (this is the form of In_2O_3 stable at room temperature and ambient pressure). However, in some samples (notably those having high nominal concentrations of tin and heated at lower temperatures), small peaks due to a SnO_2 (rutile) phase[123] were apparent. No peaks due to SnO[124], β-SnO[125] or Sn_3O_4[126] phases were observed. In order to estimate the amount

of tin dioxide present, a physical mixture containing known proportions (roughly 1:10 by weight) of SnO_2 (Koch-Light puriss) and In_2O_3 (Koch-Light 99.999%) was prepared and a diffraction trace was obtained. From the relative intensities of the strongest peaks for In_2O_3 ((222)) and SnO_2 ((110)), the percentages of tin dioxide in the ITO ceramics were estimated. The results are summarised in table 2. Note that the concentrations are expressed in at.% Sn in the form of SnO_2. Thus a comparison with the bulk nominal doping level gives an idea of the residual concentration of tin dissolved in the In_2O_3 lattice. Due to the very low intensity of the SnO_2 peaks, the figures may be in error by up to 50%.

Table 2 Tin dioxide content of ITO ceramics as determined by XRD.

nominal tin content (at.%)	firing temperature (^oC)	Sn in form SnO_2 (at.%)
1	1000	0
	1200	0
	1360	0
4	1000	1-2
	1200	1-1.5
	1360	0
6	1000	5-6
	1200	2-3.5
	1360	0

It can be seen that none of the pellets heated at the highest temperature contained a SnO_2 phase. However, at lower temperatures and doping concentrations of $\geqslant$4 at.% Sn, tin dioxide phases were clearly observed, and in some cases the amount of tin present as SnO_2 was substantial. Thus we suggest that the solubility limit of tin in powder samples of In_2O_3 calcined at 1000^{o}C is rather lower

than the figure of 6 ± 2 at.% put forward by Frank *et al*[90] for samples annealed up to this temperature. We feel that the discrepancy is due solely to a more careful analysis of the diffraction traces. However, we are confident that samples annealed at the highest temperature of 1360°C are monophasic.

The solubility limit determined for ITO ceramics is very different from that found for thin films, where it has been reported that no separate SnO_2 phase appears until doping concentrations of up to 60 at.% Sn are reached[89].

Diffraction traces were obtained from several of the samples both before introduction into the electron spectrometer and on removal from it, following the radio-frequency heating processes used to clean the sample inside the spectrometer. No change in the traces was observed after removal from the spectrometer.

Lattice parameters for most of the ITO ceramics were very similar, and were within 0.1% of that of pure In_2O_3. Typical parameters were:

a_o=10.11Å (sample containing nominally 1 at.% Sn calcined at 1000°C)

a_o=10.12Å (sample containing nominally 4 at.% Sn calcined at 1360°C)

The corresponding value for In_2O_3[113] is

a_o=10.118Å (26°C)

However, the lattice parameter of the sample containing nominally 6 at.% Sn was found to increase with calcining temperature as indicated below:

calcining temperature/°C	lattice parameter/Å
1000	10.13
1200	10.15
1360	10.18

This finding is in accord with the work of Frank et al[119] on ITO thin films, where the lattice constant was found to increase steadily with increasing tin concentration in the range 2-20 at.% Sn, the trend becoming experimentally significant at around 6 at.%. This is tentatively attributed to the larger effective charge of the Sn^{4+} ions which causes a repulsion force which cannot be completely compensated by the free electron gas[119].

ii) Electron Microscopy

An elemental analysis of several of the samples was obtained using transmission electron microscopy (TEM). Micrographs were also obtained using scanning electron microscopy (SEM). The instrument used for both techniques was a JEOL JEM-2000FX electron microscope, and was operated by Mrs. Ann Stoker. A typical base pressure was 10^{-6}mbar. The beam energy used for both SEM and TEM was 200keV. X-ray spectra of individual crystallites as small as 0.1μm may be obtained routinely with a spatial resolution (determined by the lateral diffusion of the beam) down to around 10nm. X-ray emission is monitored using a Tracor lithium-drifted silicon thin window X-ray detector. This is capable of detecting low energy (<100eV) emissions.

The samples, in the form of finely divided powders were suspended in chloroform, and dispersed on 3mm copper grids coated with amorphous carbon films.

In the SEM mode, the focussed electron beam was scanned across the surface of the sample. The image was produced by a synchronously rastered electron beam on a CRT face, whose brightness was modulated by the secondary electron emission from the sample. Typical micrographs obtained are shown in figure 7.

a)

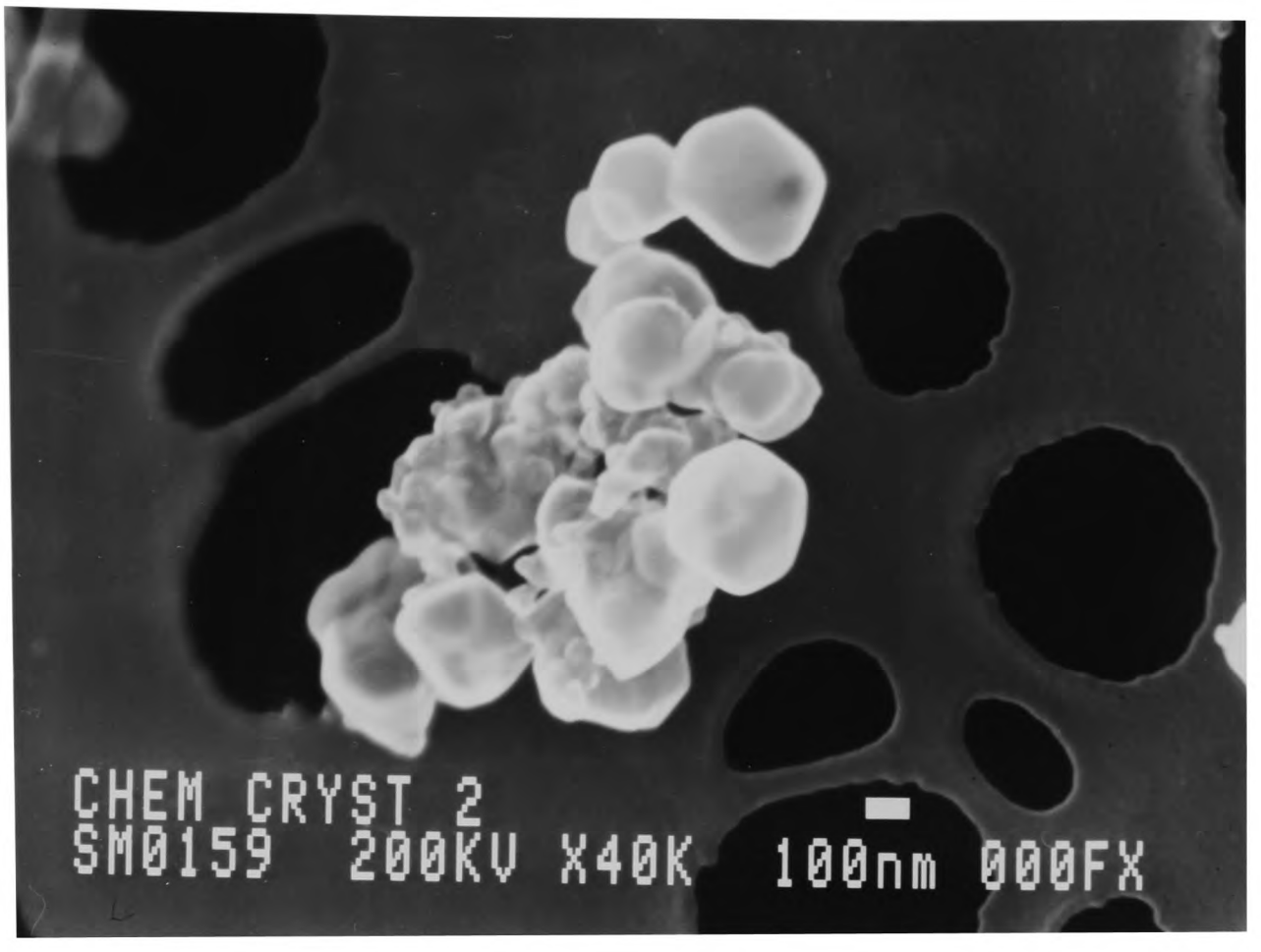

b)

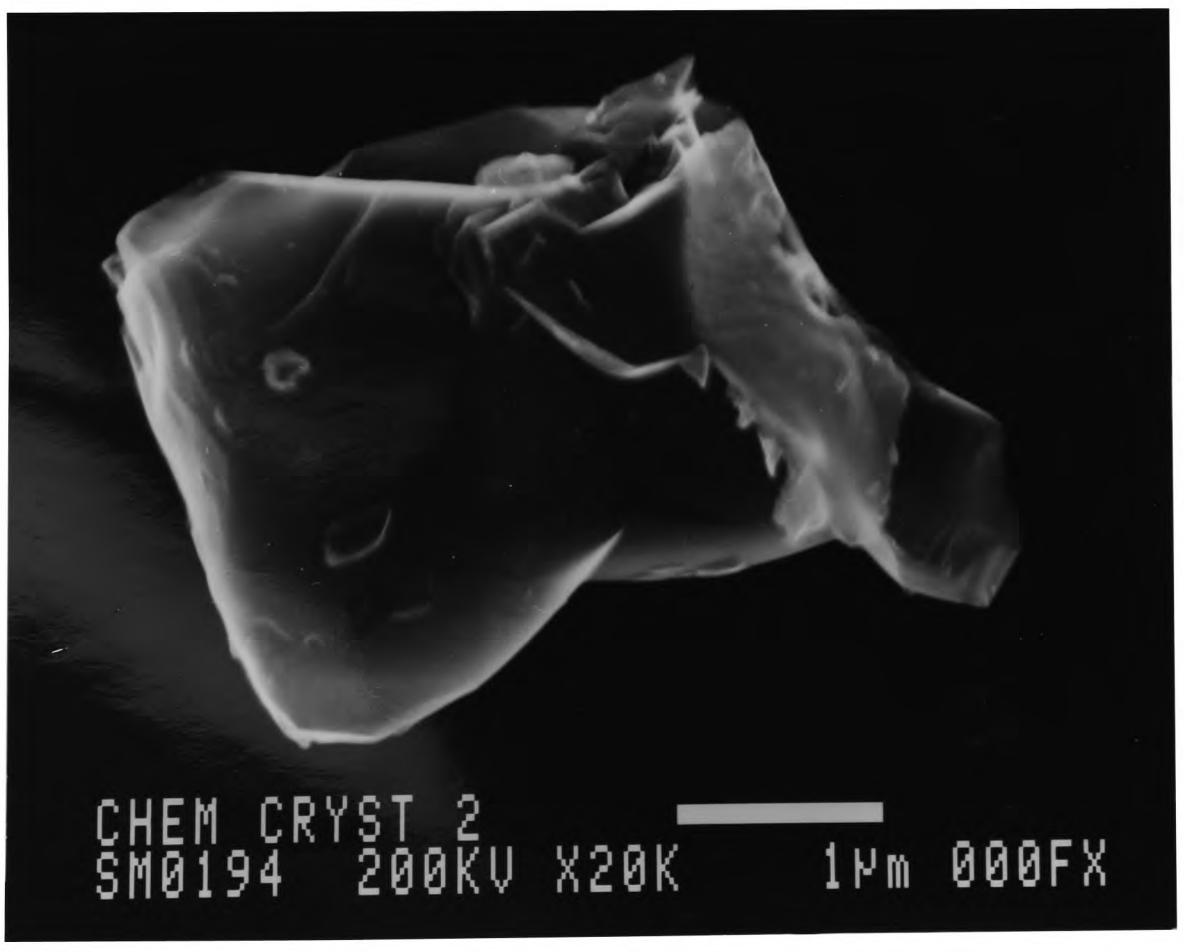

Figure 7: Micrographs of an ITO powder containing 6 at.% Sn after calcining at 1000°C (a) and 1360°C (b). Beam energy, magnification and scale are indicated.

This shows two SEM photographs of the sample containing nominally 6 at.% Sn, after calcining at 1000°C (7a)) and then at 1360°C (7b)). Both images are very bright against the dark background of the amorphous carbon film, indicating a high degree of crystallinity. The sample heated at the lower temperature consisted of two distinct types of particle; small rounded crystallites with diameter up to ∿1000nm, and aggregates of very tiny crystallites having a diameter of ∿200nm, such as that shown in figure 7a). After heating to 1360°C, the sample was seen to consist entirely of rather larger (∿2000nm) angular crystallites having distinct faces, as shown in figure 7b). Samples heated at the intermediate temperature of 1200°C tended to consist of clusters of angular crystallites with diameter up to 1000nm.

An elemental analysis of several samples was obtained using the characteristic X-ray emission spectra produced when the electron beam is transmitted through the sample (TEM mode). The Kα and Kβ lines of tin and indium were found to be sufficiently well separated to allow the individual peaks to be observed. Emission spectra of SnO_2 (Koch-Light puriss) and In_2O_3 (Koch-Light 99.999%) used as standards were obtained. For a thick specimen, the concentration c_x, of the element x present in the specimen is related to the intensity I_x of a characteristic emission line of x by the equation

$$c_x = kI_x/c_Z c_A c_F \qquad (3)$$

where k is a constant and c_Z, c_A and c_F are corrections for atomic number effects, absorption and fluorescence, respectively[127]. In the thin crystal limit, these corrections should be negligible, so that for two elements x and y present in the sample, we can write

$$c_x/c_y = k_{xy} I_x/I_y \qquad (4)$$

This approximation, known as the ratio method should apply under

the normal working conditions of a transmission electron microscope[127]. Using the oxygen Kα signal as a common peak between the two standards therefore, the percentage of tin present in the ITO samples was readily obtained. This method has been shown to be accurate typically to within ±1% by comparison with atomic absorption spectroscopy[127].

It was found that the Sn signal obtained from samples containing nominally 1 at.% Sn was too weak for the tin content to be reliably estimated. However, a number of samples containing nominally 4 and 6 at.% Sn were successfully examined. The electron beam samples a circular area of ~500nm diameter. It was found that samples heated at 1200°C or 1360°C showed a homogeneous tin distribution (on the scale of the experiment), having a tin content consistent with the nominal doping level. Typical results are shown below:

calcining temperature (°C)	nominal Sn content (at.%)	observed Sn content (at.%)
1360	6	6±2 at.%
1200	4	5±2 at.%

Large error limits are given, as the tin peaks used are relatively small.

However, a sample containing nominally 6 at.%, and fired at the lowest temperature of 1000°C was shown to have a very inhomogeneous tin distribution, the sampled concentrations varying between barely detectable amounts (a few percent) and 37% Sn. Moreover, the highest tin concentrations appeared to be present only in aggregates of crystallites of the type shown in figure 7a), and only very low concentrations were present in the rounded single crystallites which were also present in the sample. This result is

not surprising, as the X-ray diffraction results of the previous section reveal that this sample contains of the order of 5 at.% Sn in the form of a separate SnO_2 phase.

The investigation by electron microscopy therefore shows that the samples are well crystallised. It also confirms that the ITO ceramics are refractory at the calcining temperatures used, with no significant loss of tin occurring. The nominal doping level is obviously representative of the true bulk tin concentration. SEM pictures show that the morphology of the samples changes as the calcining temperature increases, with larger, more angular crystallites being produced at higher temperatures. At lower firing temperatures, TEM demonstrates a non-uniform tin distribution consistent with the presence of a separate tin dioxide phase.

iii) Solid State Laser-Induced Raman Spectroscopy

Spectra of pure In_2O_3 (Koch-Light 99.999%) and of a variety of the ITO pellets were obtained by Dr.R.G. Egdell at Imperial College, London. The Raman spectra are excited with a relatively weak blue line of a krypton laser ($\backsim$21,000cm^{-1}) in order to minimise the intensity of the fluorescent background. The spectrometer employs a Spex Ramalog 5 triple monochromator coupled to a Spex Datamate data acquisition system.

Typical results obtained are shown in figure 8. The spectra consist of a series of peaks superimposed on a strong background due to fluorescence from surface hydroxyl groups (resulting from adsorption of atmospheric water). Undoped In_2O_3 (figure 8a)) gives lines due to Raman-active phonons at 467cm^{-1}, 500cm^{-1} and 633cm^{-1} in agreement with literature values[128]. Lines at 414cm^{-1} and

a)

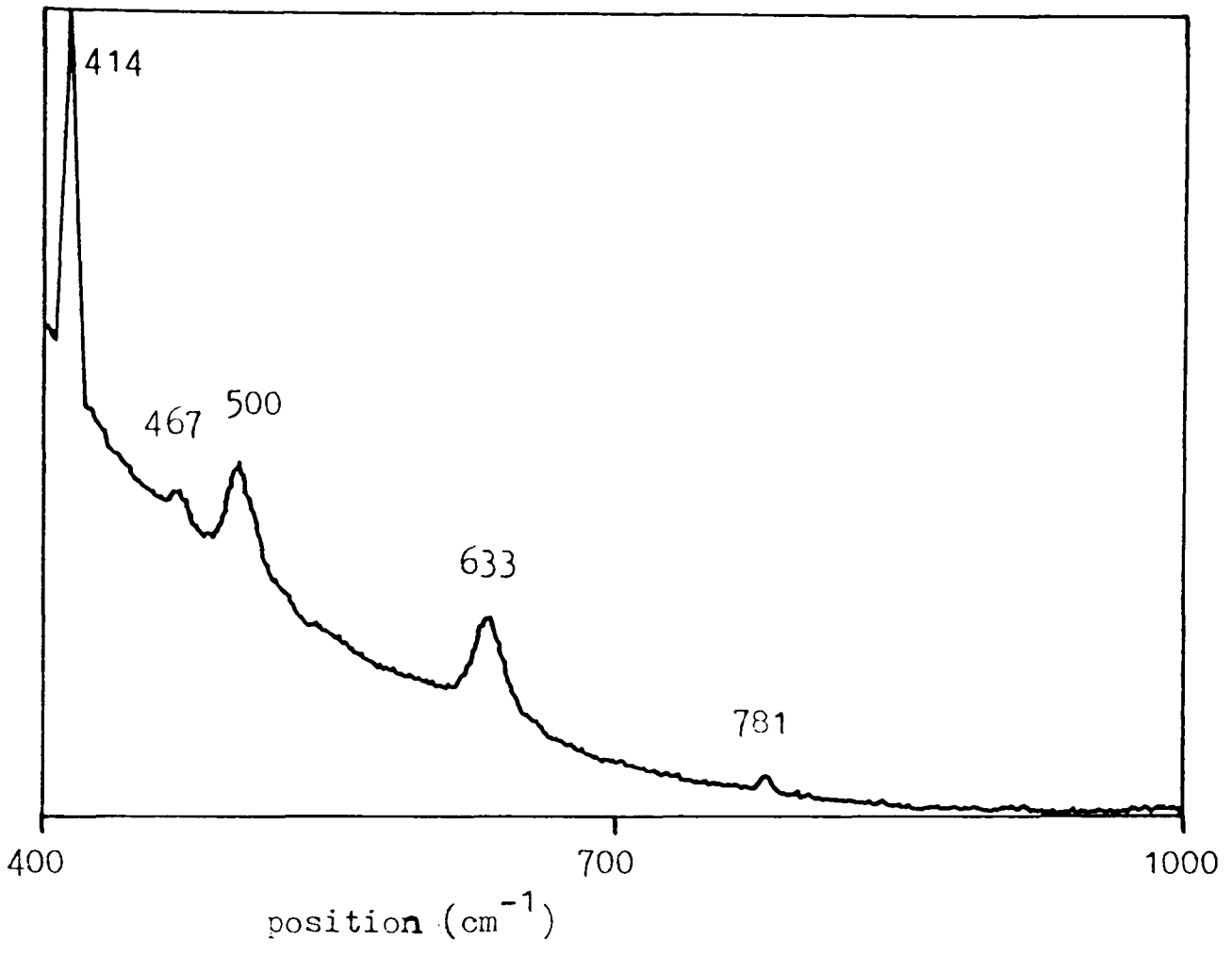

b)

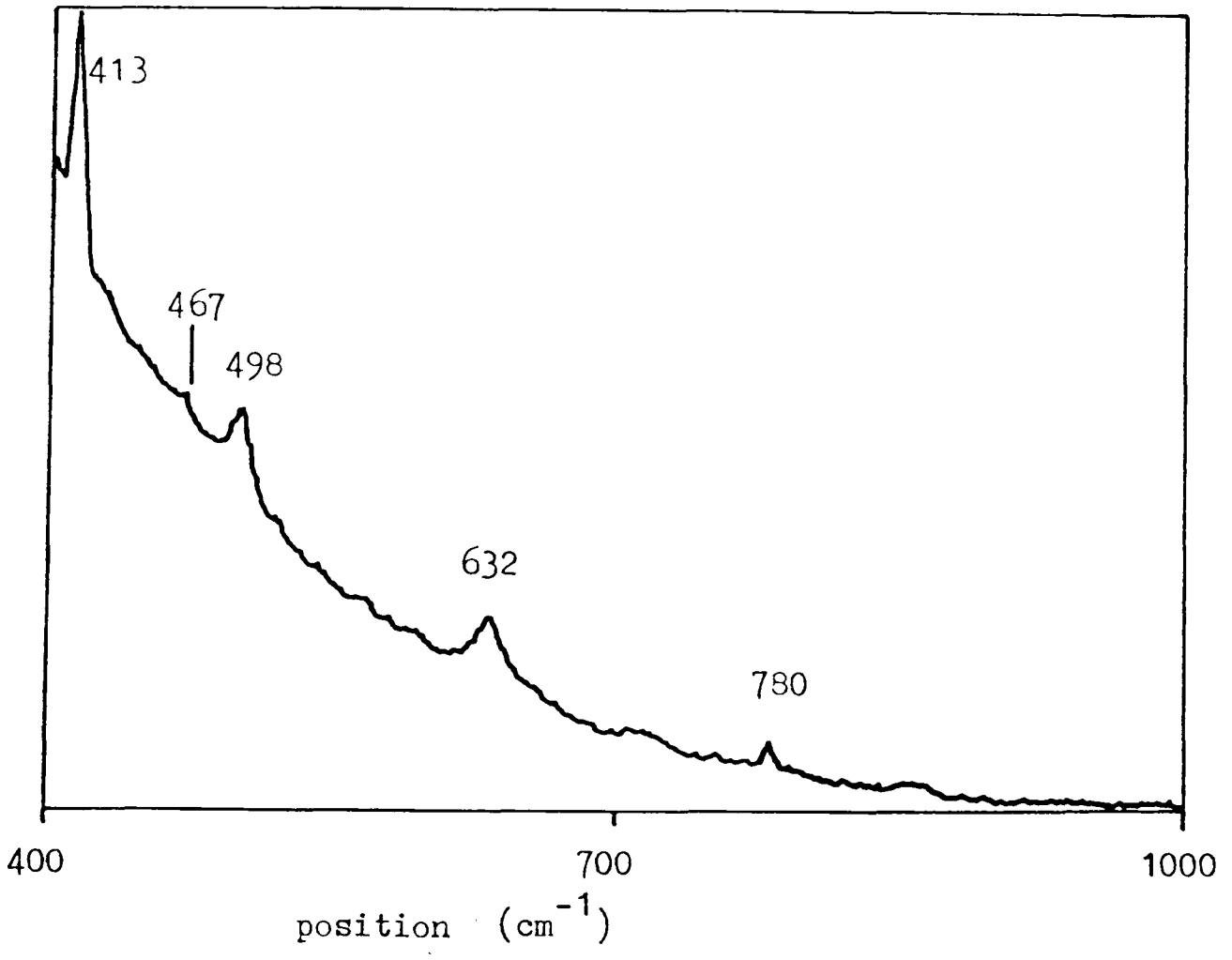

Figure 8: Laser-induced Raman spectra excited with a krypton laser for
a) undoped indium oxide
b) an ITO ceramic containing 4 at.% Sn and fired at 1000°C

781 cm^{-1} are laser plasma lines caused by impurities in the laser output. The spectra obtained from the ITO pellets were very similar to that of pure In_2O_3. A typical spectrum (for a sample containing 4 at.% Sn and calcined at 1000°C) is shown in figure 8b). The coincidence of the phonon frequencies between the doped and undoped material confirms that the ITO pellets consist in the main of a well crystallised In_2O_3 phase, which is largely undisturbed by the introduction of the tin dopant.

4.3.3 Investigation by Electron Spectroscopy

Before introduction into the electron spectrometer, the ITO pellets were mounted in specially constructed platinum sample trays and were secured by platinum wires. Heating by radio-frequency induction in the preparation chamber of the spectrometer (base pressure 5.10^{-8}mbar) was found to be necessary in order to obtain spectroscopically clean samples. Each pellet was heated overnight at a temperature approximately equal to its firing temperature (i.e. 1000°C, 1200°C or 1360°C). This was seen as a necessary precaution to minimise the possibility of any further reaction occurring during the cleaning procedures. After cleaning in this way, the Mg KαXPS spectra indicated that no carbon or other contaminants were present on the surfaces of the samples. Surface cleanliness was routinely monitored by HREEL spectra, which, under vacua of 10^{-10}mbar remained free of loss signals due to hydrocarbons or other contaminants for up to 12 hours. Recleaning was routinely carried out overnight.

4.4 Results for the Ceramic Materials

4.4.1 X-ray Photoelectron Spectroscopy

For each pellet, narrow scan spectra were obtained of the metal 4d, 3d, 3p and Auger peaks. Figures 9 and 10 give typical examples of the results obtained. Figure 9 shows XPS in the metal 3d region for pellets containing 1%, 4% and 6% Sn. All pellets were calcined at 1000^{o}C. The splitting of the metal peaks is due to spin-orbit coupling (section 1.2.3b)). The growth of the tin peaks with increasing doping level is evident. Figure 10 shows three spectra of the metal 4d region taken from a sample containing nominally 6 at.% Sn, but calcined at three different temperatures. Here, the spin-orbit splitting of the d levels is small and is not experimentally resolvable. It can be seen that the amount of tin on the surface of the sample decreases regularly as the sample calcining temperature is increased. Following the subtraction of background and satellite structure (section 2.5), it is possible to derive values for the relative intensities of tin and indium peaks by numerical integration of the experimental data.

As has been discussed (section 1.2.1ii)), the attenuation of the photoelectron flux within a solid is given by

$$I(x) = I_o(x)\exp(-x/\lambda) \qquad (5)$$

where I(x) is the emerging flux of photoelectrons, and $I_o(x)$ is the flux of electrons of energy E originating at a depth x below the surface. λ is the electron mean free path length, which is a function of electron kinetic energy. As the tin and indium peaks being compared are close in energy, λ may be regarded as constant, and the photoelectron intensity is then dependent on I_o. This is in turn dependent on a number of factors:

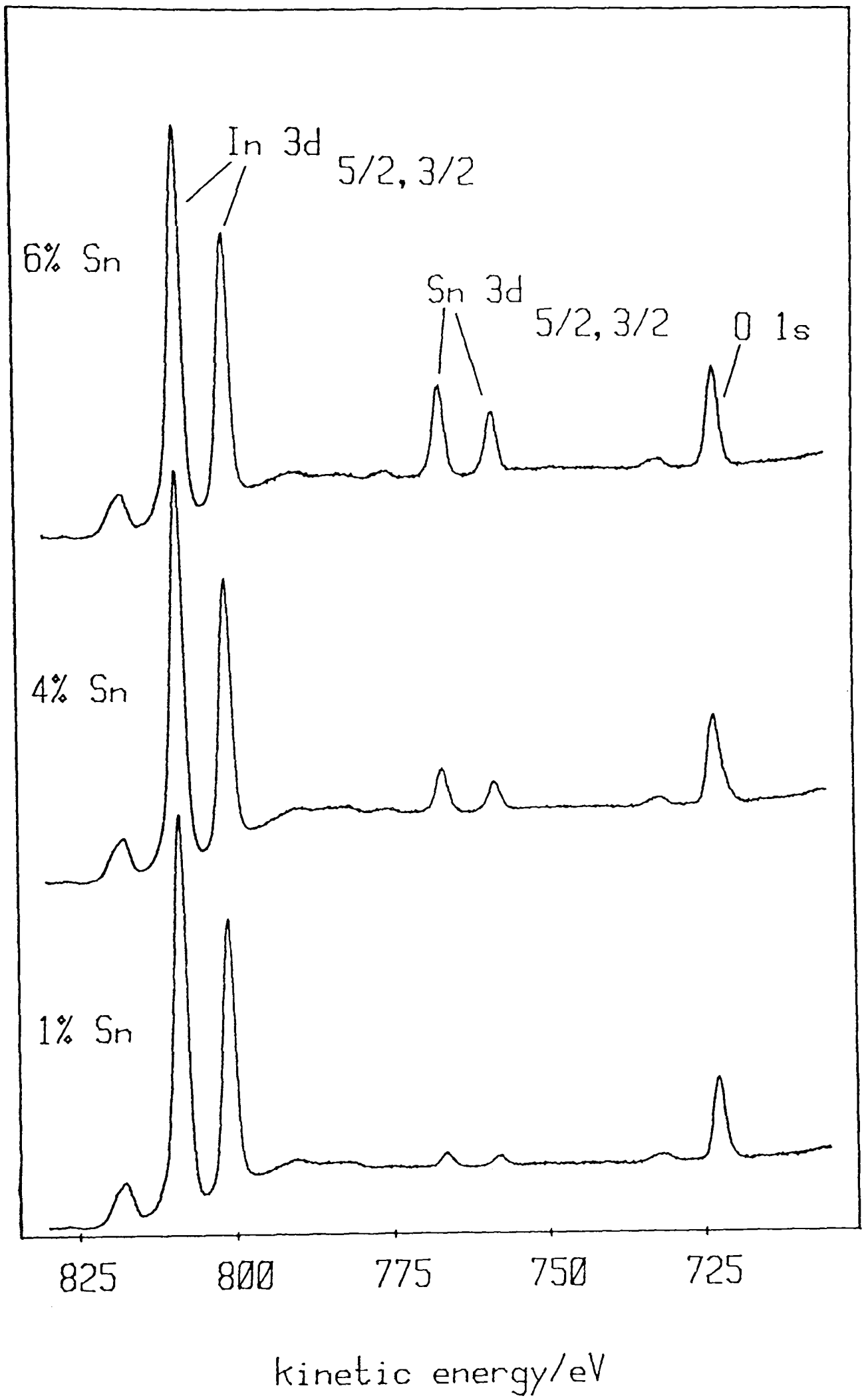

Figure 9: Examples of Mg KαXPS of ITO ceramics fired at 1000°C, in the metal 3d region. Peaks to the left of the main features are due to satellite radiation.

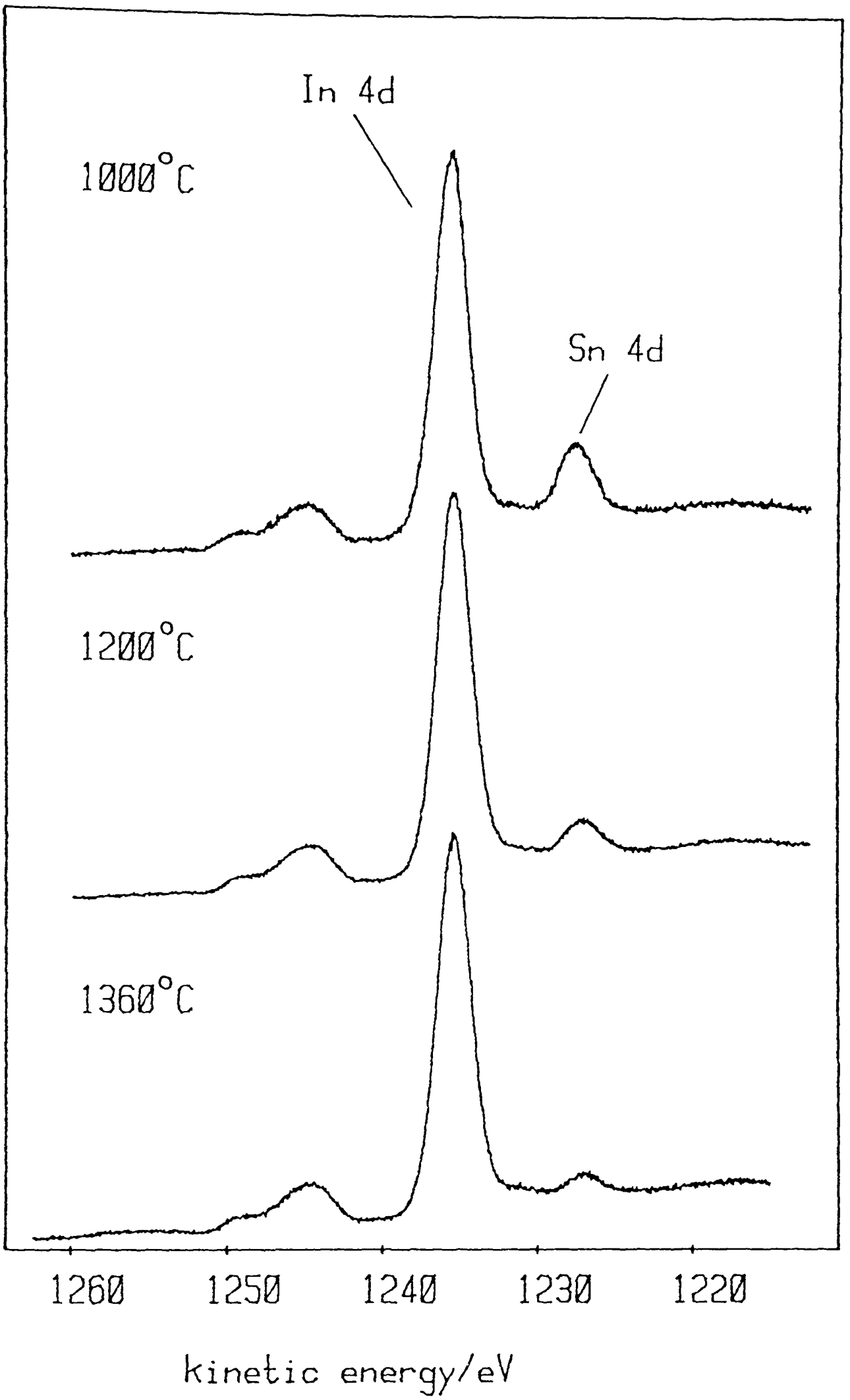

Figure 10: Examples of Mg Kα XPS of ITO ceramics containing 6 at.% Sn, in the metal 4d region. Firing temperatures are indicated. Peaks to the left of the main features are due to satellite radiation.

i) the photon flux (assumed constant as the penetration depth of the photon flux is large compared with λ)

ii) the escape probability of photoelectrons (assumed constant, as this is a function of KE which is similar for the levels to be compared)

iii) the spectrometer sensitivity (assumed constant[92])

iv) the ionisation cross-sections for the levels considered

v) the number of atoms of the element sampled by the technique

Thus, for say, indium and tin 3d peaks we have

$$I_{Sn}/I_{In} = \sigma_{Sn:3d^n Sn}/\sigma_{In:3d^n In}, \qquad (6)$$

so that the tin:indium ratio as sampled by the technique is readily obtained, by correcting the numerical intensities for the ionisation cross-sections of the levels involved. Values of the ionisation cross-sections were taken from the tabulations of Evans et al[10] and Urch[129]. The resulting ratios for several pellets are compared with the bulk atom ratios N(Sn)/N(In) in table 3.

Table 3 The experimental tin:indium ratios, n(Sn)/n(In), determined from comparison of the tin and indium 4d, 3d, and 3p peaks. The kinetic energy ranges of these peaks are indicated.

Sn content (at.%)	N(Sn)/N(In)	firing temperature (°C)	n(Sn)/n(In)		
			4d 1260-1210eV	3d 830-705eV	3p 600-475eV
6	0.0638	1000	0.144	0.187	0.189
		1200	0.057	0.097	0.097
		1360	0.029	0.065	0.067
4	0.0417	1000	0.049	0.096	0.108
		1360	0.019	0.056	0.058
1	0.0101	1000	0.007	0.027	0.036
		1200	0.007	0.021	0.026

Ratios determined from Auger peaks, although showing the same general trends, are not included. This is because the weak In 3s peak at 428eV kinetic energy lies between the Sn and In Auger peaks, and may be contributing to the integrated Sn peak intensity. Similarly, the Sn $3p^{1/2}$ peak is not used as this coincides with the oxygen Auger peak at 511eV kinetic energy.

The data selected in table 3 serves to illustrate the general trends observed. The tin:indium ratio at the surface of the pellets as sampled by XPS increases with nominal tin concentration, but decreases as the final firing temperature of the pellet is raised. The majority of the data (with the exception of that for pellets fired at 1360°C taken from the 4d peaks - see below) gives a tin concentration greater than the nominal doping level, indicating that some segregation of tin to the surface has occurred. Data taken from the 3d and $3p^{3/2}$ peaks indicates that the tin concentration at the surface may be 2.5 - 3 times the nominal doping level for samples calcined at 1000°C. The amount of surface segregation decreases as the firing temperature is raised. Simple thermodynamics[130] leads to the following relationship between surface (s) and bulk (b) tin cation site occupancies:

$$\theta_s/(1-\theta_s) = \theta_b/(1-\theta_b)\ \exp -\Delta H/RT \qquad (7)$$

where ΔH is the heat of segregation. Thus, this type of variation might be expected if the heat of segregation is small and exothermic.

Moreover, the tin:indium ratio as sampled by electrons in different kinetic energy ranges (i.e. having differing penetration depths, λ) is not the same, and tends to increase with decrease in KE and thus in λ. This variation would not be expected if there were a thick tin rich surface "phase"; if this were the case then electron energy dependent variations in photoelectron mean-free-path length could not influence XPS intensity ratios. The observation of this phenomemnon suggests that segregation must be restricted to a layer at the surface

which is relatively thin (of the same order of magnitude as the penetration depth of the electrons used, ~10Å). This limits the surface enrichment to the top few atomic layers.

An apparent anomally in the results is seen for samples fired at 1360°C. Here the tin:indium ratio as determined from the 4d peaks is appreciably less than the bulk doping level. This would appear to indicate a depletion in tin at depths sampled by electrons in the higher KE range, having path lengths of around 15Å.

Thus the XPS results appear to suggest that tin segregation is restricted to the top few atomic layers, which overlie a region which is tin-deficient. In order to provide corroborating evidence for this model, a sample containing nominally 6% tin and fired at 1360°C was subjected to a mild argon-ion etch (1kV argon ions at $2\mu Acm^{-2}$ for 5 minutes, estimated to be sufficient to remove only a few Angstroms of material from the surface). The tin signals were found to be dramatically reduced, the tin 3d signal being reduced in intensity by roughly 50%. A further etch (2kV argon ions at $10\mu Acm^{-2}$ for 5 minutes, estimated as sufficient to remove around 20Å from the surface), resulted in the almost complete removal of the tin 3d signals. Narrow scan spectra of the metal 3d peaks before and after etching the sample are shown in figure 11. After radio-frequency heating overnight in the preparation chamber of the spectrometer, at a temperature approximately equal to the final firing temperature of the pellet, the tin signals were found to have increased in intensity, as shown in figure 11.

Reduction in tin:indium ratio on sputter etching samples of ITO films has been reported[116,118]. In one case, the effect has been attributed to differential sputtering[116]. However, this conclusion was based on results from a hot-pressed sputtering target containing 9 mole % SnO_2. The sample etched in our experiment had previously been

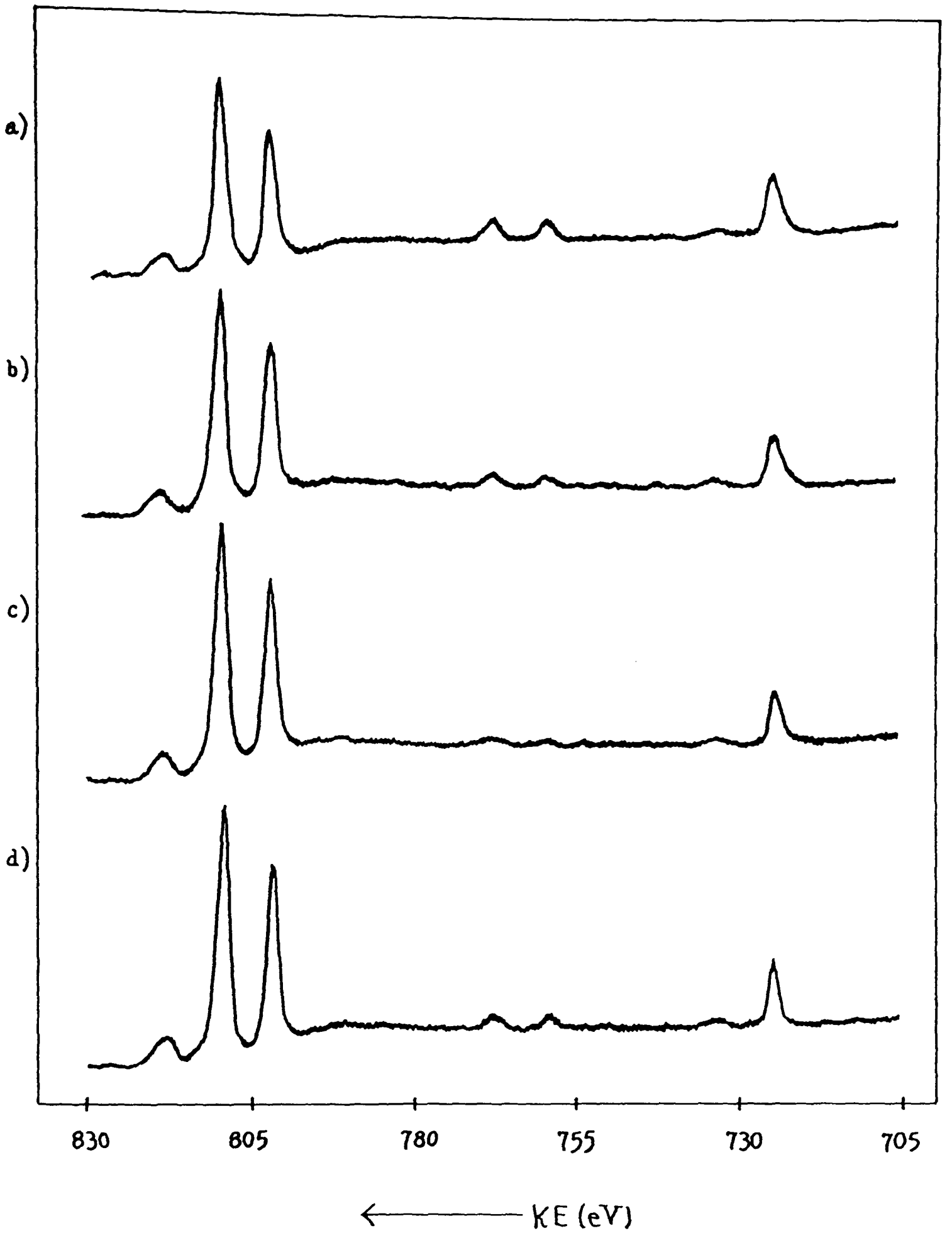

Figure 11: Narrow scan Mg KαXPS for a ceramic containing 6 at.% Sn and calcined at 1360°C
a) before argon-ion etch
b) after etching with 1kV argon ions at $2\mu Acm^{-2}$ for 5 minutes
c) after etching with 2kV argon ions at $10\mu Acm^{-2}$ for 5 minutes
d) after annealing overnight at roughly 1300°C in the preparation chamber of the spectrometer.

shown by X-ray diffraction to contain no separate SnO_2 phase. Whilst a SnO_2 phase may be preferentially removed by argon-ion etching, we consider it unlikely that tin atoms contained in an In_2O_3 phase will be so removed, particularly under the mild conditions used.

Further evidence for the surface model proposed is provided from the consistency of values for surface occupancy and heat of segregation which are obtained from calculations using this model. These calculations are described in the following sections.

4.4.2 Surface Occupancy

The model of the surface employed is one in which a fraction θ of surface cation sites are occupied by tin. A layer which is depleted in tin underlies this topmost surface layer. Etching results suggest that the depth of this layer is larger than the mean-free-path length of electrons detected in XPS. If this is the case, then a model in which the contribution to the photoelectron flux from tin ions in the bulk is negligible should provide a good fit to the experimental data. Using equation (5), a simple expression for the intensity ratio between tin and indium signals can be written:

$$I_{Sn}/I_{In} = (\sigma_{Sn}/\sigma_{In})\ [1-\exp(-D/\lambda)]/[(1-\theta)+\exp(-D/\lambda)] \qquad (8)$$

Here D is the separation (normal to the surface) between adjacent cation containing planes, λ is the electron mean-free-path length, and σ are the ionisation cross-sections for the relevant sub-shell. The mean-free-path length for use in this equation was estimated using the theory developed by Szajman and Leckey[14,15].

These authors have derived a simple analytical expression for the mean-free-path of electrons in free-electron-like metals, assuming that the electron scattering that leads to photoelectron attenuation can

be described using a bulk jellium model for the solid. An analogous formula applicable to semiconductors, insulators, and non-free-electron-like metals has also been derived[14]. Both equations agree well with experiment. These equations have been further simplified by Leckey and co-workers[15], who have shown that λ in a wide range of materials is described by a formula giving a dependence on electron kinetic energy of the form $AE^{3/4}$, where A is sample dependent. More explicitly we have:

$$\lambda(E) = 1.8\bar{E}E^{3/4}/E_p^2 \qquad (9)$$

(all energies in eV).

E_p is the plasmon energy characteristic of the valence electrons of the system. This is given by the expression

$$E_p = 28.8(\rho z/A)^{1/2} \quad \text{(eV)} \qquad (10)$$

where ρ is the density, A is the molecular weight, and z is the number of valence electrons per formula unit. In equation (9), E is the centroid of the optical loss function $\mathrm{Im}(-1/\epsilon)$. This can be approximated to

$$\bar{E} = E_p + E_g \qquad (11)$$

where E_g is the gap between the valence and conduction bands. In the calculation of $\lambda(E)$ from equation (9) it was assumed that O:2p, O:2s and In:4d electrons contribute to the valence electron plasmon. This is in accord with previous work by the author on antimony-doped tin dioxide ceramics[91], where it was found that the experimental data were best fitted by making a similar assumption about the Sn:4d electrons. With E_g=3.6eV[109], this gives $\bar{E}$=30.6eV. Hence we obtain

$$\lambda(E) \backsim 0.0755E^{3/4} \quad \text{(eV)} \qquad (12)$$

Thus values of λ in the kinetic energy ranges considered may be calculated. These are shown in table 4.

Empirical estimates of subshell ionisation cross-sections for use in equation (8) were taken from the tabulations of Evans et al[10] and Urch[129].

Table 4 λ-values calculated from theory of Szajman and Leckey[14,15].

orbital	kinetic energy/eV	λ/Å
In 3p	588	9.02
In $3d^{3/2}$	801	11.37
In $3d^{5/2}$	808	11.44
In 3d (av)		11.41
In 4d	1236	15.74

For the ceramic materials, there is some ambiguity in the choice of the cation-cation spacing D. For simplicity, this is taken to be the interplanar spacing between cation-containing planes in the unit cell of the In_2O_3 structure (i.e. along the [100] direction). In_2O_3 single crystals have been shown to grow preferentially in the [100] and [111] directions[131], and ITO thin films tend to exhibit a predominant <100> or <111> texture[121].

The resulting values of the surface occupancy, θ, are shown in table 5.

Table 5 Surface tin cation site occupancy values calculated from analysis of 4d, 3d, and 3p peak intensity ratios. Average values are also indicated.

Sn content (at.%)	firing temperature (°C)	surface occupancy, θ			
		4d	3d	3p	av.
6	1000	0.85	0.80	0.65	0.77
	1200	0.36	0.44	0.36	0.39
	1360	0.19	0.31	0.26	0.25
4	1000	0.31	0.44	0.40	0.38
	1360	0.13	0.27	0.22	0.21
1	1000	0.04	0.13	0.14	0.11
	1200	0.05	0.11	0.11	0.09

Data for the sample containing nominally 1 at.% Sn and calcined at 1360^{o}C are omitted, as it was felt that the tin signals from this sample were not sufficiently strong to allow for reliable integration of the peaks. Considering the simplicity of the model used and the assumptions made, the values of surface occupancy obtained using data from the 4d, 3d and 3p peaks show a good degree of consistency. The divergence is larger for the samples containing 1 at.% Sn than for the higher concentrations; this is probably due to a decrease in the accuracy of integration of the peak areas as the tin peaks become smaller. The data shows consistent trends both with doping level and with firing temperature.

4.4.3 The Heat of Segregation

From the values obtained for the surface coverage, rough estimates of the heat of segregation of tin to the surface of In_2O_3 can be obtained, using equation (7). The temperature T used corresponds to that used in the final firing of the pellet, as it is assumed that an equilibrium is established during firing which is quenched on cooling the pellet. Table 6 shows the values obtained.

Table 6 Heats of segregation of tin to the surface of ITO ceramics

Sn content (at.%)	firing temperature (^{o}C)	ΔH_{seg}/kJmol^{-1}
6	1000	-33
	1200	-23
	1360	-19
4	1000	-23
	1360	-18
1	1000	-21
	1200	-22

It can be seen that the heats of segregation are reasonably consistent, apart from the very high value obtained for the sample containing 6 at.% Sn and fired at 1000°C. However, it must be borne in mind that XRD results demonstrate that this sample contains of the order of 5% tin in the form of tin dioxide, so the physical significance of this result is unclear. The results obtained from this pellet would certainly not be expected to fit well to the simple model used. Likewise, the smaller amounts of tin dioxide present in some of the other samples (section 5.3.2i)) may go some way towards explaining the small differences observed in the values of ΔH_{seg} for samples having the same doping level, but fired at different temperatures. Thus we may conclude that the heat of segregation of tin to the surface of the ITO ceramics is around $-20 kJmol^{-1}$. This value is similar to values (of around $-25 kJmol^{-1}$) previously obtained by the author for the heat of segregation of antimony to the surface of tin dioxide ceramics[82,91]. A full comparison of these results with those obtained from the ITO ceramics is given in section 4.7.1.

4.4.4 Ultra-Violet Photoelectron Spectroscopy

He I UPS over the complete composition range 1 - 6% are shown in figure 12. The two dominant features of each spectrum are the filled valence band which has a sharp onset at about 3eV below the Fermi energy, and the strong secondary electron background with which it merges at about 10eV below E_f. Tin doping appears to have little effect on the overall shape of the valence band. This confirms that the valence band is, as expected, predominantly oxygen 2p in character. The O:2p bandwidth cannot be deduced from the He I spectra due to the strong background, but a value of around 10eV seems realistic, and would be similar to the valence band width observed for tin dioxide ceramics[93].

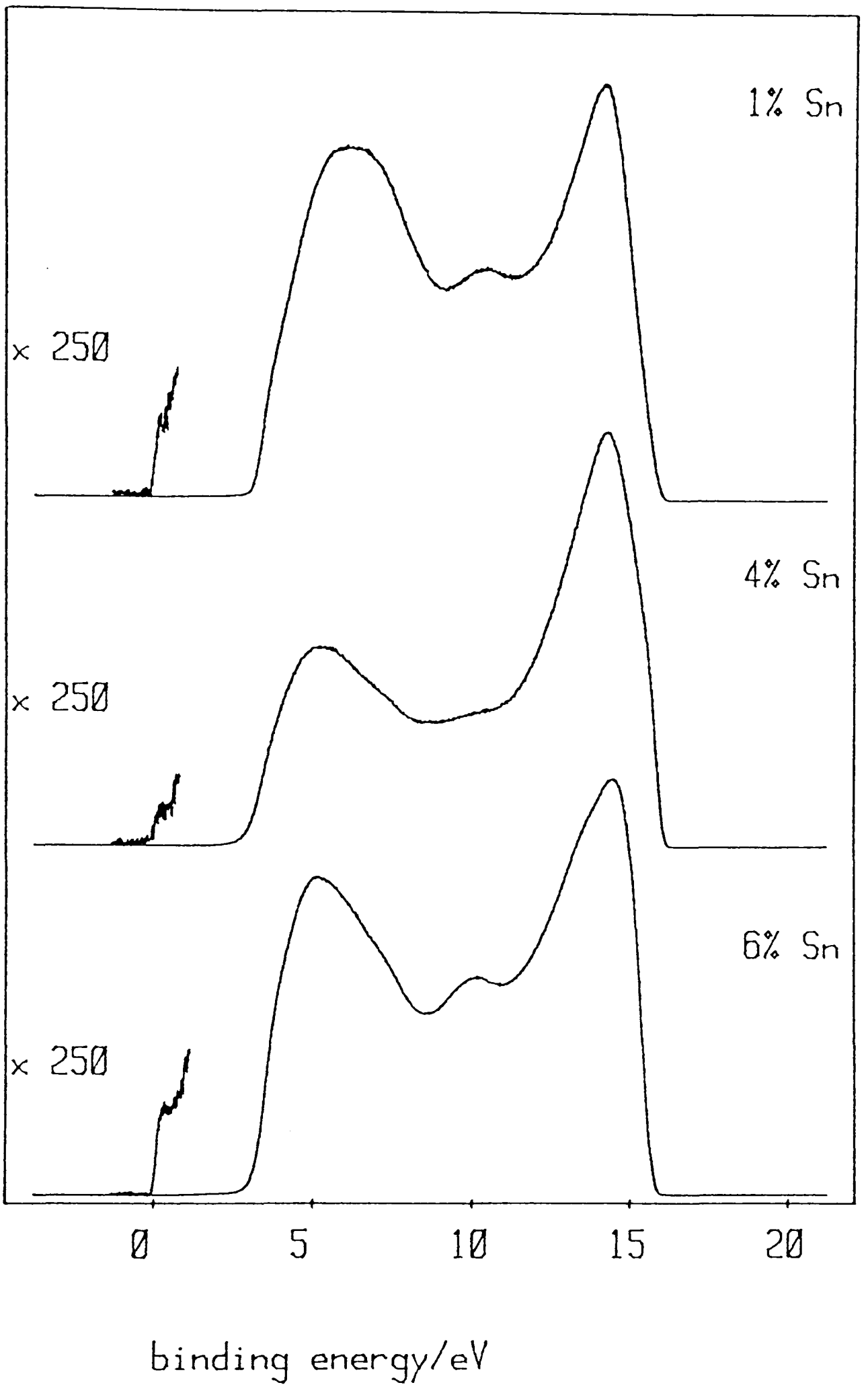

Figure 12: He I photoelectron spectra of ITO ceramics for various doping levels. All samples were calcined at 1360°C. Binding energies are relative to the Fermi energy. The spectra have been stripped of structure due to He Iβ and He Iγ radiation.

The large bandwidth suggests strong In-O covalency.

On subtracion of structure due to He Iβ($h\upsilon$=23.09eV) and He Iγ ($h\upsilon$=23.75eV) radiation from the raw spectra (appendix I), a weak peak close to the Fermi energy is observed. This is due to electrons in the conduction band of the samples, corresponding to free carriers introduced by tin doping. The band gap (measured from the base of the conduction band to the onset of the valence band) is approximately 2.5eV, in accord with the value of the indirect band gap of 2.6eV obtained by Weiher and Ley[110].

The He I photoelectron spectra represent an important direct measurement of the band structure of the material, which was recently reported as being unknown in most respects[132]. The only available information to date appears to be concerning the direct[109] and indirect[110] band gaps, and the region around the bottom of the conduction band[121,131].

Subtraction of satellite structure allows the relative intensity of the conduction band to be estimated. Taking the conduction and valence bands to be defined by their high binding energy minima, the ratios of intensities of the conduction bands and valence bands shown in table 7 were obtained. The weakness of the conduction band, and the strong background of secondary electron emission means that these figures are prone to large errors, and the results must be regarded as giving the correct order of magnitude only.

If each tin atom introduced by doping was electrically active, i.e. was contributing one electron to the conduction band of the material, the ratio I(CB)/I(VB) might be expected to increase linearly with increasing tin doping level. This type of behaviour has been observed for ITO thin films, where a linear variation of free electron density has been observed for concentrations up to 5-6 at.% Sn[89]. The ITO ceramics clearly do not show this behaviour. The conduction to valence

Table 7 The conduction band:valence band intensity ratios for ITO ceramics having various doping levels. Data for samples containing 1 at.% Sn and fired at 1000°C and 1200°C are omitted as the very small conduction bands could not be reliably integrated.

Sn content (at.%)	firing temperature (°C)	I(CB)/I(VB)x10^5
1	1360	3.3
4	1000	3.1
	1200	7.1
	1360	6.6
6	1000	9.4
	1200	8.7
	1360	5.9

band intensity ratios appear to show random fluctuations with both calcining temperature and nominal doping level. However, within the accuracy of the integration, the values obtained for the higher doping levels (where the integration is likely to be most successful) may be regarded as remaining roughly constant, giving a conduction band to valence band intensity ratio of around $7x10^{-5}$.

The carrier concentration giving rise to this ratio may be estimated by using O:2p and In:5s matrix elements for ionisation from valence and conduction bands respectively. The bottom of the conduction band is expected to be predominantly In 5s-like in character, justifying this assumption[116]. Thus we have

$$I(CB)/I(VB) = 2x.\sigma(In:5s)/18.\sigma(O:2p) \qquad (13)$$

where x is the fraction of tin atoms which have donated an electron to the conduction band. The numerical factors arise as there are 18 O:2p electrons and two In:5s electrons per formula unit. One electron ionisation cross-sections were obtained from the calculations of Fadley et al[11], giving

$$I(CB)/I(VB) = 2.2x10^{-5}n \qquad (14)$$

where n is the atomic percentage of tin contributing free carriers. Using a conduction band to valence band intensity ratio of $7x10^{-5}$ as

estimated for pellets doped with 4 and 6 at.% Sn, this gives a value for n of 3.1 at.%. The simple model used in equation (13) is likely to give a high value of n, as some of the more tightly bound valence states are not accessible to He I UPS. Thus we may conclude that even in the sample containing 6 at.% Sn, the amount of substitutionally incorporated tin is less than around 3 at.%, at the penetration depths sampled by UPS. This finding is at variance with the work of Frank et al[90] on similar ceramics where it was concluded that up to doping levels of 6 at.% Sn, each dissolved tin atom could be electrically active. This result is discussed further in the following section.

4.4.5 Electron Energy Loss Spectroscopy

Typical examples of the HREEL spectra obtained in the specular direction with a 25eV electron beam are given in figure 13. This shows spectra for samples calcined at 1200°C, containing 1%, 4% and 6% Sn. Vibrational structure due to the excitation of surface optical phonons is seen immediately to the right of the elastic peak. The main feature of the spectra is a rather broader peak at an energy loss of approximately 0.5eV for the 1% sample. This moves to progressively higher energy loss relative to the elastic peak as the bulk tin content increases. This peak is due to the excitation of the conduction electron surface plasmon. Overtones are clearly visible in expanded scans of the spectrum (figure 13). Such overtones are a common feature of HREEL spectra. They are similar to those observed in infra-red spectroscopy, but arise by a different mechanism. In HREELS, the total loss probability is so large that electrons may sequentially excite two or more plasmons or phonons in separate loss events, leading to overtone and combination structure.

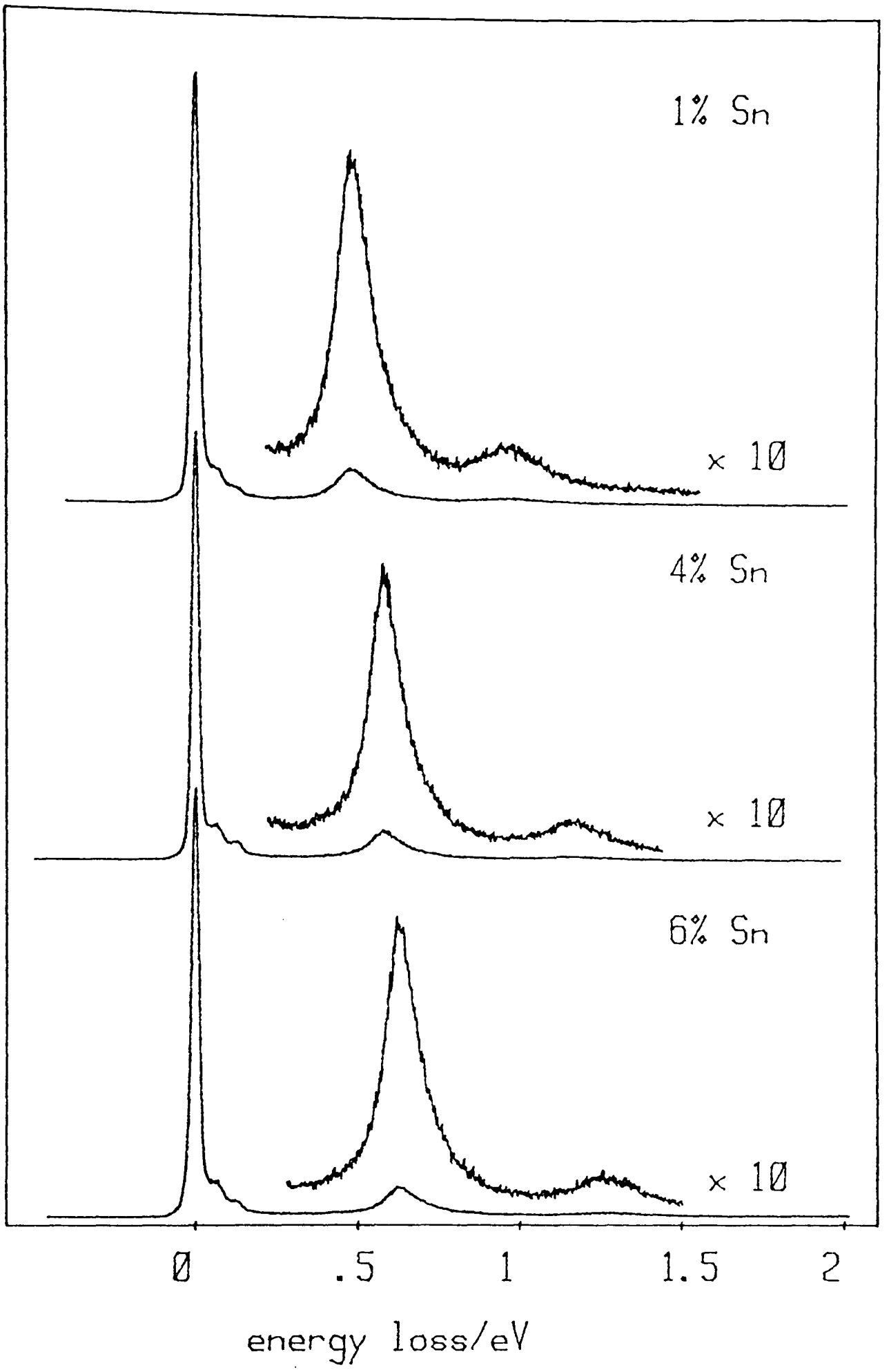

Figure 13 HREEL spectra of ITO ceramics excited with a 25eV electron beam. All samples were fired at 1200°C. FWHM ∿ 50meV.

As we have already seen (Chapter 3, section 3.2), the loss peaks of figure 13 correspond to the condition

$$\mathrm{Re}\ (\varepsilon(\omega)) = -1 \qquad (15)$$

It has been suggested that the transition from non-metallic to metallic behaviour, as a function of concentration or pressure, can be regarded as a polarisation catastrophe induced by local fields[133-135]. This idea is expressed by equation (16) for the long-wavelength dielectric function $\varepsilon(\omega)$ arising from an array of damped oscillators, with the effects of local fields included through the Clausius-Mossotti formula[136]:

$$\varepsilon(\omega) = \varepsilon_\infty + ne^2/[m^*\varepsilon_o(\omega_o^2-\omega^2+i\omega\gamma)-ne^2/3] \qquad (16)$$

Here n is the concentration of oscillators, each with dynamic charge e and effective mass m^*, ω_o and γ are the frequency and damping constant for a single oscillator, ε_o is the permittivity of free space, and ε_∞ is the background (high frequency) dielectric constant.

In the metallic regime, local field corrections vanish[137] and we have

$$\varepsilon(\omega) = \varepsilon_\infty + ne^2/m^*\varepsilon_o(\omega_o^2-\omega^2+i\omega\gamma) \qquad (17)$$

As the damping constant for plasmon oscillations is generally small, we may write

$$\varepsilon(\omega) = \varepsilon_\infty + ne^2/m^*\varepsilon_o(\omega_o^2-\omega^2) \qquad (18)$$

When ω_o=0, equation (18) reduces to the Drude dielectric function for a free-electron gas. Equating (18) to the loss condition for EELS, (15), and rearranging we obtain

$$(\omega_{sp}^2-\omega_o^2) = ne^2/\varepsilon_o(\varepsilon_\infty+1)m^* \qquad (19)$$

where ω_{sp} is the surface plasmon frequency. Thus simple plasmon theory predicts that the square of the plasmon frequency should vary linearly

with the number of free carriers. Such behaviour has been observed in thin films of ITO doped with up to around 5% Sn[89,107]. This is illustrated in figure 14.

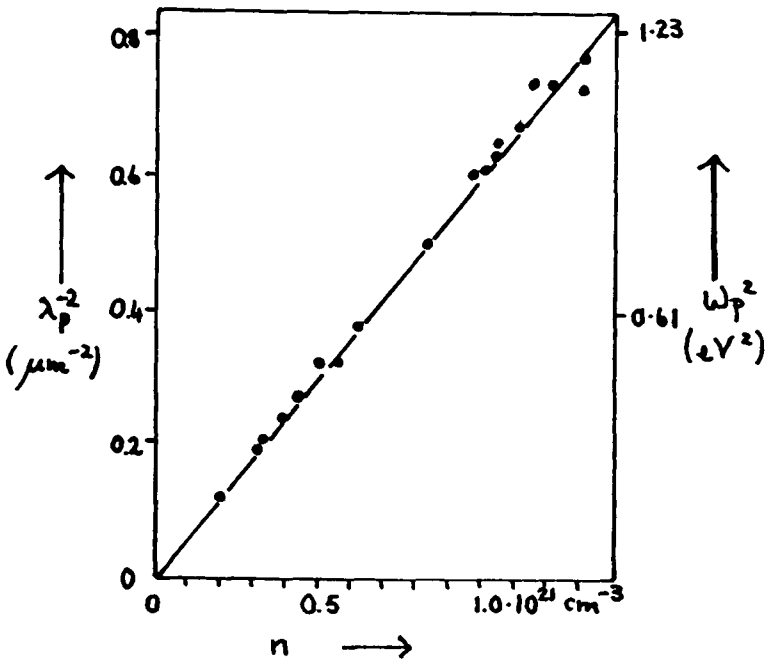

Figure 14:[107] The inverse square of the plasmon wavelength, as a function of the free-electron density n, showing linear dependence in accordance with the Drude model.

The graph does not pass exactly through the origin. This is because when n=0, we have

$$\omega_{sp}^2 = \omega_o^2 \qquad (20)$$

where $\hbar\omega_o$ is the single-particle donor level to conduction band excitation energy. The measurements of Weiher[131] suggest a donor level about 0.03eV below the conduction band minimum for low n. Thus the intercept of the graph is very small. The slope of the graph in figure 14 yields an electron effective mass (via equation (19)) of $0.35m_e$.

Table 8 shows the surface plasmon frequencies (and their squares) obtained for all the ceramic samples studied. The plasmon frequency increases with increasing doping level for all firing temperatures, but clearly by much smaller amounts than would be expected if each

incorporated tin atom were contributing one electron to the conduction band of the sample. This accords with the findings from UPS (section 4.4.4). The plasmon frequencies vary with firing temperature, but in a random way. This behaviour is contrasted with that previously observed for antimony doped tin dioxide ceramics[82,91] in section 4.7.1.

Table 8 Plasmon frequencies for the ITO ceramics

Sn content (at.%)	firing temperature (^{o}C)	plasmon frequency, ω_{sp} (eV)	ω_{sp}^2 (eV^2)
1	1000	0.485	0.235
	1200	0.477	0.228
	1360	0.472	0.222
4	1000	0.525	0.275
	1200	0.577	0.333
	1360	0.580	0.336
6	1000	0.535	0.286
	1200	0.625	0.391
	1360	0.605	0.366

Equation (19) may be used to calculate the free carrier concentration giving rise to the plasmon from the observed plasmon frequency. Estimates of the high frequency dielectric constant ε_∞ and electron effective mass m^* are taken from the work of Köstlin et al on thin films[89,107]. Thus we have $\varepsilon_\infty=4$ and $m^*=0.35m_e$. These values are in agreement with the work of Ohhata et al[138], who found an effective mass which was weakly concentration dependent, varying from $0.31m_e$ at $10^{19}cm^{-3}$ to $0.43m_e$ at $8.2x10^{20}cm^{-3}$. The high frequency dielectric constant was also found to vary from $\sim$4 - 3 in the same concentration range.

The carrier concentrations calculated from equation (19) are shown in table 9 which also gives their equivalents in at. % Sn. For comparison purposes, the percentage of tin in the form of tin dioxide in each pellet as determined by XRD is shown.

Table 9 Free carrier contents for the ITO ceramics determined from HREELS

Sn content (at.%)	firing temperature (^{o}C)	n ($10^{21}cm^{-3}$)	n (at.% Sn)	SnO_2 content (at.% Sn)	"residual" Sn content (at.%)
1	1000	0.298	0.96	0	0
	1200	0.289	0.93	0	0
	1360	0.283	0.91	0	0
4	1000	0.350	1.12	1-2	1
	1200	0.422	1.36	1-1.5	1
	1360	0.427	1.37	0	2.5
6	1000	0.363	1.17	5-6	0
	1200	0.496	1.59	2-3.5	2.5-1
	1360	0.464	1.49	0	4.5

The results appear to show (within the limits of experimental error), that at a dopant concentration of 1%, the tin is substitutionally incorporated into the In_2O_3 lattice, each tin atom donating one electron to the conduction band of the sample. However, at higher doping levels this is not the case, the free carrier tin concentration for most samples only attaining a value which is slightly over 1 at.%. The maximum attained is around 1.6 at.% for the sample with a nominal tin doping level of 6 at.%, fired at 1200^{o}C. These results are likely to be more accurate than the UPS results of the previous section, as the plasmon frequencies may be accurately measured, and the analysis used involves fewer assumptions. Taking this into consideration, these results are fully consistent with the results from UPS, in that they again demonstrate that the free carrier concentration at the sampling depth of the technique is markedly less than the nominal tin content for samples containing 4 and 6 at.% Sn.

Moreover, for these samples, it can be seen that there is generally a shortfall between the nominal doping level, and the sum of the tin dioxide content and the tin substitutionally incorporated, as sampled by

EELS. An estimate of this "residual" tin content is given in table 9. This effect is most evident at the highest firing temperature of 1360°C. This phenomenon is discussed in section 4.7.2.

4.5 Experimental: ITO Thin Films

As a continuation of the work on ceramics, samples of ITO thin films were obtained. These were prepared at the Thin Film Laboratory in the Department of Electrical Engineering, Imperial College, London, by Dr.M.J. Lee. The films were deposited on 10mm diameter quartz discs (Jencons (Scientific) Ltd) by radio-frequency sputtering from a pressed mixed oxide target containing 9 mole % SnO_2. The sputtering was carried out in an atmosphere of $4x10^{-3}$mbar argon. The nominal film thickness was 500Å.

Of particular interest in the investigation of the thin films by electron spectroscopy was the plasmon frequency observed in HREELS. It has already been demonstrated that in samples of the ceramic material fired for prolonged periods, and hence well equilibrated, the plasmon frequencies obtained were generally considerably lower than those normally observed for thin films having the same composition. The maximum surface plasmon frequency attained was 0.625eV for a sample containing 6 at.% Sn. An ITO film having the same level of doping and prepared under optimum conditions would be expected to show a bulk plasmon frequency of around 1.1μm (1.13eV)[89], as determined by infra-red reflectivity. The small correction between surface and bulk plasmon frequencies (Chapter 1 section 1.3.2) only accounts for a small part of this discrepancy.

We believe the ITO films to be prepared under non-equilibrium conditions. In particular, the substrate temperature used is low ($\sim$550^{o}C). Thus it was important to examine the films in the as-received state, precluding any possibility of cleaning the samples by annealing prior to recording spectra, as with the ceramic samples (section 4.3.3). In order to minimise surface contamination, the films were ultrasonically cleaned in isopropanol and then washed with double-distilled water before being mounted in platinum sample trays and introduced into the spectrometer.

XPS and HREEL spectra only were recorded. It was found that, due to the quartz substrate, electrical contact between the films and the sample earth was not sufficiently good to prevent sample charging. As a result, UPS spectra could not be observed.

The effect of both resistive and radio-frequency heating in vacuo on the HREEL spectra was investigated. The quartz substrate appeared to withstand radio-frequency heating at around 1200^{o}C for short periods ($\sim$2 hours). After radio-frequency heating at temperatures above 500^{o}C, the HREEL spectra were free of loss signals due to hydrocarbons or other contaminants, and the carbon signals in the Mg KαXPS spectra were greatly reduced from those observed prior to annealing. However, prolonged calcining in air outside the spectrometer at temperatures comparable to those used in the preparation of the ITO ceramics was not found to be feasible, due to softening of the quartz substrate.

The optical transmission of the films were recorded, both in the as-received state and after annealing. This was done using a Perkin-Elmer 330 spectrometer, having a range 2600-185nm (0.48-6.7eV), and a resolution of 0.7nm. The films were mounted against a background of analar MgO in a Spectrasil glass reflectance cell, an MgO pellet being used as the compensating standard.

4.6 Results for the Thin Films

4.6.1 X-ray Photoelectron Spectroscopy

Narrow scan XPS obtained from the films in the metal 4d, 3d, 3p and Auger signal regions were very similar to those obtained from the ceramic samples (section 4.4.1). Examples are shown in figure 15.

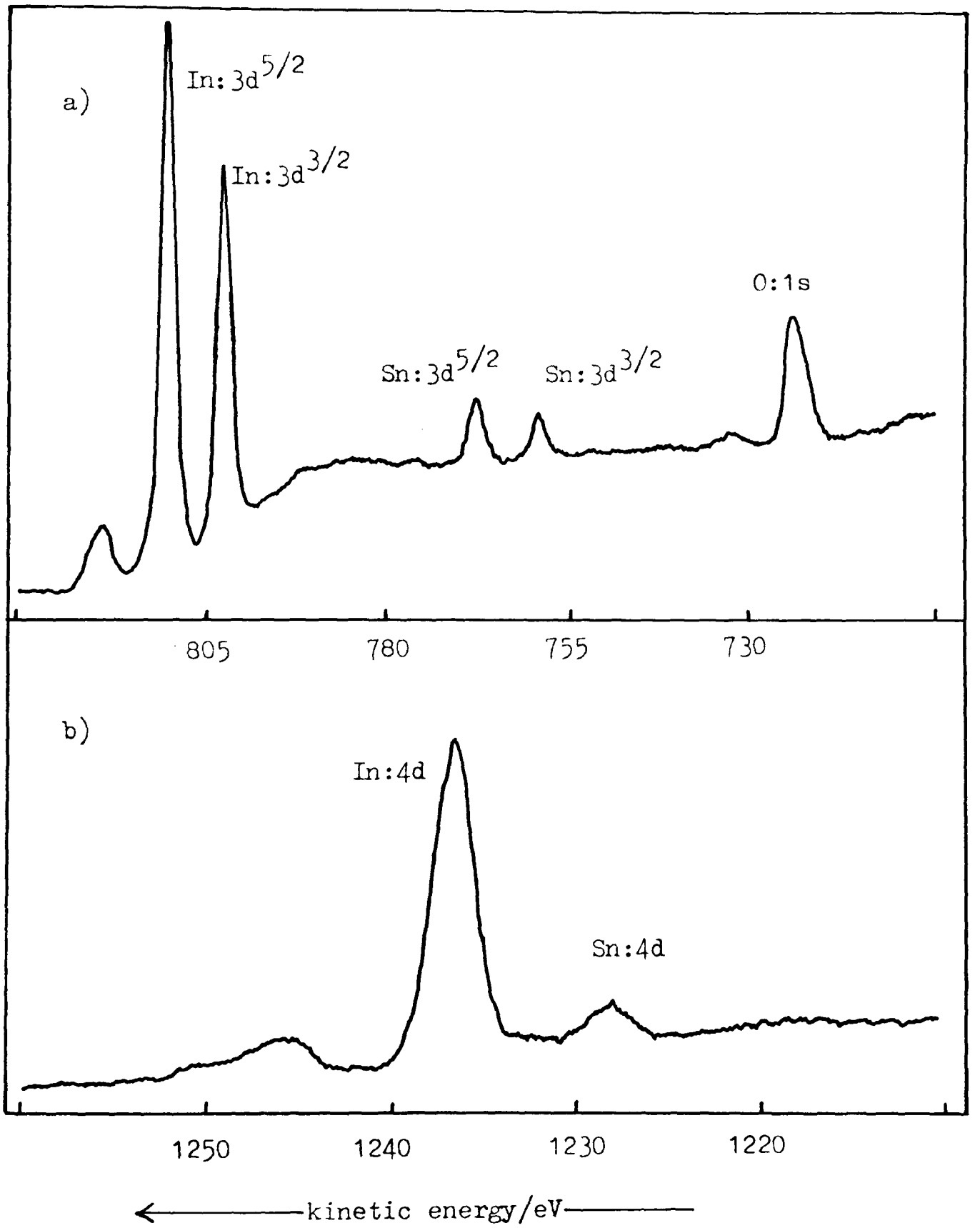

Figure 15 Examples of Mg Kα XPS spectra from an as-received ITO pellet
a) in the metal 3d region
b) in the metal 4d region.

At this stage in the work, the spectra were output on the XY recorder, due to malfunction of the Ortec multi-channel analyser, which could not be repaired. Thus the spectra could not be saved on disc for subsequent data analysis. The figures obtained for the tin:indium ratio are therefore estimates only.

XPS spectra were recorded of the as-received films and of the films after heating at temperatures between 360°C and 1200°C. The tin content as sampled by XPS was estimated. The results are shown in table 10.

Table 10 The experimental tin:indium ratios, n(Sn)/n(In), for ITO films after various heat treatments, determined from comparison of the tin and indium 4d and 3d peaks.

heat treatment	n(Sn)/n(In)	
	4d	3d
as-received	0.086	0.096
1 hr 700°C in vacuo	0.088	0.093
12 hrs 700-1000°C in vacuo	0.076	0.096
12 hrs 1000°C, 2 hrs 1200°C in vacuo	0.083	0.104

In contrast with the results from ceramic samples, the tin contents obtained from the 3d and 4d peaks are quite similar, especially in the as-received film and after mild annealing. Moreover, the tin contents obtained correspond well with the doping level of the pressed target used in film production (9 at.%,n(Sn)/n(In)=0.099). In all samples, there is a small difference between the tin contents given by analysis of the metal 3d and 4d peaks, with the value given by the 3d peaks being the larger; this difference appears to be greatest at the higher annealing temperatures. No significant change in tin:indium ratio was

observed in the XPS spectra after subjecting the films to a mild argon-ion etch using conditions similar to those used to etch the ceramic samples (1kV argon ions at $2\mu Acm^{-2}$ for 5 minutes).

Thus the XPS results appear to show that the films prior to annealing have a reasonably uniform tin distribution. The fact that electrons in the 3d kinetic energy range yield a higher tin content than the corresponding 4d electrons indicates that a small amount of segregation must have occurred. The extent of this segregation appears to increase on annealing the film. However, it is clear that the segregation is not so marked as in the case of the ITO ceramics.

4.6.2 Electron Energy Loss Spectroscopy

HREEL spectra of the ITO films prior to annealing, and after annealing in the preparation chamber of the spectrometer at various temperatures between $360^{o}C$ and $1200^{o}C$ were recorded. Typical spectra obtained in the specular direction with a 25eV electron beam are shown in figure 16. As is the case with the ceramic samples (section 4.4.5), the main feature of the spectra is the broad plasmon peak, which in this case shifts dramatically to higher energy loss as the annealing temperature increases, attaining values considerably higher than those observed in spectra of the ceramics. In all the spectra, peaks due to the excitation of surface optical phonons are observed immediately to the right of the elastic peak. These are strongest in the spectrum of the as-received film, which also shows a strong C-H stretch at around 0.36eV and a C-C stretch (and C-H bend) at around 0.17eV[72], due to hydrocarbon contamination. The intensity in the SO phonon region appears attenuated in the spectra recorded after annealing, and signals due to surface contamination disappear on annealing the film at temperatures above $500^{o}C$.

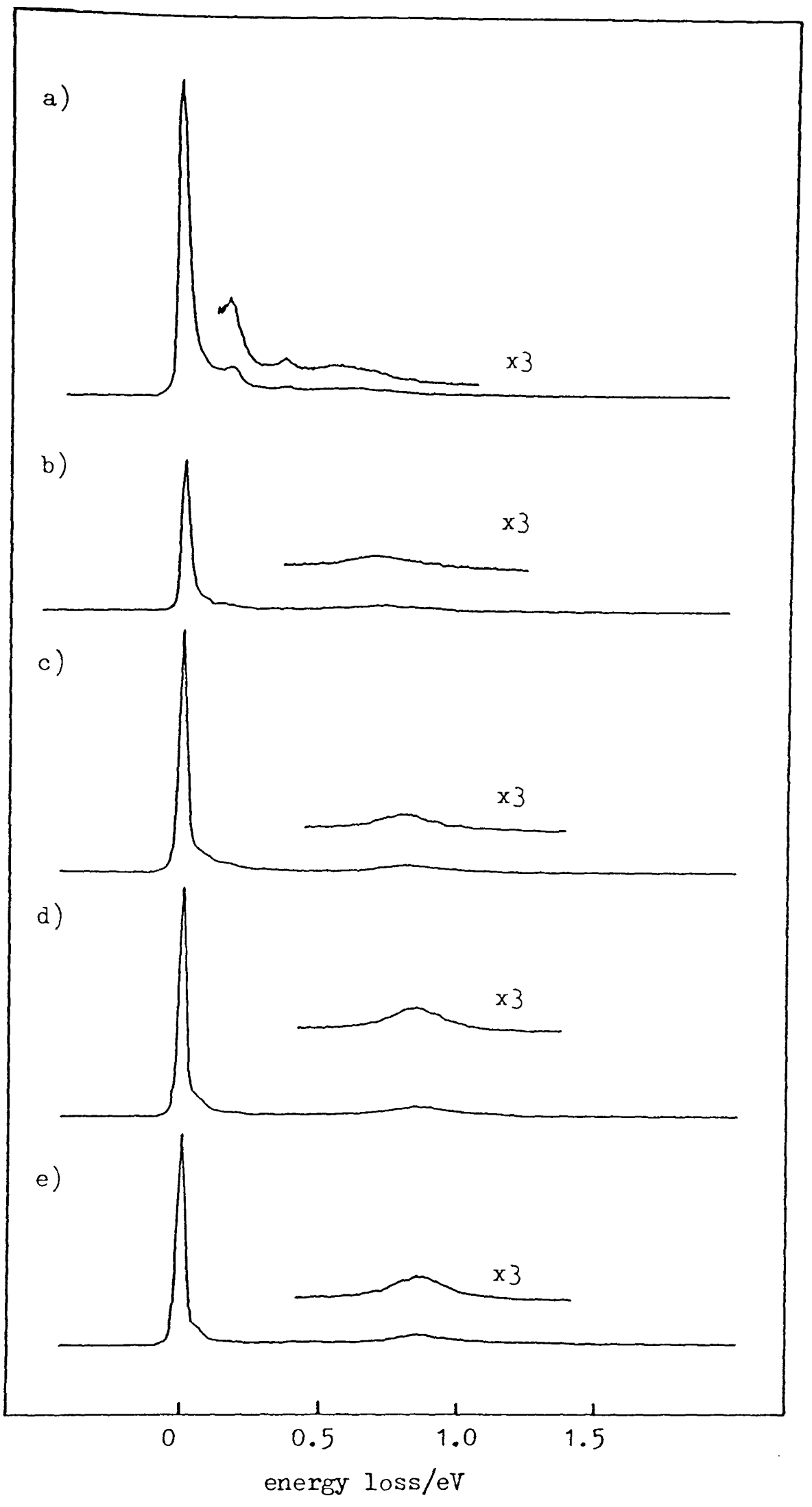

Figure 16 HREEL spectra of ITO thin films excited with a 25eV electron beam. FWHM ∿40meV.
a) the as-received film showng hydrocarbon contamination
b) after 12 hrs resistive heating at 500°C
c) after 1 hr radio-frequency annealing at 700°C
d) after 12 hrs radio-frequency annealing at 700-1000°C
e) after 12 hrs radio-frequency anealing at 1000°C and 2 hrs at 1200°C
All heat treatments were undertaken in vacuo.

Plasmon frequencies at various annealing temperatures are given in table 11, together with the carrier concentrations which give rise to these frequencies. These are calculated using equation (19), making the same assumptions as for the ITO ceramics (section 4.4.5).

Table 11 Plasmon frequencies for the ITO thin films and the free carrier concentrations, n, which give rise to them.

heat treatment	plasmon frequency (eV)	n ($10^{21}\frac{n}{cm}^{-3}$)	n (at.% Sn)
as-received	0.554	0.389	1.25
12 hrs 360°C*	0.559	0.396	1.27
12 hrs 500°C*	0.688	0.600	1.93
1 hr 700°C	0.808	0.828	2.66
12 hrs 700-1000°C	0.856	0.929	2.98
12 hrs 1000°C	0.865	0.949	3.05
12 hrs 1000°C, 2 hrs 1200°C	0.867	0.953	3.06

* resistive heating used; all other treatments used radio-frequency induction.

It can be seen that the free carrier concentration increases with vacuum annealing temperature, to a maximum of $\sim 10^{21} cm^{-3}$, corresponding to 3 at.% Sn substitutionally incorporated. This value corresponds reasonably well with maximum carrier concentrations of $1.3 \times 10^{21} cm^{-3}$ normally observed in such films after heating in a reducing atmosphere, as measured by Hall effect and electrical conductivity[89]. (The value obtained is, however, a little lower than expected - this is discussed in the following section.) It thus appears that heating in vacuo has the same effect as the reducing treatment used by Köstlin et al[89,107,119], i.e. it dramatically increases the free electron content of the films. Note, however, that the maximum free electron content observed corresponds to only around 3 at.% substitutionally incorporated

tin, which is substantially less than the tin concentration sampled by XPS. We thus conclude that at these doping levels, not all tin atoms are electrically active. This is again in accord with the findings of the above authors[89,107,119]. The decrease in intensity in the SO phonon region with increasing carrier concentration is expected, as the free electrons tend to screen out the dielectric response of the crystal to the potential of the incoming electron, leading to diminished scattering intensity[87].

4.6.3 Optical Transmission

The effect of the vacuum annealing process on the optical properties of films was investigated by recording the optical transmission of the samples (in the range 2600-185nm) both before heating, and after annealing at the highest temperature used (1200°C). The resulting traces, showing the region where the samples transmit strongly are shown in figure 17. In both cases, the transmission is very high in the visible region of the spectrum, attaining values of around 80%. Distinct interference fringes at high transmission as observed by other authors[88,89,107] are not seen, as the film thickness is small compared with the wavelength of the incident light. The observed transmission is, however, in very good agreement with that recorded by Fan and Bachner[88] from a "thin" (0.12μm) film prepared by the same technique. At around 1μm, the transmission drops - this corresponds with a rise in reflectivity (as illustrated in figure 2[88]). This effect is determined by the plasmon oscillation of the free electrons, and as the two samples demonstrate, the transmission edge shifts to shorter wavelengths with increasing annealing temperature, in the same way as the plasmon observed in HREELS.

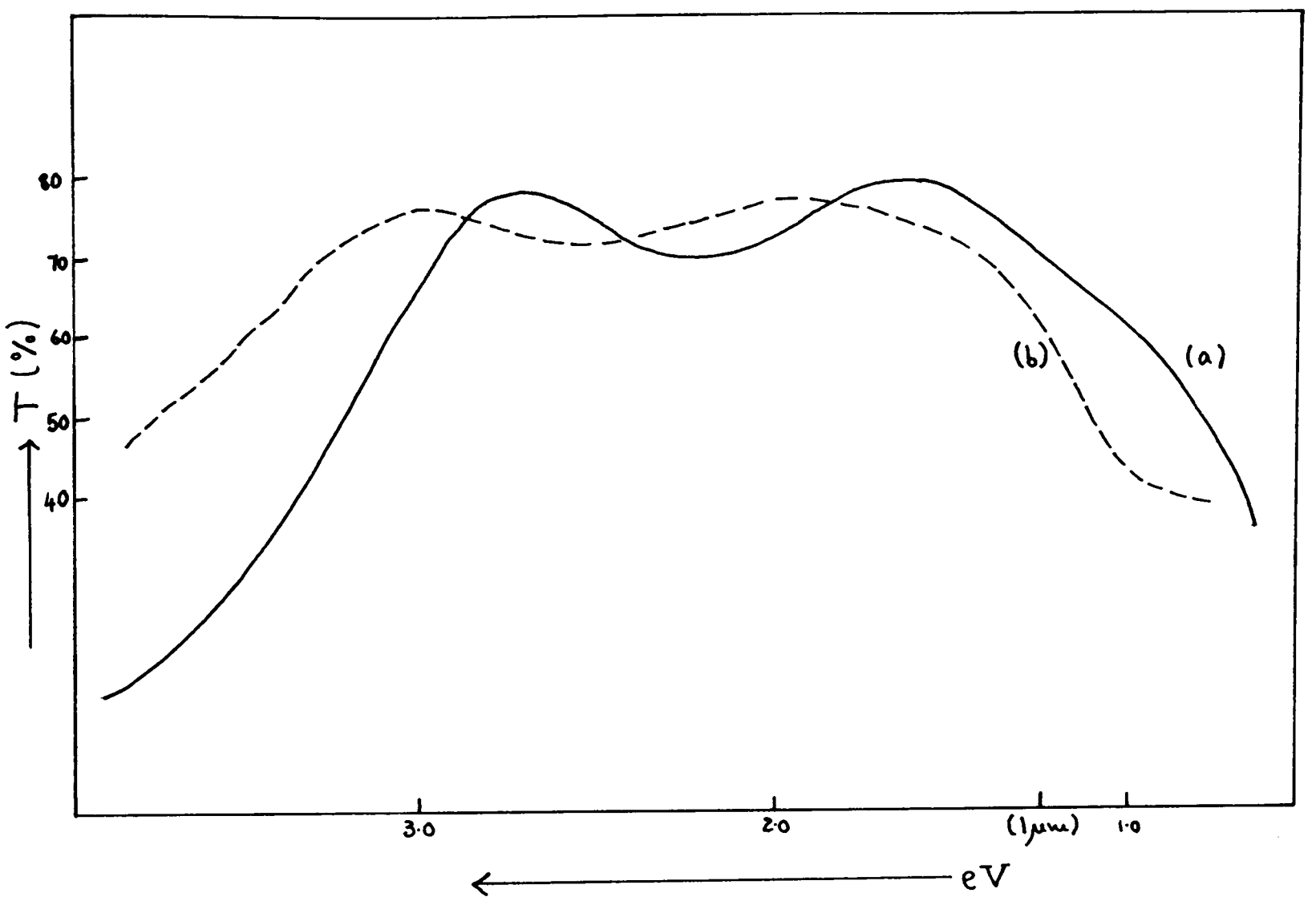

Figure 17: Optical transmission for the ITO thin films
a) prior to annealing
b) after annealing in vacuo for 12 hrs at 1000°C, then 2 hrs at 1200°C

As the penetration depth of the technique must be of the order of the wavelength of the light employed, i.e. large compared with HREELS, we expect the plasmon to be observed at the bulk loss condition, when the real part of the dielectric function becomes zero,

$$\mathrm{Re}(\varepsilon(\omega)) = 0 \qquad (21)$$

As we have seen, the surface plasmon loss as observed in HREELS corresponds to the loss condition given in equation (15). As was shown in Chapter 1 section 1.3.2, this leads to the following relationship:

$$\omega_{sp}/\omega_p = [\varepsilon_\infty/(\varepsilon_\infty+1)]^{1/2} \qquad (22)$$

where ω_{sp}, ω_p are the surface and bulk plasmon frequencies, and ε_∞ is

the high frequency dielectric constant. Again taking ε_∞=4 (in accord with the work of Köstlin et al[89,107]), we have

$$\omega_{sp} = 0.894\omega_p \qquad (23)$$

Thus we expect the plasmon frequency determined from HREELS to be lower than that from optical transmission. The plasmon frequency can be estimated from the transmission spectra by noting that this frequency, as determined from analysis of the optical constants by Köstlin et al[89] occurs very close to the intersection of the transmission and reflectivity curves. This occurs at around 1/3 the height of the transmission edge. The estimated plasmon frequencies for the two traces are shown in table 12, together with the HREELS surface plasmon frequencies observed from the same films. Also shown is the surface plasmon frequency from optical transmission using equation (23). The carrier concentration giving rise to the bulk plasmon frequency from optical transmission is calculated by equating the bulk loss condition (21) to equation (18).

Table 12 Bulk plasmon frequencies for the ITO thin films from optical transmission, together with predicted and experimental surface plasmon frequencies.

heat treatment	bulk plasmon frequency (eV)	surface plasmon frequency (eV)	
		OT*	HREELS
as-received	0.70[a]	0.63	0.554
12 hrs 1000°C, 2 hrs 1200°C	1.10[b]	0.98	0.867

* via equation (23)

[a] corresponding to a free carrier concentration of $0.50\times10^{21}cm^{-3}$ or 1.60 at.% Sn

[b] corresponding to a free carrier concentration of $1.23\times10^{21}cm^{-3}$ or 3.95 at.% Sn

It can be seen that in both cases the surface plasmon frequency predicted from optical transmission is higher than the surface plasmon frequency found in HREELS. After vacuum annealing the film, this difference is particularly dramatic. Moreover, the carrier concentration given by the bulk plasmon frequency from transmission after annealing corresponds almost exactly with the optimum concentration of $1.3 \times 10^{21} cm^{-3}$ observed by Köstlin et al[88,89,107,119]. This concentration is consistent with ~4 at.% Sn substitutionally incorporated, in accord with the solubility limit of tin in indium oxide (section 4.3.2i)). Thus it appears that the plasmon frequency from optical transmission may yield the most realistic estimates of the bulk free carrier concentration. (Those obtained from the HREELS measurements of the preceeding section, although of the right order of magnitude, yield rather lower values.)

A surface plasmon (in addition to the bulk plasmon) may be observed in the spectral reflectance of thin films having rough surfaces[89]. However, the resulting surface and bulk plasmon frequencies in this case do satisfy equation (22), which results from a simple Drude model for the dielectric function[89]. Thus it appears that HREELS and optical transmission give different plasmon frequencies in this case. Possible reasons for this rather startling result are discussed in section 4.7.3.

4.7 Discussion and Conclusions

4.7.1 Comparison with Antimony-Doped Tin Dioxide Ceramics

The behaviour of the ITO ceramics shows marked differences from that observed in previous work by the author[82,91] and others[92,93] on antimony-doped tin dioxide ceramics.

Ceramics having antimony doping levels between 0.1 and 3 at.% Sb (corresponding to the solubility limit of antimony in the rutile structure of SnO_2[91,139,140]) were prepared by Dr.P.J. Tavener using a coprecipitation technique similar to that used for the ITO ceramics[92]. The precipitates were calcined in air at 1000°C for fourteen days. Initial characterisation of the samples by XRD, TEM, SEM and AES revealed that all the samples consisted of a single, well crystallised rutile phase, having a homogeneous concentration of antimony consistent with the nominal doping level.

Examples of the Mg KαXPS spectra obtained in the metal 3d regions are shown in figure 18. It can be seen that the amount of antimony at the surface of all the samples is large compared with the nominal doping levels. Analysis of the spectra showed pronounced surface segregation for all samples. Comparison of antimony:tin ratios for 3d and 4d peaks indicated that antimony enrichment was restricted to the top few atomic layers, as for the ITO ceramics[92]. This model was therefore adopted in the calculation of surface occupancies, which revealed that in the sample containing 3 at.% antimony, all surface cation sites were occupied by the dopant. Segregation was therefore more pronounced than in the ITO ceramics. There was no evidence of sub-surface depletion at the calcining temperatures used (1000°C), but this only became experimentally evident in the ITO ceramics at temperatures in excess of 1000°C. The heat of segregation obtained from the surface occupancy values was found to vary from $-29.5 kJmol^{-1}$ to $-23.5 kJmol^{-1}$ as the antimony content increased from 0.1 to 2.5 at.%. This decrease was seen as consistent with increased cation-cation repulsion as the amount of antimony segregated to the surface increased.

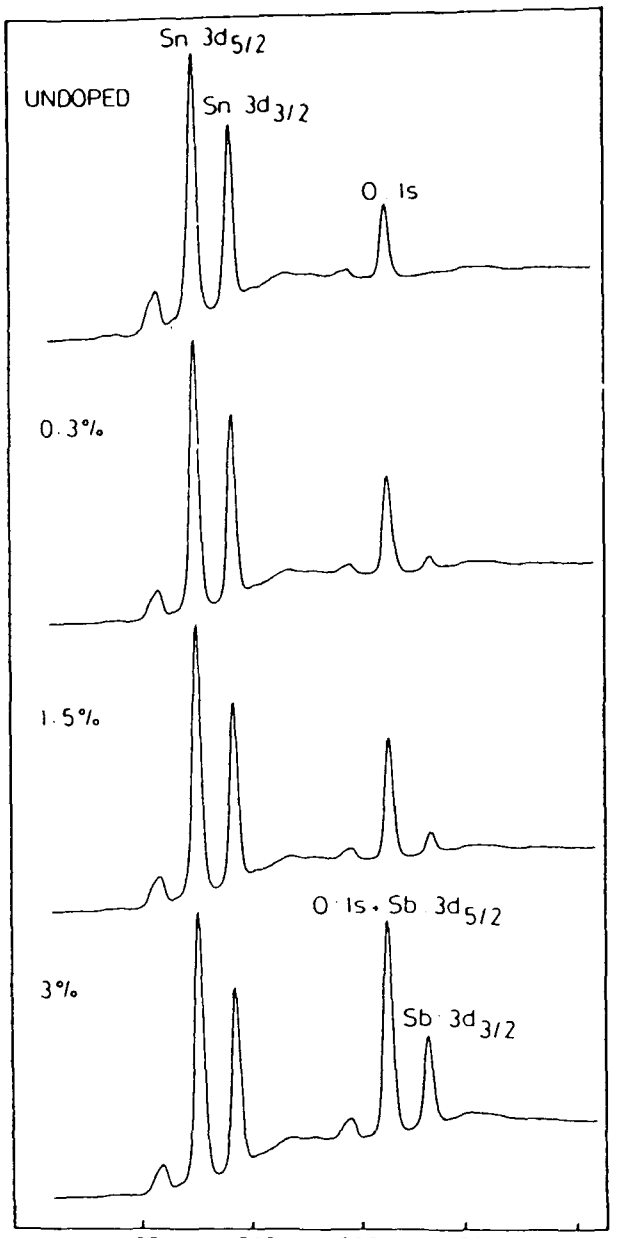

Figure 18: Examples of Mg Kα XPS of antimony-doped tin dioxide ceramics in the metal 3d region. Peaks to the left of the main features are due to satellite radiation.

Typical He I UPS spectra are shown in figure 19. These show similar features to those of the ITO ceramics (section 4.4.4), the two main features being due to excitation from the O:2p valence band, and the secondary electron background. However, in marked contrast with the behaviour of the ITO system, it can be seen that the intensity of the conduction band increases with nominal doping level. Analysis of the spectra revealed that this increase was linear, and that the intensity of the conduction band was consistent with all the incorporated antimony being electrically active and donating one electron to the conduction

band. Thus in this case, UPS probed the bulk nominal conduction electron concentration over the composition range studied, in contrast with the ITO ceramics.

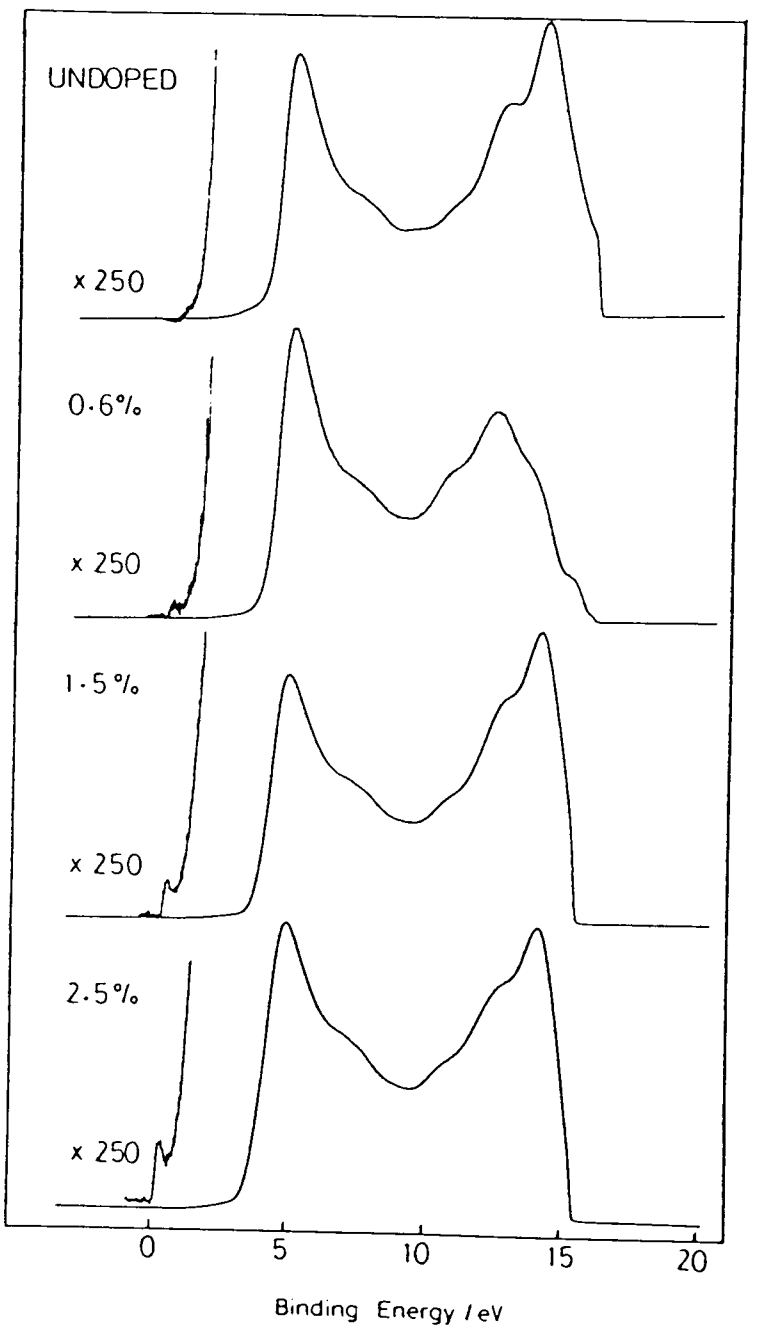

Figure 19: He I photoelectron spectra of antimony-doped tin dioxide ceramics for various doping levels. Binding energies are relative to the Fermi energy.

HREEL spectra obtained from the antimony-doped tin dioxide ceramics are shown in figure 20. The plasmon peak, although not as prominent as that observed from the ITO ceramics, moves to higher energy loss with increasing doping level. Moreover, as demonstrated by figure 21, the

observed plasmon frequency obeys equation (19), suggesting that HREELS probes a free electron concentration consistent with all antimony being substitutionally incorporated. The value obtained from the intercept for ω_o (the single-particle donor level to conduction band excitation energy) is 0.173eV, in good agreement with a literature value of 0.15eV[141]. This contrasts with the results for the ITO system, which suggest that the free carrier concentration sampled by HREELS is markedly less than the nominal tin content for samples containing 4 and 6 at.% Sn.

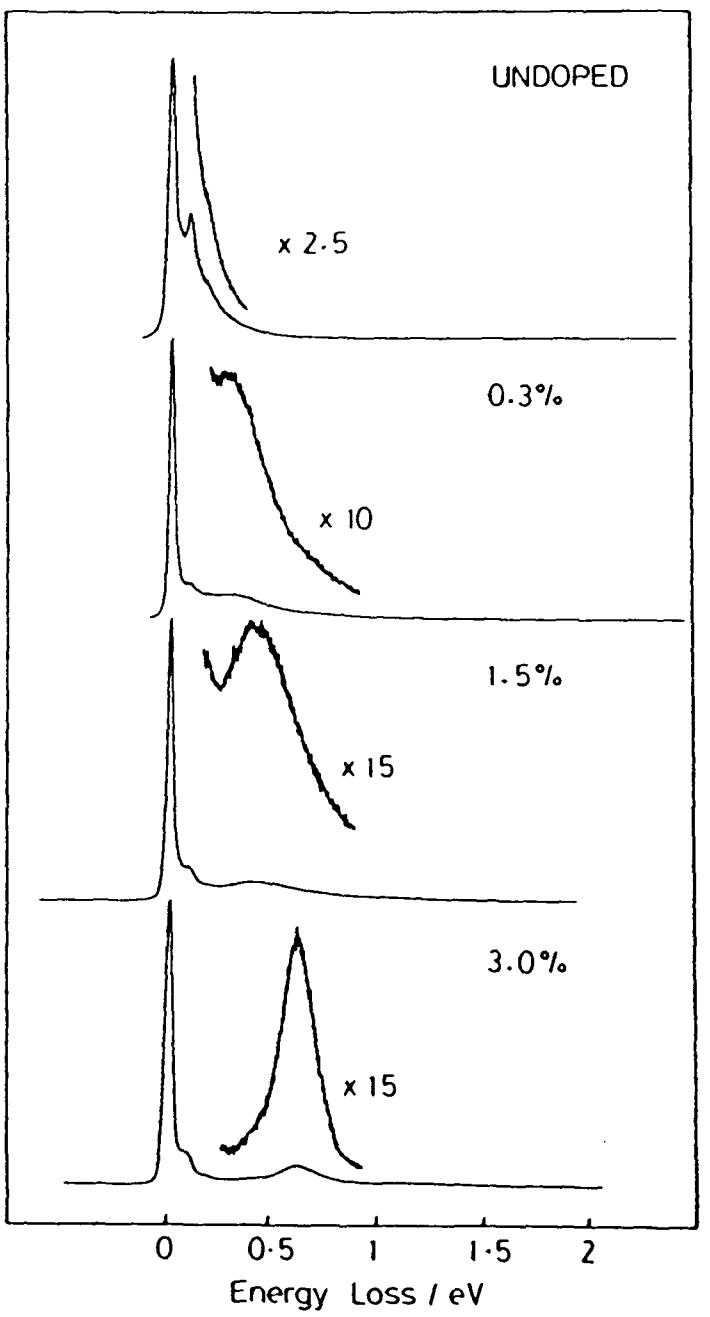

Figure 20: HREEL spectra of antimony-doped tin dioxide ceramics excited with a 25eV electron beam (FWHM ∿ 50meV).

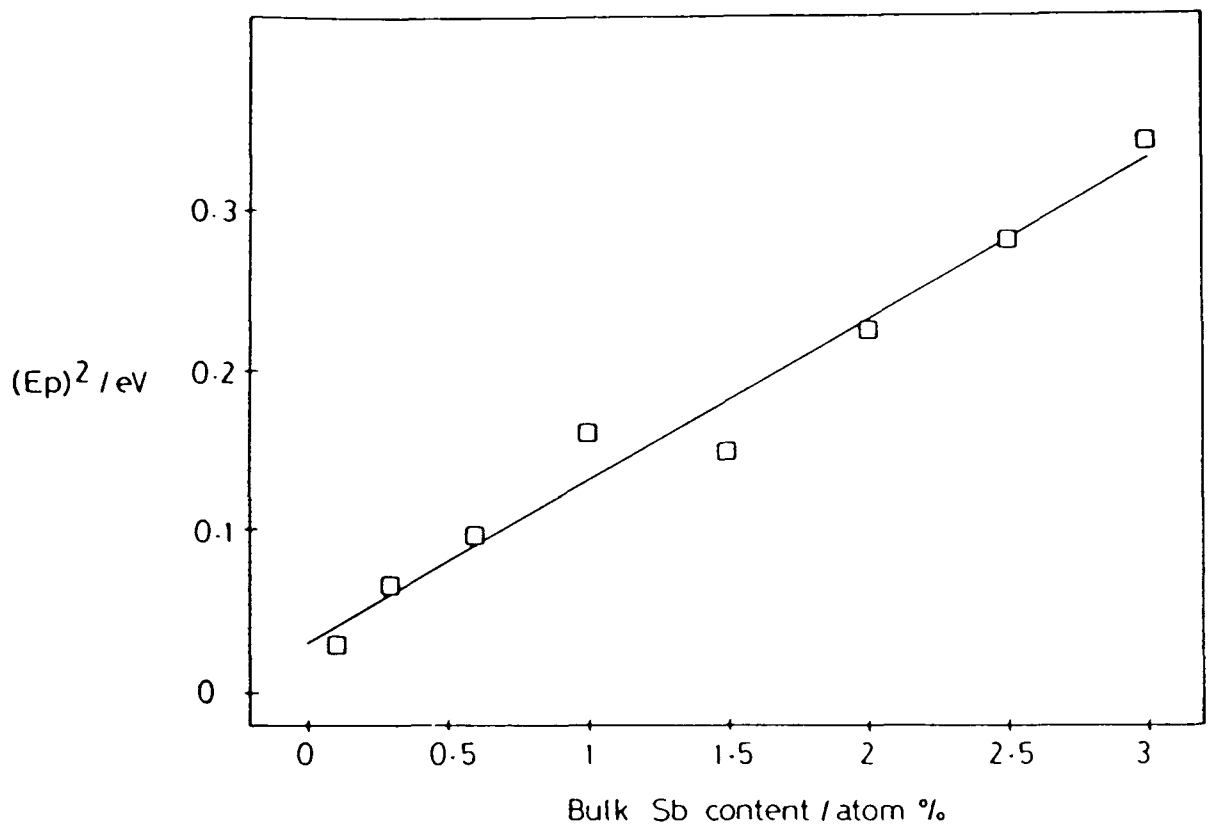

Figure 21: Variation of the square of the plasmon frequency with bulk nominal antimony content in antimony-doped tin dioxide ceramics.

The model therefore proposed for the tin dioxide ceramics was one in which there is marked segregation of antimony to the topmost surface layer, followed by an abrupt return to the bulk composition (in which all the incorporated antimony donates one electron to the conduction band). Moreover, the high concentration of antimony in the surface layer cannot be contributing electrons to the conduction band, as if this were the case, the conduction electron concentration sampled in HREELS and UPS would be around a factor of 10 higher. Thus it is envisaged that the asymmetric environment of the surface antimony cations leads to strong s-p hybridisation which splits a local lone-pair-like surface state off from the bulk conduction band. The gas phase UPS spectrum of the "model" compound Sb_4O_6 [142] suggests that Sb(III) lone-pair states overlap significantly with O:2p states. Thus

it is expected that the surface state is obscured by the O:2p valence band in UPS spectra of the ceramics. However, UPS spectra of single crystal SnO_2[82] provided evidence for the existence of this surface state. Tin dioxide is naturally oxygen deficient, so that Sb(III) ions may be readily accommodated at the surface due to the flexibility in surface oxygen content. The ease of accommodation of Sb(III) ions with their lone pairs at the surface of the material was seen as a force driving the segregation, as such ions would not readily adopt the octahedral coordination of the bulk SnO_2 structure.

4.7.2 The ITO System

It has been demonstrated that the properties of well-equilibrated, ceramic samples of ITO are considerably different from those of ITO thin films, as commonly prepared. XPS results for the ITO ceramics show that there is pronounced segregation of tin to the surface of the material, with a considerable proportion of surface cation sites being occupied by tin in most cases (table 5). In contrast, in the thin films, although there is some evidence for segregation, particularly after vacuum-annealing the films at temperatures up to 1200°C, it is clear that rather less surface segregation has occurred. The degree of surface segregation in the ceramic samples decreases with increasing calcining temperature, consistent with an exothermic heat of segregation. This has been estimated, from XPS results, to be around $-20 kJmol^{-1}$.

The XPS results for the ceramics may be fitted by a model in which, in addition to a high tin concentration in the surface layer, there is a layer depleted in tin immediately below the surface. In addition, the free carrier concentration in the ceramics sampled by UPS and HREELS is considerably less than the bulk nominal doping level for samples

containing 4 and 6 at.% tin. This discrepancy is not explained by the concentrations of a separate tin dioxide phase present in some samples. The free carrier concentration sampled by HREELS in vacuum annealed ITO films is considerably higher than that in the ceramics, and corresponds well with the solubility limit of tin in indium oxide as determined by XRD. (The small concentration of oxygen vacancies present in In_2O_3 as prepared is ignored throughout, as the maximum resulting free carrier concentration is at least an order of magnitude less than that introduced by tin doping at the levels used[121,143-5].)

The penetration depth, λ, of the surface plasmon in HREELS is governed by

$$\lambda = v/\omega \qquad (24)$$

where v is the velocity of the electron beam normal to the surface, and ω is the plasmon frequency. This is about 30Å using a 25eV beam to probe a 0.5eV excitation. The effective sampling depth in UPS is determined by the electron path length in the relevant kinetic energy regime, and is probably of the order of 5-10Å. As has been shown, in XPS, the electron pathlength is 10-15Å. This gives an order of surface sensitivity as shown:

$$\underset{\text{increasing surface sensitivity}}{\text{UPS} > \text{XPS} > \text{HREELS}}$$

Superficially, then, it is difficult to reconcile the observed surface enrichment in tin with the low conduction electron concentration probed by UPS and HREELS. We may conclude that tin enrichment does not arise from a surface "phase" which is thick compared with the sampling depths of UPS, XPS and HREELS. If this were the case, then each tin ion in a regular cation site would be expected to donate one electron to the conduction band, giving a surface free carrier concentration much higher than that found experimentally. The fact that the tin:indium ratio from

XPS spectra in different kinetic energy ranges is not constant confirms this.

Thus, it appears that segregated tin ions do not contribute electrons to the conduction band. Segregation of the separate tin dioxide phase known to be present in some samples would have this effect. However the presence of a bulk tin dioxide phase at the surface would not lead to the electron energy dependent XPS intensity ratios observed. A localised surface state similar to that postulated for the antimony-doped SnO_2 ceramics may then be proposed. Again, we may suppose that the asymmetry of the surface environment of the tin ions leads to s-p hybridisation, splitting off a local lone-pair-like surface state from the conduction band. Thus, provided segregation is restricted to the topmost cation plane, segregated tin ions do not contribute electrons to the conduction band. As has been discussed (section 4.2), In_2O_3 is naturally somewhat reduced, the bixbyite structure allowing for considerable flexibility in oxygen content. This would allow for the accommodation of Sn(II) ions at the surface of the material without development of a surface charge. If this model is correct, then, as we would intuitively expect tin to have a lesser tendency than antimony to show an (N-2) valency, we expect the extent of segregation to be less, and the heat of segregation to be smaller than for the antimony-doped tin dioxide ceramics. This is found to be the case.

In contrast, however, with the tin dioxide ceramics, HREELS probes a carrier concentration lower than the bulk nominal doping level in most cases. Two possible explanations may be considered. Either HREELS is sampling a layer of low tin concentration, or the bulk free carriers are being removed by some trapping effect. If the latter is the case, it may be supposed that the prolonged calcining of the ceramic samples in air had the effect of introducing an uncontrolled amount of oxygen into

the materials as described by Köstlin et al[89,90,107,119] and discussed in section 4.2. Interstitial oxygen incorporated in the vacant tetrahedral sites of the bixbyite structure produces a strong trapping effect, neutralising the substitutionally incorporated tin donors, $In_{2-\delta}Sn_{\delta}^{\cdot}(O_i'')_{\delta/2}O_3$. We may suppose that defect "clusters" as proposed by Frank and Köstlin[119] are present. These clusters contain interstitial oxygen atoms, and have the effect of removing free carriers. The clusters proposed are $(Sn_2^{\cdot}O_i'')$, $(Sn_2O_4)^x$ and $(Sn_2^{\cdot}O_i'')(Sn_2O_4)^x$, as discussed in section 4.2. It was hoped that information about the local environment of the tin atoms, and hence about the possible existence of such clusters might be gained using ^{119}Sn nmr. However, it was found that no signals distinguishable from side bands could be obtained from the ceramic samples.

The free carrier concentration sampled by HREELS in the thin films rose dramatically on vacuum annealing in accordance with the trapping model. Thus our results on thin films are entirely consistent in this way with those of Köstlin, and provide further evidence for the trapping effect of excess oxygen introduced during film preparation. However, we must note that the ceramic samples were also subjected to high temperature vacuum annealing overnight in order to produce spectroscopically clean samples. Even after this procedure, low free carrier concentrations were obtained. It seems surprising that it should be more difficult to remove excess oxygen from the ceramic samples than from the thin films. Therefore, in the case of the ceramics, it seems appropriate to consider the alternative explanation for the low carrier concentrations observed.

If, in the ceramic samples, HREELS is sampling a layer of low tin concentration, this layer must have a thickness at least of the order of the penetration depth of the technique, i.e. $\sim$ 30Å. However, the presence of a partly-depleted layer would be consistent with the XPS

results from the ceramic samples, which can only be explained by such a layer. This layer might be created if, as the sample heating temperature was raised, some slight evaporation of tin from the surface was occurring. In this case, superimposed on the segregation occurring in the equilibrated samples would be a dynamic effect due to the evaporation, resulting in a loss of tin in the layers close to the surface. This evaporation must be small, as TEM studies (section 4.3.2ii)) have established that the tin concentration in the samples is consistent with the nominal doping level. The discrepancy between the carrier concentration given by HREELS and the nominal doping level is greatest at the highest calcining temperature (1360^{o}C), which would tend to support this model. At this temperature, there is some evidence of vapour transport of material during heating as small crystallites were found to have formed during firing. However, this may be due to transport of the bulk material, as pure, undoped In_2O_3 is relatively volatile (c.f. SnO_2) and is stabilised by tin doping.

Thus there is a certain amount of evidence to support the existence of a sub-surface depletion layer in the ceramics, the evidence from XPS and HREELS taken in conjunction being particularly powerful. A physical picture of how such a layer may arise may also be envisaged. However, this does not rule out the possibility of the low free-carrier concentration observed being due to a complex combination of part-depleted layer effects and effects due to donor trapping by interstitial oxygen not removed by vacuum annealing.

The abnormal surface composition of the ceramics contrasts with that of the thin films, where little segregation was observed. This confirms the view that in the films (in contrast with the ceramics), thermal equilibrium has not been attained. Fan and Goodenough[116] have suggested that a tin-rich surface layer is only found at the surface if the substrate temperature is high enough relative to the film deposition

rate during manufacture to permit equilibrium to be established. Jarzebski[121] cites incomplete attainment of thermal equilibrium as a major cause of discrepancies in the literature in the properties of films prepared by different techniques. In such cases, the electrical properties of the films depend on factors such as the history of the samples, the oxygen pressure, heat treatment temperature and time, and the nature of other gases present in the ambient atmosphere[102,105,146-152].

The optical transmission of the films suggests that, in vacuum annealed samples, tin is substitutionally incorporated up to its solubility limit. However, there is a startling discrepancy between the plasmon frequency measured by HREELS and that from transmission measurements. This forms the subject of the final section of this chapter.

4.7.3 The Surface/Bulk Plasmon Frequency Discrepancy

It has so far been assumed that the surface plasmon frequency from HREELS is correctly given by equation (19). As ω_o in this case is negligible[131], we obtain

$$\omega_{sp}^2 = ne^2/\varepsilon_o(\varepsilon_\infty+1)m^* \qquad (25)$$

This equation clearly does not give a surface plasmon frequency consistent with the bulk plasmon frequency from optical transmission in the case of the ITO films. Four possible reasons may be considered:

i) The Drude dielectric function used to derive the equation is not realistic in the region where $Re(\varepsilon(\omega))=-1$. However, this seems very unlikely as the approximation is widely and successfully used. In particular, we have already noted that the model has been used

extensively to explain the optical and electrical properties of ITO thin films[88,89,107,121,138].

ii) The high frequency dielectric constant used is too high. This seems unlikely, as ε_∞ would have to be reduced to unrealistically low values to bring the surface and bulk plasmon frequencies into coincidence via equation (22).

iii) The electron effective mass m^* used is too high. This could be caused by band narrowing at the surface. However, any such effect expected theoretically should occur very close to the surface, and should not extend far enough into the bulk to explain the observed phenomenon[153].

iv) There is some depletion of the near-surface free-carrier concentration. If this is the case, then it must be regarded as a different effect to that observed in the ceramic samples, as the surface plasmon frequency observed, though low, is very much higher than those found for ceramics having comparable doping levels. It is also not possible in this case that such an effect is a dynamic one caused by slight evaporation of surface tin.

In order to investigate the last possibility further, we may consider a model for the surface region as shown in figure 22. The material is regarded as consisting of a semi-infinite substrate of dielectric constant $\varepsilon_b(\omega)$, upon which is a layer of thickness d characterised by a dielectric constant $\varepsilon_s(\omega)$.

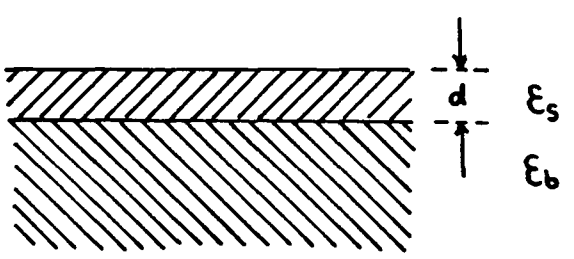

Figure 22: The model used to drive the loss function $P(k,\omega)$ of equation (26).

Expressions for the loss function, $P(\underline{k},\omega)$ have been derived for this generalised two layer model[37,154]:

$$P(k,\omega) = (2\hbar k/\pi)[1+n(\omega)]\,\mathrm{Im}\{-1/(\tilde{\varepsilon}(k,\omega)+1)\} \tag{26}$$

where

$$\tilde{\varepsilon}(k,\omega) = \varepsilon_s(\omega)[1+\Delta(\omega)\exp(-2kd)]/[1-\Delta(\omega)\exp(-2kd)] \tag{27}$$

with

$$\Delta(\omega) = [\varepsilon_b(\omega)-\varepsilon_s(\omega)]/[\varepsilon_s(\omega)+\varepsilon_b(\omega)] \tag{28}$$

and

$$n(\omega) = [\exp(\hbar\omega/k_BT)-1]^{-1} \tag{29}$$

Let us assume that the surface layer contains no free carriers. In this circumstance we may approximate the dielectric constants as follows:

$$\varepsilon_s(\omega) = \varepsilon_\infty \tag{30}$$

$$\varepsilon_b(\omega) = \varepsilon_\infty[1-(\omega_p^2/\omega^2)] \tag{31}$$

in accordance with the Drude formula, where ω_p is the bulk plasmon frequency. Such a "depletion" layer may exist at the surface of a semiconductor even in the absence of adsorbates, due to the presence of surface states which bend the conduction and valence bands upwards at the surface on n-type material[155]. The upward band bending results in a space charge layer which is depleted of free carriers. A short description of such effects is given in Chapter 5 which gives preliminary results for n-type systems where such layers were deliberately created by adsorption of Cl_2 and NO_2. "Dead" layers have also been postulated at semi-conductor surfaces in the absence of band bending[156]. In such layers, free carriers are present, but those in the surface layer are plasmon inactive.

On substituting (30) and (31) into (28), we obtain

$$\Delta(\omega) = [1-(2\omega^2/\omega_p^2)]^{-1} \tag{32}$$

The loss condition in HREELS is given by

$$\mathrm{Re}(\tilde{\varepsilon}(k,\omega)) = -1 \tag{33}$$

Substituting (32) into (27) and equating with (33), we obtain, after some algebra:

$$2\omega^2 = \omega_p^2[1+\eta\exp(-2kd)] \tag{34}$$

where $\eta = (\varepsilon_\infty - 1)/(\varepsilon_\infty + 1)$.

As the depletion layer becomes infinitely thin, we have

$$\lim_{d \to 0} \omega^2 \longrightarrow \omega_p^2[\varepsilon_\infty/(\varepsilon_\infty+1)] \tag{35}$$

which corresponds correctly with equation (22).

For an infinitely thick layer we have

$$\lim_{d \to \infty} \omega^2 \longrightarrow \omega_p^2/2 \tag{36}$$

Thus, if a surface depletion layer of this kind exists, the observed surface plasmon frequency could only be shifted from ω_p by an amount $(\omega_p - \omega_p/\sqrt{2})$. In practice, the shift observed will obviously be less than this, as at infinite thickness, the intensity of the plasmon will be completely attenuated. Thus, whilst this model can adequately explain the plasmon frequency discrepancy observed in the ITO thin films, it does not explain the lower plasmon frequencies observed in the ceramics. In the latter case, the model envisaged is one in which the free carrier concentration sampled by HREELS is reduced, either by trapping effects or by evaporation of surface tin, yielding a low plasmon frequency consistent with the carrier concentration sampled. In contrast, in the model considered here, we are considering the effect on the bulk plasmon of a thin surface layer which contains no carriers, and hence has no observable plasmon frequency. Such a completely depleted layer would intuitively be expected to be rather thin in this case, as it must have the effect of diminishing the intensity of the plasmon, which is nontheless still clearly observed.

The total loss probability in HREELS is given by

$$P_{tot} = (\pi e^2/2\hbar v)[(\tilde{\varepsilon}(0)-1)/(\tilde{\varepsilon}(0)+1) - (\tilde{\varepsilon}(\infty)-1)/(\varepsilon(\infty)+1)] \qquad (37)$$

(this is obtained by integrating equation AII(10).)

We may obtain values of $\tilde{\varepsilon}(0)$ and $\tilde{\varepsilon}(\infty)$ using equation (27):

$$\tilde{\varepsilon}(0) = \mu\varepsilon_\infty \qquad (38)$$

$$\tilde{\varepsilon}(\infty) = \varepsilon_\infty \qquad (39)$$

where $\mu=(1+\exp(-2kd))/(1-\exp(-2kd))$.

Substituting in (37) we obtain

$$P_{tot} = (\pi e^2/2\hbar v)[(\mu\varepsilon_\infty-1)/(\mu\varepsilon_\infty+1) - (\varepsilon_\infty-1)/(\varepsilon_\infty+1)] \qquad (40)$$

A complete theory based on the two layer model requires a numerical integration over the wave-vector, k. In the present model we have simplified the calculations by assuming that the most probable k value, equal to ω/v, contributes to the spectrum.

Values of ω^2 and P_{tot} from (34) and (40) were calculated as a function of kd, assuming a value of ε_∞ of $4^{89,107}$ as previously. The results are summarised in figure 23. It can be seen that the square of the plasmon frequency, ω^2, decreases at roughly the same rate that the plasmon intensity is attenuated. Thus the model predicts that a significant change in frequency will be observed before the plasmon intensity is completely attenuated. This is in accord with the observation of a reasonably intense plasmon in HREEL spectra from the thin films. An important prediction of the model is that the loss probability should be lowered in the presence of the overlayer from its value of roughly 0.65 ($P_{tot}/(\pi e^2/2\hbar v)=0.4$) in the absence of the overlayer. Unfortunately, as has been stated, spectra at this stage of the work could not be stored on disc due to malfunction of the Ortec multi-channel analyser. Thus quantitative analysis of the HREEL spectra is not possible. However, examination of figure 16 shows that the area

of the plasmon peak relative to that of the elastic loss is certainly lower than the predicted value. From the spectrum for the film vacuum annealed at the highest temperature (16e)), we may estimate that the plasmon intensity is only around 1/5 the intensity of the elastic peak. Using a ratio of 0.2 ($P_{tot}/(\pi e^2/2\hbar v)=0.12$), we may predict the bulk plasmon frequency which will be observed in optical transmission from figure 23, putting $\omega=0.867$ as determined from HREELS (table 11). The value obtained is $\omega_p=1.15$eV, in excellent agreement with the value of 1.1eV determined from optical transmission (table 12). A similar procedure for the as-received film (figure 16a)) yields a predicted bulk plasmon frequency of 0.74eV, again in good agreement with the value of 0.7eV from optical transmission.

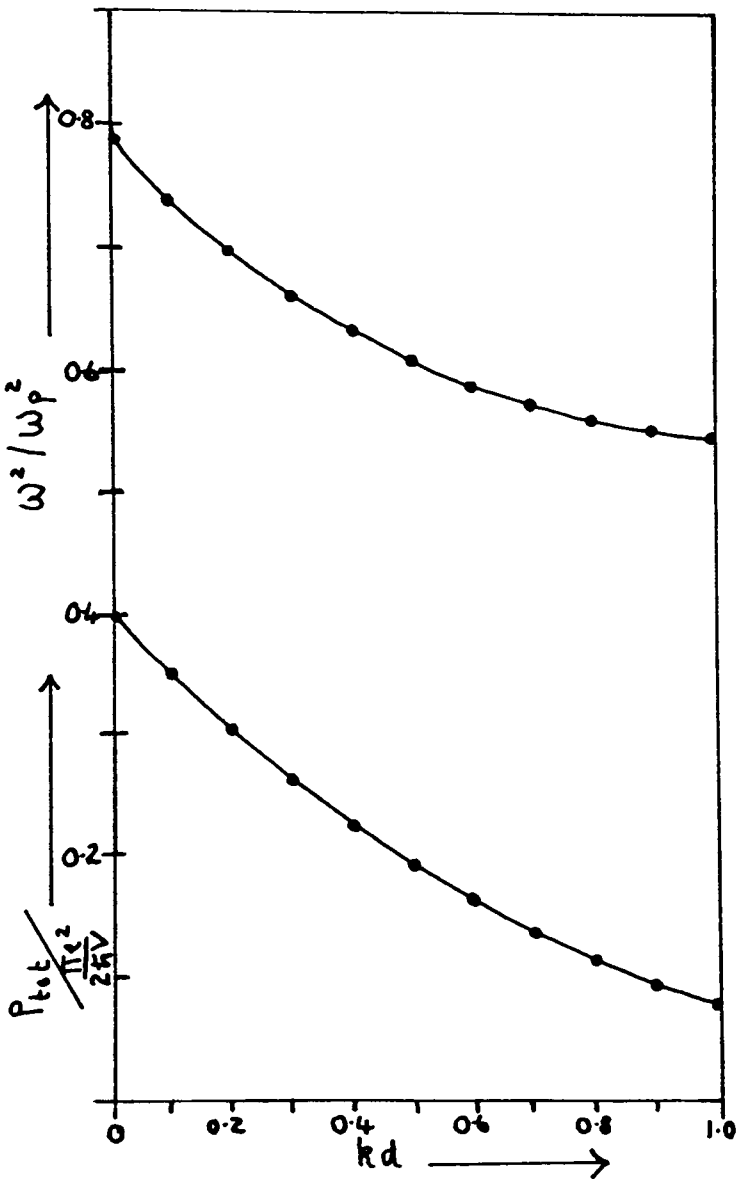

Figure 23: The shift in plasmon frequency and attenuation in plasmon intensity as a function of kd predicted using a depletion layer model for ITO thin films. The upper trace shows the variation in ω^2/ω_p^2, while the lower curve shows $P_{tot}/(\pi e^2/2\hbar v)$.

The value of kd obtained from figure 23 corresponding to ω_p=1.15eV gives a value for d, the depth of the depleted layer of ~10Å (k=ω/v=1/λ, equation (24)). Thus the two layer model adequately describes both the shift in the observed surface plasmon frequency, and its attenuation for the thin films.

The predictions of this model may be contrasted with those of the model suggested for the ceramic samples, where we envisage that a layer partly depleted in carriers exists below the surface. The depth of this layer would be at least of the order of the sampling depth of HREELS, so would be thick compared with the fully depleted layer described above. The two models will be denoted depletion layer model (DLM) and partly depleted layer model (PDLM).

i) The DLM suggests that, for the thin films, no free carriers should be present in the top 10Å of the material. The PDLM suggests that a low concentration of free carriers should be observable at the surface, consistent with the UPS results from the ceramics.

ii) The DLM predicts that the surface plasmon frequency observed should shift in the way shown in figure 23 with increasing depth of the layer. The maximum theoretical shift should be (ω_p-ω_p/$\sqrt{2}$). Shifts consistent with this model are observed in the HREELS of the thin films. This type of shift has also been observed in studies of hydrogen-ion bombarded GaAs (100)[155], and in XPS work on oxide layers on Mg[157]. The two layer model has been used with success to fit results for both depletion layers (resulting from H_2^+/H^+ bombardment of GaAs (100)[155]) and accumulation layers (created by growing a conducting Ag overlayer on GaAs (100)[158]).

In the PDLM, the surface plasmon frequency observed is due to the free carriers present in the partly depleted layer itself, provided that the thickness of this layer is of the order of the penetration depth of the technique (~30Å) or larger. The frequency

is then predicted by the free-carrier concentration sampled in accordance with equation (25), and hence much lower frequencies may be obtained at the surface, as found for the ceramic samples. The relationship between surface and bulk plasmon frequencies should be given by equation (22).

iii) In the DLM, the intensity of the surface plasmon is attenuated by the presence of the depleted layer in accordance with figure 23. Attenuation consistent with this model is observed in the thin film samples.

In the PDLM, no such attenuation should occur, and the loss probability should be given by equation (37). Assuming $(\tilde{\varepsilon}(0)-1)/(\tilde{\varepsilon}(0)+1)\backsim 1$ (as $\varepsilon(0)$ will be large), this gives $P_{tot}\backsim 0.6$ for ITO. However, we observe that the integrated plasmon intensity (with overtones) for typical HREEL spectra of the ceramics (figure 13), whilst higher than that typically observed on thin films gives a value for P_{tot} of only 0.3. Thus, the possibility of a gradual rise in free carrier concentration on travelling into the sample (i.e. a mixture of the two models) is likely to be more realistic.

iv) The DLM predicts that the plasmon frequency should change with the incident beam energy (as this changes k and hence kd). The PDLM predicts that no such change should occur (at least if the sampling depth remains within the depletion layer). For the ceramic samples, no such change was observed for beam energies ranging from 25-200eV (using the gun used for LEED as an electron source to produce the high energy electron beams). For a 0.6eV excitation (typical of the HREELS plasmon frequencies for the ceramics), this corresponds to penetration depths in the range 20-65Å. However, no change in plasmon frequency was observed in HREELS of the thin films for beam energies ranging from 25-100eV. In addition, there

appeared to be no significant change in the plasmon intensity on changing the beam energy. This again reinforces the view that the real situation may be better represented by a model in which the carrier concentration rises on travelling down into the sample. The theoretical treatment of such a model would, however, be very complex.

Thus, the shift in the frequency and attenuation in intensity of the surface plasmon observed in the HREELS of the ITO thin films is adequately explained by a two layer model in which the surface layer is completely depleted of free carriers. However, there is evidence to suggest that a model in which there is a gradual rise in free carrier concentration on travelling into the sample is likely to be more realistic. Further experimental and theoretical work is planned to investigate this very interesting phenomenon. In particular, HREEL spectra need to be obtained at rather better resolution than is available on our spectrometer in order to investigate possible small changes in plasmon frequencies and intensities, and the broadening of spectra expected to result from the dependence of the plasmon frequency on k. In addition, it would be interesting to develop theories which would predict the effect of a surface depletion layer on the SO phonons of the substrate, as well as on the surface plasmon.

Chapter Five

Band Bending and Surface Depletion Layers:

The Effects Created by the Adsorption of NO_2 and Cl_2 on TiO_2 and Sb-Doped SnO_2

5.1 Introduction

The purpose of this chapter is to present preliminary results from studies aimed at the deliberate creation of surface layers depleted of free carriers, of the type described in Chapter 4, section 4.7.3.

The presence of surface depletion (or accumulation) layers on substrates such as Ge and Si is already well established, and is of importance in semiconductor technology[159]. In such covalent semiconductors, there is often a high density of surface states in the band gap region, which gives rise to band bending[160-164]. An example is (100) GaAs, where the conduction and valence bands bend upwards at the surface of the n-type material[155]. The barrier height is pinned by the presence of surface states at a value close to 0.8eV[165], even in the absence of any oxide or other overlayer. The upward band bending results in a space-charge layer which is depleted of free carriers.

This Chapter describes experiments to deliberately create such layers on n-type oxide substrates, by the adsorption of electron withdrawing species. The substrates were antimony-doped tin dioxide ceramics and single crystal rutile. The readiness with which a gaseous species might withdraw electrons from a particular substrate would be expected to be related to the balance between the workfunction of the sample, and the sum of the heat of formation of the negatively charged species (e.g.$1/2Cl_2+e^- \longrightarrow Cl^-$) and the attraction between the negatively charged species and its image charge in the surface. The most important variable in this sum is the electron affinity of the gaseous species. On this basis, the gases chosen for the adsorption studies were Cl_2 and NO_2.

The formation of a depletion layer on an n-type semiconductor may be modelled as shown in figure 1.

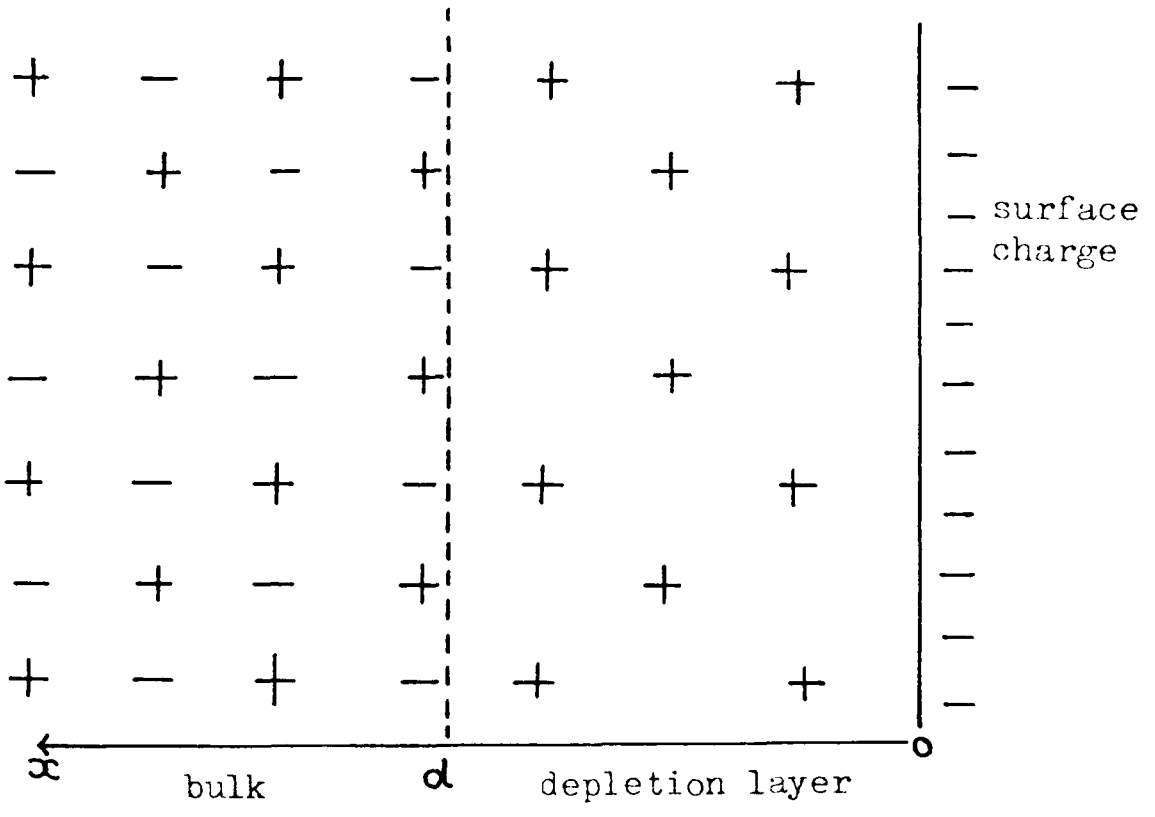

Figure 1: The model used to describe a depletion layer on an n-type semiconductor.

It is assumed that all mobile carriers are depleted from a well-defined layer of thickness d, so that the thermal distribution of carriers is ignored. This is obviously an approximation to the real situation where we might envisage a gradual return to the bulk free carrier concentration on moving through the surface into the depletion layer (as discussed in section 4.7.3). The carriers from the depletion layer are removed to the surface, in this case by the action of an electron withdrawing adsorbate. If the bulk donor concentration is N_d, then the unbalanced charge density in the depletion layer is $+N_d e$.

The potential, V created satisfies the one-dimensional Poisson equation:

$$d^2V/dx^2 = -\rho(x)/\varepsilon\varepsilon_o \qquad (1)$$

where $\rho(x)$ is the charge per unit volume (constant over (y,z) planes), ε is the permittivity of free space, and ε_o is the static dielectric

constant of the medium. Using the boundary conditions

$$V=0,\ dV/dx=0 \text{ for } x\leqslant -d \tag{2}$$

and putting $\rho=N_d e$, we obtain, for $-d\leqslant x\leqslant 0$

$$V = -N_d e(x+d)^2/2\varepsilon\varepsilon_o, \tag{3}$$

$$dV/dx = -N_d e(x+d)/\varepsilon\varepsilon_o \tag{4}$$

and for $x\geqslant 0$,

$$V = -N_d e d^2/2\varepsilon\varepsilon_o,\ dV/dx=0 \tag{5}$$

(as the surface charge density N_s $(=dN_d)$ at x=0 cancels the change in dV/dx, leaving V constant.)

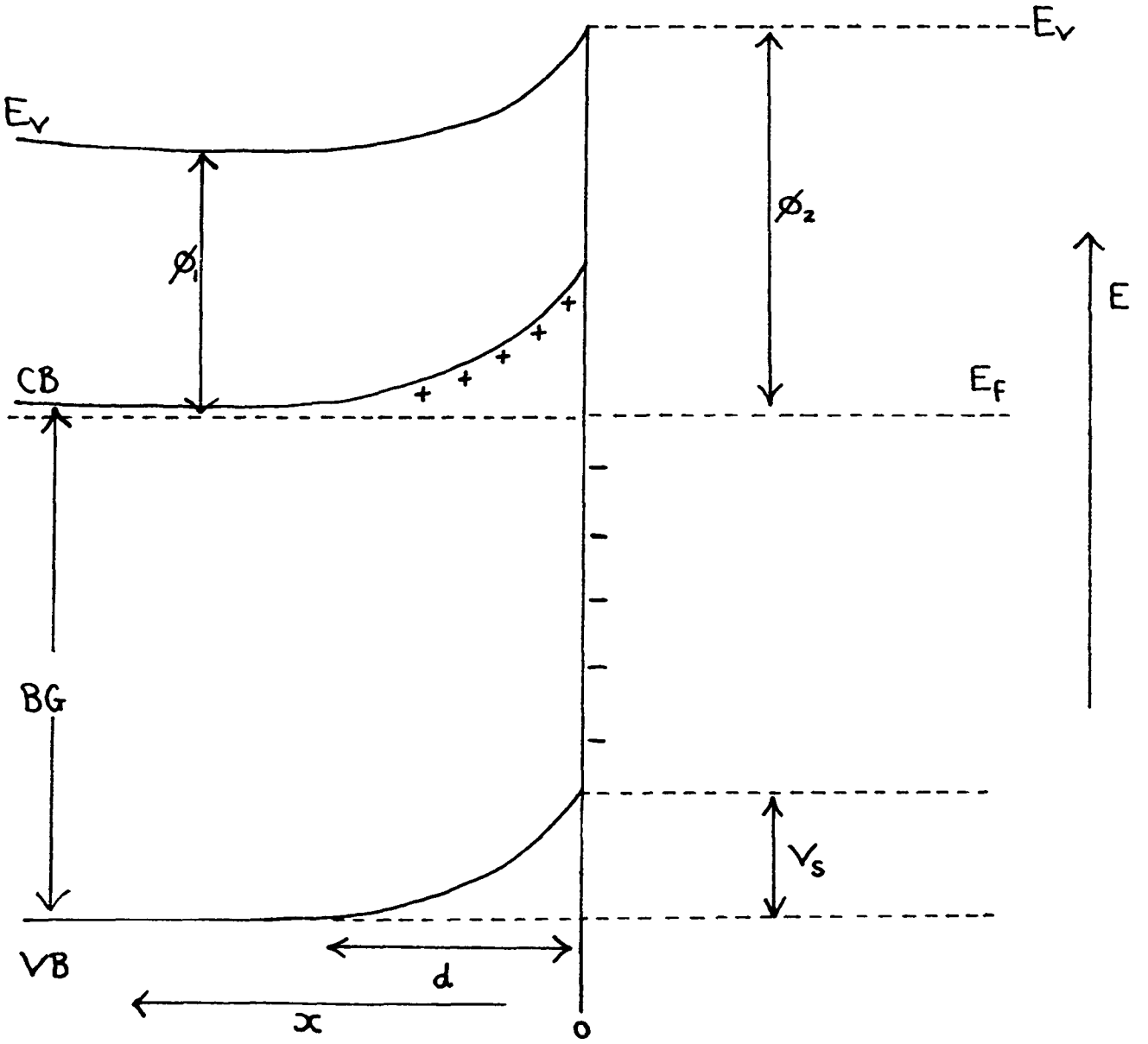

Figure 2: Band diagram for a depletion layer on an n-type semiconductor. The conduction and valence bands (CB, VB) and the band gap (BG) are indicated. E_v, E_f are the vacuum and Fermi levels respectively. The latter is pinned by the presence of donor states below the conduction band edge. φ_1, φ_2 represent the work function of the sample before and after the creation of a surface depletion layer.

Thus we obtain the band diagram of figure 2. Here the vertical scale is electron energy (=-eV). Parabolic upward band bending consistent with equation (3) occurs in the depleted surface region. The valence band edge is shifted to higher energy by an amount V_s, given by

$$V_s = N_d e d^2 / 2\varepsilon\varepsilon_o \qquad (6)$$

Hence, the depth of the depletion layer d is

$$d = [2\varepsilon\varepsilon_o V_s / N_d e]^{1/2} \qquad (7)$$

As

$$d = N_s / N_d \qquad (8)$$

then the surface charge density, N_s is given by

$$N_s = [2\varepsilon\varepsilon_o N_d V_s / e]^{1/2} \qquad (9)$$

There is some ambiguity here over the value of ε_o which should be used in the depleted region. The "effective" ε_o probably lies somewhere between 1 (the value for free space), and the value for the bulk substrate.

5.2 Experimental

The antimony-doped tin dioxide ceramics used were previously prepared by Dr.P.J. Tavener by a co-precipitation technique described elsewhere[92]. Samples containing 0.1 at.% and 1 at.% antimony were used. The rutile crystal used was a polished (001) face, cut by Mr.G.Read of the Clarendon Laboratory from a crystal supplied by Professor J. Cunningham of the University College, Cork. The crystal orientation was confirmed by Laue Back Reflection (described in Chapter 3, section 3.5).

The gases used were research grade, and were introduced into the gas handling line of the spectrometer via a $100cm^{-3}$ glass ampule. The NO_2 required was prepared in situ by introducing roughly equal amounts of O_2 and NO into the previously evacuated ampule.

Before experiments were carried out, the samples were mounted in platinum trays, and were cleaned in the preparation chamber of the spectrometer (base pressure $5x10^{-8}$mbar). The ceramic samples were typically resistively heated at 820K for at least 12 hours. The rutile crystal was heated by radio-frequency induction at 1300K for a similar period. After these procedures Mg KαXPS and HREEL spectra indicated that virtually no carbon or other contaminants were present on the surfaces of the samples.

The samples were then exposed to either Cl_2 or NO_2 for several minutes in the fast entry lock of the spectrometer. After exposure the samples were transferred to the preparation chamber until desorption of gas from the samples was sufficiently low to allow them to be transferred to the main chamber (base pressure 10^{-10}mbar).

Of primary importance to the present discussion was the determination of the work funcions of the samples both before and after adsorption. These were accurately measured by applying a negative bias (1-5V) to the sample, to allow the transmission of electrons leaving the sample with zero kinetic energy. The shift in the position of the SEED edge of the spectrum with increasing bias was noted. It was found that the initial work function of the clean sample tended to be dependent on the previous history of the sample. The work function of the rutile crystal was influenced by the heating period used in sample cleaning. This is presumably a reflection of the degree of reduction of the sample, which, as we have seen (Chapter 3, section 3.5) may be readily varied. It was found that cleaning both the rutile and tin dioxide

samples after adsorption did not return the work function reliably to its initial value. Moreover, our spectrometer does not at present incorporate any means of accurately measuring gas exposures. Thus, the gas dosage was not reproducible. In addition, at this stage of the work, the majority of the spectra were output onto the XY recorder only, due to the unfortunate demise of the Ortec multi-channel analyser. Thus the amount of quantitative data analysis which could be undertaken was limited.

Thus, the results presented in the following sections may be regarded as preliminary only, and represent the start of an extended programme of research which is continuing in this laboratory.

5.3 Results

5.3.1 Adsorption on Antimony-Doped Tin Dioxide Ceramics

a) Chlorine Adsorption

Typical examples of widescan Mg KαXPS spectra, recorded before and after dosing with chlorine are shown in figure 3. After dosing, a small Cl:2p peak is evident at 1060eV. There is some evidence for the Cl:2s peak at 985eV, but this is partly obscured by peaks at 990 and 1005eV due to the very strong 4d peaks of tungsten impurities previously known to be present in the ceramic samples.

The surface chlorine coverage may be estimated from the intensity of the Cl:2p peak. We envisage that a chlorine layer of thickness d overlies the substrate. The intensity due to the adsorbed chlorine may then be expressed by integrating equation (5) of Chapter 4:

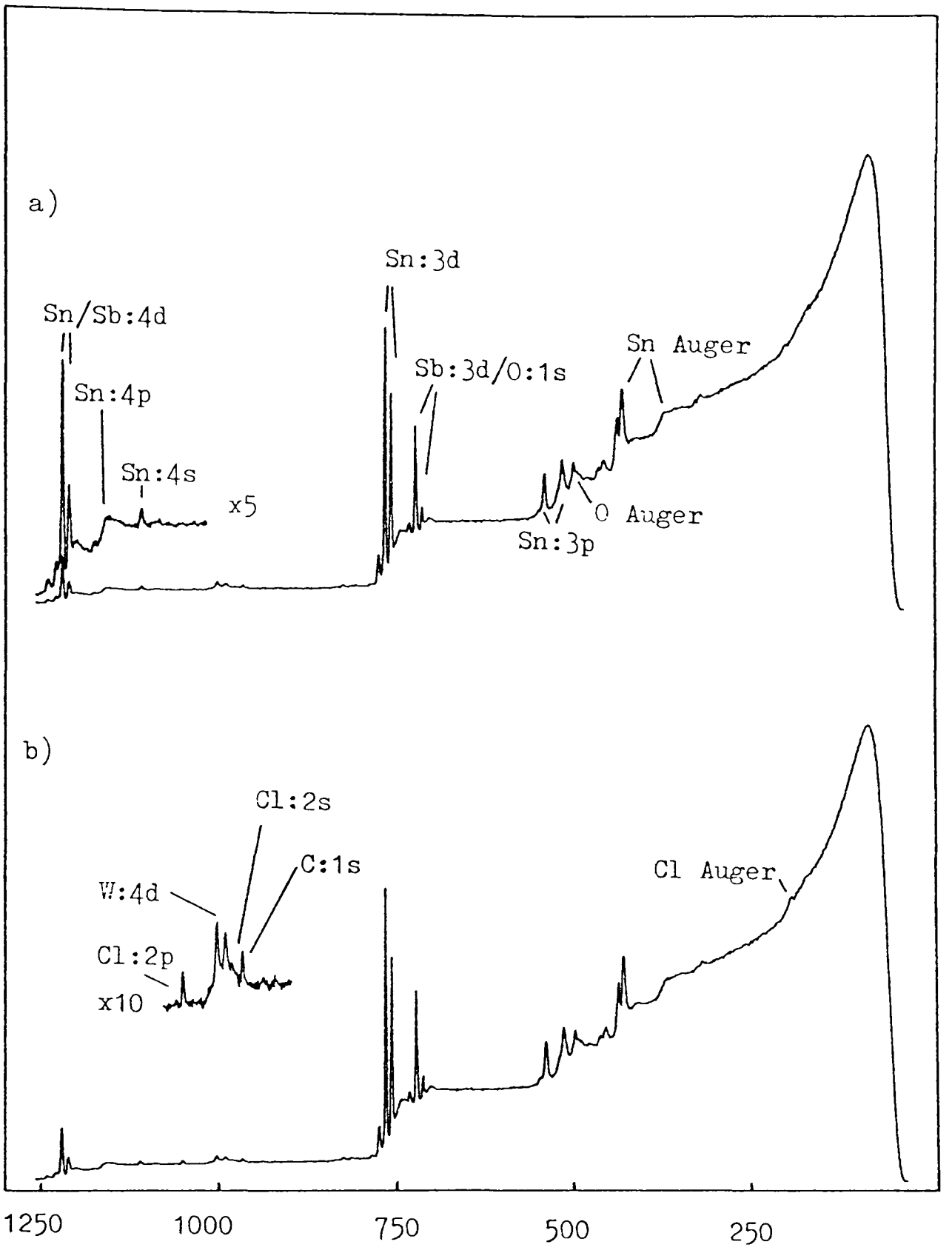

Figure 3: Typical widescan Mg KαXPS spectra for an antimony-doped tin dioxide ceramic containing 1 at.% Sb
a) before doing with chlorine
b) after dosing

$$I(Cl) = I_o(Cl)\int_o^d \exp(-x/\lambda_{Cl})dx \qquad (10)$$

The intensity due to tin may be similarly obtained using $d \to \infty$ as the integration limits. A ratio of peak heights may then be obtained:

$$I(Sn)/I(Cl) = N_{Sn}\sigma_{Sn}\lambda_{Sn}\exp(-d/\lambda_{Sn})/N_{Cl}\sigma_{Cl}\lambda_{Cl}T_R(1-\exp(-d/\lambda_{Cl})) \qquad (11)$$

Ionisation cross sections, σ, were obtained from the tabulation of Evans et al[10]. Sn:3d and Cl:2p peaks were compared. A mean-free-path length for Sn:3d electrons was obtained from previous work by the author[82], and a value for Cl:2p electrons was obtained by extrapolation using equation (9) of Chapter 4. T_R is a factor which corrects for the change in relative analyser transmission function between the kinetic energy ranges of the peaks compared, as the Cl:2p and Sn:3d peaks are well-separated. This was obtained from measurements by a previous worker[92]. N_{Cl}/N_{Sn} is the number of chlorine atoms adsorbed per surface tin atom at monolayer coverage. Using lattice parameters for tin dioxide[166] and typical atomic and ionic radii for chlorine[167], this was estimated to be roughly one, regardless of whether Cl atoms or Cl^- ions were adsorbed. Using the experimentally determined peak intensities (and including the intensity of the antimony 3d peaks in I(Sn)), a value for d of 0.67Å was obtained. For a monolayer coverage, we assume d to be comparable with a typical Sn-Cl bond length ($\sim$2.4Å[167]). The result obtained is then compatible with 0.3 monolayer chlorine coverage.

Typical He I UPS spectra for a ceramic containing 1 at.% Sb before and after dosing with Cl_2 are shown in figure 4. These spectra have been stripped of satellite structure due to He Iβ and γ radiation using the programme described in Appendix I.

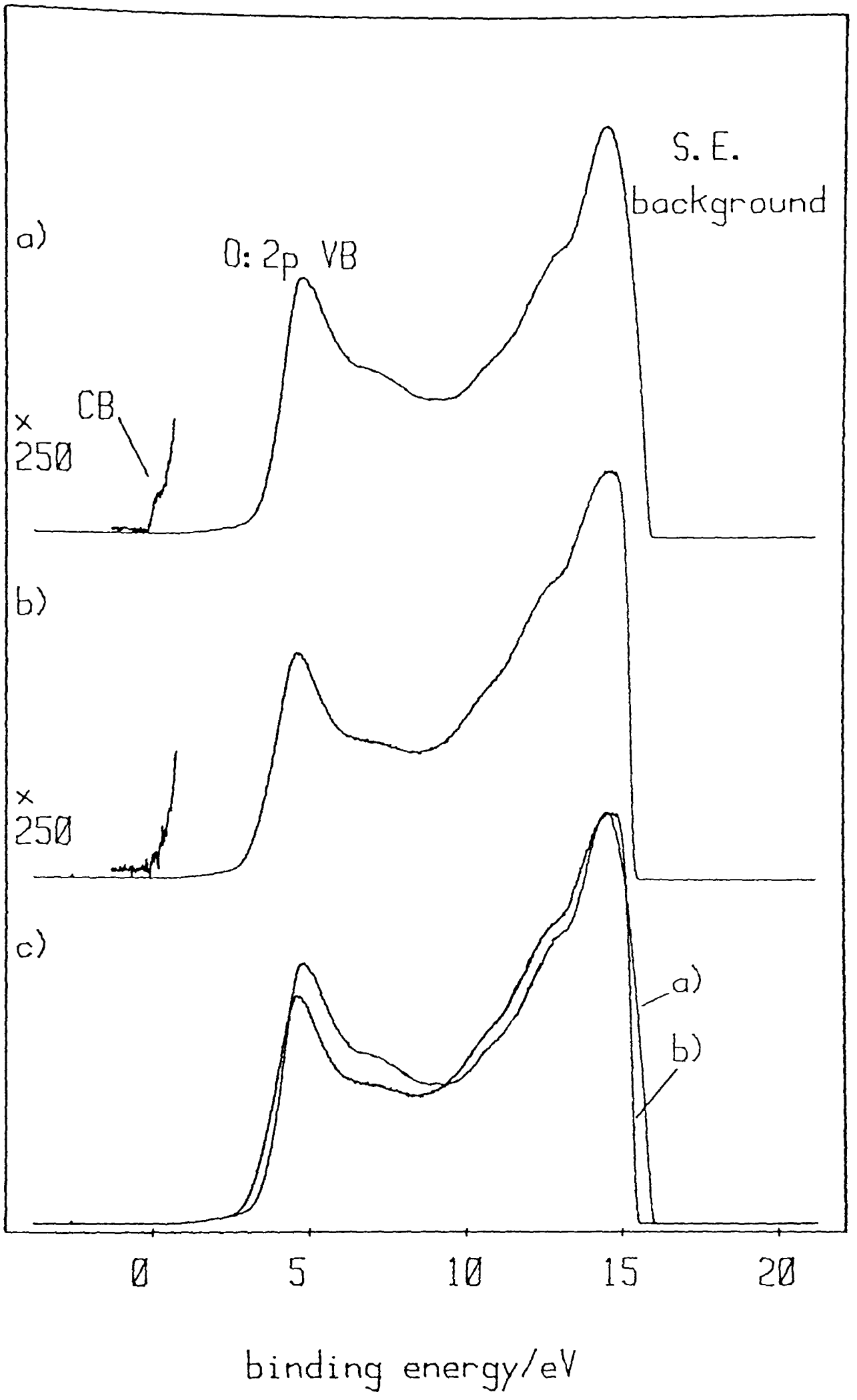

Figure 4: Typical He I UPS spectra for an antimony-doped tin dioxide ceramic containing 1 at.% Sb
a) before dosing with chlorine
b) after dosing
c) a) and b) superimposed, showing the changes which occur on dosing. The spectra have been stripped of structure due to He Iβ and γ radiation.

It can be seen that the SEED edge has shifted after dosing, corresponding to a change in workfunction of the sample (as determined by biasing experiments) of 0.7eV (from 5.2eV to 5.9eV). (Note that the positions of the SEED edges in the unbiased spectra of figure 4 do not accurately reflect this change, which may only be accurately determined by biasing the samples.) This is evidence of some charge separation having occurred at the surface.

The valence band edge also shifts on dosing, but by an amount smaller than the work function change. Thus we have

$$V_s < \varphi_2 - \varphi_1 \qquad (12)$$

in contrast with the expectations of the simple model of figure 2 where the valence band edge shifts by an amount equal to the work function change. Possible reasons for this observation are discussed in section 4.4. The shift may be estimated by linearly extrapolating the edge to zero intensity in an expanded scan of the base of the valence band. This gives a value for V_s of 0.25eV. Using equation (7), an estimate of the depth of the depletion layer created may be obtained, using values of the static dielectric constant for SnO_2 taken from the work of Summit[168]. This gives d~11Å. We have already seen (Chapter 4, section 4.7.3) that there is evidence for the existence of depletion layers at the surfaces of n-type materials even in the absence of adsorbates. Thus the value obtained for d may represent additional depletion created by adsorption of electron withdrawing species.

It is evident that the conduction electrons of the sample close to the surface (within the penetration depth of UPS) are removed on dosing, as the conduction band signal disappears. This is further evidence for the creation of a depletion layer. However, equation (7) predicts that

$$d \propto (1/N_d)^{1/2} \qquad (13)$$

where N_d is the number of donors present in the bulk. Experiments using a substrate doped with only 0.1 at.% antimony gave values for $(\varphi_2 - \varphi_1)$ and V_s similar to those obtained from figure 4, indicating that the DLM does not entirely describe the changes occurring on dosing. However, if a depletion layer exists at the surface before adsorption, we might expect the effects of changing the bulk free carrier concentration to be lessened.

Figure 5 shows HREEL spectra recorded in the specular direction with a 40eV beam, both before and after adsorption on a substrate containing 1 at.% Sb. The main feature of the spectra is the rather broad surface plasmon peak at ~0.35eV energy loss. Three very small, but nontheless experimentally reproducible changes are observed after dosing. The plasmon intensity is slightly attenuated, its frequency is slightly lowered, and the intensity of the surface phonons (at <0.1eV energy loss) is slightly increased. The attenuation and shift of the plasmon frequency is expected on the basis of the DLM, as was discussed in Chapter 4, section 4.7.3. An increase in the SO phonon intensity is also expected if the surface free carrier concentration is reduced, as the free electrons tend to screen out the dielectric response of the material to the potential of the incoming electron, leading to diminished scattering intensity[87]. Thus the changes observed, though small, are entirely consistent with the DLM. No shift in frequency of the plasmon with beam energy either before or after dosing was observed, as would be expected for a depleted layer. However, in view of the very small changes observed on dosing, these changes may be too small to be resolvable. According to the DLM, the shift in surface plasmon frequency should be described by

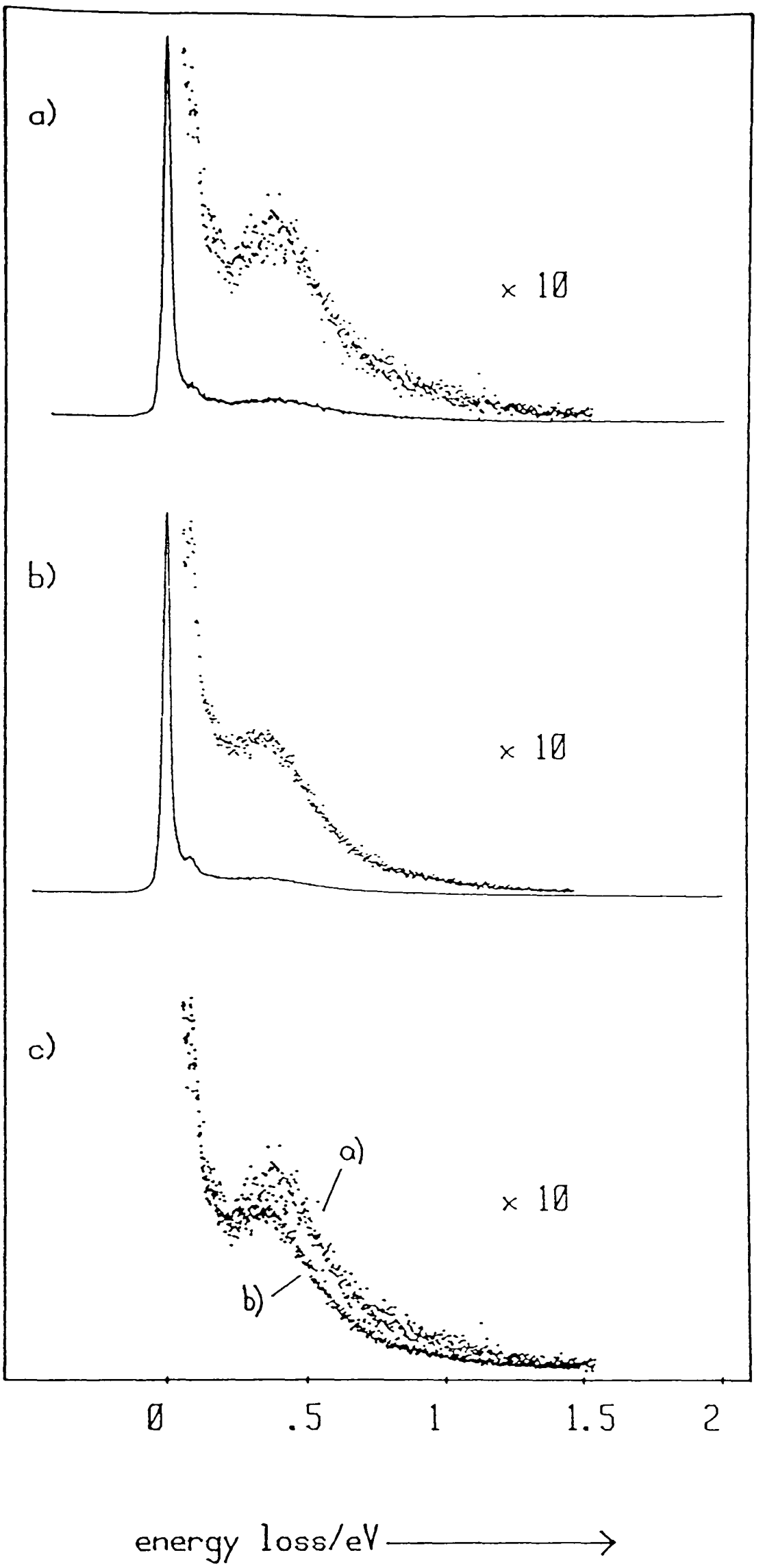

Figure 5: HREEL spectra recorded in the specular direction using a 40eV electron beam for an antimony-doped tin dioxide ceramic containing 1 at.% Sb.
a) before dosing with chlorine
b) after dosing
c) expanded scans of a) and b) superimposed, showing the small changes which occur on dosing.

$$\omega^2 = (\omega_p^2/2)[1+\eta\exp(-2kd)] \qquad (14)$$

where $\eta = (\varepsilon_\infty - 1)/(\varepsilon_\infty + 1)$, as discussed in section 4.7.3.

As $k=\omega/v$, then for a rather low bulk plasmon frequency such as that expected for a tin dioxide ceramic containing 1 at.% Sb, the shifts in surface plasmon frequency might be expected to be rather small.

b) Nitrogen Dioxide Adsorption

Widescan Mg Kα XPS spectra were recorded before and after dosing with NO_2. After dosing, very small N:1s peaks were seen in some, but not all dosed spectra. The low intensity (which is too small to allow estimation of surface coverage) is due to the very low ionisation cross-section of the N:1s electrons (σ=0.384[10]) compared with, for example, the Sn:3d electrons (σ=6.26[10]).

Figure 6 shows typical examples of UPS spectra (output onto the XY recorder) before and after dosing with NO_2. The changes observed are very similar to those seen after adsorption of chlorine. The work function change ($\varphi_2 - \varphi_1$) is 0.45eV (from 5.15eV to 5.6eV), with $V_s \sim 0.25$eV. The shift in work function varied with the amount of NO_2 introduced into the spectrometer; the maximum work function change observed was 0.8eV. Both gases seem to have very similar effects on the electronic sturcture of the tin dioxide ceramics.

UPS spectra were recorded as the samples were resistively heated after dosing with NO_2. The work function remained constant (indicating that there was no desorption from the surface) up to the maximum probe temperature of 600°C. At this probe temperature, the actual sample temperature is likely to be of the order of 300°C.

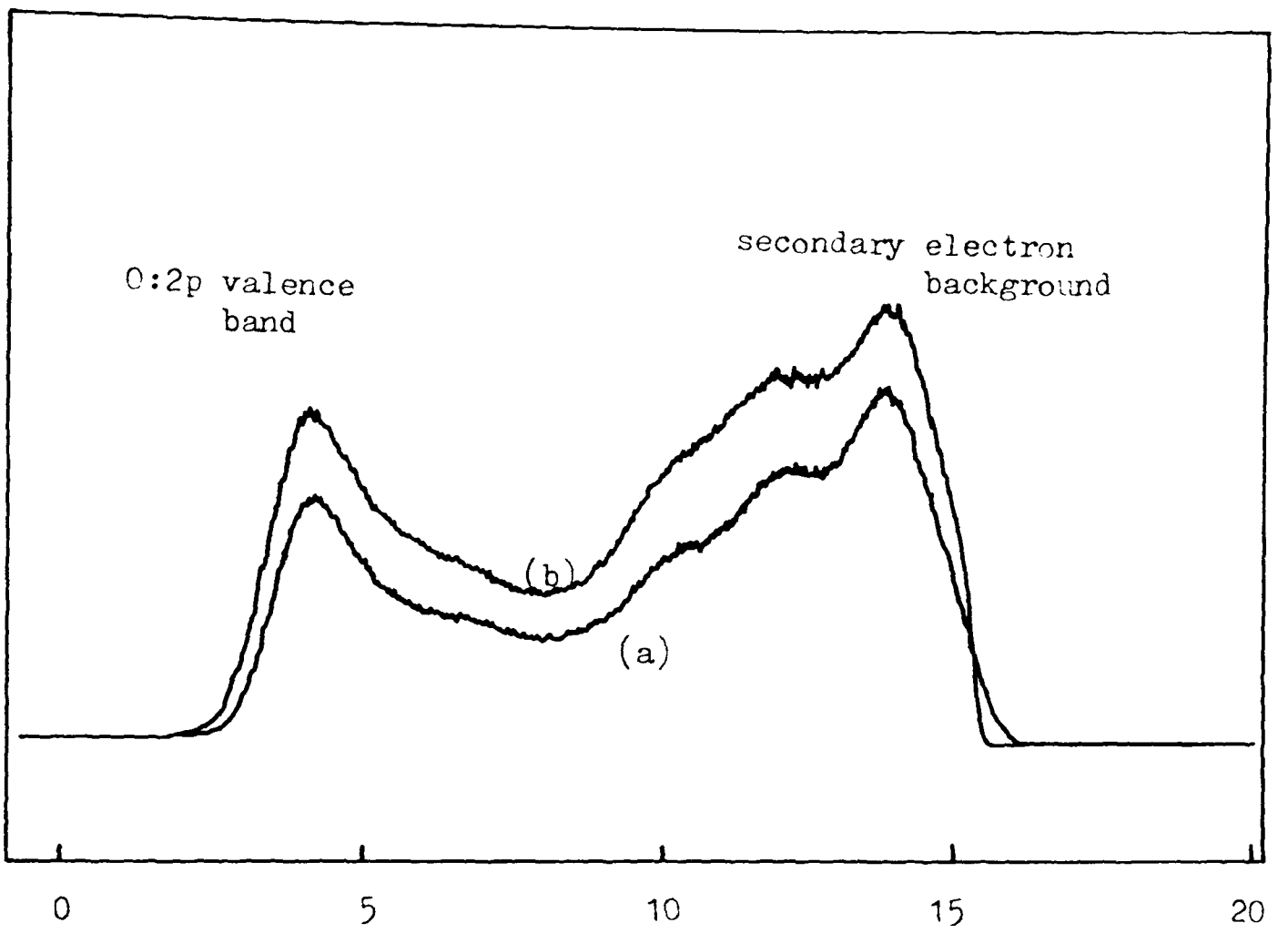

Figure 6: He I UPS spectra for an antimony-doped tin dioxide ceramic containing 1 at.% Sb
a) before dosing with nitrogen dioxide
b) after dosing

5.3.2 Adsorption on Rutile (001)

a) Chlorine Adsorption

Adsorption of chlorine on the clean rutile crystal resulted in the appearance of large peaks due to Cl:2p (1060eV), Cl:2s (985eV)

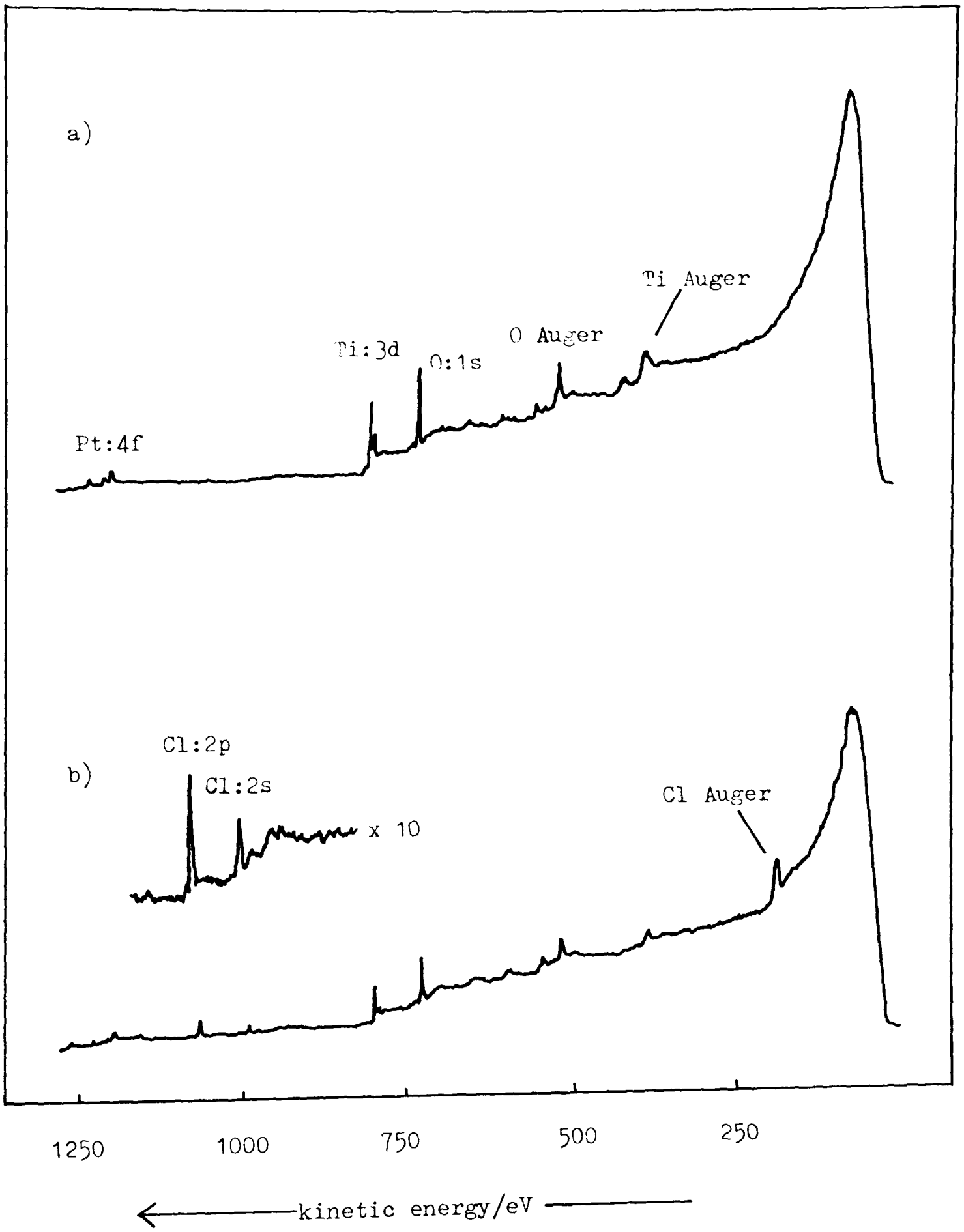

Figure 7: Widescan Mg Kα XPS for rutile (100)
a) before dosing with chlorine
b) after dosing

and Cl Auger (190eV) in the Mg KαXPS spectrum. The titanium and oxygen peaks of the substrate appeared with diminished intensity. This is illustrated in figure 7. The surface coverage was estimated using the method described in section 5.3.1a), with the required data obtained from the same sources. Cl:2p and Ti:3d peak intensities were compared. The value of d, the thickness of the adsorbate layer obtained was 5.0Å. A typical Ti^{IV}-Cl bond length is 2.2Å[167]. Thus it is clear that more than one monolayer is present. If it is assumed that the spacing between the first and second monolayers is roughly equal to 2r(Cl)=3.6Å, then the value of d obtained is consistent with ∽1.8 monolayers of adsorbed atoms. However, if the second layer is adsorbed as ions ($r(Cl^-)$=1.0Å), then the value obtained is consistent with slightly more than two monolayers adsorption. Whilst the exact nature of the adsorbed species is unclear, it is evident that chlorine is adsorbed much more readily onto the rutile crystal than onto the tin dioxide ceramics.

Figure 8 shows He I UPS spectra of rutile before and after dosing with chlorine. The spectrum before dosing shows a high concentration of states in the band gap, between E_f and the valence band edge at around 3eV below E_f. This is consistent with spectra previously obtained in this laboratory after inductively heating single crystal rutile[169], and is due to the high concentration of defects introduced by vacuum annealing. The nature of these defects, which arise from the creation of oxygen vacancies, has been discussed in Chapter 3, section 3.7. In accordance with this, the initial work function of the crystal was dependent on the annealing period used, varying between 4.2eV and 4.5eV. The changes which occur on adsorption are similar, but very much more dramatic than those observed when Sb-doped SnO_2 was used as the substrate. In the example shown, the work function is changed by 1.3eV, from 4.2eV to

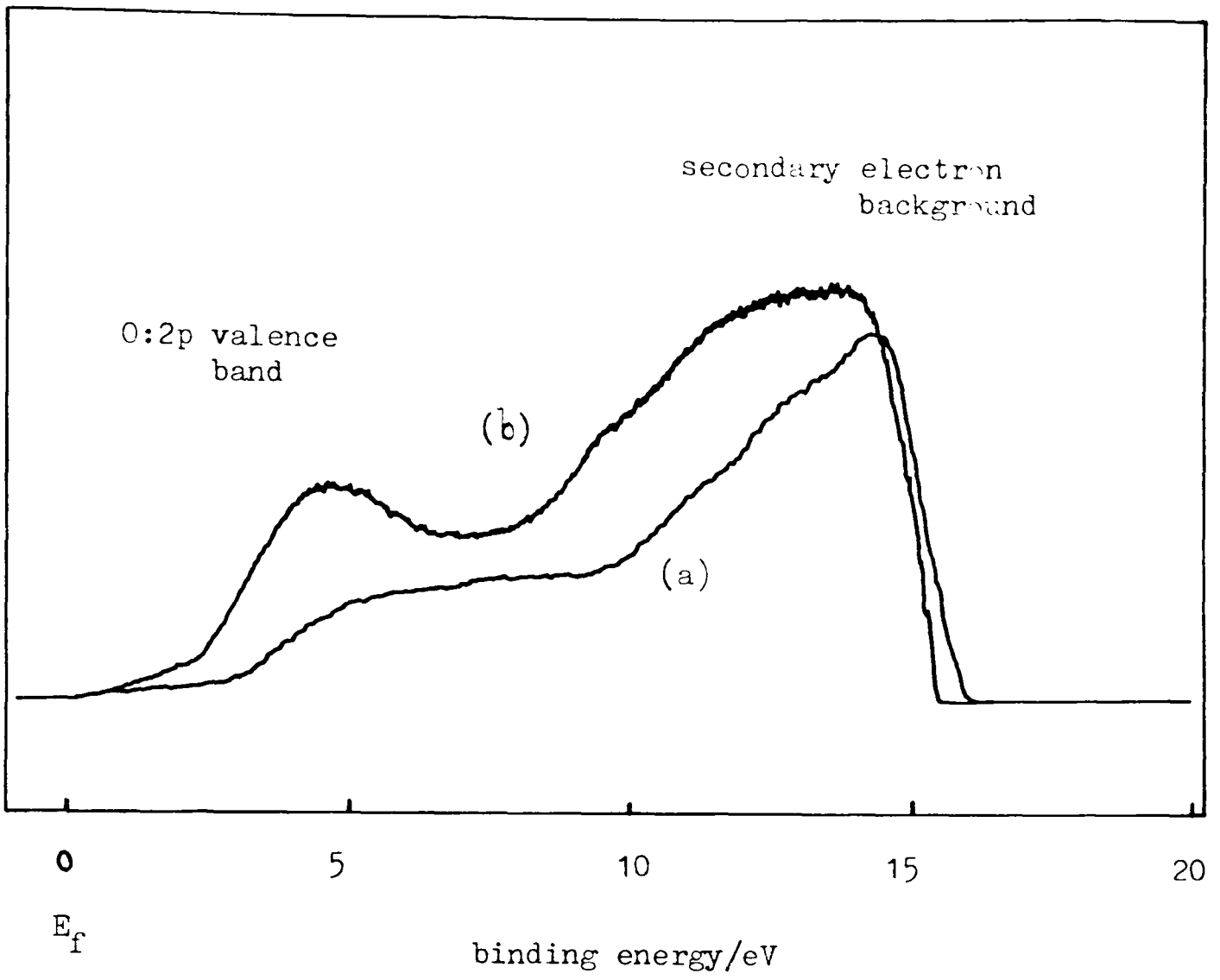

Figure 8: He I UPS spectra of rutile (001)
a) before dosing with chlorine
b) after dosing

5.5eV. The shift in the valence band edge is difficult to estimate due to the intensity in the band gap region, but it appears to be large, in the range 0.5-1eV. The extent of the occupied band gap states has been reduced after dosing. It is clear from these unnormalised spectra that the intensity of the spectra obtained is increased following adsorption. This appeared to be a general effect for both gases and both substrates used.

XPS spectra indicated that there was no significant desorption of chlorine on heating the sample, up to the maximum probe temperature of 600°C (sample temperature ∿300°C). However, there was a small decrease (0.5eV) in the work function of the sample on heating to this temperature, indicating that some slight desorption was occurring.

b) Nitrogen Dioxide Adsorption

Widescan Mg Kα XPS spectra were recorded before and after dosing the rutile crystal with NO_2. After dosing, a small peak due to N:1s electrons was present in the spectrum. The intensity of this peak, after correcting for cross-sections, was consistent with a surface coverage similar to that observed for chlorine adsorption (section 5.3.2a)).

He I UPS spectra before and after adsorption are shown in figure 9. Again, the changes observed are very similar to those seen after chlorine adsorption. The change in work function on dosing is 1.4eV (from 4.5eV to 5.9eV). The shift in valence band edge is large, in the range 0.75-1eV.

5.4 Conclusions

Adsorption of either NO_2 or Cl_2 on both n-type substrates used results in an increase in work function, consistent with charge separation occurring at the surface. A shift in the valence band edge is also observed, indicating band-bending at the surface as predicted by the model described in section 5.1. In accord with the DLM, the conduction band intensity in UPS from the antimony-doped tin dioxide substrates is removed on dosing. In addition, small changes in the

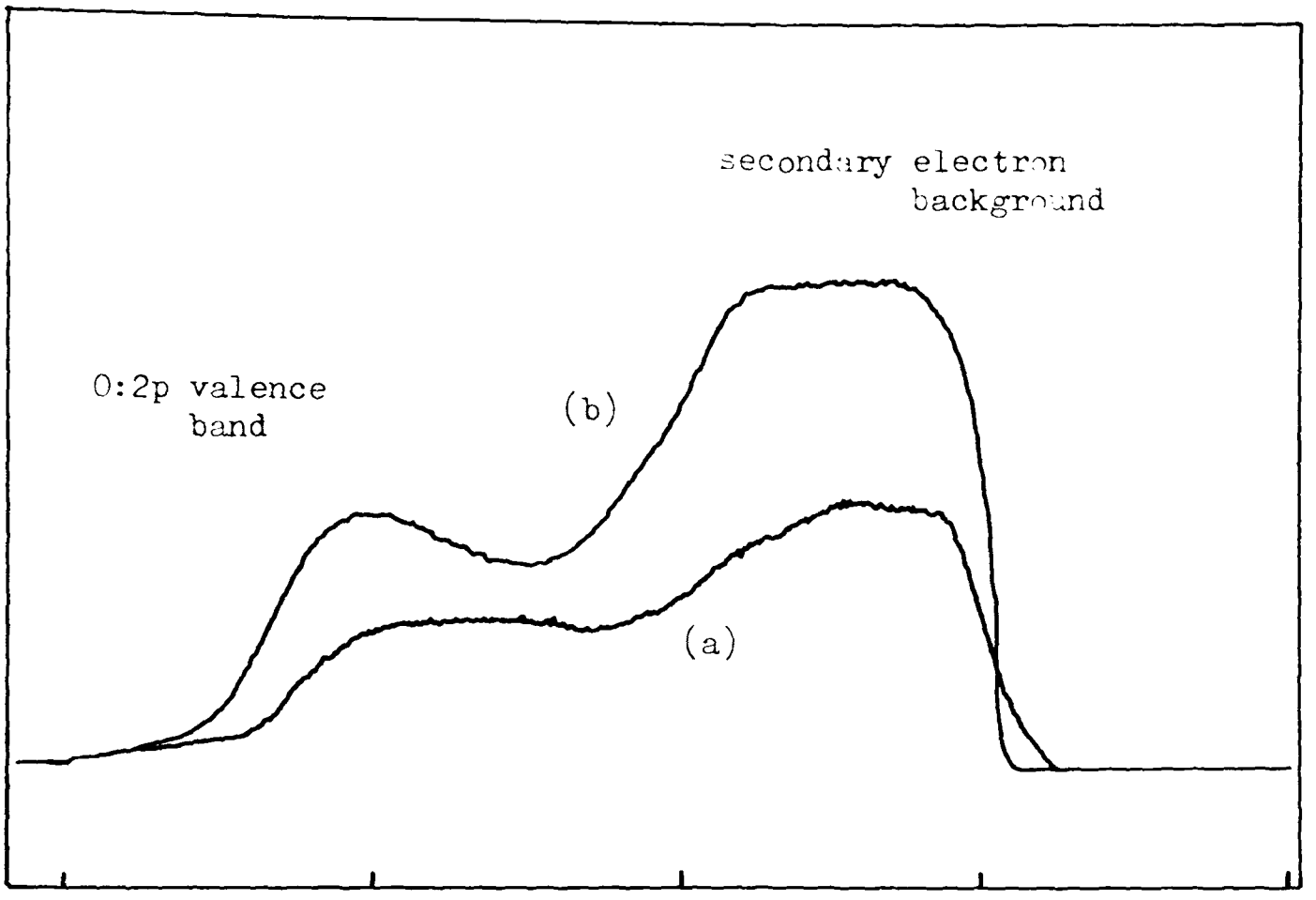

Figure 9: He I UPS spectra for rutile (001)
a) before dosing with nitrogen dioxide
b) after dosing

phonon and plasmon frequency consistent with this model (Chapter 4, section 4.7.3) are observed in the HREEL spectra of chlorine-dosed antimony-doped tin dioxide.

However, it is consistently observed that the change in workfunction on dosing is larger than the shift in the valence band edge, indicating that the vacuum level is raised at the surface as shown in figure 10. Two factors may contribute towards this. If surface

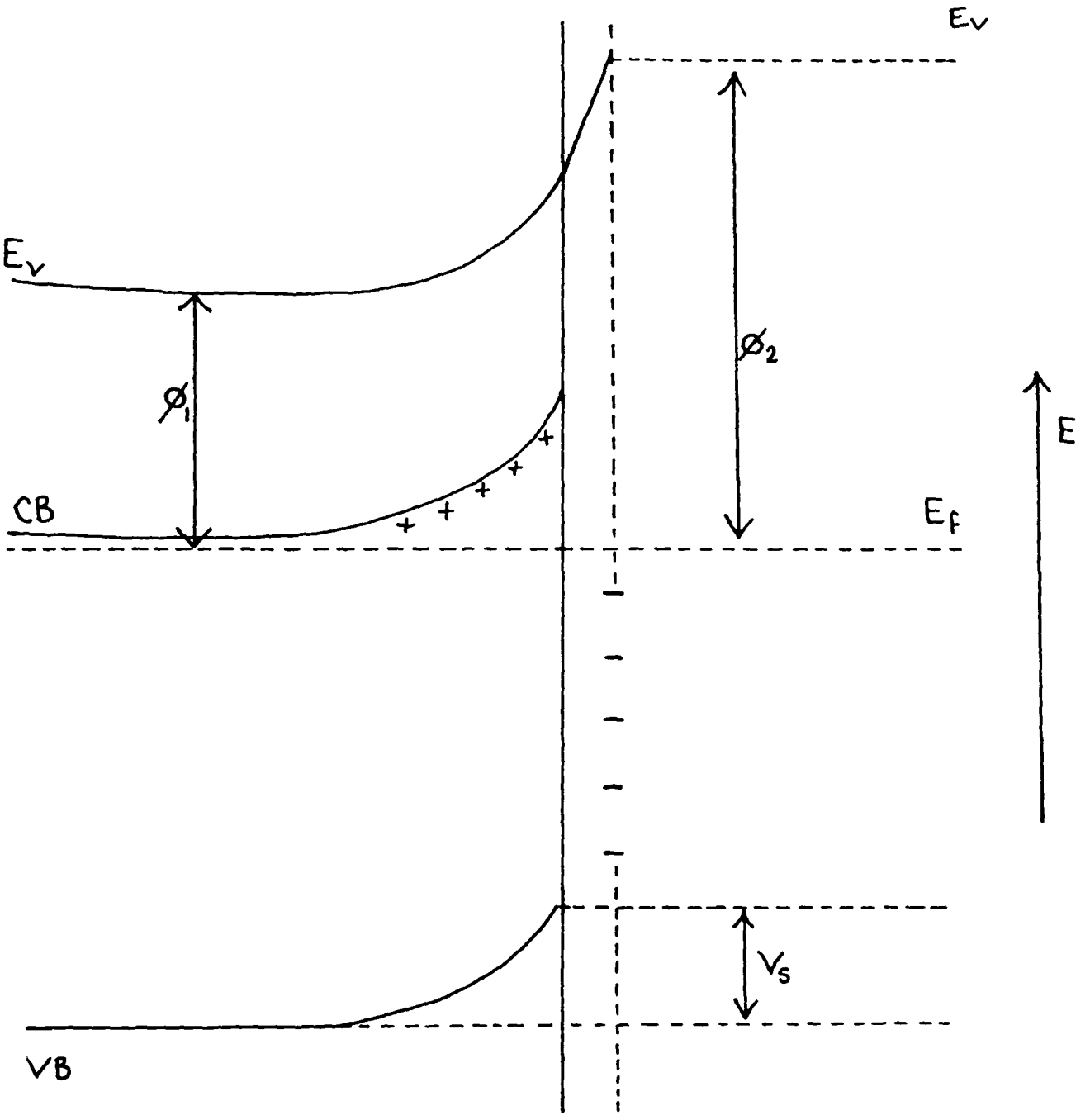

Figure 10: Band diagram for a depletion layer on an n-type semiconductor with a raised vacuum level, E_v, at the surface. The conduction and valence bands (CB, VB) are indicated. The Fermi level, E_f is pinned by the presence of donor states below the conduction band edge. φ_1, φ_2 represent the work function of the sample before and after the creation of a surface depletion layer.

states are present which donate electrons to the adsorbate, then this would change the work function of the sample, whilst having no effect on the position of the bulk valence band edge. As has been discussed (section 4.7.1), a lone-pair-like sp hybrid surface state has been previously proposed for the antimony-doped tin dioxide ceramics[82,91]. It is evident from the UPS of the rutile crystal that surface states (due to oxygen vacancy creation) are produced by annealing in vacuo.

In addition, we note that an additional potential change in accordance with equation (5) will occur between the surface and the adsorbate layer (as illustrated in figure 10). This change may be quite substantial, as in this region, ε_o is equal to 1, its value in vacuo. This may lead to a further raising of the vacuum level.

The changes observed on dosing are very much more marked for the rutile crystal than for the tin dioxide ceramics. XPS reveals that, after chlorine dosing, the surface Cl coverage is almost 2 monolayers for rutile, but is only around 0.3 monolayers for tin dioxide. This marked difference in substrate affinity for electron-withdrawing species is probably due to the high concentration of surface oxygen vacancy defects introduced by annealing the rutile crystal in vacuo, as observed in UPS. It seems likely that chlorine and nitrogen dioxide would readily withdraw electrons from the resulting Ti^{3+}-□ complexes (section 3.7).

The changes in work function, and the shift in the valence band edge on dosing are also much larger for the rutile crystal than for the tin dioxide ceramics. For the latter, V_s is typically ∿0.25eV, giving a depletion layer depth, via equation (7) of ∿11Å. For rutile, V_s appears to be typically ∿0.7eV. The depth of the depletion layer created in this case cannot be estimated without a knowledge of N_d, the donor concentration present. However, if the surface coverages from XPS are

used to obtain a surface charge density, then the values of N_d obtained for the rutile crystal via equation (8) are one or two orders of magnitude higher than those which would typically be expected in the vacuum-reduced rutile crystal[170]. This is further evidence for the participation of surface, in addition to bulk states in the electron donation process.

The study of surface depletion layers on metal oxides is of technological importance, particularly in the field of gas sensors, where doped tin dioxide ceramics are already widely employed[171-176]. The preliminary results presented here reveal that electron spectroscopy may be effectively employed to monitor the creation of these layers by adsorption of gases. Band bending may be directly monitored by UPS, whilst XPS yields information on surface coverage of adsorbates. Changes in the HREEL spectra of the substrate may also yield information on sub-surface carrier depletion.

It is clear that the effects observed on dosing are sensitively dependent on the surface defect concentration initially present in the substrate. This is in turn dependent on the precise sample cleaning conditions. It is therefore important that a detailed study of the effects of sample cleaning treatments on defect concentrations is undertaken, and that methods of producing surfaces which are as nearly stoichiometric as possible are devised before quantitative studies are carried out. This is at present underway in this laboratory. The results presented here represent an encouraging start to an extended programme of research which is currently being undertaken.

Appendices

Appendix I

The Removal of Satellite Fine Structure due to He Iβ and He Iγ Radiation in He I UPS Spectra

Satellite structure due to He Iβ and He Iγ radiation may often appear in the same region of a UPS spectrum as weak features of interest such as the conduction band. It is therefore essential for quantitative analysis that such structure is removed. The core section of the computer programme used is listed below:

```
430 INPUT#10,E1,E2
440 INPUT "Workfunction";WF
450 INPUT"Sample bias";SB
460 CA=-INT((WF+SB-E2)*1022/25)+1023
470 CB=-INT((WF+SB+1.87-E2)*1022/25)+1023
472 CC = -INT((WF+SB+2.525-E2)*1022/25)+1023
480 TEXT
501 PRINT "DEFAULT VALUES:
502 PRINT "intensity ratios He b/a=0.017,He g/a=0.0017"
503 PRINT "DO YOU WISH TO CHANGE THESE VALUES?(Y/N)
504 INPUT A$
505 IF A$="N" OR A$ ="n" THEN GOTO 509
506 PRINT "ENTER NEW INTENSITY RATIOS He b/a,g/a
507 INPUT BA,GA
508 GOTO 510
509 BA=0.017:GA=0.0017
510 FOR N=1 TO CB
511 CD =CB-N+1
512 CE =CA -N+1
515 P(CD) =P(CD)-BA*P(CE)
520 NEXT N
521 FOR N=1 TO CC
522 CF=CC-N+1
524 P(CF)=P(CF)-GA*P(CE)
525 NEXT N
```

.

.

.

Plot corrected spectrum P(1).....P(N)

Notes to the Programme

430 E_1, E_2 are the energy limits of the spectrum.

450 The sample bias, SB, is normally zero.

460 This is the channel number corresponding to the energy of the SEED edge of the spectrum produced by He Iα radiation.

470, 472 Corresponding points for He Iβ radiation and He Iγ radiation.

501 This section provides for alteration of the default values[23] of the intensity ratios He Iβ/He Iα and He Iγ/He Iα.

515 P(CD) etc. are the values of the signal intensity at channel numbers CD etc. in the spectrum. Here the contribution due to He Iβradiation is stripped from the spectrum for each channel number up to and including CB.

524 A similar procedure is carried out for He Iγ radiation.

Appendix II

Classical Dielectric Theory of Electron Energy Loss[177]

Motion parallel to the surface is neglected, so the physical picture is as shown below:

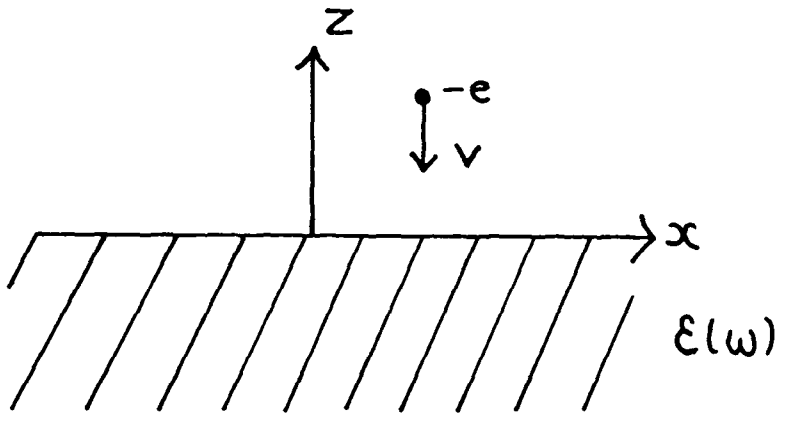

Figure AII.1: Model for the dielectric theory of EELS.

The electron trajectory is described by

$$z = v|t| \qquad \text{AII(1)}$$

with t=0 the time of impact.

An induced electric field is created by the incoming electron which polarises the dielectric medium. The resulting work done by the induced field can be expressed as

$$W = -\int_0^\infty 2\pi \underline{k}\, d\underline{k} \int_0^\infty d\omega \hbar\omega P(\underline{k},\omega) \qquad \text{AII(2)}$$

where $P(\underline{k},\omega)$ is the probability of the electron losing energy $\hbar\omega$ to an excitation with wave vector $\underline{k}$.

The electron is assumed to be a point charge which rebounds from the surface with unchanged velocity. The potential $\varphi(\varrho,z,t) \equiv \varphi(\underline{r},t)$ ($\varrho \equiv (x,y)$) satisfies Poisson's equation:

$$\nabla^2\varphi(\underline{\rho},z,t) = 4\pi e\delta(\underline{\rho})\delta(z-v|t|) \qquad (z>0) \qquad \text{AII(3)}$$

$$\nabla^2\varphi(\underline{\rho},z,t) = 0 \qquad (z<0) \qquad \text{AII(4)}$$

The boundary conditions for solving these equations are

i) $\varphi \longrightarrow 0$ as $z \rightarrow \pm\infty$

ii) $E_z\ (z=+0) = \varepsilon(\omega)E_z\ (z=-0)$

(where $E=-\nabla\varphi$ is the electric field)

iii) $E_{x,y}\ (z=+0) = E_{x,y}\ (z=-0)$

The potential $\varphi(\underline{r},t)$ is Fourier transformed with respect to $\underline{\rho}$ ($\underline{\rho} \longrightarrow \underline{k}$) and t ($t \longrightarrow \omega$). The result is a second order differential equation for the Fourier component $\varphi(\underline{k},z,\omega)$. The solution for $z>0$ is

$$\varphi(\underline{k},z,\omega) = [8\pi e/v(\underline{k}^2+\omega^2/v^2)]\{[\varepsilon(\omega)/(\varepsilon(\omega)+1)]\exp(-\underline{k}z)-\cos(\omega/v)z\} \qquad \text{AII(5)}$$

(the constants are obtained from a consideration of the boundary conditions).

The work done on the electron must then be calculated. The work done per unit time on the electron is given by

$$dW/dt = Fv = \pm\int d\underline{\rho}\int_0^\infty dz\ vE_z(\underline{\rho},z,t)\delta(\underline{\rho})\delta(z-v|t|)e \qquad \text{AII(6)}$$

(+ for $t<0$, - for $t>0$).

W is obtained by integrating this expression with respect to t and $\underline{\rho}$ after converting to the $(\underline{k},z,\omega)$ representation. The resulting expression may be compared with equation AII(2), giving the following expression for $P(\underline{k},\omega)$:

$$P(\underline{k},\omega) = [4e/\hbar\omega(2\pi)^3]\ \mathrm{Im}\int_0^\infty dz\ E_z(\underline{k},z,\omega)\sin(\omega/v)z \qquad \text{AII(7)}$$

Substituting for $E_z(\underline{k},z,\omega)$ (obtained from $E=-\nabla\varphi$), one obtains, after some rearrangement:

$$P(\underline{k},\omega) = \frac{4e^2\underline{k}v^2}{\pi^2\hbar(\underline{k}^2v^2+\omega^2)^2}\ \mathrm{Im}[-1/(\varepsilon(\omega)+1)] \qquad \text{AII(8)}$$

As has been discussed (Chapter 3, section 3.2), the dipole scattering mechanism leads to predominant forward scattering, with an angular distribution less than the acceptance angle of our analyser system. Thus we are effectively sampling all $\underline{k}$. The $\underline{k}$-integrated loss probability is thus given by

$$P(\omega) = \int d^2\underline{k}\ P(\underline{k},\omega) = \int_0^\infty 2\pi k P(k,\omega)dk \qquad \text{AII(9)}$$

The factor of 2π arises from the angular integration of $P(\underline{k},\omega)$, as this is performed in polar coordinates, $\underline{k}=(k,\varphi)$. In this treatment, $P(\underline{k},\omega)$ is independent of φ. The radial k integration may be performed analytically, giving

$$P(\omega) = e^2/v\hbar\omega\ \mathrm{Im}[\varepsilon(\omega)-1]/[\varepsilon(\omega)+1] \qquad \text{AII(10)}$$

or

$$P(\omega) = 2e^2/v\hbar\omega\ \mathrm{Im}[-1/(\varepsilon(\omega)+1)]$$

The total loss probability is so large that it is quite likely that one electron may excite more than one phonon in separate loss events[177]. This is taken into account by self-convoluting the single phonon loss spectrum. Thus if $P_1(\omega)$ is the single phonon loss function, the probability of a two-phonon loss signal at energy $\hbar\omega$ is

$$P_2(\omega) = 1/2\int_0^\infty P_1(\omega')P_1(\omega-\omega')d\omega' \qquad \text{AII(11)}$$

and in general the probability of an n-phonon loss is

$$P_n(\omega) = 1/n!\int_0^\infty P_1(\omega')P_{n-1}(\omega-\omega')d\omega' \qquad \text{AII(12)}$$

The total spectrum is then represented by

$$P(\omega) = P_0(\omega)+P_1(\omega)+P_2(\omega)+..... \qquad AII(13)$$

Here n=0 corresponds to the elastic peak. The progression of multiple loss intensities is given by $x^n/n!$, where x is the intensity of the first loss relative to that of the elastic peak.

Appendix III

Modification of the Classical Dielectric Theory to take into account the Tensor Properties of the Dielectric Function[75,76]

As we have seen, the classical dielectric theory of EELS yields the following equation for the loss function:

$$P(\omega) = e^2/v\hbar\omega \, \mathrm{Im}[\varepsilon(\omega)-1]/[\varepsilon(\omega)+1] \qquad \text{AIII(1)}$$

where $\varepsilon(\omega)$ is the scalar dielectric function. This result must be generalised when ε is a tensor quantity as in anisotropic materials. The first step is again to solve Poisson's equation for the potential $\Phi(\underline{r},t)$ using suitable boundary conditions:

$$\vec{\nabla}.\varepsilon.\vec{\nabla}\Phi(\underline{r},t) = 4\pi e\delta(\underline{r}-\underline{r}_e(t)) \qquad \text{AIII(2)}$$

where $\underline{r}_e(t)$ is the classical electron trajectory, considered to be the specular trajectory ($\underline{v}_{\parallel}t$, $v_{\perp}|t|$) (parallel motion is not neglected in this treatment). ε is one in vacuum and is the dielectric tensor of the crystal on the material side of the surface. Taking the latter as the xy plane and the surface outward normal as the z axis (as in figure AIII.1), ε can be written in block form:

$$\varepsilon = \begin{pmatrix} \varepsilon_{\rho\rho} & \underset{\sim}{\varepsilon}_{\rho z} \\ \underset{\sim}{\varepsilon}_{\rho z} & \varepsilon_{zz} \end{pmatrix} \qquad \text{AIII(3)}$$

where $$\varepsilon_{\rho\rho} = \begin{pmatrix} \varepsilon_{xx} & \varepsilon_{xy} \\ \varepsilon_{yx} & \varepsilon_{yy} \end{pmatrix}$$

and $$\varepsilon_{\rho z} = \begin{pmatrix} \varepsilon_{xz} \\ \varepsilon_{yz} \end{pmatrix}$$

Again, the potential $\Phi(\underline{r},t)$ is Fourier transformed with respect to $\underline{\rho}$ and t. The result is that the Poisson equation AIII(2) reduces to a second order differential equation for the Fourier component $\Phi(\underline{k},z,\omega)$.

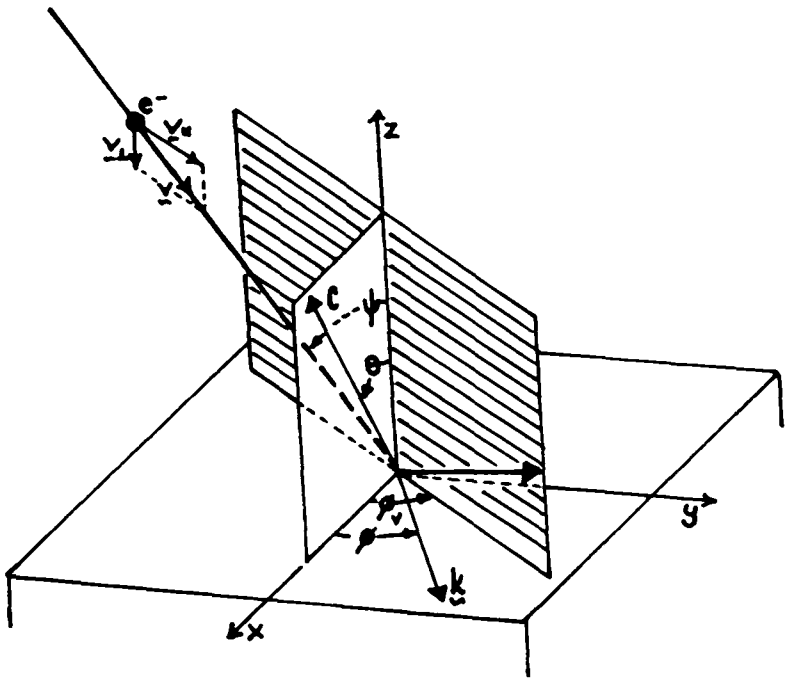

Figure AIII.1:[75] Definition of the geometrical parameters required by the dielectric theory of EELS at a uniaxial crystal surface. The c-axis is chosen to lie in the xz plane and makes an angle θ with the surface normal. The electron velocity $\underline{v}$ has incidence angle ψ and azimuthal angle φ_v. $\underline{k}$ is the resultant phonon wave vector.

The solutions are

$$\Phi(z>0) = A\exp(-kz) - 8\pi e v_\perp / [\Omega^2 + k^2 v_\perp{}^2] \cos\Omega z / v_\perp \qquad \text{AIII(4)}$$

$$\Phi(z\leqslant 0) = B\exp(\alpha z) \qquad \text{AIII(5)}$$

A and B are determined from the boundary conditions at z=0. The work done on the electron can then be calculated, and hence $P(\underline{k},\omega)$, as before (Appendix II).

The resulting expression is

$$P(\underline{k},\omega) = \frac{4e^2 \underline{k}v^{\ 2}}{\pi^2 \hbar (\Omega^2 + \underline{k}^2 v_\perp{}^2)^2} \, \mathrm{Im}[-1/(\zeta(\underline{k},\omega)+1)] \qquad \text{AIII(6)}$$

This is analogous with the equation derived for $P(\underline{k},\omega)$ from the classical theory (Appendix II, equation AII(8)), with two changes. Firstly, as a result of the inclusion of motion parallel to the surface in the treatment, the frequency ω is replaced by Ω, where

$$\Omega = \omega - \underline{k}.\underline{v}_{\parallel} \qquad \text{AIII(7)}$$

Secondly, $\xi(\omega)$ is replaced by a complex function arising from the tensor properties of the dielectric function:

$$\xi = \varepsilon_{zz}[(\underline{k}.\varepsilon_{\rho\rho}.\underline{k})/k^2\varepsilon_{zz} - (\underline{k}.\underline{\varepsilon}_{\rho z})^2/k^2\varepsilon_{zz}^2]^{1/2} \qquad \text{AIII(8)}$$

In a uniaxial crystal, this expression can be simplified:

$$\xi = \varepsilon_{zz}/k[(\varepsilon_{\parallel}\varepsilon_{\perp}/\varepsilon_{zz}^2)k_x^2 + (\varepsilon_{\perp}/\varepsilon_{zz})k_y^2]^{1/2} \qquad \text{AIII(9)}$$

Here the c-axis has been chosen to lie in the xz plane, and makes an angle θ with the surface normal (figure AIII.1). $\varepsilon_{\parallel}$ and $\varepsilon_{\perp}$ are the two principle components of ε.

As with the classical theory, we have

$$P(\omega) = \int d^2\underline{k}\ P(\underline{k},\omega) \qquad \text{AIII(10)}$$

In equation AIII(10), the $\underline{k}$ integration limits are determined by the maximum momentum transfer allowed by the spectrometer aperture. The integration is performed in polar coordinates, $\underline{k}=(k,\varphi)$. The radial k integration is done analytically as ξ depends only on φ. The result is:

$$P(\varphi,\omega) = (2e^2/\pi^2\hbar v_{\perp}\omega)\int_0^{2\pi} d\varphi I(\varphi,\omega).\mathrm{Im}[-1/(\xi(\omega)+1)] \qquad \text{AIII(11)}$$

where

$$I(\varphi,\omega) = [y_c(\eta y_c-\omega)/(\eta y_c-\omega)^2+y_c^2] + \mathrm{atn}\{(\eta^2+1)y_c/\omega - \eta\} + \mathrm{atn}\,\eta \qquad \text{AIII(12)}$$

with

$$y_c = k_c(\varphi) v_\perp ,$$

$$\eta = (v_\parallel / v_\perp) \cos(\varphi - \varphi_v) ,$$

$$k_c(\varphi) = k_o \Psi_a \cos\psi [1 - \sin^2\psi . \sin^2(\varphi - \varphi_v)]^{-1/2}$$

$\underline{k}_o$ is the electron wave vector incident at an angle ψ with the surface normal. φ_v is the azimuthal angle of the plane of incidence, and Ψ_a is the spectrometer half-acceptance angle.

Appendix IV

Prediction of HREEL Spectra taking into account the Tensor Properties of the Dielectric Function in the case where the c-axis is directed along the Surface Normal: Programme FTSOPHW2

The computer programme is reproduced below, followed by notes:

```
10 INPUT "What power of 2";NO: GOSUB 740
20 INPUT "Energy span, in eV";EE
30 INPUT "V cos theta";VV
40 INPUT "Epsilon hf (perpendicular)";ER
50 INPUT "Epsilon hf (parallel)";EL
60 INPUT "Number of phonon modes corresponding to E perpendicular to c";NR
70 PRINT "input energy (eV), width (eV), intensity"
80 FOR I=1 TO NR
90 INPUT WR(I),GR(I),ZR(I)
100 ZR(I)=ZR(I)*WR(I)^2
110 GR(I)=GR(I)
120 NEXT I
130 INPUT "Number of phonon modes corresponding to E parallel to c";NL
140 PRINT "Input energy (eV), width (eV), intensity"
150 FOR I=1 TO NL
160 INPUT WL(I),GL(I),ZL(I)
170 ZL(I)=ZL(I)*WL(I)^2
180 GL(I)=GL(I)
190 NEXT I
200 NW=RO: W1=EE/RO: DW=W1
210 W1=W1-DW
220 SM=0
230 TO=0
240 C=0
250 FOR N=1 TO NW
260 W1=W1+DW
270 DL=2*DW/W1/VV
280 E1=ER
290 E2=0
300 FOR I=1 TO NR
310 AR=WR(I)^2-W1^2
320 BR=W1*GR(I)
330 CR=AR*AR+BR*BR
340 E1=E1+ZR(I)*AR/CR
350 E2=E2-ZR(I)*BR/CR
360 NEXT I
370 L1=EL
380 L2=0
```

```
390 FOR I=1 TO NL
400 AL=WL(I)^2-W1^2
410 BL=W1*GL(I)
420 CL=AL*AL+BL*BL
430 L1=L1+ZL(I)*AL/CL
440 L2=L2-ZL(I)*BL/CL
450 NEXT I
460 XX=E1*L1-E2*L2
470 YY=L1*E2+L2*E1
480 M2=SQR(XX*XX+YY*YY):M=SQR(M2)
490 IF XX=0 THEN TH=-ATN(1): GOTO 550
500 TH=0.5*ATN(YY/XX)
510 T1=TH
520 IF (TH-T0)>0.9 THEN C=C+1:GOTO 540
530 IF (T0-TH)>0.9 THEN C=C-1:GOTO 540
540 TH=TH-2*C*ATN(1)
550 CT=COS(TH):ST=SIN(TH)
570 X(N)=-M*ST/((M*CT+1)^2+M*M*ST*ST)*DL
580 T0=T1
590 SM=SM+X(N)
600 NEXT N
610 PRINT"Total loss intensity =",SM
620 GOSUB 1110
630 INPUT"elastic peak width (eV)";WW:  GW=WW*RO/EE
640 INPUT"elastic peak position (eV)";EP:  NS=EP*RO/EE
650 INPUT"temperature (eV)";TT:   KT=TT*RO/EE
660 GOSUB 2030
670 GOSUB 1400
680 GOSUB 1880
690 GOSUB 1950
700 GOSUB 1780
710 GOSUB 1660
720 GOSUB 2120
730 END
740 REM...SET UP ARRAYS
750 F=.1
760 RO=INT(2^NO+F)-1: N1=NO-1: R1=INT(2^N1+F)-1: N2=N1-1: R2=INT(2^N2+F)-1
770 DIM X(RO),XR(R1+1),XI(R1+1),YR(R1),YI(R1),CO(R1),SI(R1),CH(R1),SH(R1)
780 A=8*ATN(1)/(R1+1):B=A/2
790 FOR I=0 TO R1
800 CO(I)=COS(I*A): SI(I)=SIN (I*A)
810 CH(I)=COS(I*B): SH(I)=SIN(I*B)
820 NEXT I:   RETURN
830 REM.............................
840 REM.............................
850 REM...BIT REVERSAL (YR,YI) TO (XR,XI)
860 FOR IX=0 TO R1: IY=0
870 FOR IV=0 TO N2
880 A=INT(2^IV+F):  B=INT(2^(N2-IV)+F)
890 IY=IY+B*(IX AND A)/A
900 NEXT IV
910 XR(IY)=YR(IX):  XI(IY)=YI(IX)
920 NEXT IX:     RETURN
```

```
1640 REM.............................
1650 REM.............................
1660 REM...BACK TRANSFORM (XR,XI)TO REALX
1670 YR(0)=(XR(0)+XR(R1+1))/2:YI(0)=(XR(R1+1)-XR(0))/2
1680 FOR I=1 TO R2+1:  IN=R1+1-I
1690 X1=(XR(I)+XR(IN))/2:   X2=(XR(I)-XR(IN))/2:   Y1=-(XI(I)+XI(IN))/2:  Y2=-(X
I(I)-XI(IN))/2
1700 YR(IN)=X1-SH(I)*X2-CH(I)*Y1
1710 YR(I)=X1+SH(I)*X2+CH(I)*Y1
1720 YI(IN)=-Y2-CH(I)*X2+SH(I)*Y1
1730 YI(I)=Y2-CH(I)*X2+SH(I)*Y1
1740 NEXT I:  GOSUB 850:  GOSUB 950
1720 YI(IN)=-Y2-CH(I)*X2+SH(I)*Y1
1730 YI(I)=Y2-CH(I)*X2+SH(I)*Y1
1740 NEXT I:  GOSUB 850:  GOSUB 950
1750 FOR I=0 TO R1
1760 X(2*I)=XR(I):  X(2*I+1)=-XI(I)
1770 NEXT I: GOSUB 1110: RETURN
1780 REM.............................
1790 REM.............................
1800 REM...SHIFT FT BY NS CHANNELS
1810 Q=8*NS*ATN(1)/RO
1820 FOR I=0 TO R1+1
1830 CX=COS(I*Q):  SX=SIN(I*Q)
1840 RX=CX*XR(I)-SX*XI(I)
1850 XI(I)=CX*XI(I)+SX*XR(I)
1860 XR(I)=RX
1870 NEXT I:      RETURN
1880 REM.............................
1890 REM.............................
1900 REM...EXPONENTIAL OF FT
1910 FOR I=0 TO R1+1
1920 EXX=EXP(XR(I))
1930 XR(I)=EXX*COS(XI(I)):  XI(I)=EXX*SIN(XI(I))
1940 NEXT I:   RETURN
1950 REM.............................
1960 REM.............................
1970 REM...LORENZTIAN BROADENING
1980 WG=2*GW/RO/LOG(2)
1990 FOR I=1 TO R1+1
2000 GF=EXP(-I*WG)
2010 XR(I)=GF*XR(I):  XI(I)=GF*XI(I)
2020 NEXT I:   RETURN
2030 REM.............................
2040 REM.............................
2050 REM...THERMAL EXCITATION WITH B-E STATISTICS
2060 FOR I=1 TO R1:  II=R0+1-I
2070 KX=I/KT: IF KX>20 THEN RETURN
2080 XX=X(I)/(EXP(KX)-1)
2090 X(I)=X(I)+XX:  X(II)=X(II)+XX
2100 NEXT I
2110 RETURN
```

```
930 REM.............................
940 REM.............................
950 REM...FFT ROUTINE ON (XR,XI)
960 FOR S=0 TO N2
970 T=INT(2^S+F): D=INT(2^(N2-S)+F)
980 FOR Z=0 TO T-1
990 L=D*Z
1000 FOR I=0 TO D-1
1010 A=2*I*T+Z:  B=A+T
1020 F1=XR(A):  F2=XI(A)
1030 P1=CO(L)*XR(B): P2=SI(L)*XI(B)
1040 P3=SI(L)*XR(B): P4=CO(L)*XI(B)
1050 XR(A)=F1+P1-P2: XI(A)=F2+P3+P4
1060 XR(B)=F1-P1+P2: XI(B)=F2-P3-P4
1070 NEXT I:  NEXT Z:  NEXT S
1080 RETURN
1090 REM.............................
1100 REM.............................
1110 REM...PLOT X
1120 X1=0: X2=0
1130 FOR I=0 TO R0
1140 IF X1>X(I) THEN X1=X(I)
1150 IF X2<X(I) THEN X2=X(I)
1160 NEXT I:  XP=150/(X2-X1)
1170 GRAPH 1: CALL"RESOLUTION",0,2
1180 FOR I=0 TO R0
1190 CALL"PLOT",I,XP*(X(I)-X1),3
1200 NEXT I:     RETURN
1210 REM.............................
1220 REM.............................
1230 REM...PLOT (XR,XI)
1240 X1=0: X2=X1: Y1=X1: Y2=X1
1250 FOR I=0 TO R1
1260 IF X1>XR(I) THEN X1=XR(I)
1270 IF X2<XR(I) THEN X2=XR(I)
1280 IF Y1>XI(I) THEN Y1=XI(I)
1290 IF Y2<XI(I) THEN Y2=XI(I)
1300 NEXT I: XP=75/(X2-X1)
1310 IF (Y2-Y1)<.001 THEN YP=1:GOTO 1330
1320 YP=75/(Y2-Y1)
1330 GRAPH 1: CALL"RESOLUTION",0,2
1340 FOR I=0 TO R1
1350 CALL"PLOT",I,XP*(XR(I)-X1)+100,3
1360 CALL"PLOT",I,YP*(XI(I)-Y1),3
1370 NEXT I:   RETURN
1380 REM.............................
1390 REM.............................
1400 REM...FORWARD FT: REAL X TO (XR,XI)
1410 FOR I=0 TO R1
1420 YR(I)=X(2*I):  YI(I)=X(2*I+1)
1430 NEXT I:  GOSUB 850:  GOSUB 950
1440 XR(0)=XR(0)+XI(0):XR(R1+1)=XR(0)-2*XI(0):XI(0)=0
1450 FOR I=1 TO R2+1:  IN=R1+1-I
1460 X1=(XR(I)+XR(IN))/2: X2=(XR(I)-XR(IN))/2:  Y1=(XI(I)+XI(IN))/2:  Y2=(XI(I)-
XI(IN))/2
1470 XR(IN)=X1-CH(I)*Y1-SH(I)*X2
1480 XI(IN)=-Y2+SH(I)*Y1-CH(I)*X2
1490 XR(I)=X1+CH(I)*Y1+SH(I)*X2
1500 XI(I)=Y2+SH(I)*Y1-CH(I)*X2
1510 NEXT I:   RETURN
1520 REM.............................
1530 REM.............................
1540 REM...PLOT POWER SPECTRUM FROM (XR,XI)
1550 X1=0:  FOR I=0 TO R1
1560 X(I)=XR(I)^2+XI(I)^2
1570 IF X(I)>X1 THEN X1=X(I)
1580 NEXT I:  XP=160/X1
1590 CALL"RESOLUTION",0,2
1600 FOR I=0 TO R1
1610 CALL"PLOT",I,0,3
1620 CALL"LINE",I,XP*X(I),3
1630 NEXT I:  RETURN
```

```
2120 REM     puts data in file
2130 PRINT " INSERT DISC FOR FILING DATA"
2140 PRINT "THEN TYPE FILENAME -- ------ ---"
2150 INPUT F$
2160 RESET
2170 CREATE #10 , F$
2180 R0=R0+1
2190 PRINT #10, R0
2200 PRINT "  LABEL FOR FILE?"
2210 INPUT LINE LB$
2220 PRINT #10, LB$
2220 PRINT #10, 1
2240 R0=R0-1
2250 FOR N=1 TO R0
2260 PRINT #10 , X(N)
2270 NEXT N
2280 PRINT #10,E1,",",E2
2290 CLOSE #10
2300 RETURN
```

Notes to the Programme

10 The power of 2 input defines the number of points in the spectrum.

20-190 Inputs the necessary information. VV is the z component of the beam velocity.

200-450 Calculates the real (E_1,L_1) and imaginary (E_2,L_2) parts of the dielectric function for both $\varepsilon_\perp$ and $\varepsilon_\parallel$ at each point in the spectrum, via equation (12) of Chapter 3.

460-570 The quantity $(\varepsilon_\perp(\omega)\varepsilon_\parallel(\omega))^{1/2}$ is expressed in the form

$$(x+iy)^{1/2}=r^{1/2}(\cos\theta/2 + i\sin\theta/2)$$

where $\theta/2=1/2\tan^{-1}y/x$, and $r=(x^2+y^2)^{1/2}$. This is then inserted into the loss function $P(\omega)$ in line 570. Lines 500-540 are necessary to provide continuity to the loss function, as BASIC automatically defines an angle in the range $-\pi/2<\theta<\pi/2$. The loss function is calculated at each point in the spectrum.

590-620 The total loss intensity is calculated, and the loss function is plotted.

The remainder of the programme self-convolutes the spectrum, in accordance with the Poisson distribution, and broadens all the lines by a specified elastic peak width. The elastic peak is assumed to be a Lorentzian line shape. Bose-Einstein statistics are used in lines 2050-2100 to introduce anti-Stokes peaks into the spectrum. The resulting spectrum is plotted and stored on disc. The convolution and plotting routines were written by Dr.P.A. Cox and have been described elsewhere[177].

Appendix V

Prediction of HREEL Spectra taking into account the Tensor Properties of the Dielectric Function in the case where the c-axis lies in the Surface Plane: Programme FTSOPHW3

A portion of the programme is reproduced below, followed by notes:

```
5 PRINT"anisotropic materials - general case, c-axis in surface"
10 INPUT "What power of 2";NO: GOSUB 950
20 INPUT "Energy span, in eV";EE
30 INPUT "Beam energy, in (eV)";BE
50 INPUT "Angle between plane of incidence and plane containing c and z axes,
 degrees";FV
60 FV=FV*8*ATN(1)/360
70 INPUT "Incidence angle with z axis, in degrees (usually specular)";PS
80 PS=PS*8*ATN(1)/360
90 VC=((2*BE/27.2)^0.5)*COS(PS)
100 VS=((2*BE/27.2)^0.5)*SIN(PS)
105 KO=VS
110 INPUT "Spectrometer half-acceptance angle";FA
120 FA=FA*8*ATN(1)/360
130 F0=0
140 F1=8*ATN(1)
150 INPUT"Number of phi values included in Simpson's rule integration (must be o
dd)";MF
160 INPUT "Epsilon hf (perpendicular)";ER
170 INPUT "Epsilon hf (parallel)";EL
180 INPUT "Number of phonon modes corresponding to E perpendicular to c";NR
190 PRINT "input energy (eV), width (eV), intensity"
200 FOR I=1 TO NR
210 INPUT WR(I),GR(I),ZR(I)
220 ZR(I)=ZR(I)*WR(I)^2
230 GR(I)=GR(I)
240 NEXT I
250 INPUT "Number of phonon modes corresponding to E parallel to c";NL
260 PRINT "Input energy (eV), width (eV), intensity"
270 FOR I=1 TO NL
280 INPUT WL(I),GL(I),ZL(I)
290 ZL(I)=ZL(I)*WL(I)^2
300 GL(I)=GL(I)
310 NEXT I
```

```
320 NW=RO: W1=EE/RO: DW=W1
330 W1=W1-DW
340 SM=0
370 FOR N=1 TO NW
380 W1=W1+DW
390 E1=ER
400 E2=0
410 FOR I=1 TO NR
420 AR=WR(I)^2-W1^2
430 BR=W1*GR(I)
440 CR=AR*AR+BR*BR
450 E1=E1+ZR(I)*AR/CR
460 E2=E2-ZR(I)*BR/CR
470 NEXT I
480 L1=EL
490 L2=0
500 FOR I=1 TO NL
510 AL=WL(I)^2-W1^2
520 BL=W1*GL(I)
530 CL=AL*AL+BL*BL
540 L1=L1+ZL(I)*AL/CL
550 L2=L2-ZL(I)*BL/CL
560 NEXT I
570 AA=E1*L1-E2*L2
580 BB=L1*E2+L2*E1
590 CC=E1*E1-E2*E2
600 DD=2*E1*E2
610 REM .....Integration by Simpson's rule
620 W1=W1/27.2
630 M=MF-1
640 DF=(F1-F0)/M
650 F=F0
660 GOSUB 2330
670 SS=IL
680 IC=2
690 FOR I=1 TO M-1
700 F=F+DF
710 GOSUB 2330
720 IF IC=2 THEN IC=4 ELSE IC=2
730 SS=SS+IC*IL
740 NEXT I
750 F=F+DF
760 GOSUB 2330
770 IP=DF/3*(SS+IL)
780 W1=W1*27.2
790 X(N)=-IP*DW/VC/W1/(8*ATN(1)*ATN(1))
800 SM=SM+X(N)
810 NEXT N
820 PRINT"Total loss intensity =",SM
```

.

.

.

```
2330 REM.......calculates IL
2340 ET=COS(F-FV)*VS/VC
2350 YC=VC*KO*FA*COS(FS)/((1-SIN(FS)*SIN(FS)*SIN(F-FV)*SIN(F-FV))^0.5)
2360 AC=AA*COS(F)*COS(F)+CC*SIN(F)*SIN(F)
2370 BD=BB*COS(F)*COS(F)+DD*SIN(F)*SIN(F)
2380 IF AC=0 THEN TH=-ATN(1):GOTO 2440
2390 TH=0.5*ATN(BD/AC)
2410 IF AC<0 THEN TH=TH-2*ATN(1): GOTO 2440
2420 IF BD>0 THEN TH=TH+4*ATN(1): GOTO 2440
2440 CT=COS(TH):ST=SIN(TH)
2460 M2=SQR(AC*AC+BD*BD):M1=SQR(M2)
2470 IM=ST*M1/((M1*CT+1)^2+M1*M1*ST*ST)
2480 I4=YC*YC*ET-YC*W1
2490 I5=(ET*YC-W1)^2+YC*YC
2500 I1=I4/I5
2510 I2=ATN(((ET*ET+1)*YC/W1)-ET)
2520 I3=ATN(ET)
2530 IL=(I1+I2+I3)*IM
2540 RETURN
```

Notes to the Programme

5-310 Inputs the necessary information, and calculates VC and VS, corresponding to the two components of the velocity, $v\cos\phi$, $v\sin\phi$ (figure AIII.1).

320-560 Calculates the real (E_1,L_1) and imaginary (E_2,L_2) parts of the dielectric function for $\varepsilon_\perp$ and $\varepsilon_\parallel$ at each point in the spectrum, as for FTSOPHW2.

570-760 For the special case considered, we have

$$\zeta=[\varepsilon_\parallel(\omega)\varepsilon_\perp(\omega)\cos^2\varphi+\varepsilon_\perp(\omega)^2\sin^2\varphi]^{1/2}$$

This is again reduced to the form

$$(AC+iBD)^{1/2}=r^{1/2}(\cos\theta/2 + i\sin\theta/2)$$

where $\theta/2=1/2\tan^{-1}BD/AC$, and $r=((AC)^2+(BD)^2)^{1/2}$. The imaginary part of the loss function $P(\varphi,\omega)$ (equation AIII(11)) is then calculated at each point in the spectrum in line 2470. In a subroutine (line 2330), η and k_c are calculated in terms of φ (equation AIII(11)), and the integral required is reduced to the form $\int_o^{2\pi}(I_1+I_2+I_3)*IM\ d\varphi$. The integration is performed using Simpson's rule (lines 610-770), in accordance with the expression

$$\int_a^b f(x)dx = h/3\{f_0+f_n+4(f_1+f_3+\ldots f_{n-1})+2(f_2+f_4+\ldots f_{n-2})\} \qquad AV(1)$$

which is defined as shown in figure AV.1.

The number of values over which this integration is performed is input by the operator in line 150. A suitable value was found to be ~15. The integration is performed for each point in the spectrum.

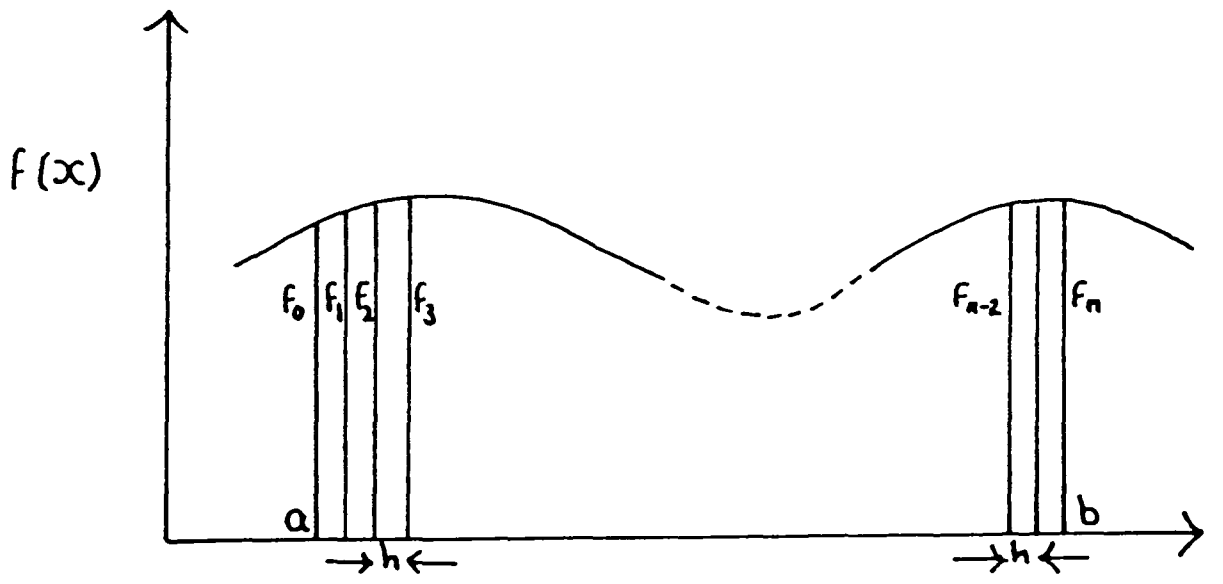

Figure AV.1: Integration of a function f(x) using Simpson's rule.

770-820 The loss function $P(\omega)$ is calculated at each point in the spectrum. The total loss intensity is calculated, and the loss function is plotted.

The remainder of the programme, which convolutes and broadens the loss function, and introduces anti-Stokes losses, is identical to FTSOPHW2 (Appendix IV).

References

1. D.W. Turner and M.I. Al Jobory, J. Chem. Phys., 37, (1962), 3007.
2. M.I. Al Jobory and D.W. Turner, J. Chem. Soc., 5, (1963), 5141.
3. K. Siegbahn et al, "ESCA: Atomic, Molecular and Solid State Structure studied by means of Electron Spectroscopy", Almquist and Wilksells, Uppsala, (1967).
4. see e.g. C. Kunz in "Photoemission in Solids II. Case Studies", Topics in Applied Physics, 27, ed. L. Ley and M. Cardona, Springer-Verlag, Berlin (1979).
5. A. Einstein, Ann. Phys., 17, (1905), 132.
6. C.N. Berglund and W.E. Spicer, Phys. Rev., 136A, (1964), 1030.
7. see e.g. C. Caroli, D. Lederer-Rozenblatt, B. Roulet and D. Saint-James, Phys. Rev., B8, (1973), 4552.
8. A. Liebsch, Phys. Rev., B13, (1976), 544.
9. J.B. Pendry, Surf. Sci., 57, (1976), 679.
10. S. Evans, R.G. Pritchard and J.M. Thomas, J. Electron Spectrosc. Relat. Phenom., 14, (1978), 341.
11. S.M. Goldberg, C.S. Fadley and S. Kono, J. Electron Spectrosc. Relat. Phenom., 21, (1981), 285.
12. see e.g. L. Ley, M. Cardona and R.A. Pollak, in "Photoemision in Solids II. Case Studies", Topics in Applied Physics, 27, ed. L. Ley and M. Cardona, Springer-verlag, Berlin, (1979).
13. A.F. Orchard, "Handbook of X-ray and UV Photoelectron Spectroscopy", ed. D. Briggs, Heyden, London, (1977).
14. J. Szajman and R.C.G. Leckey, J. Electron Spectrosc. Relat. Phenom., 23, (1981), 83.
15. J. Szajman, J. Liesegang, J.G. Jenkin and R.C.G. Leckey, J. Electron Spectrosc. Relat. Phenom., 23, (1981), 97.

16. D.A. Shirley in "Photoemission in Solids I. General Principles", Topics in Applied Physics, 26, ed. M. Cardona and L. Ley, Springer-Verlag, Berlin, (1978).

17. P.M. Williams in "Handbook of X-ray and UV Spectroscopy", ed. D. Briggs, Heyden, London, (1977).

18. W.D. Grobman and E.E. Koch in "Photoemission in Solids II. Case Studies", Topics in Applied Physics, 27, ed. L. Ley and M. Cardona, Springer-Verlag, Berlin, (1979).

19. N.V. Smith in "Photoemission in Solids I. General Principles", Topics in Applied Physics, 26, ed. M. Cardona and L. Ley, Springer-Verlag, Berlin, (1978).

20. see e.g. G.V. Hansson and S.A. Flodstrom, Phys. Rev., B17, (1978), 473.

21. J.A.R. Samson, "Techniques of Vacuum Ultra-Violet Spectroscopy", John Wiley, New York, (1967).

22. R. Samson, Part II Thesis, Oxford,(1982).

23. M.G. Hynes, Part II Thesis, Oxford, (1984).

24. M.O. Krause and J.G. Ferreira, J. Phys., B8, (1975), 2007.

25. see e.g. R. Manne and T. Aberg, Chem. Phys. Lett., 7, (1970), 282.

26. T.A. Carlso, M.O. Krauze and W.E. Moddeman, J. Phys. (Colloques), 32, (1971), C4.

27. P.A. Cox, D.Phil. Thesis, Oxford, (1973).

28. S. Evans, Chem. Phys. Lett., 23, (1973), 134.

29. D.A. Shaw, G.C. King, F.H. Read and D. Cvejanovic, J. Phys., B15, (1982), 1785.

30. B.G. Williams and A.J. Bourdillon, J. Phys., C15, (1982), 6881.

31. J. Geiger, "Electronen und Festkörper", 128, Sammlung Vieweg, Braunschweig, (1968).

32. H. Raether, "Springer Tracts in Modern Physics", 38, Springer-Verlag, Berlin, (1968), 85.

33. G.D. Mahan in "Elementary Excitations in Solids, Molecules and Atoms: Part B", ed. J.T. Devreese, A.B. Kunz and T.C. Collins, Plenum, New York, (1974).

34. R.F. Wallis, Prog. Surf. Sci., 4(3), (1974), 233.

35. A.A. Lucas and M. Sunjic, Prog. Surf. Sci., 2, (1972), 75.

36. R. Fuchs and K.L. Kliewer, Phys. Rev., 140, A2076, (1965).

37. H. Ibach and D.L. Mills, "Electron Energy Loss Spectroscopy and Surface Vibrations", Academic Press, New York, (1982).

38. P.A. Cox and A.A. Williams, Surf. Sci., 152/153, (1985), 791.

39. J. Pendry, "Electron Diffraction", Academic Press, New York, (1974).

40. "ESCALAB Operating Instructions", V.G. Scientific.

41. R.D. Willmer, Part II Thesis, Oxford, (1981).

42. M.D. Hill, Part II Thesis, Oxford, (1981).

43. M.D. Hill, D.Phil. Thesis, Oxford, (1984).

44. "Model 6240B Multichannel Analyser Operating Manual", Ortec.

45. P.A. Cox, W.R. Flavell, A.A. Williams and R.G. Egdell, Surf. Sci., 152/153, (1985), 784.

46. M.S. Wrighton, D.S. Ginley, P.T. Wolczanski, A.B. Ellis, D.L. Morse and A. Linz, Proc. Nat. Acad. Sci. USA, 72(4), (1975), 1518.

47. A. Jujishima and K. Honda, Nature, 238, (1972), 37.

48. "Solar Energy Conversion: Solid State Physics Aspects", in Topics in Applied Physics, 31, ed. B.O. Seraphim, Springer-Verlag, Berlin, (1981), and references therein.

49. A. Inone, T. Ono and T. Ohhara, Japan Kokai Patent, (1977), (Cl.BO1J27/16).

50. K. Nishimoto, S Yokoyama and T. Sera, Japan Koka Tokkyo Koko Patent (1980), (Cl.BO1J23/30).

51. e.g. L.A. Kasatkina and S.V. Ratina, Mosk. Khim.-Tecknol. Inst im. D.I. Mendeleeva, 99, (1978), 96.

52. e.g. S. Nishizaka, T. Abe and Y. Miyakoshi, Japan Koka Patent (1977), (C1.C07D307/89).

53. P.A. Cox, R.G. Egdell, S. Eriksen and W.R. Flavell, J. Electron Spectrosc. Relat. Phenom., (1986), in press.

54. B.N.J. Persson, Solid State Commun., 24, (1977), 573.

55. D.M. Newns in "Vibrational Spectroscopy of Adsorbates", Springer Series in Chemical Physics, 15, ed. R.F. Willis, Springer-Verlag, Berlin, (1980).

56. H. Froitzheim in "Electron Spectroscopy for Surface Analysis", Topics in Current Physics, 4, Springer-Verlag, Berlin, (1977), 205.

57. H. Ibach, J. Vac. Sci. Technol., 9, (1972), 713.

58. H. Ibach, Phys. Rev. Lett., 24, (1970), 1416.

59. G.J. Schutz, Rev. Mod. Phys., 45, (1973), 423.

60. e.g. L Sanche and M. Michaud, Phys. Rev. Lett., 47, (1981), 1008.

61. e.g. J.E. Demuth, D.S. Schmeisser and Ph. Avouris, Phys. Rev. Lett., 47, (1981), 1166.

62. J.G. Gay, W.A. Albers Jr. and F.J. Arlinghaus, J. Phys. Chem. Solids, 29, (1968), 1449.

63. R.S. Katiyar, J. Phys., C3, (1970), 1087.

64. W.G. Spitzer, R.C. Miller, D.A. Kleinman and L.E. Howarth, Phys. Rev., 126, (1962), 1710.

65. L.L. Kesmodel, J.A. Gates and Y.W. Chung, Phys. Rev., B23, (1981), 493.

66. S. Bhagarantam and T. Venkatarayudu, Proc. Indian Acad. Sci., 9A, 224, (1939).

67. F. Gervais and B. Piriou, J. Phys., C7, (1974), 2374.

68. F. Gervais, D. Billard and B. Piriou, Rev. Int. Htes. Temp. et Réfract., 12, (1975), 58.

69. B. Piriou, Rev. Hautes Tempér. et Réfract., 3, (1966), 109.

70. G. Rocker, J.A. Schaefer and W. Gŏpel, Phys. Rev., B30(7), (1984), 3704.

71. G.D. Mahan, unpublished.

72. P.J. Tavener, D.Phil. Thesis, Oxford, (1985).

73. J.L. Amorós, M.J. Buerger and M.C. de Amorós, "The Laue Method", Academic Press, New York, (1975), 135.

74. R.H. Tait and R.V. Kasowski, Phys. Rev., B20(12), (1979), 5178.

75. A.A. Lucas and J.P. Vigneron, Solid State Commun., 49, (1984), 327.

76. M. Liehr, P.A. Thiry, J.J. Pireaux and R. Caudano, J. Vac. Sci. Technol., A2(2), (1984), 1079.

77. V.E. Henrich, G. Dresselhaus and H.J. Zieger, Phys. Rev. Lett., 36, (1976), 1335.

78. W.J. Lo, Y.W. Chung and G.A. Somorjai, Surf. Sci., 71, (1978), 199.

79. W. Göpel, J.A. Anderson, D. Frankel, M. Jaehnig, K. Phillips, J.A. Schäfer and G. Rocker, Surf. Sci., 139, (1984), 333.

80. M.L. Knotek and P.J. Feibelman, Phys. Rev. Lett., 40, (1978), 964.

81. D.C. Cronemayer, Phys. Rev., 113, (1959), 1222.

82. W.R. Flavell, Part II Thesis, Oxford, (1983).

83. S. Ferrer and G.A. Somorjai, Surf. Sci., 94, (1980), 41.

84. Y.M. Chung, W.J. Lo and G.A. Somorjai, Surf. Sci., 64, (1977), 588.

85. V.E. Henrich, G. Dresselhaus and H.J. Zeiger, Solid State Commun., 24, (1977), 623.

86. V.E. Henrich, G. Dresselhaus and H.J. Zeiger, Phys. Rev., B17, (1978), 4908.

87. P.A. Cox, M.D. Hill, F. Peplinski and R.G. Egdell, Surf. Sci., 141, (1984), 13.

88. J.C.C. Fan and F.J. Bachner, J. Electrochem. Soc., 122, (1975), 1719.

89. H. Köstlin, R. Jost and W. Lems, phys. stat. sol. (a), 29, (1975), 87.

90. G. Frank, H. Köstlin and A. Rabenau, phys. stat. sol. (a), 52, (1979), 231.

91. R.G. Egdell, W.R. Flavell and P.J. Tavener, J. Solid State Chem., 51, (1984), 345.

92. P.J. Tavener, Part II Thesis, Oxford, (1982).

93. P.A. Cox, R.G. Egdell, C. Harding, A.F. Orchard, W.R. Patterson and P.J. Tavener, Solid State Commun., 44, (1982), 837.

94. J.-C. Manifacier, L. Szepessy, J.F. Bresse and M. Perotin, Mat. Res. Bull., 14, (1979), 109.

95. F. Buigez, G. Bomchill, S. Galzin and A. Monfret, Colloque Microélectronique, Montpellier, (16-19 Nov 1976), 146.

96. E. Giani and R. Kelly, J. Electrochem. Soc.: Solid State Science and Technology, 121, (1974), 394.

97. J. Kane and H.P. Schweitzer, Thin Solid Films, 29, (1975), 155.

98. G. Frank, E. Kauer and H. Köstlin, Thin Solid Films, 77, (1981), 107.

99. H.W. Lehmann and R. Widmer, Thin Solid Films, 27, (1975), 359.

100. D.B. Frazer and H.D. Cook, J. Electrochem. Soc., 119, (1972), 1368.

101. J.L. Vossen, RCA Rev., 32, (1971), 289.

102. O.P. Agnihotri, A.K. Sharma, B.K. Gupta and R. Thangaraj, J. Phys., D11, (1978), 643.

103. D.K. Ranadive, F.T.J. Smith and R.P. Khosla, Proc. 6th Intern. Conf. Chemical Vapour Deposition, (1977), (The Electrochem. Soc. 1978), 448.

104. R. Groth, phys. stat. sol., 14, (1966), 69.

105. H. Hoffman, J. Pickl, M. Schmidt and D. Krause, Appl. Phys., 16, (1978), 239.

106. V.M. Vainshtein, and V.I. Fistul', Sov. Phys. Semicond., 4, (1971), 1278.

107. H. Köstlin in Festkörperprobleme, 22, (1982), 229.

108. H. Köstlin, Elektrizitätsverwertung, 49, (1974), 458.

109. e.g. G. Rupprecht, Z. Phys., 139, (1954), 504
E. Kauer and R. Rabenau, Z. Naturf., 13, (1958), 533.

110. R.L. Weiher and R.P. Ley, J. Appl. Phys., 37, (1966), 299.

111. J.H.W. de Wit, J. Solid State Chem., 20, (1977),143.

112. J.H.W. de Wit, G. van Unen and M. Lahey, J. Phys. Chem. Solids, 38, (1977), 819.

113. R.W.G. Wyckoff, "Crystal Structures", 2, Interscience, New York, (1964), 4.

114. M. Hecq, A. Dubois and J. van Cakenberghe, Thin Solid Films, 18, (1973), 117.

115. J.R. Bosnell and R. Waghorne, Thin Solid Films, 15, (1973), 141.

116. J.C.C. Fan and J.B. Goodenough, J. Appl. Phys., 48, (1977), 3524.

117. K.D.J. Christian and S.R. Shatynski, Thin Solid Films, 108, (1983), 319.

118. N.R. Armstrong, A.W.C. Lin, M. Fujihira, and T. Kuwana, Anal. Chem., 48, (1976), 741.

119. G. Frank and H. Köstlin, Appl. Phys., A27, (1982), 197.

120. G. Frank, R. Olazcuaga and A. Rabenau, Inorg. Chem., 16, (1977), 1251.

121. Z.M. Jarzebski, phys. stat. sol. (a), 71, (1982), 13.

122. Swanson, Gilfrich and Ugrinic in NBS Standard X-ray Diffraction Powder Patterns, NBS Circular 539, 5, (1955), set 6-0416, 26.

123. ASTM Powder Diffraction File, set 5-467.

124. Swanson, Fuyal and Ugrinic in NBS Standard X-ray Diffraction Powder Patterns, NBS Circular 539, 4, (1955), 29.

125. ASTM Powder Diffraction File, (1967), set 7-195, 213.

126. JCPOS Powder Diffraction File, (1974), set 16-737, 214.

127. A.K. Cheetham and A.J. Skarnulis, Anal. Chem., 53, (1981), 1060.

128. W.B. White and V.G. Keramidas, Spectrochim. Acta, 28A, (1972), 501.

129. D.S. and M.J.S. Urch, "ESCA(Mg) - Auger Table", supplied by V.G. Scientific, East Grinstead, (1981).

130. G.A. Somorjai, "Chemistry in Two Dimensions: Surfaces", Cornell University Press, Ithaca, (1981).

131. R.L. Weiher, J. Appl. Phys., 33, (1962), 2834.

132. I. Hamberg, C.G. Granqvist, K.-F. Berggren, B.E. Sernelius and L. Engström, Phys. Rev., B30, (1984), 3240.

133. K.F. Herzfeld, Phys. Rev., 39, (1927), 701.

134. K.-F. Berggren, J. Chem. Phys., 60, (1974), 3399 and 61, (1974), 2989.

135. P.P. Edwards and M.J. Sienko, Acc. Chem. Research, 15, (1982), 87.

136. J.S. Blakemore, "Solid State Physics", Saunders, Philadelphia, (1974).

137. P.A. Cox, Solid State Commun., 45, (1983), 91.

138. Y. Ohhata, F. Shinoki, and S. Yoshida, Thin Solid Films, 59, (1979), 255.

139. D.R. Pyke, R. Reid and R.J.D. Tilley, J. Chem. Soc. Faraday Trans. I, 76, (1980), 1174.

140. S.P. Kowalczyk, Ph.D. Thesis, Univ. of California, (1976).

141. J.A. Marley and R.C. Dockerty, Phys. Rev., 140, (1965), A304.

142. R.G. Egdell, M.H. Palmer and R.H. Findlay, Inorg. Chem., 19, (1980), 1314.

143. C.E. Wickersham and J.E. Greene, phys. stat. sol. (a), 47, (1978), 329.

144. M. Mizuhashi, Thin Solid Films, 70, (1980), 91.

145. H.K. Müller, phys. stst. sol., 27, (1968), 723.

146. E. Shanti, A. Banerjee, V. Dutta and K.L. Chopra, Thin Solid Films, 71, (1980), 237.

147. J.A. Thornton and V.L. Hedgcoth, J. Vac. Sci. Technol., 13, (1976), 117.

148. J.F. Smith, A.J. Aronson, D. Chen and W.H. Class, Thin Solid Films, 72, (1980), 469.

149. W.G. Haines and R.H. Rube, J. Appl. Phys., 49, (1978), 304.

150. J.C.C. Fan, F.J. Bachner and G.H. Foley, Appl. Phys. Lett., 31, (1977), 773.

151. H. Hoffman, A. Dietrich, J. Pickl and D. Krause, Appl. Phys., 16, (1978), 381.

152. M. Mizuhashi, Thin Solid Films, 76, (1981), 97.

153. P.A. Cox, private communication.

154. H. Froitzheim, H. Ibach and D.L. Mills, Phys. Rev., B11, (1975), 4980.

155. L.H. Dubois and G.P. Schwartz, J. Vac. Sci. Technol., B2, (1984), 101.

156. A. Ritz and H. Lüth, Phys. Rev. Lett., 52, (1984), 1242.

157. K. Siegbahn, J. Electron Spectrosc. Relat. Phenom., 5, (1974), 1.

158. L.H. Dubois, G.P. Schwartz, R.E. Camley and D.L. Mills, Phys. Rev., B29, (1984), 3208.

159. C.D. Kohl, Appl. Phys., A30, (1983), 127.

160. e.g. J. Pollman in Proc. 4th Conf. on Solid Surfaces, Suppl. a la Revue "Le Vide, les Couches Minces", 201, (1980), 7.

161. S. Trokman, A. Many, Y. Goldstein, G. Heiland, D. Kohl and H. Moorman, J. Phys. Chem. Solids, 42, (1981), 937.

162. J. Lux, D. Kohl and G. Heiland, "Le Vide, les Couches Minces" suppl., 201, (1980), 991.

163. R. Matz and H. Lüth, Phys. Rev. Lett., 46, (1981), 500.

164. M. Liehr and H Lüth, J. Vac. Sci. Technol., 16, (1979), 1200.

165. K. Jacobi, Surf. Sci., 132, (1983), 1.

166. R.W.G. Wyckoff, "Crystal Structures", 1, Interscience, New York, (1964), 250.

167. J.E. Huheey, "Inorganic Chemistry. Principles of Structure and Reactivity", Harper and Row, New York, (1978).

168. R. Summit, J. Appl. Phys., 39, (1968), 3762.

169. R.D. Sulley, unpublished.

170. A. Hamnett in Landolt-Börnstein, "Numerical Data and Functional Relationships in Science and Technology", New Series, ed. K.-F. Hellwege and O. Madelung, 3/17g, (1984), Springer-Verlag, Berlin.

171. P.K. Clifford and D.T. Tuma, Sensors and Actuators, 3, (1983), 233.

172. P.K. Clifford and D.T. Tuma, Sensors and Actuators, 3, (1983), 255.

173. P.K. Clifford, Plenary Lecture, Proc. Sensors Conf., Fukuoka Meeting, (Sept. 1983), 135.

174. M. Nitta, S. Kanefusa, and M. Haradome, J. Electrochem. Soc., 125, (1978), 1676.

175. M. Nitta, S. Kanefusa, K. Hoshino, Y. Taketa, and M. Haradome, Nippon Daigaku Seisan Kogakubu Hokoku A, 9(1), (1976), 131.

176. M. Nitta, S. Kanefusa, K. Hoshino, Y. Taketa, and M. Haradome, Nippon Daigaku Seisan Kogakubu Hokoku A, 9(1), (1976), 137.

177. P.A. Cox, private communication, F.J. Peplinski, Part II Thesis, Oxford, (1983).